University of Alberta

Modeling and Experimental Study of an HCCI Engine for Combustion Timing Control

by

Mahdi Shahbakhti

A thesis submitted to the Faculty of Graduate Studies and Research in partial fulfillment of the requirements for the degree of Doctor of Philosophy.

Department of Mechanical Engineering

Fall 2009
Edmonton, Alberta

Examining Committee

Dr. C. R. (Bob) Koch (Supervisor), Mechanical Engineering

Dr. M. David Checkel, Mechanical Engineering

Dr. Farbod Fahimi, Mechanical Engineering

Dr. Jason Olfert, Mechanical Engineering

Dr. Biao Huang, Chemical Engineering

Dr. James S. Wallace, Mechanical Engineering, University of Toronto

To those who have made my life a meaningful journey.

Abstract

Homogeneous Charge Compression Ignition (HCCI) is a promising method for combustion engines to provide a substantial reduction in fuel consumption and formation of both nitrogen oxides and soot pollutants in automotive and stationary engines. Control of HCCI combustion timing is essential for the successful integration of the HCCI concept in real applications. This thesis concentrates on control oriented modeling and experimental study of HCCI combustion for control of ignition timing in HCCI engines.

A detailed experimental study of HCCI with over 600 operating points on two different engines is done to characterize the complex relationship among the engine variables, the ignition timing and the exhaust temperature. This leads to identifying regions with distinct patterns of cyclic variation for HCCI ignition timing. In addition, main influential factors on the variations of ignition timing and exhaust temperature in HCCI engines are determined. A dynamic full-cycle physics based Control Oriented Model (COM) is derived from using the experimental data and simulations from an HCCI thermo-kinetic model. The COM is validated with a large number of transient and steady-state experimental points. The validation results show that the COM captures the key HCCI dynamics with a high degree of accuracy for control applications. The COM is computationally efficient and all inputs of the model can be readily measured or estimated on a real engine. This makes the COM simple and fast enough for use as an off-line simulation bed to design and evaluate different strategies for physics-based control of combustion timing in HCCI engines.

Acknowledgements

It is a great pleasure to take this opportunity to express my gratitude to the many people who have helped or supported this work.

I am heartily thankful to my supervisor, Dr. Bob Koch, whose encouragement, guidance and support from the initial to the final level enabled me to accomplish this work. He introduced me to HCCI engines and used his invaluable wealth of knowledge to mentor my understanding of the subject and to build up my research skills. At the same time Dr. Koch has been a wonderful counselor. He has always given me valuable advice for my future academic life and supported me to get a chance to teach a graduate course during my Ph.D.

I would also like to thank Dr. M. David Checkel for helping me to overcome both technical and teaching challenges during my Ph.D. His profound knowledge and generous sharing of time have contributed substantially to my understanding of combustion engines.

I am grateful to Dr. Farbod Fahimi for his valuable comments during this research, as well as the examination committee for their thorough feedbacks on the manuscript of the thesis.

I graciously acknowledge Robert Lupul and Adrian Audet for their contributions in collecting most of the experimental data for this work. I am profoundly indebted to them for their time and help. Thanks are also due to technician Bernie Faulkner for his help in making the setup for valve profile measurements.

Many thanks are deserved to my co-authors Kevin Swan, Ahmad Ghazimirsaied, and Patrick Kirchen for their work which significantly contributed to the quality of this thesis. Thanks to Dr. Vahid Hosseini and Dr. Paitoon Kongsereeparp for a lot of stimulating discussions which helped me to have a better understanding of my research subject. Special thanks to Masoud Mashkornia for his help to enhance my English language skills.

Thanks to my colleagues at room 4-28 as well as numerous friends at the University of Alberta for all the fun we have had. I will always remember the friendship formed in these five years.

Lastly, my family and Jie Sun are those whom I can not thank enough for their love, encouragement and supporting me spiritually throughout this work.

Table of Contents

List of Tables

List of Figures

Nomenclature

Acronyms

aBDC	after Bottom Dead Center.
aTDC	after Top Dead Center.
AFR	Air Fuel Ratio.
BD	Burn Duration.
bTDC	before Top Dead Center.
CAD	Crank Angle Degree.
CAI	Controlled Auto-Ignition.
CDF	Cumulative Distribution Function.
CF	Cool Flame.
CFD	Computational Fluid Dynamics.
CFR	Cooperative Fuels Research.
CI	Compression Ignition.
CO	Carbon Monoxide.
CO_2	Carbon Dioxide.
COM	Control Oriented Model.
COV	Coefficient of Variations.
CV	Control Volume.

DFM	Dual Fuel Modulation.
dp3Lim	Threshold Limit for 3^{rd} Derivative of Pressure Trace.
ECU	Engine Control Unit.
EGR	Exhaust Gas Recirculation.
EIA	Energy Input Air.
EIF	Energy Input Fuel.
EOC	End of Combustion.
EVC	Exhaust Valve Closing.
EVO	Exhaust Valve Opening.
FPGA	Field-Programmable Gate Array.
GEV	Generalized Extreme Value.
GHG	Greenhouse Gas.
HC	Hydrocarbons.
HCCI	Homogeneous Charge Compression Ignition.
H_2O	Water Vapor.
HL	Heat Loss.
HRR	Heat Release Rate.
HTR	High Temperature Reactions.
IMEP	Indicated Mean Effective Pressure.
IVC	Intake Valve Closing.
IVO	Intake Valve Opening.
KIM	Knock Integral Model.

LTR	Low Temperature Reactions.
MIMO	Multi-Input Multi-Output.
MFB	Mass Fraction Burned.
MKIM	Modified Knock Integral Model.
NASA	National Aeronautics & Space Administration.
N_2	Nitrogen Gas.
ND	Normal Distribution.
NOx	Oxides of Nitrogen.
O_2	Oxygen Gas.
ON	Octane Number.
P	Products.
PCM	Phase-Change Materials.
PDF	Probability Density Function.
PFI	Port Fuel Injection.
PM	Particulate Matter.
PRBS	Pseudo-Random Binary Sequence.
PRF	Primary Reference Fuel.
R	Reactants.
RPM	Revolution per Minute.
SI	Spark Ignition.
SOC	Start Of Combustion.
STD	Standard Deviation.

TDC	Top Dead Center.
TKM	Thermo-Kinetic Model.
UEGO	Universal Exhaust Gas Oxygen (sensor).
VVA	Variable Valve Actuation.
VCR	Variable Compression Ratio.
VVT	Variable Valve Timing
W/M	Weak/Misfired.

Symbols

A	Area [m^2].
AFR	Air Fuel ratio [-].
B	Bore [m].
CA_X	Crank angle for X% burnt fuel [CAD aTDC].
C_D	Discharge coefficient [-].
C_v	Constant-volume specific heat capacity [$\frac{\text{kJ}}{\text{kg.K}}$].
C_p	Constant-pressure specific heat capacity [$\frac{\text{kJ}}{\text{kg.K}}$].
C_r	Compression ratio [-].
CoC	Newtonian reference frame.
CoC	Completeness of combustion [-].
$\triangle T$	Exhaust gas transport delay [s].
d_v	Exhaust valve diameter [m].
EGR	Fraction of exhaust gas recirculated [-].

f_c	Cutoff frequency [$\frac{1}{\mathrm{CAD}}$].
h	Enthalpy [$\frac{\mathrm{kJ}}{\mathrm{kg}}$].
h_c	Convective heat transfer coefficient [$\frac{\mathrm{W}}{\mathrm{m^2.K}}$].
k	Ratio of specific heat capacities [-].
L	Instantaneous cylinder height [m].
L_v	Exhaust valve axial lift [m].
LHV	Lower heating value of fuel [$\frac{\mathrm{kJ}}{\mathrm{kg}}$].
m	Mass [kg], but [g] in Eq. (E.1).
N	Engine speed [rpm] ; Number of moles [mole].
Φ	Equivalence ratio [-].
OF	Overlap factor [-].
PW	Pulse width [ms].
P	Pressure [kPa].
Q	Heat [kJ].
R	Gas constant [$\frac{\mathrm{kJ}}{\mathrm{kg.K}}$], but [$\frac{\mathrm{J}}{\mathrm{kg.K}}$] in Eq. (5.22).
ρ	Density [$\frac{\mathrm{kg}}{\mathrm{m^3}}$].
S	Stroke [m].
S_p	Piston speed [$\frac{\mathrm{m}}{\mathrm{s}}$].
t	Time [s].
τ_f	Mean evaporation time for the fuel film flow [s].
τ_m	AFR sensor measurement time constant [s].
T	Temperature [K], but [C] in Eq. (4.1) and (3.5).

θ	Crank angle [CAD].
U	Internal energy [kJ].
V	Volume [m^3].
W	Work [kJ].
x	Fuel split parameter [-].
X_r	Residual gas mass fraction [-].
X_d	Mixture dilution fraction [-].
y	Mass fraction [-].

Subscripts

a	air.
b	burned ; base point.
c	compression.
ce	(flow) from cylinder to exhaust.
ch	charge (air+fuel+EGR).
d	duration.
dis	displacement.
e	expansion.
ec	(flow) from exhaust to cylinder.
exh	exhaust.
egr	exhaust gas recirculated.
eoc	end of combustion.

evc	exhaust valve closing.
evo	exhaust valve opening.
f	fuel.
ff	fuel film.
fi	fuel injected.
fv	fuel vapor.
g	cylinder gas.
i	cycle/specie number.
iso	isooctane.
inj	injected.
ivc	intake valve closing.
ivo	intake valve opening.
m	(intake) manifold .
mix	mixture.
mot	motoring.
r	residual gas ; reference.
R	Reference.
o	upstream of exhaust valves.
p	piston.
r	residual gas.
s	(in-cylinder) surface.
soc	start of combustion.
t	total gas.
T	downstream of exhaust valves.
u	universal.
v	(exhaust) valve.
w	cylinder walls.

Chapter 1

Introduction

Greenhouse Gas (GHG) emissions and fuel consumption are two major worldwide environmental and energy challenges in the new century. Given the large number of vehicles manufactured worldwide (estimated 15-20 million road vehicles per year), transportation is one of the largest sources of both greenhouse gas emissions and fuel consumption in the world. For instance, transportation is Canada's largest single source of greenhouse gas emissions with 26% of total GHG in Canada coming from this section [1]. One major solution to decrease emissions and fuel consumption in transportation is the use of cleaner and more efficient combustion in engines. Homogeneous Charge Compression Ignition (HCCI) is a promising concept for combustion engines to reduce both emission and fuel consumption [2, 3]. HCCI is a high-efficiency technology for combustion engines that can be scaled to any size-class of transportation engines as well as used for stationary applications. This makes HCCI as alternative technology to conventional spark/diesel engines.

HCCI engine fundamentals, history, challenges and proposed solutions are introduced in this chapter. An important HCCI problem is then identified for this study and the research goals and the scope of this study are outlined. An overview to the structure of this thesis concludes this chapter.

1.1 BACKGROUND

1.1.1 HCCI Fundamentals

HCCI is the auto-ignition of a homogeneous mixture by compression. An HCCI engine can be described as a hybrid of SI (Spark Ignition) engine and CI (Compression Ignition) engine. As in an SI engine, fuel is homogenously premixed with air, but the fuel autoignites from compression heating, as in a CI (diesel) engine. In this way, homogeneous air-fuel mixture auto-ignites at many locations as shown in Figure 1.1. HCCI works without using any external ignition source, unlike traditional SI and diesel engines where ignition is started with either spark or injected fuel respectively.

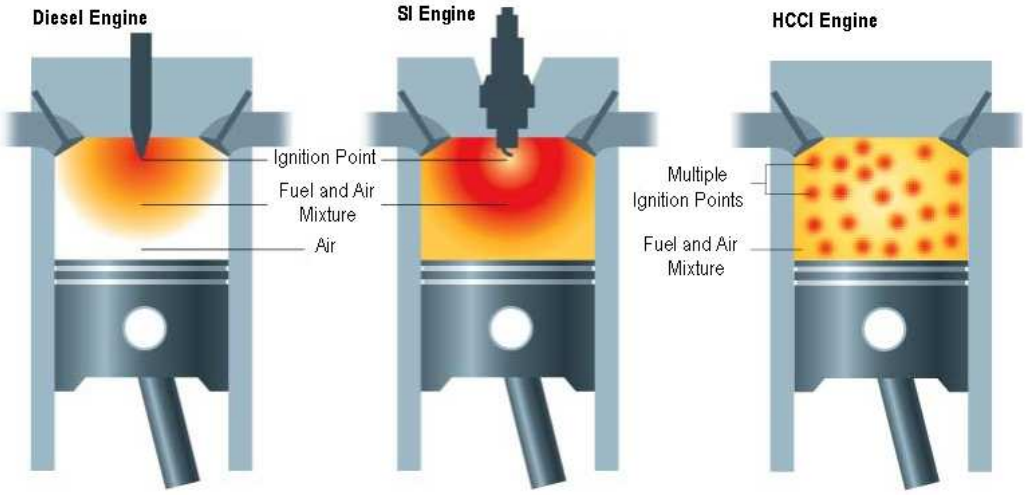

Figure 1.1: HCCI engine versus traditional engines [4].

The HCCI principle incorporates the best features of both the SI and the diesel engine principles. The mixture is homogeneous, which minimizes the Particulate Matter (PM) emissions. The mixture is compression ignited using high compression ratios, has no throttling losses and has shorter combustion duration, which leads to high efficiency. The SI principle has low efficiency at part load, where the HCCI has good efficiency. The diesel engine has similar efficiency as the HCCI

engine, but it generates higher amounts of PM and Nitrogen Oxides (NOx).

HCCI relies on the auto-ignition of highly diluted or lean air/fuel ratio mixture which allows an HCCI engine to run with a fuel consumption advantage compared to conventional spark/diesel engines. Low temperature combustion caused by the presence of excess air and diluents suppresses the rate of NOx formation. Burning of premixed lean mixtures and the absence of diffusion-limited combustion virtually remove[1] the potential for soot formation in HCCI engines [3]. These factors may eliminate the requirement for NOx and soot after-treatment systems [6]. The combination of both high efficiency and ultra-low PM and NOx emissions has made the HCCI engine an attractive alternative to traditional engines.

1.1.2 HCCI History

Although being reported in numerous research papers as a new combustion concept for reciprocating internal combustion engines, HCCI also known as Controlled Auto-Ignition (CAI) has been around for over 100 years [6]. The first patent refers to inventing a hot-bulb 2-stroke oil engine by Carl W. Weiss in 1897 [7]. In Weiss' engine, kerosene or raw fuel is injected onto the surface of a hot-bulb to prepare a homogenous vaporized mixture in a heated prechamber. Then, the prepared air-fuel mixture is transferred from the prechamber to the cylinder and the mixture is auto-ignited inside the main chamber. The Russian scientist Nikolai Semonov and his colleagues established the first theoretical and practical exploitation of chemical-kinetics controlled combustion for diesel engines in the 1930s [6]. Later in the 1970s, Semonov and Gussak [8] built the first CAI engine that controls combustion by using active species which are discharged from partially burned mixture in a separate prechamber.

The most recognized and first systematic early investigations on CAI were

[1] If HCCI combustion is implemented in a direct injection engine, non-negligible amount of soot can be generated by the engine. [5]

done by Onishi [9] and Noguchi [10] on two stroke engines in the late seventies and then on a four stroke engine by Najt and Foster in 1983 [11]. But it was not until the late 1980s that the terminology *Homogenous Charge Compression Ignition (HCCI)* was introduced by Thring [12] in his research paper on studying the effect of external EGR and air-fuel ratio on HCCI. Since the 1990s, the HCCI area had grown to a large world wide research topic [13, 14, 15]. Two main reasons for the growth of interest are the higher fuel prices and the more stringent emission level regulations to meet the upcoming EU and US emission regulations [16, 17].

HCCI technology has a high fuel flexibility and can be applied for a wide range of fuels with different octane numbers [18]. There has been a significant growth in the diversity of the fuels that HCCI engines have used. HCCI fuels range from biofuels [19, 20], to hydrocarbon fuels [21, 22] and reforming fuels [23, 24, 25]. Also, HCCI engines exhibit a large diversity in size. The 12-liter six-cylinder HCCI engine described by Olsson *et al.* [26] is one example of a large HCCI gasoline engine while the 4.1cc HCCI engine described by Manente *et al.* [27] is an example of a mini HCCI engine. In all, HCCI engines could be scaled to virtually every size of transportation engines from a small motorcycle to a large ship engine [28]. In addition, application of HCCI engines is not only limited to automotive applications but can be used for stationary applications such as oil and gas production, power generation and pipeline pumping.

Over the last few years HCCI has been extensively studied by numerous researchers to tackle HCCI challenges. Some of these main studies are briefly introduced in the next section.

1.1.3 HCCI Challenges & Proposed Solutions in Literature

There are a number of obstacles that must be overcome before the potential benefits of HCCI combustion can be fully realized in production applications. Although advantageous over traditional engines in thermal efficiency and NOx emission, HCCI combustion has several main difficulties. These include "Control of combustion timing", "Limited power output", "Homogenous mixture preparation[2]", "High unburned Hydrocarbon (HC) and Carbon Monoxide (CO) emissions", and "Weak cold-start capability".

HC and CO emissions in HCCI are normally higher than their equivalent of diesel engines [3]. However, reducing HC and CO emissions from HCCI engines is easier than reducing NOx and soot emissions from diesel engines [28]. High HC and CO emissions in HCCI are mainly due to low in-cylinder temperature caused by lean-burn or high-dilution combustion. This can result in incomplete combustion and decrease of post-combustion oxidation rates inside the cylinder [6, 3]. Results show that CO-to-CO_2 reactions in HCCI are sensitive to the combustion temperature and a minimum peak temperature of 1500 K is required to oxidize CO [64]. As the charge is made leaner by decreasing fueling, the production of HC and CO is dominated by incomplete bulk-gas reactions [65, 66]. Higher HC and CO emissions are also observed in [67] when the equivalence ratio is decreased for an HCCI engine fueled with blends of iso-Octane and n-Heptane. If the exhaust gas temperature is high enough for the oxidation process in the catalyst to occur, then high HC and CO engine-out emissions in HCCI can be significantly reduced. The oxidation catalysts can reach conversion efficiencies of up to 95%

[2]Some of the recent HCCI studies [29, 30] indicate that having temperature and mixture compositional inhomogeneities inside the cylinder can be useful to enable HCCI at a larger operating range. Their results [29] indicate the charge under some experimental conditions would not be ignited without initial temperature inhomogeneity inside the cylinder. In addition, inhomogeneity of mixture and temperature can be used to extend HCCI knock limit [30].

Table 1.1: Three main HCCI challenges and proposed solutions

HCCI Challenges	**Proposed Solutions**
Control of Combustion Timing	■ Changing temperature history of mixture: • VVT and residual/exhaust gas trapping - Exhaust gas trapping [31, 32] - Modulating intake and exhaust flows [33, 34] - Combination of both [35] • Variable Compression Ratio (VCR)[36, 37] • Variable EGR [38, 34] • In-cylinder injection timing [39, 40, 41] • Modulating intake temperature [42, 43] • Water injection [44] • Variable coolant temperature [45] ■ Changing mixture reactivity: • Modulating 2 or more fuels [46, 47, 48] • Fuel additives and reforming [49, 50, 51] • Variable EGR [38, 52]
Limited Power Output	■ Boosting intake air flow: • Super charging [53, 54, 55, 36] • Turbo charging [55, 56, 57] ■ Dual-mode engines (HCCI at low load): • SI-HCCI [52, 58, 59] • Diesel-HCCI [60, 61]
Homogenous Mixture Preparation	■ Fuel injection in a highly turbulent port flow for gaseous and highly volatile fuels [13, 62] ■ Early in-cylinder injection with sophisticated fuel injectors for diesel fuels [63, 54]

for HC and CO pollutants [68] when the catalytic converter is at operating temperature. Methods to reduce catalyst light-off time in vehicles can be used to help the catalytic converter to reach its operating temperature [69, 70, 71].

The problem of weak cold-start capability in HCCI engines can be solved by using a dual mode (SI-HCCI / CI-HCCI) technique where the engine starts in the SI / CI mode. Table 1.1 lists three major HCCI challenges and solutions proposed to address specific problems. The problem of high HC and CO emissions in HCCI is also linked to *control of combustion timing* since HC and CO emissions highly depend on the location of ignition timing as will be discussed later in Section 2.3.2. Despite a plurality of different proposed solutions, each of the proposed solutions has its own drawbacks. Variable intake temperature, variable intake pressure and variable coolant temperature have slow response time, while Variable Compression Ratio (VCR) and Variable Valve Timing (VVT) are technically difficult to implement. Practicality and cost effectiveness are main concerns with most of the proposed options such as water injection, modulating two or more fuels, etc. However a turbo/super charged, fuel-lean dual (SI-HCCI) engine equipped with VVT technology seems a promising option to address most of HCCI concerns for automotive applications.

1.2 Problem Identification and Research Scope

Ignition timing affects different aspects of the operation of HCCI engines including the operating range, the combustion stability, the engine performance and emission characteristics [72, 73, 74, 75, 76]. The main HCCI benefits and challenges are directly linked to HCCI ignition timing as shown in Figure 1.2. The operating range is influenced by ignition timing as late ignitions lead to high cyclic variation which determines the instability limit [73]. Conversely, early ignitions lead to high peak pressure and high pressure rise rate which determine the knock

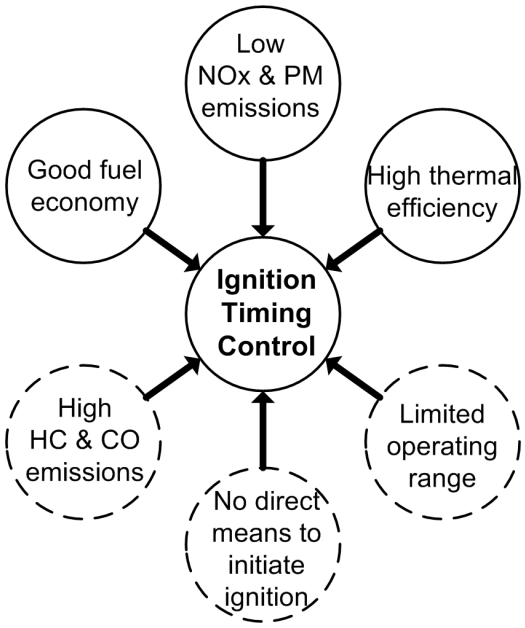

Figure 1.2: Major HCCI benefits (solid circles) and drawbacks (dashed circles) pertinent to HCCI ignition timing.

limit [72]. Combustion efficiency depends on ignition timing [77] and completeness of combustion deteriorates by shifting the ignitions later in the expansion stroke [75] which increases the potential of partial burn and misfired cycles. This can influence CO and HC emissions [74, 76]. Ignition timing also affects the peak combustion temperature which has a direct impact on NOx emissions [76]. The thermal efficiency and the engine work output are also affected by ignition timing and less work is produced by releasing energy partway down the expansion stroke for late ignitions [75].

Since ignition timing is the main control parameter in HCCI engines, the quality of HCCI operation depends on the quality of the system used to control ignition timing [74, 78]. However, control of ignition timing, particularly for a wide range of load and speed, has been recognized as the most challenging problem in HCCI engines [67, 79]. This is because of the absence of a specific event to initiate the combustion and high sensitivity of HCCI to the variations in the

charge properties [80]. Precise control of temperature, pressure and composition of the air fuel mixture is needed to prevent: misfire, excessive peak pressure or excessive pressure gradient which could damage the engine and increase NOx generation.

Understanding the effect of modifying the engine charge properties on the ignition timing is essential to be able to predict and control HCCI engines. The focus of this thesis is to perform a detailed experimental and modeling investigation into the factors influencing HCCI ignition timing. This requires identifying patterns of cyclic variations in HCCI ignition timing and determining different HCCI operating regions with distinct cyclic variation characteristics. A new dynamic physics-based computationally efficient control oriented model is developed to predict both steady state and cycle-to-cycle combustion timing for an HCCI engine. The goal is to have a model that: can predict HCCI combustion timing; has a good compromise between accuracy and computation time; and doesn't require inputs that are difficult to measure in real-time on an engine. The resulting model should be fast and accurate enough for use as a simulation bed to design subsequent control strategies in HCCI engines.

Blends of n-Heptane and iso-Octane are used as the fuel. This selection is done as n-Heptane and iso-Octane are Primary Reference Fuels (PRFs) for octane rating in internal combustion engines, and have cetane number of approximately 56 and 15, with octane numbers of 0 and 100, which is very similar to the cetane number of conventional diesel fuel and gasoline, respectively.

1.3 THESIS ORGANIZATION

This thesis is organized into seven chapters as depicted in Figure 1.3. Chapter 1 is the Introduction and Background. In Chapter 2 the influence of changing engine variables on the variations of HCCI ignition timing is experimentally doc-

umented. Sources and patterns of cyclic variations in HCCI ignition timing are identified. In addition, the relationship between exhaust temperature and igni-

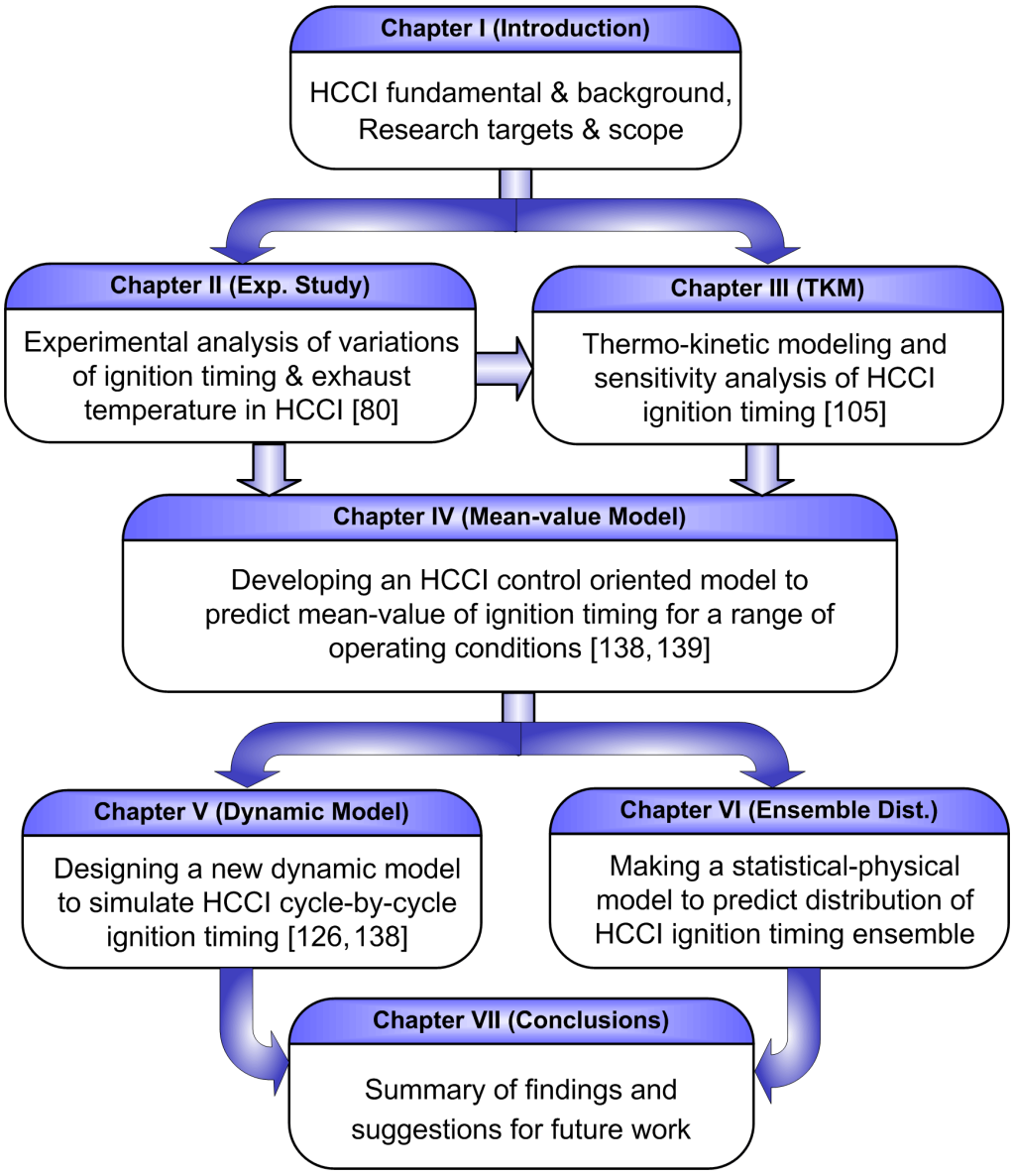

Figure 1.3: Schematic of the thesis organization. [Journal publications as a main/partial result of this thesis work].

tion timing for HCCI engines is discussed since low HCCI exhaust temperature is a limiting factor in utilizing exhaust aftertreatment systems to overcome the challenge of high HC and CO emissions in HCCI engines. Chapter 3 explains a

detailed Thermo-Kinetic Model (TKM) of HCCI combustion that is developed to predict ignition timing of the experimental engine studied in Chapter 2. Experimental data from Chapter 2 is used to validate the TKM. Then, the TKM is used to perform a sensitivity analysis of ignition timing with changing main charge variables. The TKM simulations are used later in Chapter 4 where a control-oriented model is developed to predict mean-value HCCI ignition timing. The application of the resulting model is limited to steady state HCCI operation. Thus, the mean-value model from Chapter 4 is extended to a dynamic full cycle Control Oriented Model (COM) in Chapter 5. The COM can predict the cycle-to-cycle ignition timing for transient HCCI operation. The model is experimentally validated with HCCI data in different transient fueling operations. In addition, the probability distributions of HCCI ignition timing ensembles are experimentally studied in Chapter 6 and the results are used to extend the mean-value model from Chapter 4 into a model which can predict probability distribution of ignition timing ensemble in HCCI engines. The resulting model is useful for finding HCCI running conditions that lead to unstable operation with high cyclic variation. Finally, Chapter 7 summarizes the major results from this thesis and provides recommendations for further research.

Chapter 2

Experimental Study of HCCI: Combustion Timing & Exhaust Temperature[1]

Understanding the variations of ignition timing and exhaust temperature with changing engine operating conditions is an essential step to be able to control HCCI engines for achieving fuel consumption and vehicle's emissions targets. Experimental data from two different engines is analyzed in this chapter to explain the complex relation between the engine variables and the ignition timing and the exhaust temperature in HCCI engines.

2.1 INTRODUCTION

Limited power output, difficulty in controlling combustion timing, and high HC and CO emissions are three main challenges for HCCI and are directly linked to ignition timing and exhaust temperature variations in HCCI engines. HCCI combustion timing is mainly dependent on the injected charge properties which are influenced by the temperature of residual gas from a previous cycle. Cyclic variations in HCCI combustion make the control of HCCI ignition timing more challenging particularly during transient conditions [81]. High cyclic variation (misfire) limits the operating range of HCCI engines at low load and knocking

[1]The results of this chapter are partially based on [80].

limits the operating range at high load [82]. Rapidly switching between HCCI and SI combustion to extend the engine load range [28] requires cycle-by-cycle control of ignition timing which is sensitive to cyclic variations. In addition, only for sufficiently high exhaust gas temperatures can effective exhaust aftertreatment be used to reduce high HC and CO in HCCI engines. The low exhaust gas temperature in certain operating conditions can limit the operating range in HCCI engines.

Developing new methods to properly control ignition timing and exhaust temperature for a wide operating range and combustion-mode switching requires an improved understanding of variations of ignition timing and exhaust temperature in HCCI engines. In this chapter, the influence of engine conditions on cyclic variation of ignition timing and variation of exhaust gas temperature is investigated using collected experimental data at over 600 HCCI operating points. This study, to the author' knowledge, is the first detailed analysis of cyclic variation of ignition timing and the exhaust temperature variations in HCCI engines.

2.2 CYCLIC VARIATION IN HCCI COMBUSTION

Cyclic variations in SI engines have been experimentally studied for decades [83, 84], but only some experimental studies [85, 86, 72, 87, 88, 75, 89, 90] in recent years partially investigate the cyclic variations in HCCI engines. In [85], a single-cylinder engine fueled with different PRF mixtures is run in HCCI mode to study cyclic variations of HCCI combustion. The study shows that when the octane number is decreased the distribution of combustion parameters is more concentrated around mean values and cyclic variations of performance parameters significantly decrease. In [72], limits of HCCI combustion are investigated on a single-cylinder engine for 19 different gasoline-like fuels with octane numbers higher than 60. An octane index to characterize high HCCI cyclic variation

limit and a knock limit is defined. They observe that acceptable HCCI cyclic variation occurs only within a narrow range of ignition timing around TDC. In [87], the variations of cycle resolved gas temperature and unburned hydrocarbons are discussed for a camless gasoline HCCI engine. They find a strong correlation between the combustion phasing and the gas temperature at the beginning of the compression stroke and no correlation is found between the residual (exhaust) gas temperature at the end of the expansion stroke and the combustion phasing of the next cycle. They also report that a high level of unburned hydrocarbons in the residuals is generated by quenching that occurs for late combustion timing. These hydrocarbons auto-ignite during the following gas exchange phase. Experimental results in [88] for a lean burn engine fueled with n-pentane and n-Heptane indicate that HCCI operating conditions are limited by the extent of non-homogeneity of the intake charge – both in mixture quality and temperature. They observe lower HCCI cyclic variations near to the knock limit and for higher compression ratios at a constant equivalence ratio. Stability of late-cycle auto-ignition is studied in [75, 89] for a single-cylinder diesel engine run in HCCI mode. They observe that variations of IMEP increase rapidly after a certain combustion phasing or late limit. Increasing the fueling rate retards the late limit of combustion phasing before the onset of unstable HCCI combustion. This late limit is a function of fuel as iso-Octane (PRF100) fuel tolerates less retarding of combustion phasing compared to a lower PRF blend (i.e. PRF80). Results from [90, 91] on the cyclic combustion variability of a spark-assisted gasoline engine during transition between SI mode and HCCI mode show that HCCI cyclic variation can follow a repeatable pattern of complex combustion that is not a random process. More deterministic structure is observed in cyclic variation of HCCI ignition timing as the engine operating condition is changed from the knock limit to the misfire limit [92].

Here, HCCI experimental data at a large range of operating conditions are collected and then analyzed to understand cyclic variation in HCCI engines. A primary purpose of this section is to provide detailed results and discussion of the sources of cyclic variation in an HCCI engine which can be used to further understand cyclic variation so that effective control strategies, based on physical arguments, can be developed in the future.

2.2.1 Sources of Cyclic Variation in HCCI Combustion

Cyclic variations of HCCI engines are known to be small compared to those in an SI engine but they can be very large under certain operating conditions [72, 87]. Here, four potential sources of cyclic variations in HCCI engines are briefly described.

(1) Temperature inhomogeneity & thermal stratification – a temperature gradient in the unburned charge is caused by heat transfer to different temperature surfaces (piston, valves, cylinder head) and from imperfect mixing of fuel, air and residual gas [93]. Another reason for spatial temperature differences in the cylinder is the inhomogeneous heat release from the cool flame chemistry [29]. Different measurements in HCCI engines [94, 95] show that the charge burns heterogeneously with large spatial and temporal variations and there is always a stratification in the temperature field [29]. Cyclic fluctuation in the temperature of residual gas [96] can cause cyclic thermal stratification inside the cylinder that can lead to cyclic variations in HCCI combustion. There is also a coupling between wall temperature and combustion timing and variations in wall temperature can cause variations in combustion timing and vice versa [76].

(2) Mixture compositional inhomogeneity – a spatial variation in mixture composition inside the cylinder due to the imperfect mixing of fuel, air and residual

gas. The air/fuel homogeneity at the time of combustion is influenced by the fuel preparation strategy. A Port Fuel Injection (PFI) can result in mixture composition inhomogeneity where a locally rich region with suitable temperature auto-ignites earlier [97]. The effect of charge inhomogeneity is especially pronounced at low loads [94]. Although any cyclic variation in the composition inhomogeneity of the mixture can promote the cyclic variations in HCCI engines, the temperature inhomogeneity has a larger influence on the cycle-by-cycle spatial variations of HCCI combustion than the composition inhomogeneity [97].

(3) Fluctuations in the charge AFR (Air Fuel Ratio) – cycle-by-cycle variation of the average AFR of the charge can vary considerably in PFI engines [98]. Cyclic fluctuations in the gas exchange process during intake and exhaust strokes and also incomplete vaporization of the liquid fuel particularly at very lean fuel operation can cause AFR cyclic variations [88]. These cyclic variations cause not only a variation in the mixture richness but also a variation in ratio of specific heats of the mixture which leads to differences in the charge temperature [94] and reactivity. As HCCI combustion is influenced by varying the AFR of the mixture [67, 99], cyclic variations of HCCI combustion can be caused by cyclic fluctuations in the AFR of the charge.

(4) Fluctuations of diluents – EGR and residual gases are two main sources of charge diluents in HCCI engines. The amount of diluents inside the cylinder influences HCCI combustion [97, 100], so cyclic fluctuation in both the amount and composition of diluents can cause cyclic variations in HCCI combustion which then causes a variation in amount of residual gas for the next cycle.

2.2.2 Experimental Engine Setup

A Cooperative Fuels Research (CFR) single-cylinder engine and a single-cylinder Ricardo Mark III engine with a Rover K7 head are used to carry out HCCI

experiments. The experimental data for the Ricardo engine is obtained from the HCCI experiments done in this study and the experimental data for the CFR engine is taken from [82]. Table 2.1 lists the geometrical specifications of both the CFR and Ricardo engines and Figure 2.1 is a schematic of the experimental setup used to run the Ricardo engine.

Table 2.1: Configuration of the CFR and Ricardo single-cylinder engines. (IVO: Intake Valve Opening, IVC: Intake Valve Closing, EVO: Exhaust Valve Opening, EVC: Exhaust Valve Closing, aBDC: after Bottom Dead Center)

Parameters	**CFR engine**	**Ricardo engine**
Bore × Stroke [mm]	83 × 114	80 × 88.9
Compression Ratio	12	10
Displacement [L]	0.622	0.447
Number of Valves	2	4
IVO, IVC[2] [aBDC]	$-170°$, $34°$	$-175°$, $55°$
EVO, EVC [aBDC]	$-40°$, $-165°$	$-70°$, $-175°$

Only the details for the Ricardo engine setup are described below – see [82] for CFR engine setup. The Ricardo engine has a combustion chamber with pent-roof design with a centrally located spark plug and it uses a flat top cast aluminum piston with valve reliefs. Dual camshafts located in the cylinder head operate two intake and two exhaust valves. A standard automotive fuel injector, with 3 bar fuel pressure, injects the fuel into the intake port when the intake valves are closed. The fresh intake air entering the engine is first passed through a laminar air-flow meter for flow rate measurement. Then, the fresh charge is mixed with recirculated hot exhaust gases (EGR) using an insulated return line from the exhaust to the intake manifold. Next, a supercharger driven by a variable speed electric motor adjusts the intake manifold pressure and then a 600W electrical band-type heater sets the mixture temperature to a desired value using a closed-

[2]Valve closing point is defined at the valve lift of 0.15 mm. [101]

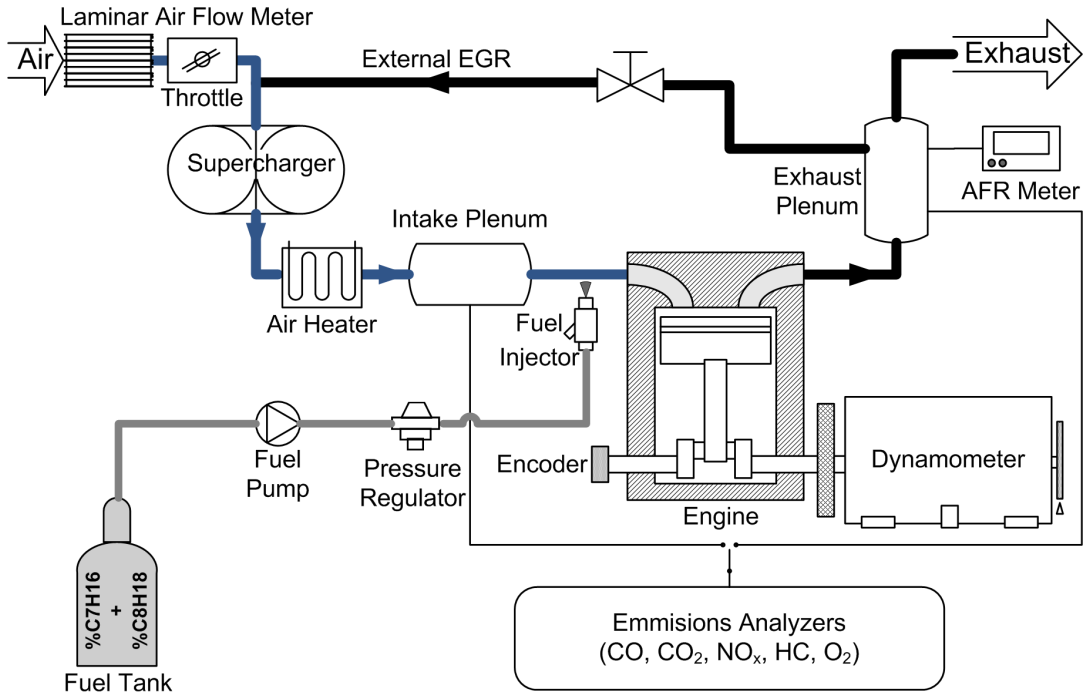

Figure 2.1: Single cylinder Ricardo engine test bench schematic

loop controller. Finally the exhaust gases exiting the cylinder are sampled for emission analysis. As shown in Figure 2.1, the emission can be sampled from either the intake manifold or from the exhaust manifold.

The engine out Air Fuel Ratio (AFR) value is measured by ECM AFRecorder 1200 UEGO with measurement accuracy of $0.01-0.03$. Intake temperature is measured with $2\,^{\circ}\mathrm{C}$ resolution using a K-type thermocouple positioned in the intake manifold before the charge entering into the cylinder. The EGR rate is determined by comparing the CO_2 concentrations in the intake and exhaust manifolds, and by assuming that all CO_2 in the intake manifold is from the exhaust gases. Measurement of the cylinder pressure is done using a Kistler water-cooled ThermoCOMP (model 6043A60) piezoelectric pressure sensor that is flush mounted in the cylinder head. Crank angle measurement with 0.1^{o} resolution, is done using a BEI optical encoder connected to the crankshaft on the front of

the engine. An emissions test bench is used to collect emissions data. NOx is measured with 1 ppm resolution using Horriba CLA-510SS emission analyzer and Horiba FIZ-510 emission analyzer is used to measure HC with 10 ppm resolution. CO is measured with 0.01% resolution using Siemens ULTRAMAT6 emission analyzer. There are also errors associated with measuring each input parameter. Table 2.2 lists the estimated uncertainty associated with measured parameters using the systematic perturbation technique described in [102].

Table 2.2: Estimated uncertainty in measured inputs for the Ricardo engine. [103]

Parameter	Value	Uncertainty (±)
B [m]	0.080	0.001
S [m]	0.089	0.001
T_{man} [°C]	64 - 141	2
N [rpm]	800 - 1200	10
λ (i.e. $1/\Phi$) [-]	1.8 - 3.5	1%
$\dot{m}_{air}$ [g/sec]	3.1 - 4.2	5%
$\dot{m}_{fuel}$ [g/sec]	0.054 - 0.134	3%
T [Nm]	5.2 - 16.9	0.1
CO [%]	0.08 - 1.21	0.01
CO_2 [%]	2.3 - 7.0	0.01
UHC [ppm]	2000 - 4700	10
NOx [ppm]	0 - 23	1

Table 2.3 details the 434 experimental engine operating points used for this study (329 points from the Ricardo engine and 105 points from the CFR engine). The maximum coolant temperature in the collected data is limited since a non-pressurized cooling system is used in the Ricardo engine setup. IMEP of the engines ranges from 3.6 bar to 9.1 bar. The engines are run for five different PRF blend fuels (PRF0, PRF10, PRF20, PRF40, PRF60)[3]. The low compression

[3]PRF number is defined as the volume percentage of iso-Octane in the fuel mixture of n-Heptane (PRF0) and iso-Octane (PRF100).

ratios of the Ricardo engine and CFR engine mean that HCCI operation occurs only for lower octane number fuels and at lower engine speeds. PRF40 for the Ricardo engine and PRF60 for the CFR engine are the highest PRFs for which HCCI operation is possible for a range of loads. Details about the operating range of the Ricardo engine is found in [103].

Table 2.3: Single cylinder engine operating conditions

Parameters	**CFR engine**	**Ricardo engine**
Engine Speed (rpm)	700	760 - 1340
Manifold Temp. (^oC)	88	60 - 161
EGR(%)	1 - 31	0 - 30
Equivalence Ratio	0.45 - 1.1	0.29 - 0.95
Manifold Pressure (kPa)	89 - 92	88 - 162
Fuel (PRF)	20, 40, 60	0, 10, 20, 40
Coolant Temp. (^oC)	96	25 - 84
Oil Temp. (^oC)	70	48 - 80

2.2.2.1 Ignition timing definition

HCCI combustion of the saturated compounds including paraffins such as n-Heptane and iso-Octane has two combustion stages [104] as shown for n-Heptane in Figure 2.2. Low Temperature Reactions (LTR), particularly reactions involving n-Heptane control the first combustion stage. The second stage combustion is controlled by High Temperature Reactions (HTR) that starts when the decomposition of H_2O_2 becomes slower than its production at a temperature around 1000^oK [67]. In this work, start of the LTR or cool flame (1^{st} stage) combustion is denoted as SOC-CF and it is defined as the crank angle where the net Heat Release Rate (HRR) is 10% of the peak of the HRR for LTR region [73]. The start of the main or HTR (2^{nd} stage) combustion, denoted here as SOC, is defined

as being the point at which the third derivative of the pressure trace with respect to the crank angle (θ) in CAD (Crank Angle Degree) exceeds a heuristically determined limit [105]:

$$dp3Lim = \left.\frac{d^3P}{d\theta^3}\right|_{ign} = \left.\frac{d^3P}{d\theta^3}\right|_{lim} \frac{\text{kPa}}{\text{CAD}^3} \tag{2.1}$$

and the dp3Lim value is determined from the available experimental data for each engine and it is chosen to be $5\frac{kPa}{CAD^3}$ and $25\frac{kPa}{CAD^3}$ for the CFR engine and the Ricardo engine respectively. More details about the method to determine SOC is found in Appendix C.

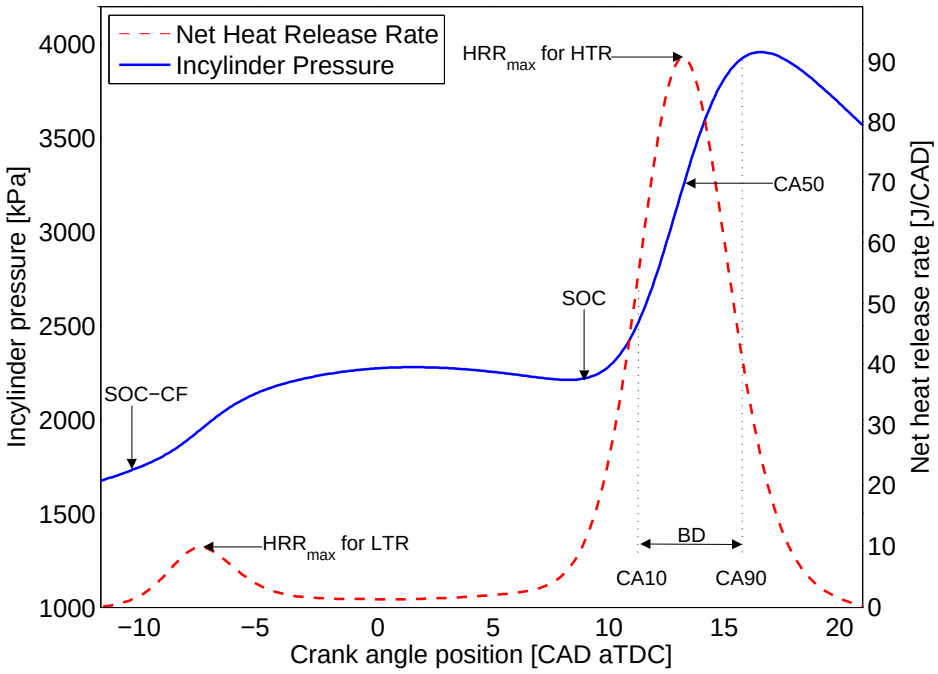

Figure 2.2: Ignition timing definitions – using in-cylinder pressure trace and net heat release rate for point #55 (PRF0, N= 1193 rpm, Φ= 0.6, EGR= 0%, T_m= 99 ^oC, P_m= 102 kPa)

The net HRR is determined using the usual heat release method [101], that applies the first law analysis on the engine charge assuming ideal gas properties. The Rassweiler method [106] is used to calculate fuel Mass Fraction Burnt (MFB)

so that crank angles of the percentage of the fuel burnt can be determined. CA10, CA50, and CA90 are defined as the crank angles for 10%, 50%, and 90% MFB respectively. Burn Duration (BD) is defined as the crank angle rotation between CA10 and CA90 as indicated in Figure 2.2.

In-cylinder pressure traces from 200 consecutive engine cycles with 0.1^o resolution are recorded for each experimental point. The experimental pressure signal is filtered with a second order Butterworth low pass filter with cutoff frequency of $f_c = 0.556\text{CAD}^{-1}$ to remove high frequency noise – so that numerically differentiating the pressure trace to get SOC based on equation (2.1) is viable. The pressure signal is filtered in the crank angle domain to avoid having to change the cutoff frequency for different engine speeds and the filtering is done in both forward and reverse directions to avoid any phase shift.

2.2.3 Results & Discussion

Variations in different engine parameters can be used to characterize HCCI cyclic variations. Pressure-related parameters and combustion-related parameters are two common parameters groups that are used to study cyclic variability of combustion engines [107, 101]. IMEP, P_{max}, and the crank angle of maximum in-cylinder pressure ($\theta_{P_{max}}$) are important pressure-related parameters. The main combustion-related parameters are SOC, BD, crank angle with the maximum heat release rate ($\theta_{HRR_{max}}$) and the maximum Heat Release Rate (HRR_{max}). Cyclic variation of ignition timing (particularly SOC) is the main emphasis of this study although other parameters are also investigated by discussing their cyclic variation trends versus those of ignition timing parameters.

Coefficient of Variations (COV) is used to measure cyclic variability of IMEP, P_{max}, HRR_{max}, and BD [87, 88, 108] and similar to other studies [75, 109, 110] Standard Deviation (STD) is used to measure cyclic variability of crank angle

based parameters such as $\theta_{P_{max}}$ and SOC [4]. The influence of different conditions on HCCI cyclic variation is better illustrated using the data from the Ricardo engine because of a wider range of operating conditions compared to the CFR engine (see Table 2.3). Except for the cases where insufficient data is available from the Ricardo engine, the cyclic variation results shown here are from the Ricardo engine and differences to the CFR engine are noted.

The two engines in this study use port fuel injection and external EGR. For the two hundred steady state cycles the range of cyclic variation in equivalence ratio is between 0.010 and 0.018 for the recorded data from ECM AFRecorder 1200 UEGO sensor with a sampling frequency of 100 Hz. A maximum of 0.5% fluctuation in the EGR rate is seen for the data based on the fluctuations of CO_2 concentrations in the intake system measured by a Siemens UltraMat 6E CO_2 gas analyzer. A maximum of ± 5 kPa cyclic variation in intake manifold pressure are observed in the recorded values from Setra 280E diaphragm pressure transducer with a sampling frequency of 100 Hz. Cool flame heat release is associated with both engines as PRF fuel is used in both cases. The cyclic variations in the Ricardo and CFR engines are attributed to the four main sources of cyclic variations described previously. As the CFR engine has a short valve overlap period of 5 CAD and Ricardo engine has zero overlap and no rebreathing strategy is used in valve timing of these two engines, no significant contribution on cyclic variations from fluctuations in mass of residual gases in these two engines is expected. For the Ricardo engine, simulation results from a previous study [73] show that ignition timing is most sensitive to the variation of mixture temperature at IVC, while equivalence ratio, mixture IVC pressure and EGR rate follow in a

[4]COV is defined as the STD of values divided by the mean of values, expressed in percent [101]. As the denominator of COV is dependent on the mean value of the parameter studied, cyclic variation for crank angle based parameters can be obscured using COV. When crank angle based parameters (e.g. SOC) approach TDC, they approach zero and COV increases despite a constant variation giving a misleading interpretation of cyclic variability.

decreasing order of importance respectively.

2.2.3.1 Cyclic Variation Patterns

Three main distinct patterns of cyclic variations are observed for SOC, P_{max}, and IMEP as shown in Figure 2.3. These distinct patterns of cyclic variations indicate that HCCI cyclic variation is not always a random phenomenon. Figure 2.3-a shows the typical cyclic variation that is the most frequent cyclic pattern observed in 84% of the Ricardo engine experiments (275 points out of 329 points). All four sources of cyclic variations can contribute to this cyclic pattern and since the variations in these sources do not follow a certain pattern or structure, unstructured fluctuations are seen in this cyclic pattern. On the other hand, Figure 2.3-b shows a nearly periodic pattern of oscillations within two limits and it can result from a periodic variation of the mixture charge. The 40 points #155-158, 163, 166-169, 225-226, 240-242, 244-245, 272-290, 296, 299-300, 322-323 in the Appendix A exhibit this oscillation pattern. The measured charge properties for these points show that they have an oscillating air mass flow into the cylinder (thus an oscillating equivalence ratio) with an oscillation period similar to the combustion timing. As HCCI combustion depends on charge properties a periodic oscillation in charge conditions can lead to periodic variation in HCCI combustion parameters (e.g. SOC, P_{max}). Figure 2.4 plots the measured intake air mass flow rate and Φ for the point #167 (periodic patten in Figure 2.3-b). Figure 2.4 shows a relatively periodic variation in the air mass flow rate and Φ with an oscillation period of about 25 cycles which is close to that of Figure 2.3-b. Examining the conditions of the points with periodic patterns show that all of these points have boosted intake pressure (114 kPa$\leq P_{man} \leq$145 kPa). The maximum fluctuation in supercharger speed is only $\pm$2 rpm for all the points from the measurements by the General Electric 5BC46AB1590B permanent magnet tachometer with a

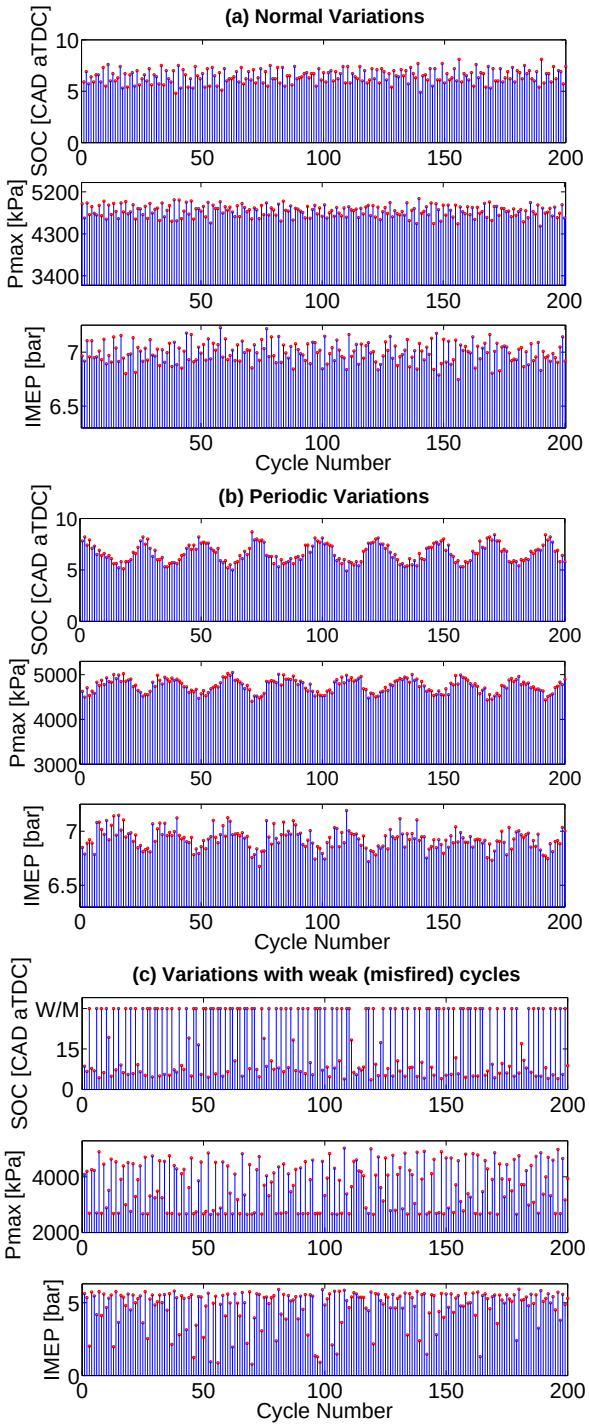

Figure 2.3: Cyclic variations patterns of SOC, P_{max}, and IMEP (a) Normal variation, #184; (b) Periodic variation, #167; (c) Variations with weak (misfire) cycles, #239. The symbol W/M in part "c" represents Weak/Mifired ignitions that didn't meet the threshold in Equation 2.1. (Ricardo – see Appendix A)

sampling frequency of 10 Hz. Thus fluctuation in supercharger speed can not be the main cause of oscillating air flow. One possible explanation is a coupling between the pulsing supercharged flow and cylinder intake flow causing a beat frequency. A cyclic variation pattern with many weak/misfired ignitions and

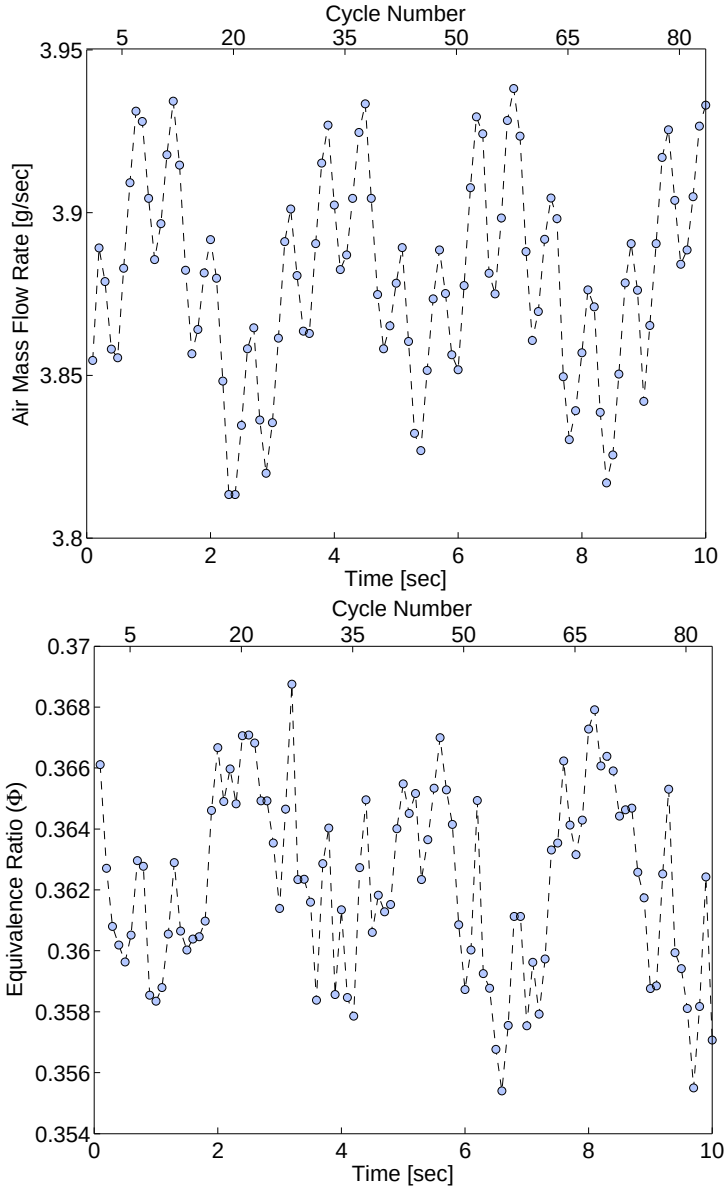

Figure 2.4: Measured air mass flow rate and equivalence ratio for #167 – Figure 2.3-b. (Note: the start point of this figure is not the same as that of Figure 2.3.)

some strong ignitions is shown in Figure 2.3-c. Examples of this pattern are the fourteen points #42, 43, 68, 72, 98, 100, 103-105, 117, 150, 187, 230, 239 listed in the Appendix A. These points have large cyclic variations of IMEP, SOC and P_{max} and both the mean of P_{max} and IMEP are generally low for these points. In HCCI mode when COV_{IMEP} exceeds about 5% the Ricardo engine approaches the partial/misfire burn limit (see COV_{IMEP} of the weak/misfired points in the Appendix A). The weak/misfired ignition cycles in this pattern results in significant amounts of unburned/partially burned fuel that are recycled to the next cycle by residuals as has been reported in [87, 75]. The recycled partially reacted fuel from a previous cycle can enhance the auto-ignition for the next cycle [75]. This can explain why some of the weak cycles in Figure 2.3-c are followed by stronger ignitions. A small amount of IMEP is still produced even for the weakest ignitions in Figure 2.3-c despite a peak pressure close to motoring conditions. For those weak ignitions a poor and late combustion in the expansion stroke is evident in the pressure trace data.

If the sources of cyclic variations have random (unstructured) or periodic (structured) variations, a *Normal* pattern or *Periodic* pattern of cyclic variation can occur. For the *Weak/Misfire* pattern, a weak misfired cycle is followed by a strong cycle which adds to the other sources of the cyclic variations. In addition, as discussed later in the section, ignition timing in weak/misfire points are late and more thermal stratification and higher sensitivity to charge temperature fluctuations are expected for late ignitions [75, 111]. To control the HCCI ignition timing to a set point, the *Weak/Misfire* pattern and *Periodic* pattern of cyclic variations should be avoided and the amplitude of cyclic variation in the *Normal* pattern should be minimized. This requires identifying the dynamics of charge fluctuations and understanding combustion dynamics between consecutive cycles.

2.2.3.2 SOC and BD Effects on Cyclic Variation

Cumulative percentage of occurrence for COV of P_{max}, IMEP and SOC plotted against their COV values for different ranges of SOC are shown in Figure 2.5 for the points with SOC occurring after TDC (314 points). The cumulative percentage of occurrence is calculated by counting how many points out of all the points with the same SOC interval have the same range of cyclic variations. For example, in Figure 2.5-a there are 120 points that have SOC between 0 and 5 CAD aTDC. As 79 out of the 120 points have STD_{SOC} less than 1 CAD, the percentage of occurrence for $STD_{SOC} < 1$ CAD is 66% for SOC occurring between 0 and 5 CAD aTDC. In Figure 2.5-a the cyclic variation of SOC for the points with SOC occurring immediately after TDC are lower than those of the points with late SOC. As the Figure shows, 66% of the points for which SOC occurs between 0 and 5 CAD aTDC (triangle symbols) have STD_{SOC} lower than 1 CAD and almost all of them have STD_{SOC} smaller than 4 CAD, but 75% of the points with SOC occurring between 10 and 22 CAD aTDC have STD_{SOC} higher than 3 CAD. A similar trend is seen in Figure 2.5-b and Figure 2.5-c for $COV_{P_{max}}$ and COV_{IMEP} where the percentage of the points with high cyclic variation increases as the SOC retards after TDC. For this engine controlling SOC closely after TDC substantially decreases high HCCI cyclic variations. A 5 degree window of SOC, between 0 – 5 CAD aTDC is found to provide the most stable HCCI combustion in terms of cyclic variations of SOC, P_{max}, and IMEP.

Higher cyclic variations by retarding ignition timing after TDC is attributed to the several effects. First, when the combustion timing retards after TDC, the piston expansion rate is higher and this counteracts the temperature rise from combustion by the cooling from piston expansion [111]. Second, a more thermally stratified charge occurs with retarding the combustion because of heat transfer [75]. Third, HCCI ignitions closer to TDC exhibit less sensitivity to the

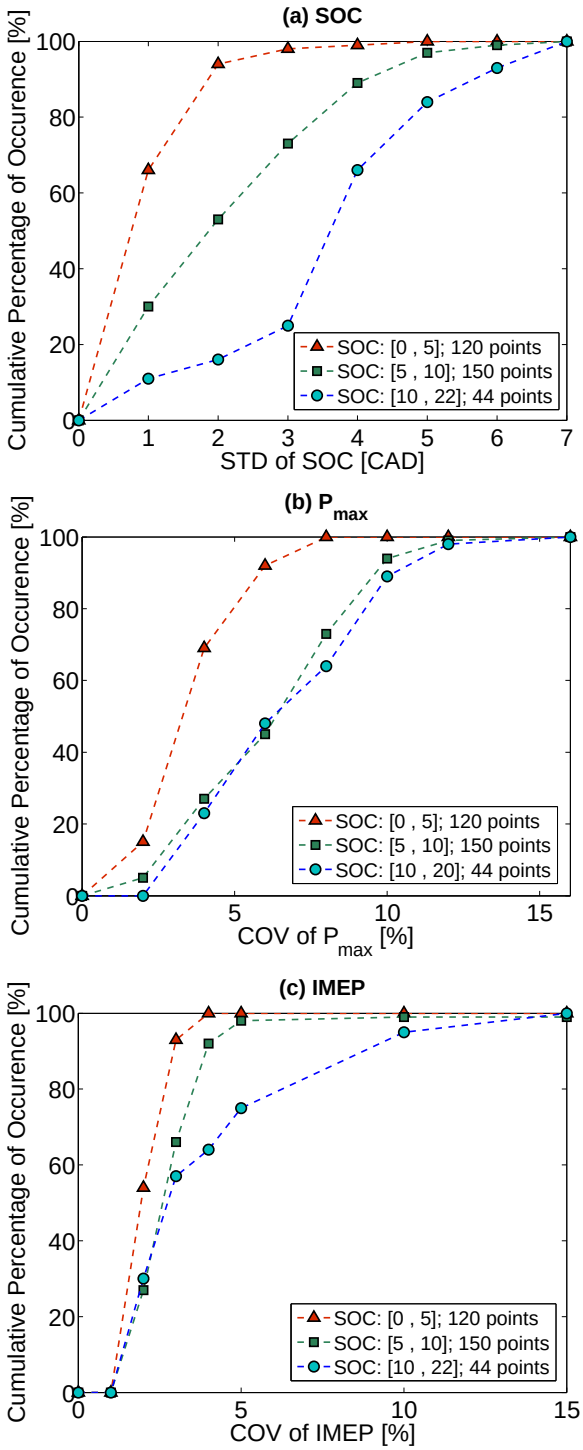

Figure 2.5: Cumulative percentage of occurrence at different SOC intervals for: (a) STD of SOC, (b) COV of Pmax and (c) COV of IMEP. (Ricardo – see Appendix A)

fluctuations of the charge temperature [111] and cycle-to-cycle variations in the core temperature have higher influence on the ignition timing for the ignitions occurring later in the expansion stroke [75]. Fourth, by retarding the combustion phasing both combustion efficiency and thermal efficiency decrease [76, 77] and completeness of combustion drops with lower peak combustion temperature [75]. In addition, pressure rise rate and peak pressure are reduced by delaying the chain reaction of burning zones due to higher piston expansion rate [77] and the work output is reduced by releasing energy partway down the expansion stroke [75] with the potential of partial burn and misfired cycles. Experimental data from the Ricardo engine in Figure 2.6 also confirms that peak pressure, maximum pressure rise rate and thermal efficiency [101] decrease by retarding the combustion timing after TDC. Late ignition after TDC not only increases cyclic variation by delaying ignition after TDC but results in [112] show that cyclic variation between cylinders also increases by retarding combustion after TDC and for late ignitions where the spread of variation can be so high that one cylinder is firing while another cylinder is not.

Variations in IMEP with changes in combustion timing are plotted in Figure 2.7 for two different scenarios: (a) constant fueling rate (variable Φ), (b) variable fueling rate (constant Φ). In Figure 2.7-a, combustion timing (CA50) is advanced from 17 CAD aTDC to 6 CAD aTDC by increasing the intake pressure from 96 kPa to 138 kPa at a constant fueling rate. As increasing the intake pressure causes the engine to intake more air into the cylinder and the amount of injected fuel is not changed, the mixture becomes leaner (Φ: 0.61$\rightarrow$0.38) with increasing manifold pressure. IMEP increases in Figure 2.7-a by advancing the combustion timing to TDC. The change in IMEP by varying combustion timing in Figure 2.7-a is about 0.5 bar which is equal to 10% change in the engine thermal efficiency for the base point of 5-bar IMEP. This confirms the significance of

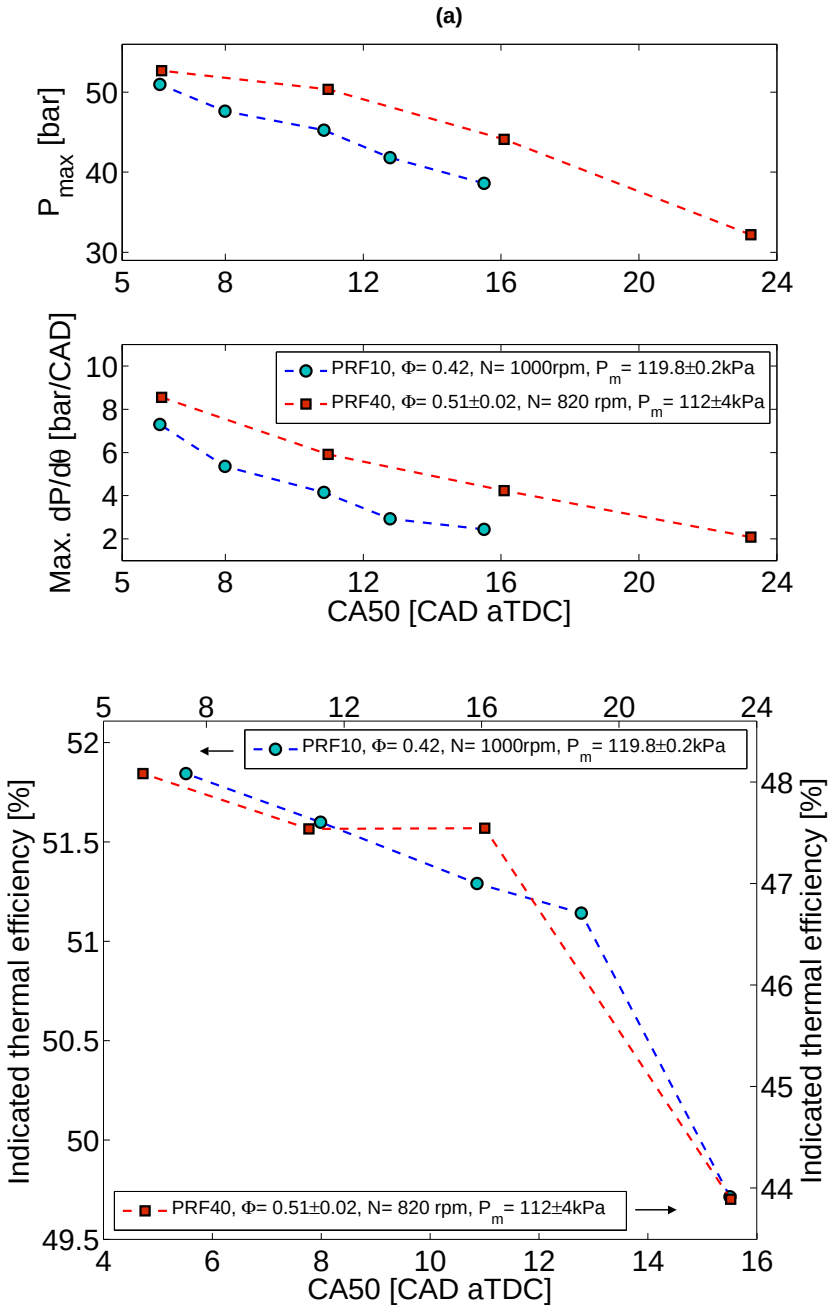

Figure 2.6: Peak pressure, pressure rise rate and indicated thermal efficiency versus CA50 variations by changing the intake temperature. (Range of T_{man} sweep is 73–112 ^{o}C for PRF10 and 63–111 ^{o}C for PRF40, Ricardo engine)

the influence from the combustion timing on the engine performance. A different scenario is shown in Figure 2.7-b that indicates an opposite trend compared to Figure 2.7-a. IMEP decreases in Figure 2.7-b by advancing the combustion

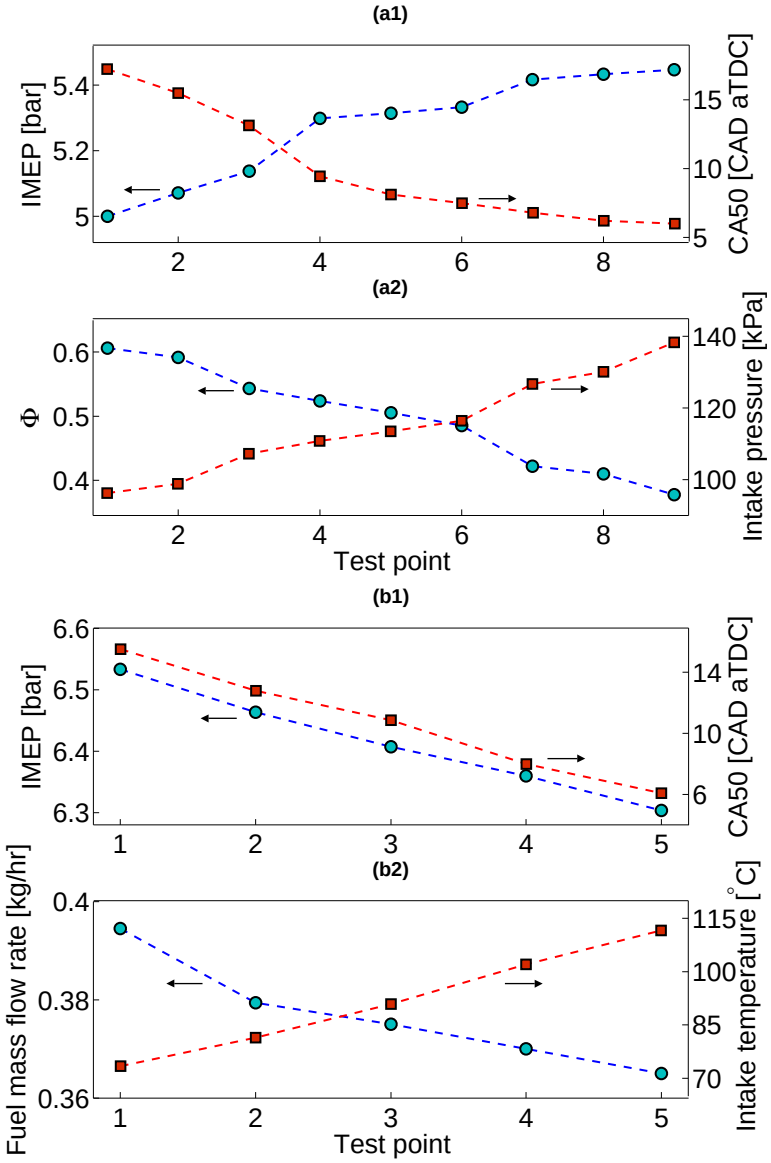

Figure 2.7: IMEP versus CA50 for (a) constant fueling rate (0.31±0.003 kg/hr) and (b) variable fueling rate. (a) PRF40, N= 810 rpm, EGR= 0%, T_m= 115 ^oC; (b) PRF10, Φ= 0.42, N= 1000 rpm, EGR= 0%, P_m= 119.8±0.2kPa. (Ricardo engine)

timing to TDC – opposite to what seen in Figure 2.7-a. In this figure CA50 is advanced from 15.5 CAD aTDC to 6.1 CAD aTDC by increasing the intake temperature from 73 ^{o}C to 112 ^{o}C and keeping Φ constant by increasing the fueling rate. IMEP in Figure 2.7-b follows the same trend as that of the fuel mass flow

rate and it increases when the fuel rate is increased. A comparison between Figures 2.7-a and 2.7-b indicates that IMEP depends more on the fueling rate rather than the ignition timing, but it highly depends on the ignition timing for the conditions that have a constant fueling rate. Other results [73, 108] from the Ricardo engine show that CA50 advances by increasing the intake temperature or intake pressure and it retards by decreasing Φ or fuel mass flow rate. CA50 variations trends in Figure 2.7 show that CA50 exhibits more dependance to the variation of intake pressure compared to that of Φ in Figure 2.7-a and it is more sensitive to the variations in the intake temperature compared to changes in the fuel rate in Figure 2.7-b for the range indicated. The sensitivity of HCCI combustion timing to inputs and conditions is important to understand not only for cyclic variation but also to be able to effectively control HCCI timing. For the controller of HCCI combustion timing, it is essential to know the effect from which charge variables are more significant than the others and which charge variable is more dominant in a competition to affect the combustion timing.

HCCI combustion phasing is not fully characterized by SOC as different burn durations (BD) can occur at the same SOC. In order to understand the cyclic variability of HCCI combustion phasing, cyclic variations of BD must also be considered. Variation in BD results when some cycles have fast combustion (small BD) and some cycles have slow combustion (large BD). BD does influence IMEP such that shorter burn durations are more likely to generate higher IMEP values as shown in Figure 2.8 which is not surprising since these cycles more closely approximate an ideal cycle having a relatively constant-volume combustion [101]. The cumulative percentage of occurrence for COV of BD versus COV_{BD} for different amounts of BD is shown in Figure 2.9 – test points as in Figure 2.5. In Figure 2.9, faster HCCI ignitions tend to have smaller cyclic variations in BD. As shown, 88% of the points with BD lower than 3 CAD have COV_{BD} smaller

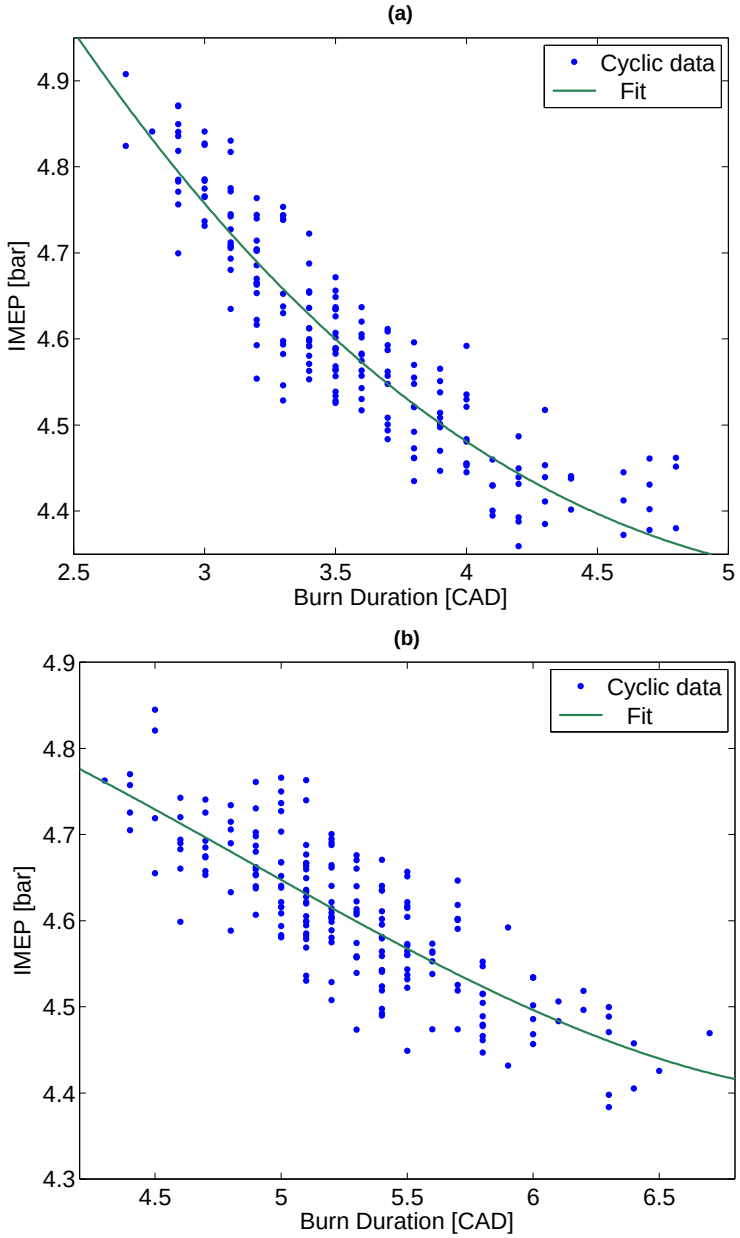

Figure 2.8: Cyclic IMEP versus burn duration for two sample operating points (a) #132, (b) #316.

than 10%, but only 20% of the points with longer burn duration ($BD > 4\,CAD$) have COV_{BD} smaller than 10%. BD increases with an increase in the octane number (PRF) at similar charge conditions (equivalence ratio, EGR rate, intake temperature and intake pressure) [67]. A step octane number transient shown in

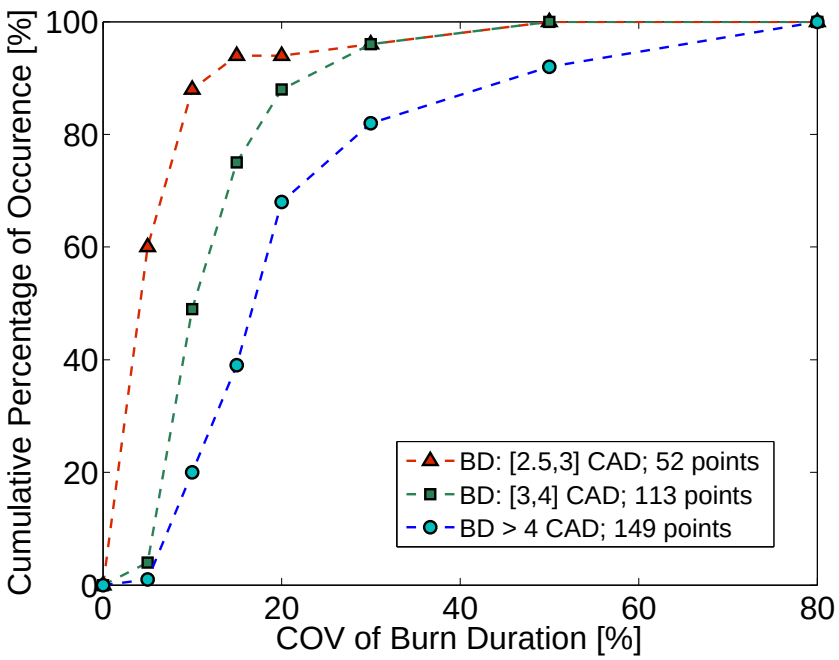

Figure 2.9: Cumulative percentage of occurrence for COV of burn duration (BD) for different BD values. (Ricardo – see Appendix A)

Figure 2.10 for 400 engine cycles confirms this. The BD increases from 4.1 CAD to 8.3 CAD and COV_{BD} more than triples from 4.5% to 14.5% when the fuel is switched at cycle 100 from PRF0 (ON=0) to PRF22 (ON=22). Therefore, less cyclic variations of BD are expected for lower PRFs (lower octane number, e.g. PRF0). If PRF fuel modulating is used to control combustion in an HCCI engine this behavior should be considered.

The results from Figure 2.3 and the findings in Figure 2.5 and Figure 2.9 are linked in Table 2.4 which lists the average SOC and average BD values for the test points with similar patterns of cyclic variations. Table 2.4 shows the points with normal cyclic pattern have the largest SOC range and they can occur in any of the SOC intervals and BD intervals shown in Figure 2.5 and Figure 2.9. Test points with a periodic pattern typically have a moderate BD, but the test points with weak/misfired pattern have late ignitions with long burn durations

and they are mainly located in the last SOC interval and the last BD interval (circle symbols) in Figure 2.5 and Figure 2.9. Controlling SOC closely after TDC and providing ignitions with short BD is one way to avoid the weak/misfired cyclic pattern.

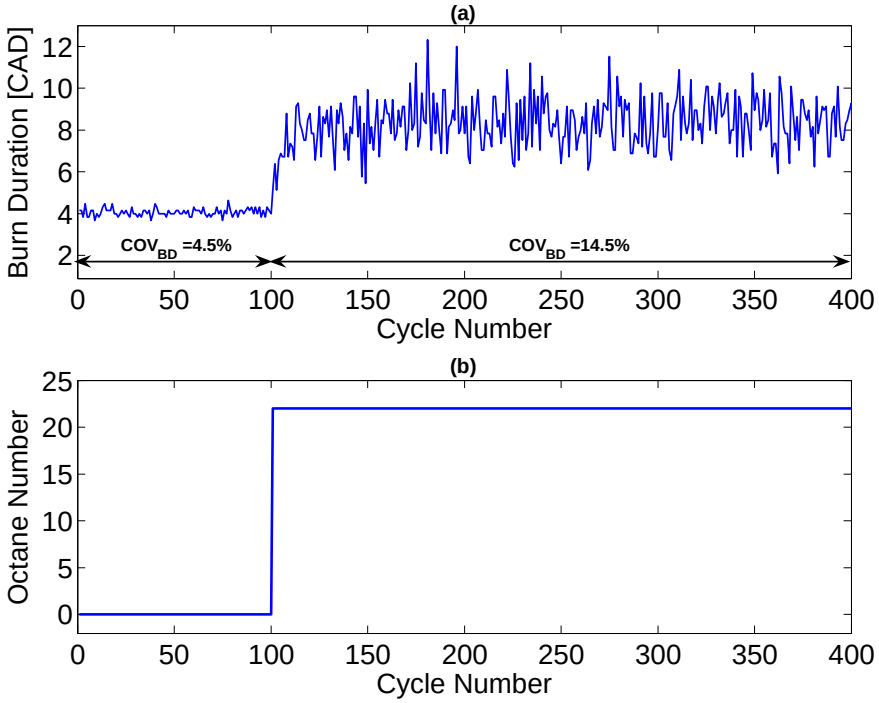

Figure 2.10: Cyclic variations of burn duration when changing octane number by switching PRF fuels at constant charge conditions. (N= 815 rpm, $\Phi = 0.42$, $T_m = 117\ ^oC$, $P_m = 110$ kPa, Ricardo engine)

Table 2.4: Distribution of average SOCs and average BDs for three cyclic variation patterns (Ricardo engine)

Pattern	**Number of Points**	**Mean of SOC** [CAD aTDC]	**STD**$_{SOC}$ [CAD]	**Mean of BD** [CAD]	**STD**$_{BD}$ [CAD]
Normal	275	6.0	3.9	4.1	1.5
Periodic	40	4.4	2.0	3.9	1.2
Misfired	14	11.9	3.7	5.0	0.7

2.2.3.3 Cyclic Variability Zoning of Combustion Parameters

Both cyclic variations of P_{max} (combustion stability) and BD, as a function of standard deviation of SOC are shown in Figure 2.11. Four different regions in Figure 2.11-a and five different regions in 2.11-b are identified with distinct patterns of variations between $COV_{P_{max}}$ and COV_{BD} with those of STD_{SOC}. The regions are summarized in Table 2.5. In region-I, a correlation is observed between the cyclic variations of P_{max} and BD with those of SOC. This region contains the points with a low SOC cyclic variation ($STD_{SOC} \leq 1.5$ CAD). As listed in Table 2.5, most of the points in region-I have SOC right after TDC and the average SOC for these points is closer to TDC compared to those of region III, IV, and V. On the other hand, region-II includes the points with a low cyclic variation of SOC and P_{max}, but with a high cyclic variation of BD.

Table 2.5: Average cyclic variations of SOC (test points in regions defined in Figure 2.11)

Region	**Number of Points**	**Mean of SOC** [CAD aTDC]	**STD**$_{SOC}$ [CAD]	**Notes (pattern)**
I	180	4.3	2.9	no misfire, often normal
II	10	1.9	2.1	knocking, no misfire
III	107	8.4	3.5	often periodic/normal
IV	21	9.0	4.3	often misfire/normal
V	11	11.8	4.1	most misfire

The ten points in region-II include cases #56, 62, 149, 158, 189, 192, 213, 234, 240, and 309. Examining the pressure traces for these points, a trend of knocking is observed in the majority of the cycles and these points are at the knock limit of the operating region for the Ricardo engine – a pressure rise rate of 7bar/CAD is defined as the threshold for the knock limit [103]. The mean pressure rise rates from 200 cycles for all ten points in region-II are shown in Table 2.6. All the 10 operating points in region-II have pressure rise rate equal or higher than the

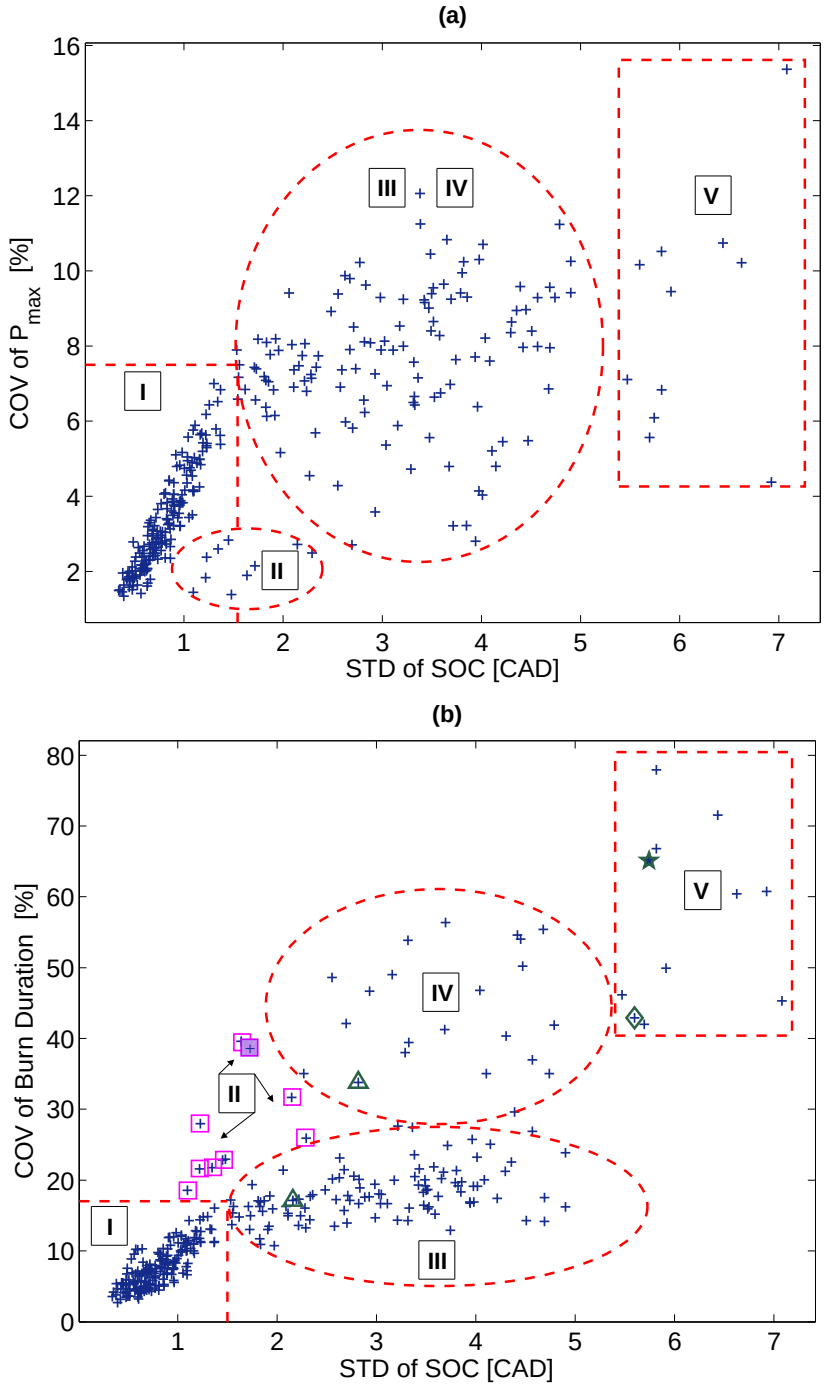

Figure 2.11: Cyclic variations of P_{max} and burn duration versus location of SOC. Region I: correlated and low cyclic variation, Region II: knocking, Region III: late ignited, Region IV: highly diluted late ignited, Region V: very high cyclic variation – unstable. (Ricardo – see Appendix A)

knock threshold for the majority of the cycles. Knock intensity of the points in region-II is also shown in Table 2.6 in terms of PPmax[5] (the maximum of peak-to-peak value of band-pass filtered pressure trace – see Figure 2.12). Table 2.6

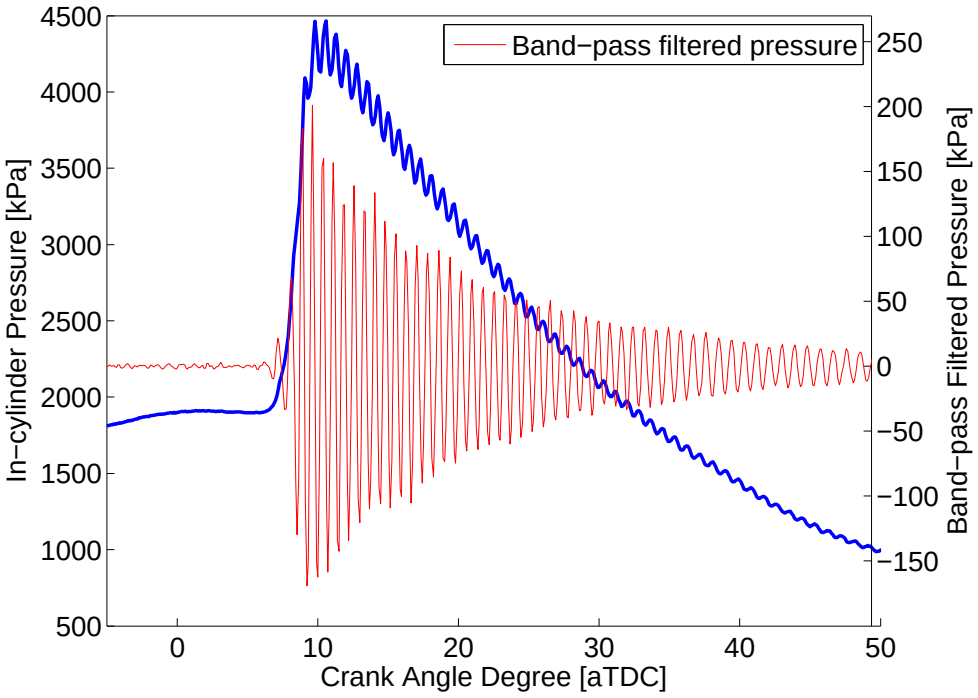

Figure 2.12: Cylinder pressure and band-pass filtered pressure traces for a knocking cycle of point #213 – filled square symbol in Figure 2.11-b. (5th-order band-pass Butterworth with passband from 5 to 20 kHz.)

shows the points in region-II range from weak knocking points (e.g. #56) to the points with heavy knocking such as point #213 – filled square symbol in Figure 2.11-b. Figure 2.12 shows the knocking pressure and band-pass filtered pressure traces for the point #213. The operating conditions of most of these points in region-II are either richer with a high intake temperature or relatively lean with a high intake temperature and high boost pressure. SOC of the points in region-II occurs close to TDC with an average SOC of 1.9 CAD aTDC as indicated in Table 2.5.

[5]PPmax is a representative knock indicator that measures the intensity of knock induced vibrations [113].

Table 2.6: Knocking characteristics for the points in region-II of Figure 2.11. (dP/dθ and PP_{max} values are mean of 200 cycles.)

Point # in Appendix A	**dP/dθ** [bar/CAD]	**Knock Intensity** PP_{max} [bar]	**Knocking Percentage** [% of 200 cycles]
56	7.0	0.57	50
62	9.3	1.25	100
149	9.3	0.77	100
158	9.6	0.96	100
189	7.9	0.75	78
192	9.9	1.02	100
213	9.8	1.22	100
234	8.4	0.52	97
240	9.7	0.92	100
309	9.2	0.63	100

Region-III in Figure 2.11 has 107 different operating points and includes late ignition points with an average SOC of 8.4 CAD aTDC. Points in region-III generally exhibit high cyclic variations of both SOC and P_{max}. Points in region-IV are cases #63, 64, 67, 89, 90, 91, 95, 102, 104, 107, 108, 114, 126, 130, 132, 150, 176, 177, 217, 241, and 317. A close examination of these points shows that most of them have either a low intake manifold temperature ($60^oC \leq T_{man} \leq 80^oC$), a lean mixture ($\Phi \leq 0.5$) or an above average EGR rate ($EGR \geq 12\%$). This observation is consistent with later results in Figure 2.19 to Figure 2.21 where the influence of the initial temperature, EGR dilution and equivalence ratio is shown on the cyclic variations of SOC.

Region-V includes the cases #68, 69, 72, 78, 79, 100, 103, 105, 178, 186, and 187. These points have a very late combustion with an average SOC of 11.8 CAD aTDC (Table 2.5). Common among most of the points in region-V are engine operating conditions that include: low coolant temperature ($T_{coolant} < 45^oC$), very lean equivalence ratio ($\Phi \leq 0.45$), low intake temperature ($T_{man} \leq 65^oC$),

high EGR rate ($EGR \geq 16\%$) or higher engine speed ($> 1100\ rpm$).

To link the regions in Figure 2.11 with cyclic patterns in Figure 2.3, it should be noted that the majority of the points in the region-V have partial burned/misfired cyclic pattern and points with the misfired pattern never appear in region-I and region-II. Test points with the periodic pattern mainly appear in region-I and region-III and they never appear in region-V. But, test points with normal cyclic pattern are found in all the five regions of Figure 2.11. Points in region-I and region-III have the highest occurrence of the normal pattern while points in region-V have the lowest occurrence of the normal patten. The majority of the test points in region-II exhibit the normal cyclic pattern.

Comparing Figure 2.11-a with 2.11-b shows that the combined region-III and region-IV in Figure2.11-a is distinct in 2.11-b. One possible reason is that ignitions for the points in region-IV are typically more retarded compared to those in region-III as seen in Table 2.5. For example the triangle symbol in region-III (point #133) has almost the same operating conditions as that of the triangle symbol (point #132) in the region-IV. The only difference is that the triangle symbol in region-IV has a more retarded ignition due to lower intake manifold temperature. Retarding combustion phasing increases mixture thermal stratification around TDC [75] and the thermal stratification highly influences the burn duration by prolonging the combustion [30]. Similarly in region-V of Figure 2.11-b, the diamond symbol (#78) and the star symbol (#79) have almost similar operating conditions but the star symbol has lower Φ which leads to more retarded ignition compared to the diamond symbol. It can be also noted that although the star symbol and the diamond symbol have almost similar cyclic variation of SOC, the star symbol exhibits higher cyclic variation of BD. This is an example for which cyclic variation of SOC and cyclic variation of BD are not directly related and hence a control of both SOC and BD are required to control

HCCI combustion. Thus, regions in Figure 2.11 show different characteristics of interrelation between cyclic variation of SOC and cyclic variation of BD. Depending in which region an operating point is located a different control approach is required to limit cyclic variations of both SOC and BD. For example in region-I the control of SOC to lower cyclic variation of SOC reduces cyclic variation of BD, but controlling SOC in region-IV and region-V does not reduce cyclic variation of BD. Characterizing effective control strategies in terms of cyclic variations of SOC and BD as in Figure 2.11 is an important step to control HCCI.

Figure 2.13 shows how coolant temperature and intake temperature influence the cyclic variation of BD for the test points running on the same fuel. As expected COV of BD increases by reducing the coolant temperature or intake temperature. For a similar temperature change ($\simeq$ 30^oC), the change in COV of BD when varying the coolant temperature is almost twice that of the change

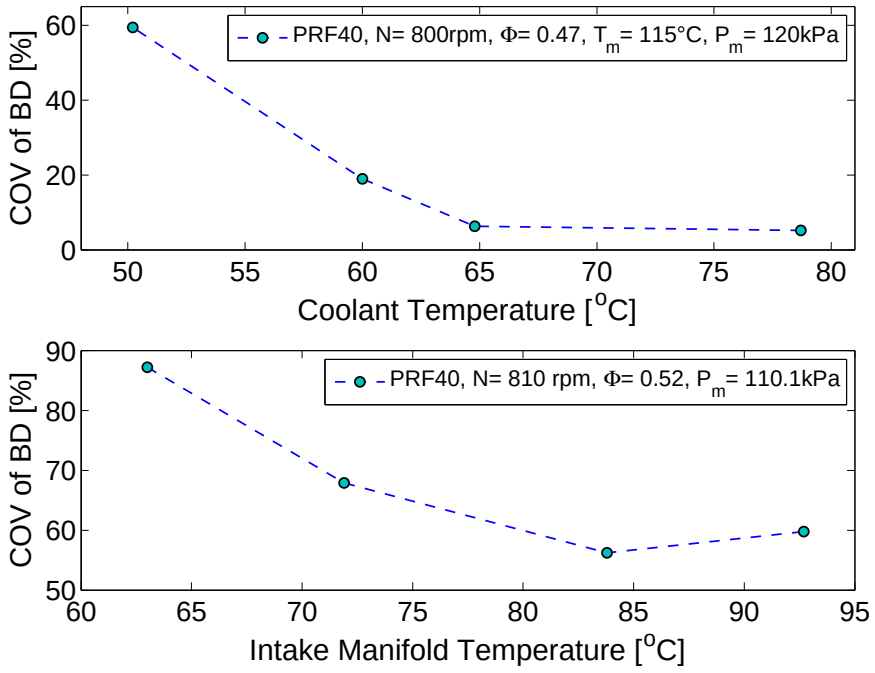

Figure 2.13: Cyclic variations of burn duration versus variations of coolant temperature and intake manifold temperatures. (Ricardo engine)

of the intake manifold temperature. This suggests that cyclic variation of BD is more sensitive to the variation of the coolant temperature compared to that of the intake temperature. This might be explained as the intake charge temperature influences the thermal state of the bulk gas in the core, but coolant (wall) temperature has more influence on the thermal boundary layer and hence on the thermal stratification [114]. As mentioned above the thermal stratification affects the burn duration in HCCI combustion. In addition, the coolant temperature has a significant impact on fuel vaporization in a PFI engine, which in turn would have an impact on charge homogeneity. This may cause a substantial change in the range of BD cyclic variation by varying the coolant temperature.

As the combustion duration of an HCCI engine can differ considerably with a same SOC, CA50 is another important alternative parameter instead of BD to measure ignition timing in HCCI engines. CA50 is a good indicator of HCCI ignition timing and it is useful for feedback control of HCCI combustion [115]. Figure 2.14 shows the changes of cyclic variations in CA50 versus those of SOC and illustrates the position of the five regions already discussed in Figure 2.11. Figure 2.14 indicates the variation of CA50 is correlated with those of SOC for the region where cyclic variation of SOC is low, region-I ($STD_{SOC} \leq 1.5$ CAD), but there is a weaker correlation when cyclic variations of SOC increase particularly in the region-II and the region-V. Thus only for region-I adjusting the cyclic variation of either SOC or CA50 is one possible method for the combustion controller to control cyclic variation of BD. Adjusting SOC is also effective to control cyclic variation of P_{max} in region-I, but this is not effective in regions II and V. Also shown is that cyclic variation of CA50 is usually lower than that of SOC because the slope of energy release in HCCI engines is so steep it is less sensitive to variations in CA50. Thus CA50 is a better indicator of HCCI ignition timing compared to the SOC for our experiments as also found in [115].

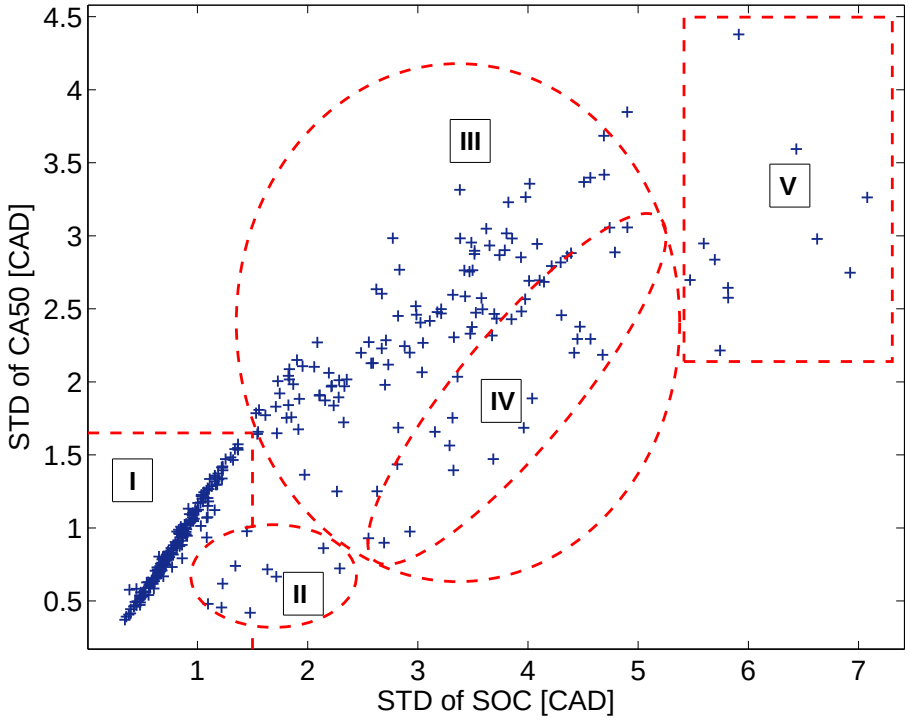

Figure 2.14: Cyclic variations of CA50 versus location of SOC with regions defined in Figure 2.11. (Ricardo – see Appendix A)

$\theta_{P_{max}}$ and $\theta_{HRR_{max}}$ (the crank angle for the maximum heat release rate) correlates linearly with CA50 as shown in the left column of Figure 2.15. The cyclic variation of both $\theta_{HRR_{max}}$ and $\theta_{P_{max}}$ correlate with that of CA50 only when the cyclic variation of CA50 is low ($\text{STD}_{CA50} \leq 1.7$ CAD) – as shown in the right column of Figure 2.15. For the design of the combustion controller, adjusting CA50 can be used to control $\theta_{HRR_{max}}$ and $\theta_{P_{max}}$ and cyclic variations of these two parameters are controlled by adjusting CA50 (when cyclic variation is low – $\text{STD}_{CA50} \leq 1.7$ CAD Regions I and II). However, for the cases with high cyclic variation, $\text{STD}_{CA50} > 1.7$ CAD the location of CA50 is not the only main factor affecting the cyclic variation. The scatter in the left column of Figure 2.15 shows this more complex response.

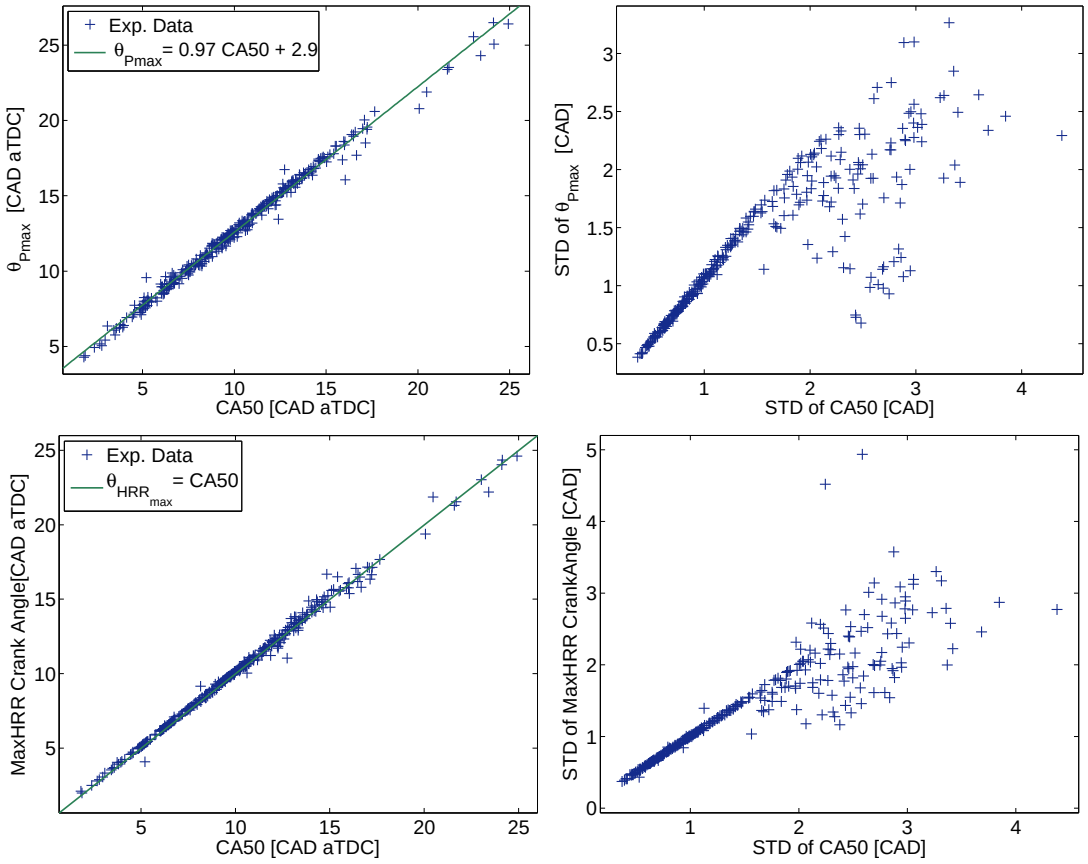

Figure 2.15: $\theta_{P_{max}}$ and $\theta_{HRR_{max}}$ versus location of CA50 and STD of $\theta_{P_{max}}$ and $\theta_{HRR_{max}}$ versus STD of CA50. (Ricardo – see Appendix A)

2.2.3.4 Cyclic Variability of 1^{st} Stage vs. 2^{nd} Stage of Combustion

The average of cyclic variations of heat release parameters in terms of STD/COV for 329 experimental points from the Ricardo engine is summarized in Table 2.7 and indicates that both HRR_{max} from the LTR region and $\theta_{HRR_{max}}$ from the LTR region have considerably less cyclic variation compared to those from the HTR region. How $\theta_{HRR_{max}}$ (for both LTR and HTR) varies as a function of equivalence ratio, intake temperature, intake pressure and coolant temperature are plotted in Figures 2.16-2.17 respectively while holding all other variables at a base case.

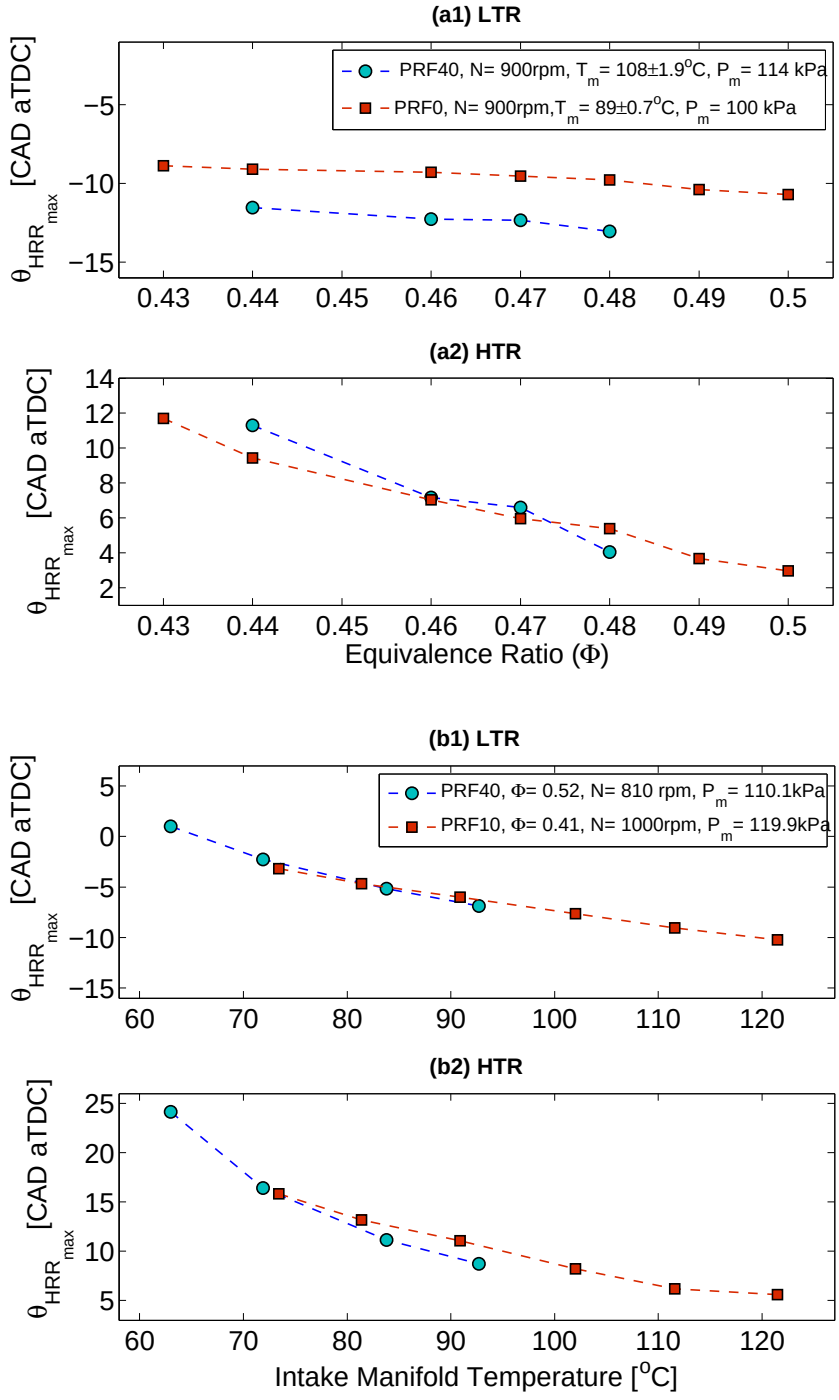

Figure 2.16: Variations in crank angle of maximum heat release rate ($\theta_{HRR_{max}}$) in HTR and LTR regions by varying intake temperature, equivalence ratio. (Ricardo engine)

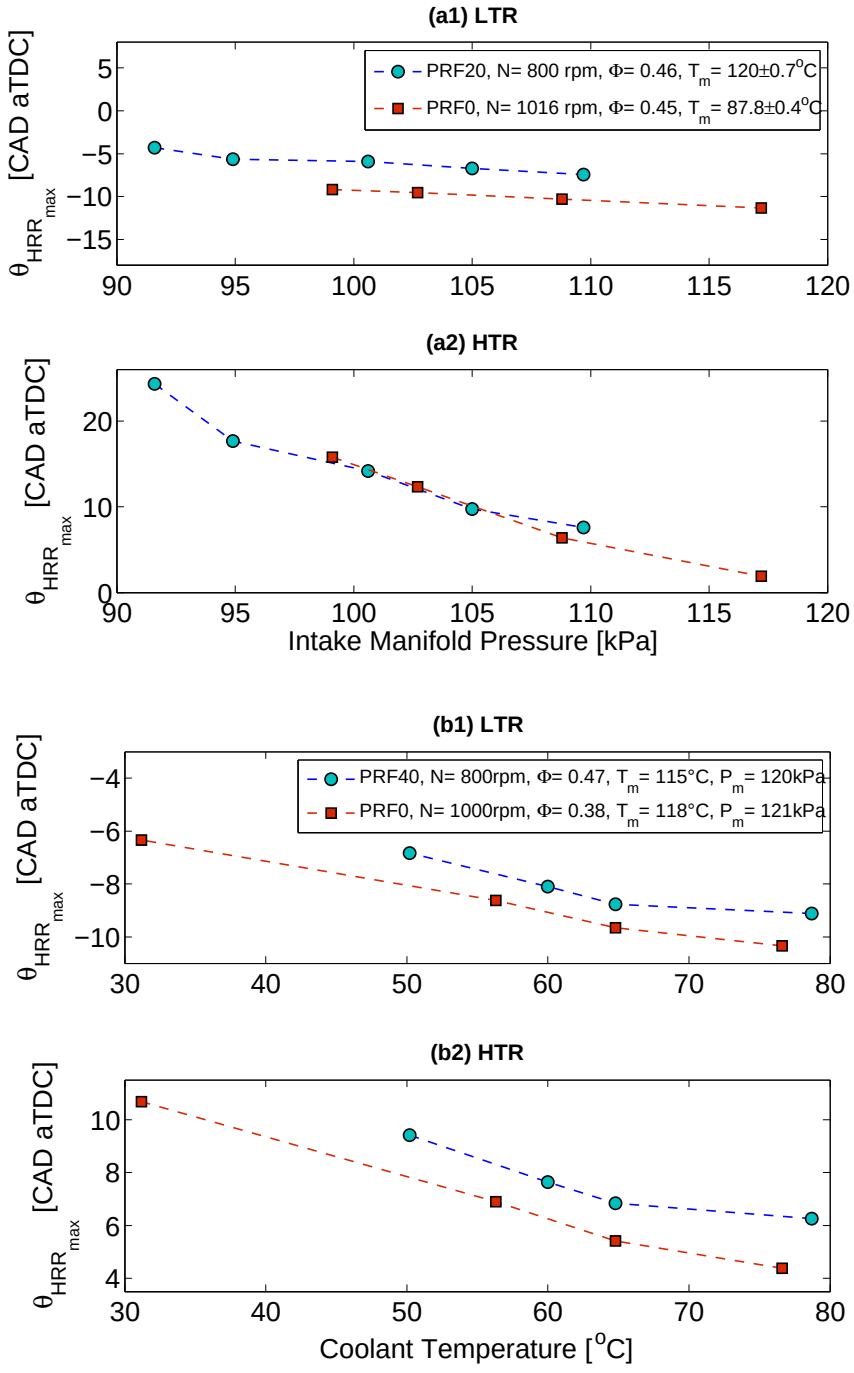

Figure 2.17: Variations in crank angle of maximum heat release rate ($\theta_{HRR_{max}}$) in HTR and LTR regions by varying intake pressure and coolant temperature. (Ricardo engine)

In Figure 2.16-a (PRF0) when Φ changes by 0.07, $\theta_{HRR_{max}}$ in HTR advances by 8.7 CAD, but $\theta_{HRR_{max}}$ in LTR changes only by 1.8 CAD. For a 30^{o}C change of

Table 2.7: Average cyclic variations of heat release parameters comparison for LTR and HTR regions

Heat release parameter	**STD[CAD]/COV[%]**
$\theta_{HRR_{max}}$ in LTR	0.7 [CAD]
$\theta_{HRR_{max}}$ in HTR	1.5 [CAD]
HRR_{max} in LTR	10.6 [%]
HRR_{max} in HTR	15.2 [%]

intake manifold temperature in Figure 2.16-b (PRF40), $\theta_{HRR_{max}}$ in HTR changes twice as much as $\theta_{HRR_{max}}$ in LTR. In Figure 2.17-a (PRF0), $\theta_{HRR_{max}}$ in HTR changes almost six times as much as $\theta_{HRR_{max}}$ in LTR for an 18 kPa change in intake manifold pressure. The effect of a 45 ^{o}C coolant temperature difference is shown in Figure 2.17-b and for the PRF0 case and $\theta_{HRR_{max}}$ changes 4 CAD in LTR and 6 CAD in HTR. Thus Figures 2.16-2.17 show that $\theta_{HRR_{max}}$ in HTR are much more sensitive to the variations of equivalence ratio, intake manifold temperature and pressure compared to those in LTR. Therefore, one possible reason for higher cyclic variation in HTR compared to LTR as noted for Table 2.7 is because the LTR in the first stage of HCCI combustion are less sensitive to variations of mixture conditions compared to HTR in the second stage of HCCI combustion. Figures 2.16-2.17 also show that in terms of $\theta_{HRR_{max}}$, the LTR is less sensitive to variations in equivalence ratio and intake pressure compared to variations in intake temperature and coolant temperature, but the HTR has a strong sensitivity to all those variables. Thus, to control HTR timing independent from LTR timing, intake pressure and equivalence ratio are better choices of control inputs compared to using intake temperature and coolant temperature.

Cyclic variation of $\theta_{HRR_{max}}$ and SOC from the second stage (HTR) of HCCI combustion is plotted as a function of the first stage (LTR) in Figure 2.18. No

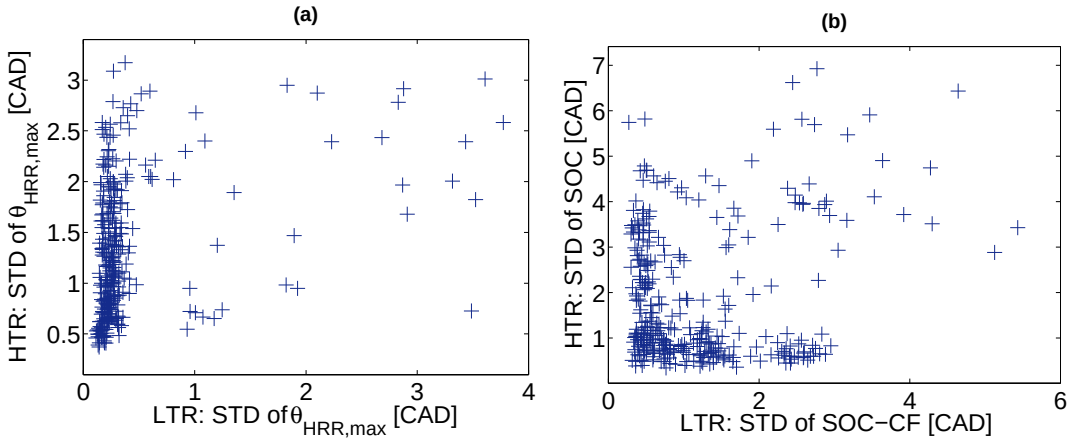

Figure 2.18: LTR versus HTR in HCCI combustion. Cyclic variation of (a) $\theta_{HRR,max}$ and (b) SOC. No correlation observed. (Ricardo – see Appendix A)

correlation is apparent between the cyclic variations of $\theta_{HRR_{max}}$ (Figure 2.18-a) and no correlation is apparent between the cyclic variation of SOC (Figure 2.18-b) for the first and second stages of HCCI combustion. This is not surprising as the first stage and second stage of HCCI combustion exhibit different levels of sensitivity to charge fluctuations (as shown in Figures 2.16-2.17). In addition, HTR is subject to piston-expansion cooling since over 95% of the 329 Ricardo points have SOC after TDC, while in LTR SOC-CF is always before TDC. Thus in the design of combustion controller, adjusting the cyclic variations for the first and second stages of HCCI combustion should be treated as independent control targets as shown with the lack of correlation in Figure 2.18 between the first and second stages of combustion.

2.2.3.5 Influence of Operating Variables on SOC Cyclic Variation

The influence of different variables on the cyclic variation of SOC are shown in Figure 2.19 to Figure 2.24. In these figures, all engine's variables are kept constant and only one variable is changed while maintaining HCCI operation. Different base cases are used as HCCI combustion is strongly dependent on the

charge initial conditions and there is also an interdependence among variables which limits the range for which the influence of one parameter can be varied.

Cyclic variation of SOC decreases with increasing intake manifold temperature (T_{man}) for PRF10 and PRF40 as shown in Figure 2.19. Higher cyclic variation at

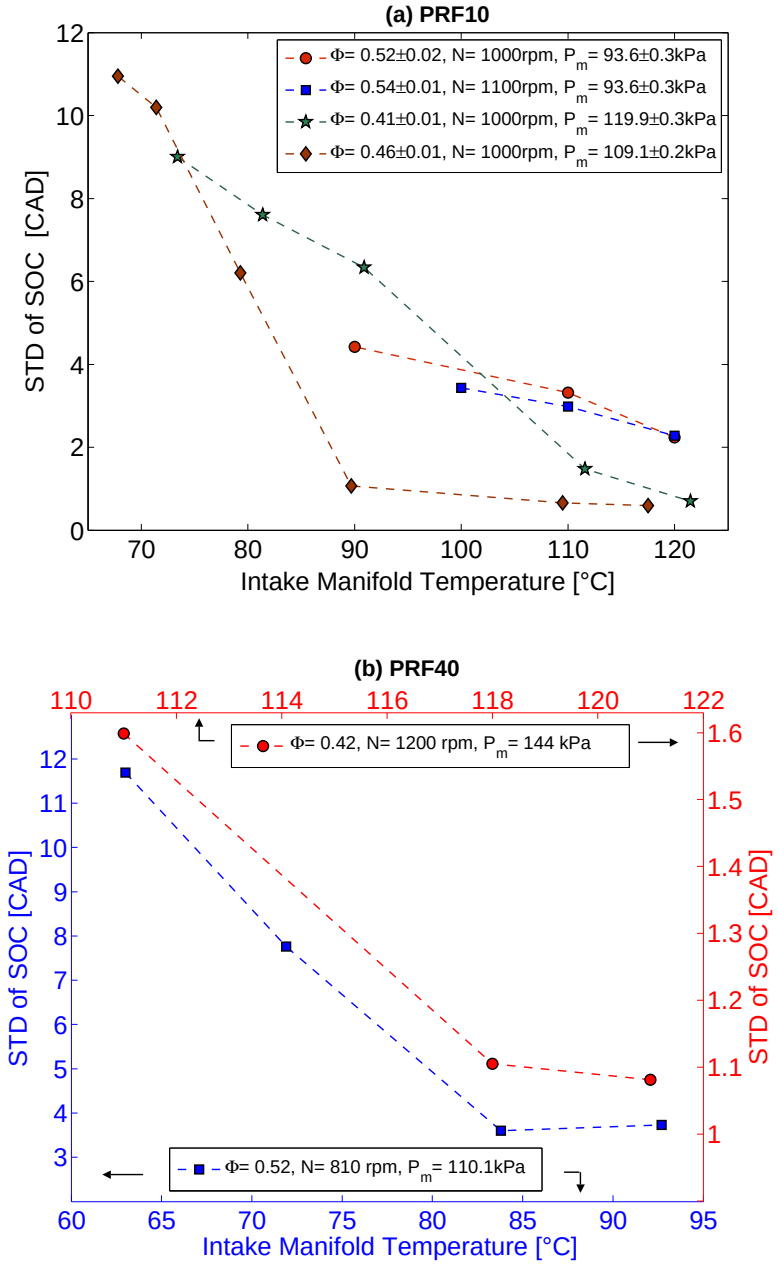

Figure 2.19: Influence of the intake manifold temperature on the cyclic variations of SOC for two fuels (a) PRF10, (b) PRF40. (EGR=0%, Ricardo engine)

lower intake temperatures may be explained by a combination of three main effects. One, cyclic variation of residual gas temperature causes cyclic variations in the core temperature which lead to cyclic variations in the auto-ignition process [75]. Higher intake temperatures also result in higher core temperatures, so similar cyclic variations of residual gas temperature are less significant at higher intake temperatures. The second effect is that SOC can be advanced closer to the TDC when T_{man} is increased. As previously mentioned, a lower level of cyclic variation is expected by moving the SOC closer to TDC. HCCI ignition timing is dependant on the temperature near TDC and the thermal stratification around TDC increases with retarding combustion phasing by decreasing the intake temperature [75]. Furthermore, for late ignitions in the expansion stroke, combustion is more sensitive to inevitable cyclic variations of TDC temperature [75]. The third effect is that a longer combustion (BD) is expected by decreasing T_{man} because a delayed auto-ignition leads to a stronger counteraction between the pressure rise and piston expansion cooling that results in a delayed auto-ignition of colder zones compared to the hottest zone in the combustion chamber [89]. As shown in Figure 2.9 shorter ignitions (smaller BD) are more likely to have less cyclic variations. In addition, results in [89] show that random fluctuation of the charge temperature has less impact on ignition timing of hot ignition (HTR) when the higher temperature-rise rates occur before SOC. Retarding combustion phasing by decreasing the intake temperature leads to a decrease in the temperature-rise before SOC and consequently a higher cyclic variation of hot ignition [89].

Figure 2.20 shows that cyclic variations of SOC increase with an increase in EGR rate for the CFR engine[6]. In-cylinder optical observations in [94] show that increasing the EGR rate causes more random developments of the auto-

[6]The engine setup for the CFR engine [82] is different from Figure 2.1 and EGR is directly routed into the midpoint of intake manifold. Thus in comparison to the setup for Ricardo engine, less time is available to mix EGR and air in the CFR flow path.

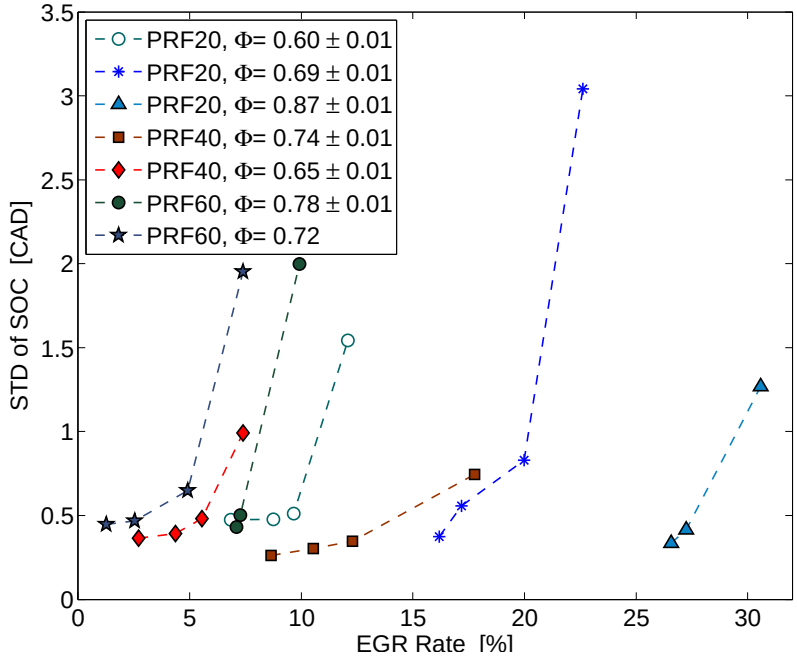

Figure 2.20: Influence of the EGR dilution on the cyclic variations of SOC. (CFR engine)

ignition sites and an increase in the rate of appearance of multiple auto-ignition sites. The duration of HCCI combustion is prolonged and SOC retards when increasing the EGR rate [67]. As mentioned above, HCCI combustion is more prone to high cyclic variation for slow and late ignitions. Since EGR slows and delays the combustion the cyclic variation is increased. Another source for higher cyclic variations compared to when EGR is not used is the fluctuations in the EGR rates due to the gas dynamics in the EGR line. Recorded data from Ricardo engine exhibited a maximum of 0.5% cyclic variation in EGR rate and an average fluctuation of 6.2% of the mean EGR rate is reported for the CFR data points [82].

The cyclic variation of SOC decreases with increasing the charge equivalence ratio for both Ricardo (Figure 2.21-a) and the CFR (Figure 2.21-b) engines. Smaller HCCI cyclic variations are also observed in [88] for the points near the knock limit, where mixtures are typically richer. Lower cyclic variation for richer

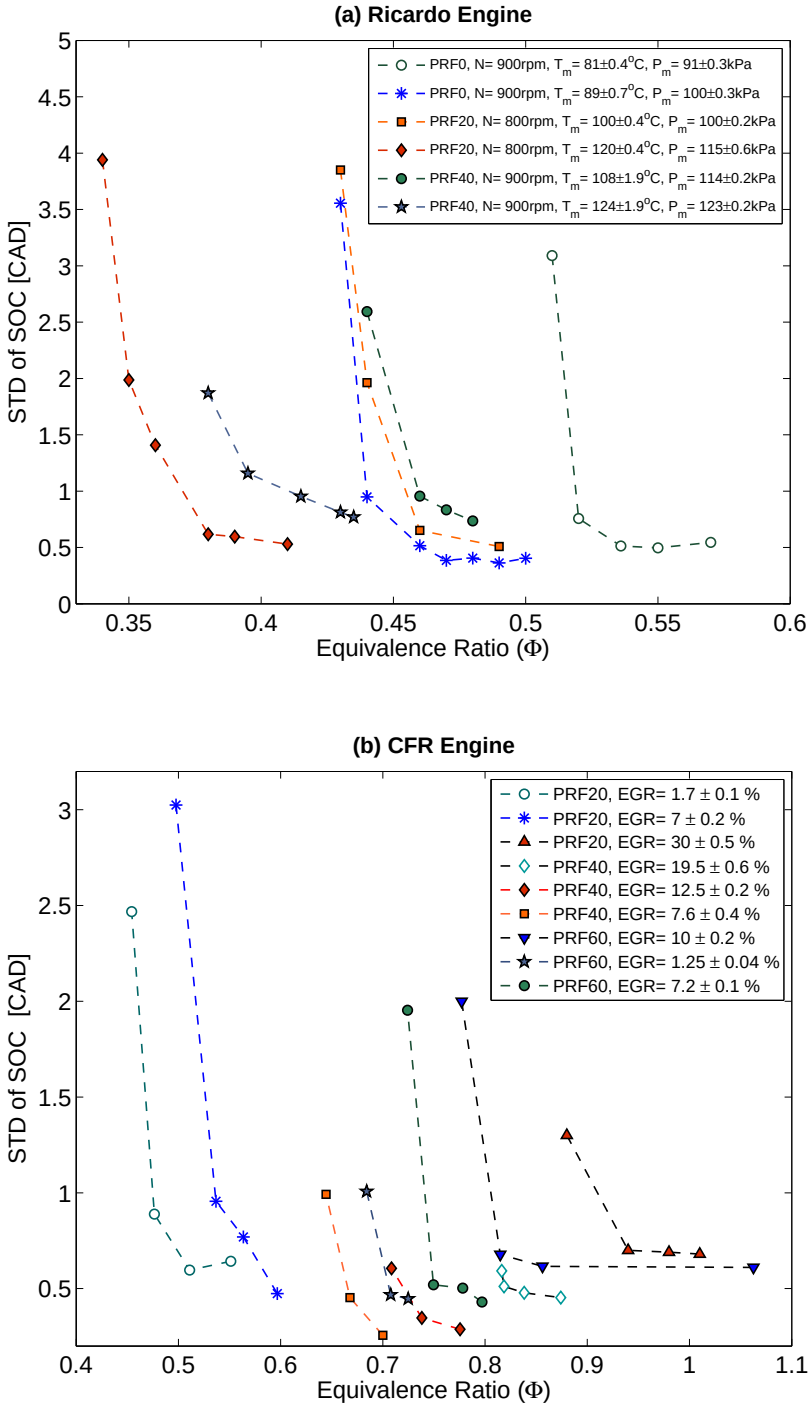

Figure 2.21: Influence of the equivalence ratio on the cyclic variations of SOC. (Ricardo and CFR engines)

mixtures can occur because SOC is advanced and the duration of HCCI combustion is shortened when Φ is increased [67, 104]. As in EGR, slower and late

ignitions are more likely to have high cyclic variation of the HCCI combustion. Results in [75] show that with changes in combustion phasing more variation occurs in combustion efficiency and thermal efficiency for leaner mixtures (lower fueling rates). This shows that leaner mixtures are more sensitive to combustion phasing variations.

The influence of the coolant temperature on the cyclic variation of SOC and on SOC is shown in Figure 2.22 and indicates that cyclic variation of SOC increases with a decrease in the coolant temperature. Decreasing coolant (wall) temperature significantly influences HCCI combustion due to a thicker thermal boundary layer and it slows bulk burning and drops combustion efficiency due to a higher heat loss and partial burning in the expanded cold thermal boundary layer [114]. Thermal stratification inside the cylinder increases when coolant temperature is lowered and this makes the HCCI combustion more sensitive to the variations of wall temperature [114]. In addition, fluctuations in the heat transfer process increase the possibility of higher cyclic variation when the coolant temperature is low. Figure 2.22-b shows a 8 CAD delay in SOC when the coolant temperature is lowered from 80^oC to 31^oC (round symbols). Comparing Figure 2.19-b (square symbols) and Figure 2.22-a (diamond symbols) it can be seen that a 30^oC temperature variation causes three times more change in cyclic variation of SOC with varying intake temperature compared to that of varying coolant temperature. This trend is opposite for the influence on cyclic variation of BD (Figure 2.13) where change in COV of BD from varying the coolant temperature is almost twice that of the intake manifold temperature. This confirms that cyclic variations of SOC is more sensitive to altering intake temperature compared to altering coolant temperature, while cyclic variation of BD exhibits more sensitivity to coolant temperature compared to the intake temperature. As previously mentioned one possible reason is the higher influence from coolant temperature

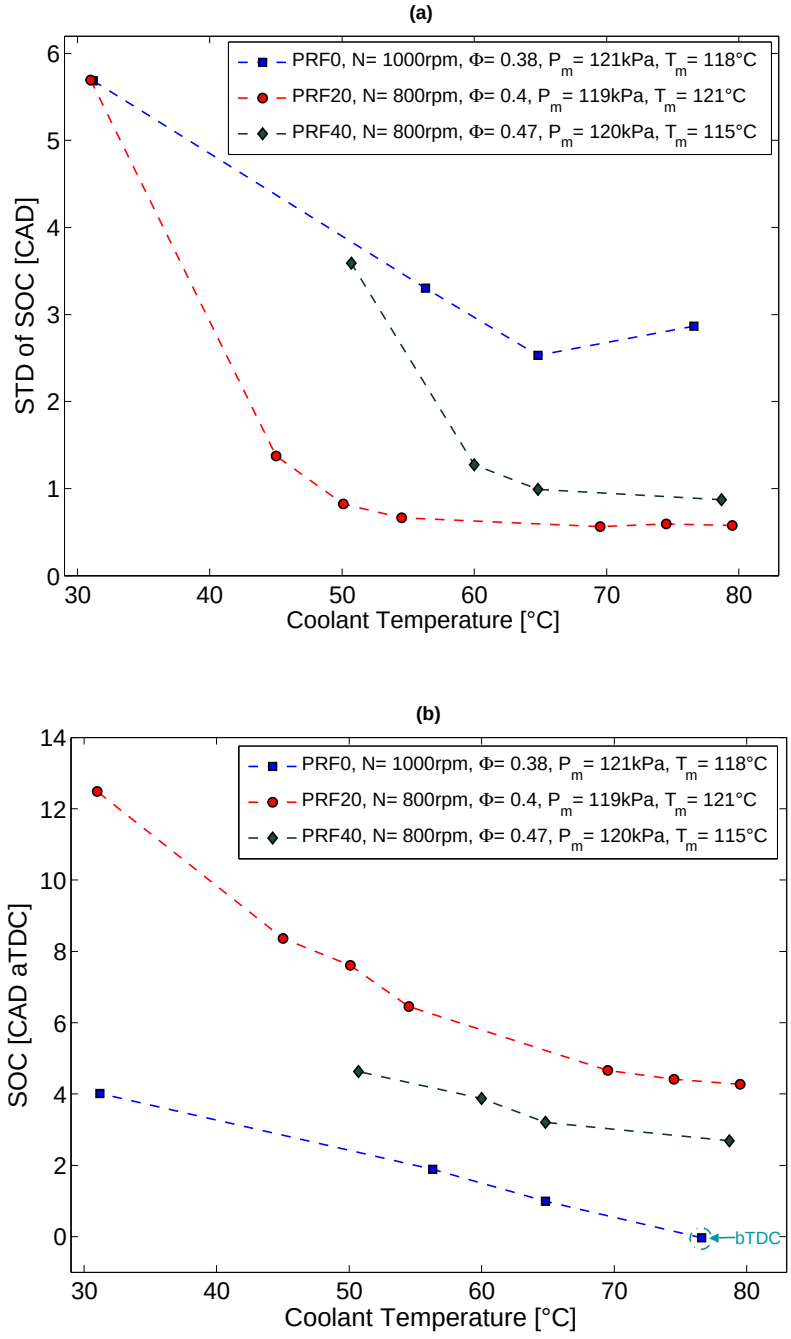

Figure 2.22: Influence of the coolant temperature on the cyclic variations of SOC. (Ricardo engine)

on thermal stratification compared to that of the intake temperature, while the intake charge temperature has more influence on the thermal state of the core gas compared to that of the coolant temperature [114].

The influence of intake pressure and engine speed on both cyclic variations of SOC and SOC are shown in Figure 2.23 and 2.24. SOC advances with an increase in the intake pressure (Figure 2.23). A decrease in the engine speed causes SOC to advance (Figure 2.24) due to the fact that HCCI combustion is a time based process dominated by the time scales of the reactions leading to auto-ignition. Increasing the engine speed reduces the amount of time for the auto-ignition reactions to occur relative to the piston motion.

Cylinder pressure is plotted as a function of crank angle in Figure 2.25 for several intake pressures (corresponding to Figure 2.23 round symbol) and for several engine speeds (corresponding to Figure 2.24 star symbol). Figure 2.25-a clearly shows that a higher intake pressure causes higher gas pressure in the compression stroke which results in earlier auto-ignition. The cylinder pressure traces in Figure 2.25-b indicates that as engine RPM increases the auto-ignition is delayed – due to the time based kinetics. The cylinder pressure traces in conjunction with Figure 2.23 and 2.24 reconfirm that the influence of engine speed and intake pressure on the cyclic variations of both SOC is highly dependent on the position of SOC. Cyclic variation of SOC is low when SOC occurs immediately after TDC but cyclic variation increases when SOC is late or early.

The effect of altering different operating variables on the cyclic variation of SOC depends on a combination of three factors: 1) how changing the variable affects the location of SOC, 2) how much the burn duration is shortened, and 3) secondary effects from changing the variable (such as thermal stability when changing the coolant temperature or the dilution rate fluctuation, the thermal and the composition inhomogenuity when changing the EGR rate). In general,

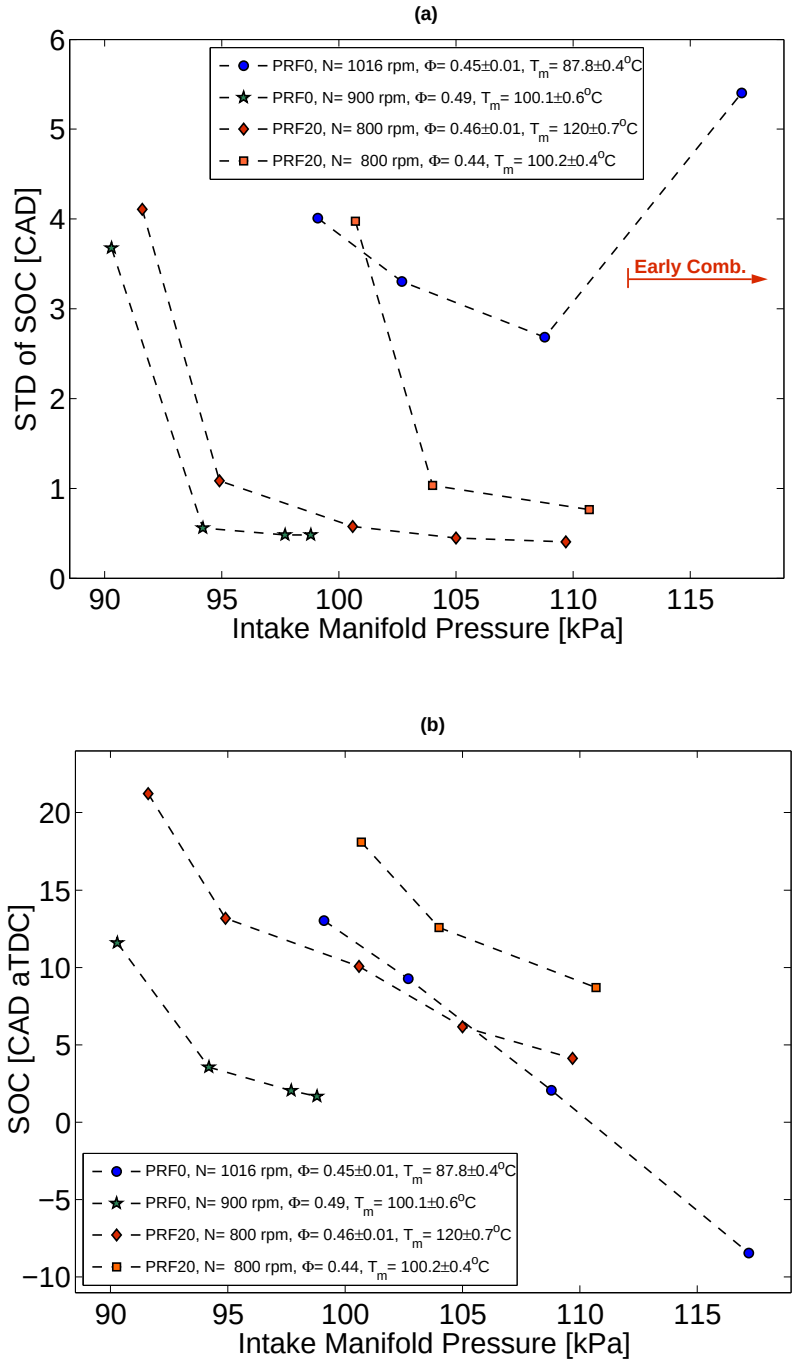

Figure 2.23: Influence of intake manifold pressure on the cyclic variations of SOC. (Ricardo engine)

a desirable operating condition for low HCCI cyclic variation tends to be high charge temperature at high equivalence ratio with low EGR dilution with SOC

occurring immediately after TDC and at fully warmed-up conditions, provided no knock occurs.

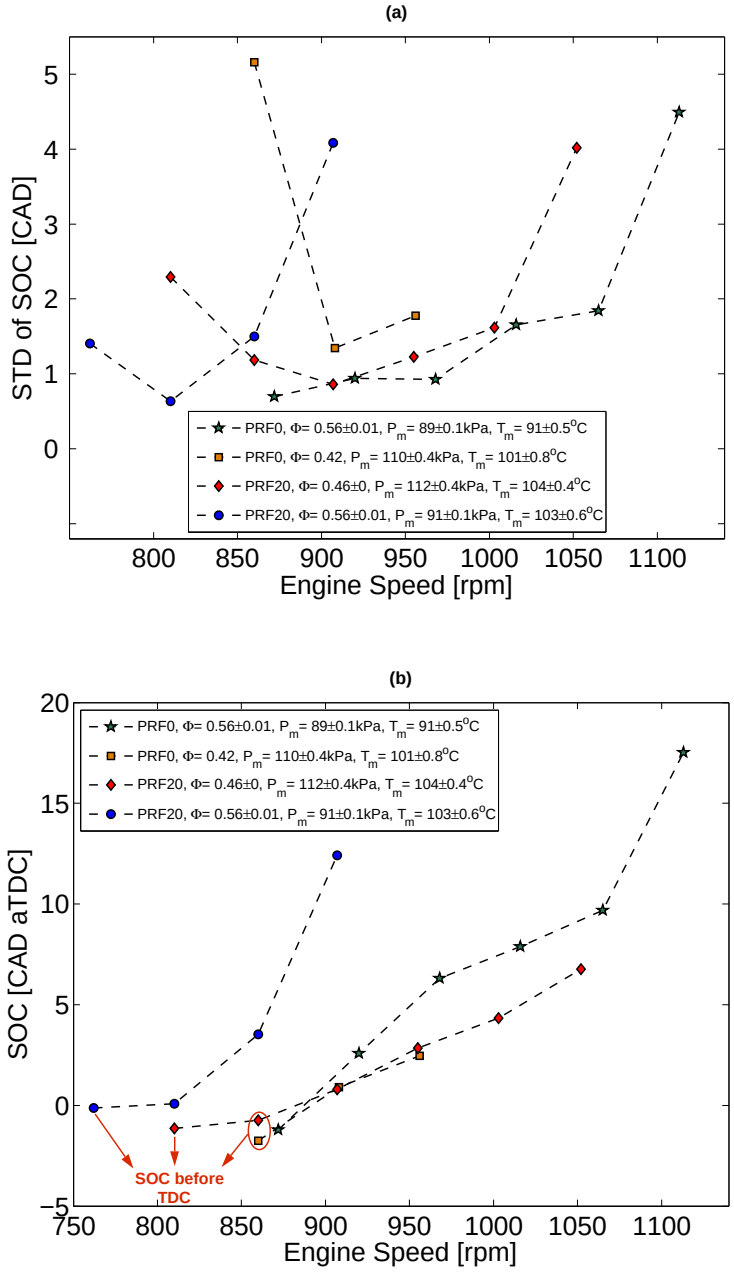

Figure 2.24: Influence of engine speed on the cyclic variations of SOC. (Ricardo engine)

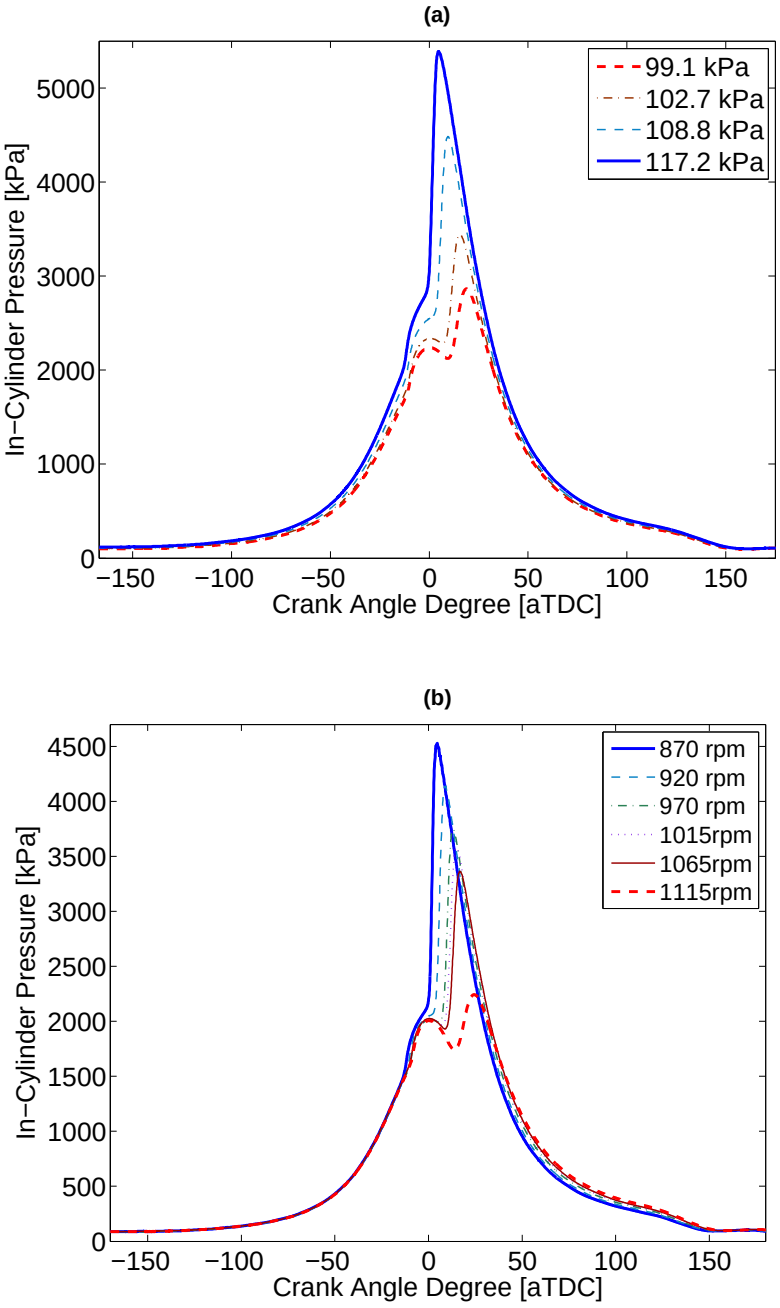

Figure 2.25: Averaged in-cylinder pressure trace variations as a function of (a) intake pressure and (b) engine speed for sample points from Figure 2.23 and Figure 2.24. (a) PRF0, $\Phi = 0.56$, $P_m = 89$ kPa, $T_m = 91^oC$; (b) PRF0, 1016 rpm, $\Phi = 0.45$, $P_m = 89$ kPa, $T_m = 87.8^oC$.

2.3 HCCI EXHAUST TEMPERATURE

High HC and CO engine-out emissions in HCCI can be mitigated by using oxidation catalysts which can reach conversion efficiencies of up to 95% for HC and CO pollutants when the catalytic converter is fully warmed up [68]. The catalytic converter must reach its operating temperature to be effective. The light-off temperature (the temperature at which the catalyst becomes more than 50% effective) is about $250 - 300\,^{\circ}\mathrm{C}$ for most of the catalysts [101, 116, 117, 118]. The light-off temperature depends on the active catalytic material and thermal inertia of the catalyst and it can be as high as $400\,^{\circ}\mathrm{C}$ [119]. The light-off temperature can be reduced to $200\,^{\circ}\mathrm{C}$ by using advanced new catalyst formulation [120] or by using modified catalyst material with a higher cell density and thinner-wall substrates [119]. However this significantly increases the cost of catalytic converters. Methods to reduce light-off time in catalysts are generally classified into active or passive systems. Typical active systems include electrically heated catalysts [121], fuel burners [122], secondary air injection [69] and after burners [70], all of which require an extra energy supply. In contrast, passive systems rely mainly on thermal management of the energy obtained from exhaust gases (e.g. by using close-coupled catalyst [71] or by using low thermal inertia manifolds [117]). The disadvantage of active systems is higher fuel consumption rate, more complexity and higher initial cost [123]. Passive systems however are completely dependant on the temperature and flow rate of exhaust gases. Since HCCI typically has low exhaust temperature, as low as $120\,^{\circ}\mathrm{C}$ [124], the HC and CO abatement by oxidation catalysts remains an important concern in HCCI engines. This could limit the desirable operating range of HCCI engines and also low HCCI exhaust temperature provides little energy for turbocharging which is often used to extend HCCI operating range for high loads [57]. Understand-

ing the factors influencing HCCI exhaust temperature is essential for a better modulation of engine charge variables to extend HCCI operating range while maintaining exhaust temperatures high enough for the catalyst.

Here, experimental data at over 340 steady-state and transient operating conditions is used to investigate the sensitivity of exhaust temperature to several charge variables at a range of engine loads. The primary aim of this section is to provide detailed results and discussion of the variables affecting the exhaust temperature in an HCCI engine. In addition since a dual mode HCCI-SI combustion is of utility for extending HCCI operating range [59], the variation in exhaust temperature during a mode switch and the difference between these two modes is described.

2.3.1 Experimental Engine Setup

Experimental measurements based on the single-cylinder Ricardo engine (Table 2.1) are recorded using the experimental setup shown in Figure 2.26. This setup is upgraded from that in Figure 2.1 by adding a new facility to measure exhaust gas temperature and also designing two separate fuel lines to be able to perform octane number switch for transient experiments.

A $1/32''$ sheathed J-Type thermocouple is used for fast exhaust temperature measurement. The thermocouple is placed in the exhaust as close as possible to the exhaust valve. The thermocouple voltage is amplified before sending to the data logging system and is sampled every crank angle degree. A polynominal fit outlined in [125] is used to calculate temperature from the amplified voltage signal. In Figure 2.26, one fuel system is used to inject n-Heptane and the other is used to inject iso-Octane. The separate flow rate control of each of these two fuels allows any desired octane number to be obtained. Both n-Heptane and iso-Octane injectors are aimed directly at the back of the intake valves.

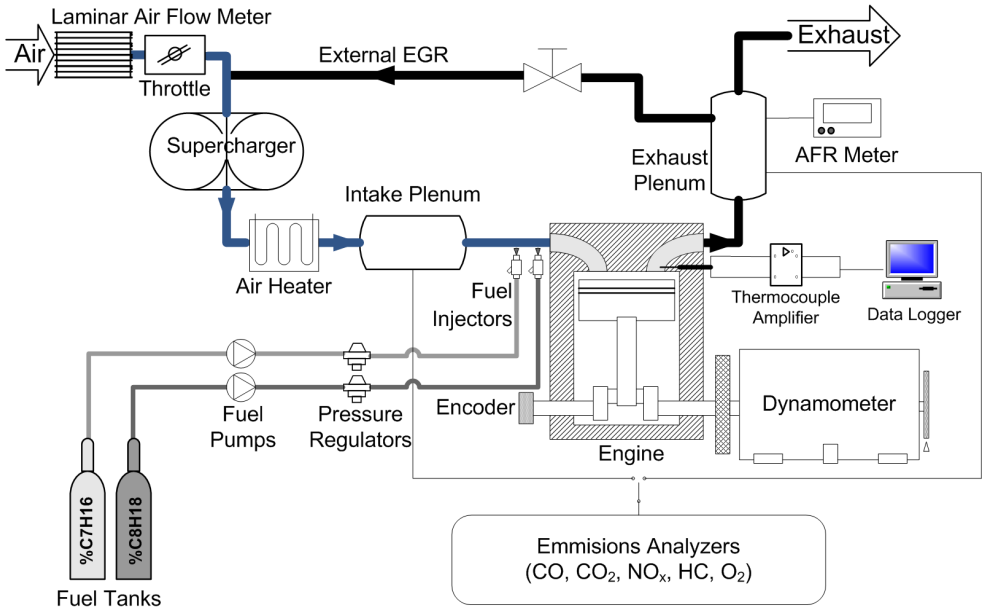

Figure 2.26: Ricardo single cylinder testbench schematic

The Ricardo engine is run to collect two types of experiment measurements: steady-state points and transient points. Table 2.8 details the experimental conditions of 340 steady-state points used in this study. Steady-state points include operation of the engine in both HCCI and SI modes. IMEP of the engine ranges between 3.8−9.2 bar in HCCI mode and 5.2−11.8 bar in SI mode. All SI test points are run with pure iso-Octane (PRF100) in stoichiometric operation and the spark timing is adjusted to give CA_{50} (crank angle where 50% of the fuel mass fraction is burnt) ∼8 CAD aTDC [103].

For each steady-state test point, pressure traces from 200 consecutive engine cycles with 0.1 CAD resolution are recorded and analyzed using an approach similar to that of Section 2.2.2. Transient tests include inter-zonal (HCCI-HCCI) and mode-switch (SI-HCCI) experiments. HCCI-HCCI transient experiments are performed by transient fueling at a constant air flow rate. Fuel injection pulse width is open loop scheduled by a dSpace MicroAutobox 1401/1501 ECU

Table 2.8: Operating conditions of 340 steady-state data points used in this study

Variables	**HCCI**	**SI**
Number of points	304	36
Fuel (PRF)	0 - 40	100
Engine speed, N [rpm]	800 - 1340	1000 - 2000
Intake manifold temperature, T_m [^oC]	59 - 162	30 - 49
Equivalence ratio, Φ	0.29 - 0.83	1.0
Intake manifold pressure, P_m [kPa]	88 - 161	60 - 111
EGR [%]	0 - 30	0
Spark timing	–	$CA_{50} \simeq 8$ CAD aTDC
Coolant temperature, $T_{coolant}$ [^oC]	41 - 84	80 - 86
Exhaust temperature, T_{exh} [^oC]	242 - 418	517 - 675

to achieve desired Φ and ON. Injected fuel mass per cycle for both injectors is estimated from the pulse width of the injectors [126]. SI-HCCI transitions is enabled by programming the ECU with an open loop look-up table for fueling, in both SI and HCCI modes. A software switch is used to command the engine from stoichiometric SI mode to HCCI mode [103]. During each transient test 450 cycles of cylinder pressure data are recorded with 0.1 CAD resolution and other engine variables are measured at a constant sample rate of 100Hz.

2.3.2 Results & Discussion

Exhaust gas temperature (T_{exh}) is experimentally documented and the effects of engine variables are investigated. First, the range of experimental T_{exh} highlights the significance of T_{exh} with respect to HCCI emissions. Next, the influence of several engine variables on T_{exh} are studied. Finally, differences in T_{exh} variations between HCCI mode and SI mode are discussed.

HCCI emission and IMEP of the Ricardo engine versus T_{exh} are shown in Figure 2.27. Results in Figure 2.27 show that T_{exh} can be as low as 242 °C in

HCCI mode and a significant portion of the data points have T_{exh} lower than typical catalyst light-off temperatures − 92 of the HCCI data points having T_{exh} lower or equal to 300°C. All of the data points with low exhaust temperature ($T_{exh} \leq 300\,°C$) have negligible NOx emissions and have reasonable IMEP. These are desirable HCCI operating points, but the low T_{exh} in these points is a limiting factor for oxidizing HC and CO pollutants in the catalytic converters. The range of T_{exh} in Figure 2.27 depends on the operating conditions the HCCI engine can run without exceeding knock/misfiring limit. HCCI exhaust temperature can be as low as 120 °C [124]. The peak T_{exh} among 304 HCCI data points in Figure 2.27 is about 400 °C. This peak temperature is considered low compared to that of SI mode for which the exhaust temperature is generally higher than 400 °C [124].

Higher HC and CO emissions are observed at lower T_{exh} in Figure 2.27-a and Figure 2.27-b. This makes the HCCI problem worse since T_{exh} is low at these conditions thus a lower oxidation rate by a catalytic converter is expected despite having the higher HC and CO emissions. Having higher HC and CO emissions at lower T_{exh} may be explained by having a lower in-cylinder gas temperature during the expansion stroke that reduces the possibility for post oxidation reactions to occur. High NOx emission points in the dashed circle of Figure 2.27-c is undesirable HCCI operation − refer to the data points #164−182 in the Appendix B. These data points are rich ($0.6 \leq \Phi \leq 0.72$) and exhibit knocking characteristics with a pressure rise rate of 7.4−11.4 bar/CAD and knock intensity of 0.4−2.2 bar based on PPmax metric. These high NOx data points are deliminated by the dashed circles in Figure 2.27-a and Figure 2.27-b and they are among the points with the lowest CO and HC emissions. High combustion temperature for these rich data points results in high NOx emission but low CO and HC emissions. These data points also have the highest T_{exh} values in T_{exh} range indicated in Figure 2.27.

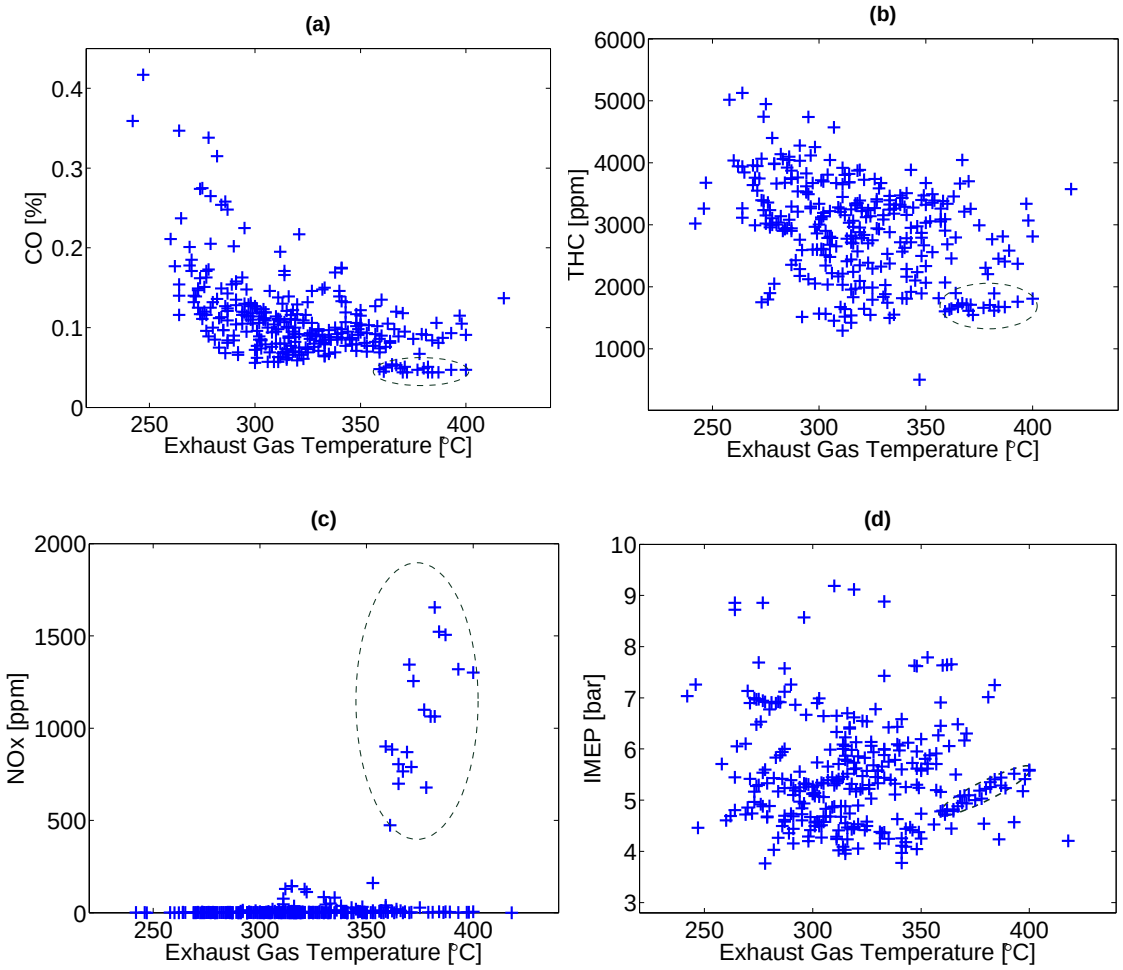

Figure 2.27: Trend of variation in HCCI exhaust gas emissions and IMEP as a function of exhaust gas temperatures in HCCI steady-state operation.

2.3.2.1 Influence of Operating Variables on T_{exh}

The engine charge variables predominantly determine the onset of auto-ignition and combustion characteristics of HCCI engines. To systematically investigate this each engine input is changed while maintaining the others constant. The six engine inputs that are varied are: intake pressure (P_m), octane number (ON), engine speed (N), intake temperature (T_m), coolant temperature (T_c), and equivalence ratio (Φ). The effects of each of these inputs on T_{exh} are studied and then they are compared with each other.

Variation of T_{exh} and in-cylinder gas temperature[7] by increasing the intake pressure are shown in Figure 2.28 (octane number, engine speed, intake temperature, equivalence ratio and coolant temperature are held constant). Higher intake

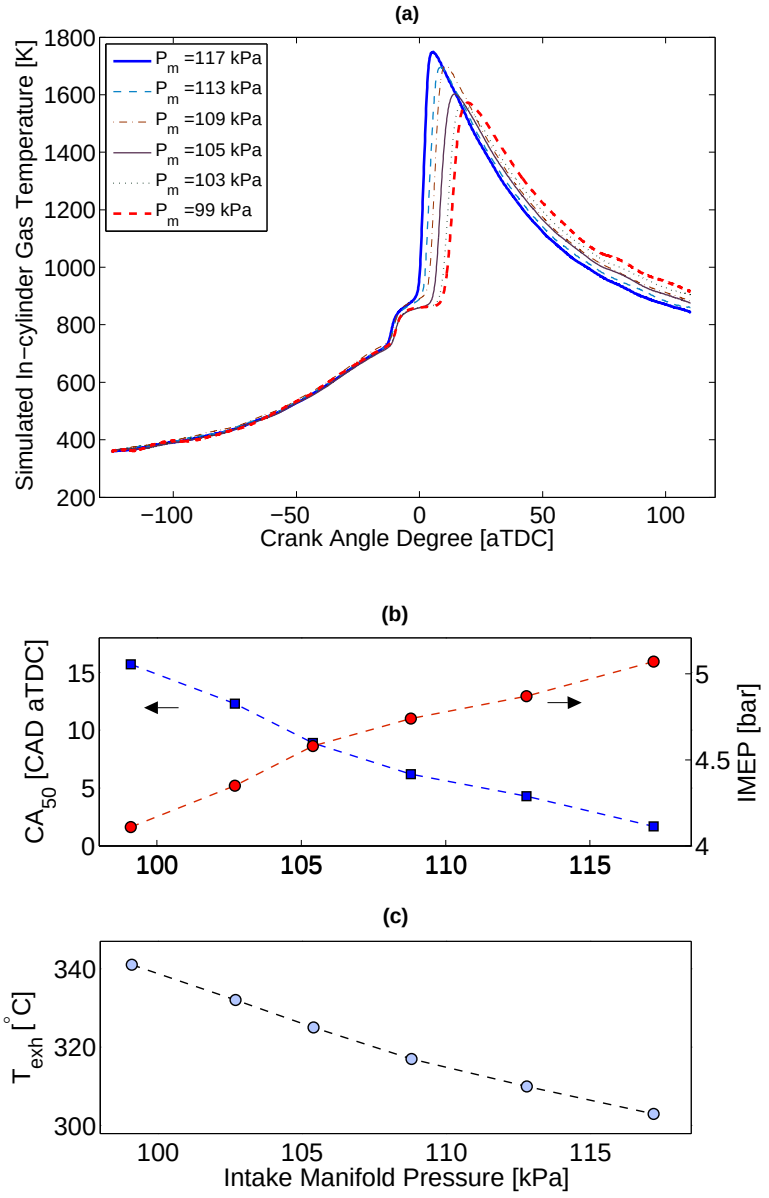

Figure 2.28: Variations of HCCI exhaust and in-cylinder temperatures as a function of the intake pressure (Fuel: PRF0, N = 1016 rpm, $\Phi = 0.44$, $T_{man} = 87.3^{o}$C − data points 81-86 in Appendix B)

[7]This temperature is calculated using recorded pressure trace and applying the ideal gas law for the closed engine cycle.

pressure in Figure 2.28-a results in earlier and shorter ignitions close to TDC that leads to higher peak temperature but lower cylinder temperature during the expansion stroke. CA_{50} in Figure 2.28 advances from 15.7 to 1.7 CAD aTDC as the intake pressure increases by 18 kPa (points #81−86 in Appendix B). When the ignition is delayed, most of the energy is released partway down the expansion stroke and this increases the exhaust temperature. T_{exh} decreases by 38 °C when the intake pressure is increased from 99 kPa to 117 kPa ($\Delta T_{exh}/\Delta P_m$ = - 2.1 °C/kPa). This is mainly caused by advancing the HCCI combustion when the intake pressure is increased. As expected, IMEP increases by boosting the intake pressure in Figure 2.28. However, T_{exh} decreases with increasing the engine load (IMEP) at a fixed equivalence ratio fueling condition. Results in Figure 2.28 combined with CA_{50} values in the Appendix B show that T_{exh} is strongly influenced by HCCI ignition timing location.

Variation of T_{exh} with changing the fuel octane number in Figure 2.29 also shows T_{exh} is very dependent on CA_{50}. T_{exh} increases by 20 °C as the octane number is increased from 22 to 40 ($\Delta T_{exh}/\Delta ON = +1.1$ °C/ON). In the transient HCCI test in Figure 2.29 during a relatively constant engine load test condition CA_{50} is delayed by about 8 CAD as octane number is changed from 22 to 40. Increasing the octane number increases the HCCI Burn Duration (BD) as shown in Figure 2.29-a where BD is doubled when ON is increased by 18 units. This leads to a prolonged combustion in the expansion stroke which results in a higher T_{exh}. In addition, the cyclic variation of CA_{50} (Figure 2.29-a) substantially increases when CA_{50} retards from 3 to 11 CAD aTDC. This behavior is discussed in more detail in [80] for the Ricardo engine and it is mainly due to the temperature rise from combustion being counteracted by the cooling from piston expansion when ignition retards and also by having more thermally stratified charge with retarding the combustion.

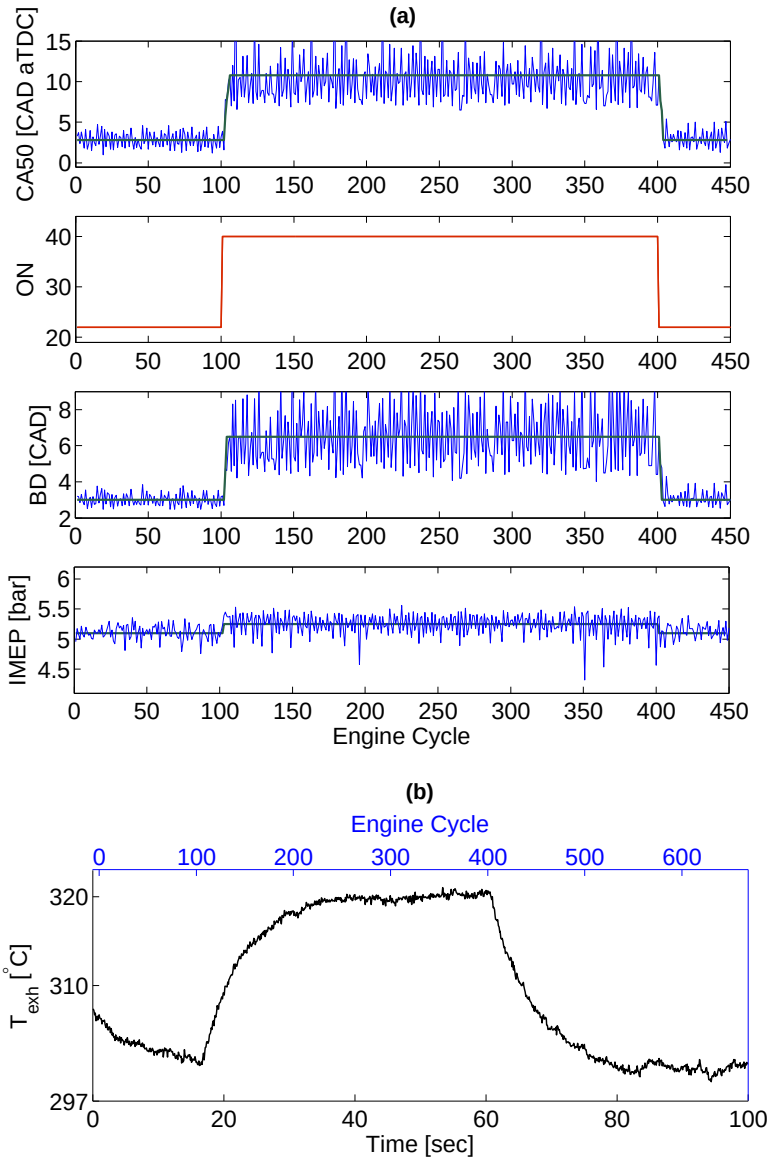

Figure 2.29: Variations in HCCI exhaust temperature with changing the fuel octane number. Note: the time scale of plot (b) in this figure starts before those of plots (a) and it ends after the last cycle of plots (a). (ON: Octane Number; N = 815 rpm, $\Phi = 0.44$, $T_m = 117^oC$, $P_m = 120$ kPa)

Variations of T_{exh} versus two engine variables in Figure 2.28 and Figure 2.29 represent two cases of having location of ignition timing (CA_{50}) as the main factor affecting T_{exh}. But other factors can also play an important role when other engine variables such as the engine speed (Figure 2.30), the coolant tem-

perature (Figure 2.31) and the intake temperature (Figure 2.32) are changed. In Figure 2.30, T_{exh} increases significantly from 315 °C to 418 °C when the engine speed increases from 873 rpm to 1113 rpm ($\Delta T_{exh}/\Delta rpm = +4.3$ °C/10rpm). This can be partly attributed to the change in ignition timing since CA_{50} retards from 1.9 to 20.2 CAD aTDC (points #62−67 in Appendix B). Changing engine speed, in addition to varying ignition timing, causes a large change in T_{exh} since less heat loss is expected at higher engine speeds [101]. This becomes more important for late ignition that have longer burn durations for which there are more time available for heat loss. When engine speed increases there is both decreased heat loss and delayed ignition timing and the two main compounding factors combine to have a significant influence on T_{exh}.

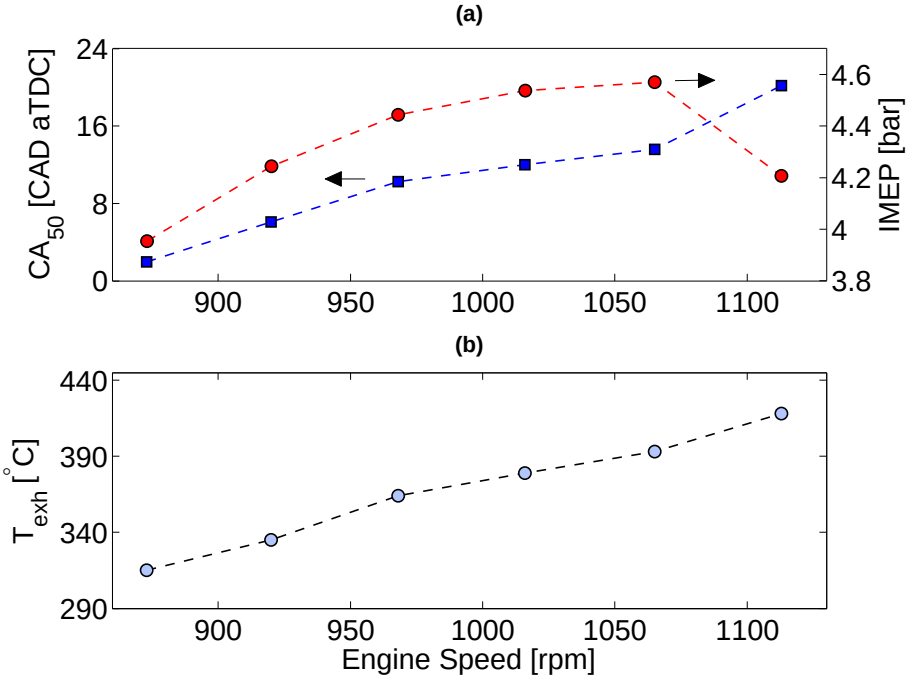

Figure 2.30: HCCI exhaust temperature variations as a function of the engine speed (Fuel: PRF0, $\Phi = 0.56$, $P_m = 89$ kPa, $T_m = 91^oC$ − data points 62-67 in Appendix B)

Variation of T_{exh} versus the coolant temperature in Figure 2.31 shows another

example that the heat loss plays an important role in addition to the ignition timing location. Decreasing coolant (wall) temperature results in a higher heat loss and retards HCCI combustion. In Figure 2.31, CA_{50} retards from 7.9 to 11.8 CAD aTDC when T_c decreases from 80 to 50 °C, thus T_{exh} is expected to increase. But T_{exh} decreases from 281 to 271 °C ($\Delta T_{exh}/\Delta T_c = +0.3$ °C/°C). This indicates the impact from the heat loss factor is stronger and opposite to that of the ignition timing location in Figure 2.31. When coolant temperature decreases there is both increased heat loss and delayed ignition timing, two main opposing factors combine to affect T_{exh}. This results in having a moderate change in T_{exh} though the coolant temperature is substantially changed in Figure 2.31.

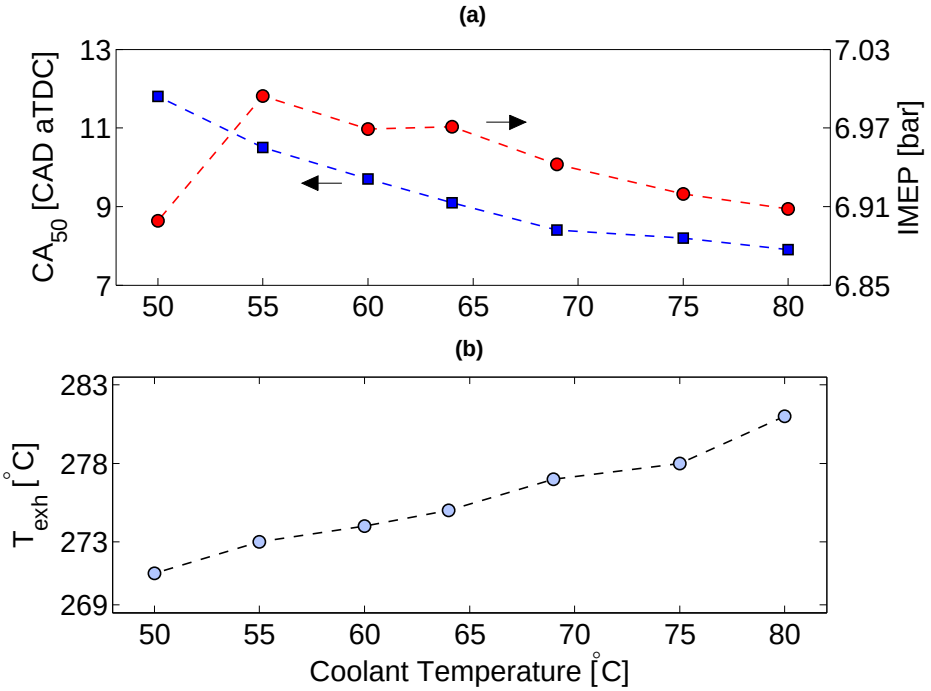

Figure 2.31: HCCI exhaust temperature variations as a function of the coolant temperature (Fuel: PRF20, N = 800 rpm, $\Phi = 0.4$, $T_{man} = 121$°C, $P_{man} = 119$ kPa – data points 157-163 in Appendix B)

Similarly, a moderate 10 °C decrease in T_{exh} despite a large intake temperature change from 73 °C to 112 °C is shown in Figure 2.32 with a slope of $\Delta T_{exh}/\Delta T_m =$

-0.3°C/°C. Concurrently, CA_{50} advances significantly from 14.9 to 6.0 CAD aTDC during the intake temperature increases (points #96−100 in Appendix B). Similar

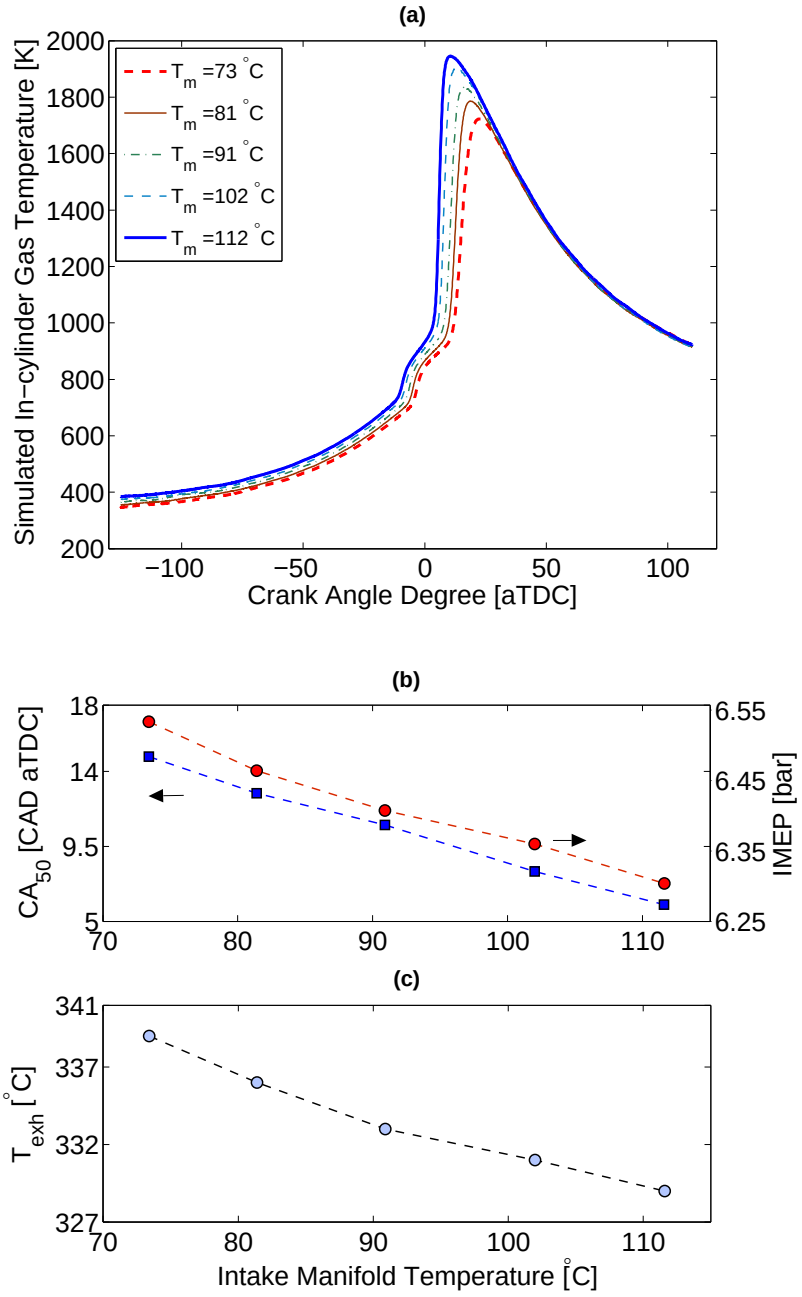

Figure 2.32: Variations of HCCI exhaust and in-cylinder temperatures as a function of the intake temperature (Fuel: PRF10, N = 997 rpm, $\Phi = 0.42$, $P_{man} = 120$ kPa − data points 96-100 in Appendix B)

to the results in Figures 2.30-2.31 this indicates there is another factor beside

CA_{50} influencing T_{exh}. The second main factor is that higher initial temperature (energy input air) at higher T_m conditions leads to higher in-cylinder gas temperature for most of the engine cycle as shown in Figure 2.32-a. This factor acts contrary to the changing ignition timing when the intake temperature is varied, thus variation in T_{exh} by changing intake temperature in Figure 2.32 is not as large as those seen in Figures 2.28−2.30.

The influence of the equivalence ratio on T_{exh} is shown in Figure 2.33. T_{exh} increases by 17 °C when Φ increases from 0.36 to 0.43. CA_{50} advances 10.5 ° when increasing the equivalence ratio. Thus, T_{exh} increases when a higher Φ is used despite advancing the HCCI combustion towards TDC. This trend is opposite to what observed in Figures 2.28−2.30 and Figure 2.32. Two opposing factors affecting T_{exh} are present in Figure 2.33 (similar to those of T_c effect in Figure 2.31

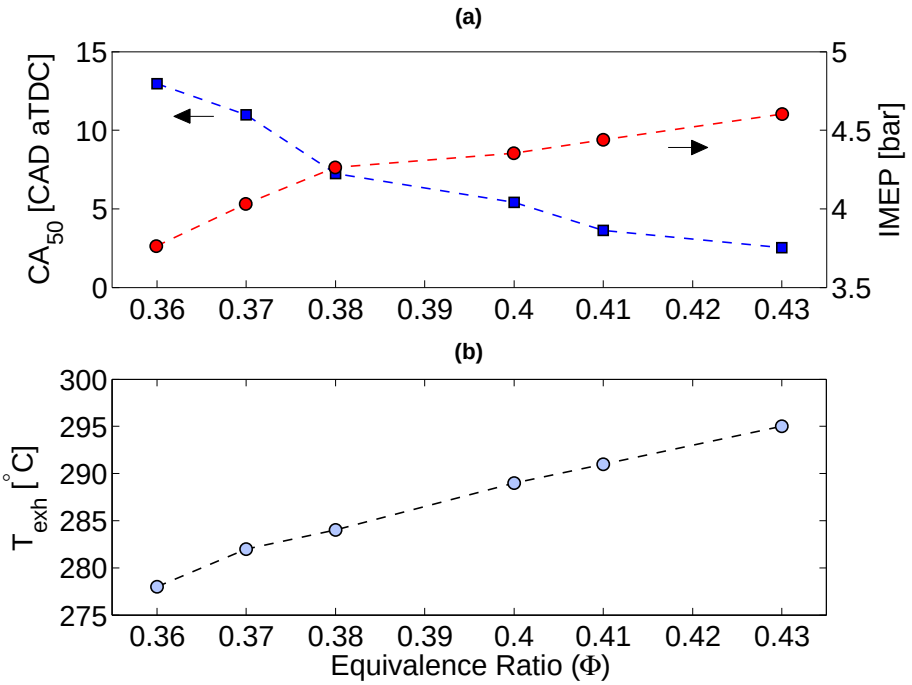

Figure 2.33: Variations in HCCI exhaust temperature with changing equivalence ratio. (Fuel: PRF0, N = 900 rpm, P_{man} = 110 kPa, T_{man} = 92 °C − data points 51-56 in Appendix B)

and T_m effect in Figure 2.32). The two opposing factors here are the ignition timing location and injected fuel energy content. More energy is released when the amount of fuel mass flow rate in the intake charge increases at a constant air mass flow rate condition (higher Φ). Here the influence from the second factor, energy input fuel, on T_{exh} is stronger than that of ignition timing location. This is opposite to the results in Figure 2.32 where the influence from ignition timing location is stronger than that of the second factor (input air temperature).

Variations in T_{exh} versus CA_{50} and specific energy input fuel are plotted in Figure 2.34 for all the 304 steady-state HCCI data points used in this study. The overall trend in Figure 2.34 is consistent with observations from previous figures and suggests an increase in T_{exh} by retarding CA_{50} or increasing energy input fuel per mass of air-fuel mixture. Variations from the overall trend in Figure 2.34 are due to the diversity of operating conditions where other inputs are also varied (see Table 2.8). For instance the dashed circle in Figure 2.34-b consists of data points[8] with either low coolant temperature ($T_c \leq 67\,^{\circ}C$) or ultra lean mixture ($\Phi \leq 0.36$). Results in Figure 2.33 and Figure 2.34 indicate the possibility that the slope of T_{exh} could change sign when Φ is increased. This behavior is in fact measured and shown in Figure 2.35. T_{exh} first increases when increasing Φ, but then begins to decrease when the intake charge is made richer than Φ=0.48. The increase in Φ from 0.43 to 0.5 results in advancing CA_{50} from 12 to 2.9 CAD aTDC (points #44−50 in Appendix B). As CA_{50} nears TDC in Figure 2.35, the effect from variation in ignition timing location (factor 1) finally overcomes the effect from changes in fuel energy content (factor 2). Data points #38−43 in the Appendix B exhibit another example of concave down behavior in T_{exh} versus variation in Φ.

[8]Data points #51, 118-120, 132, 134, 149, 163, 195-196 in Appendix B.

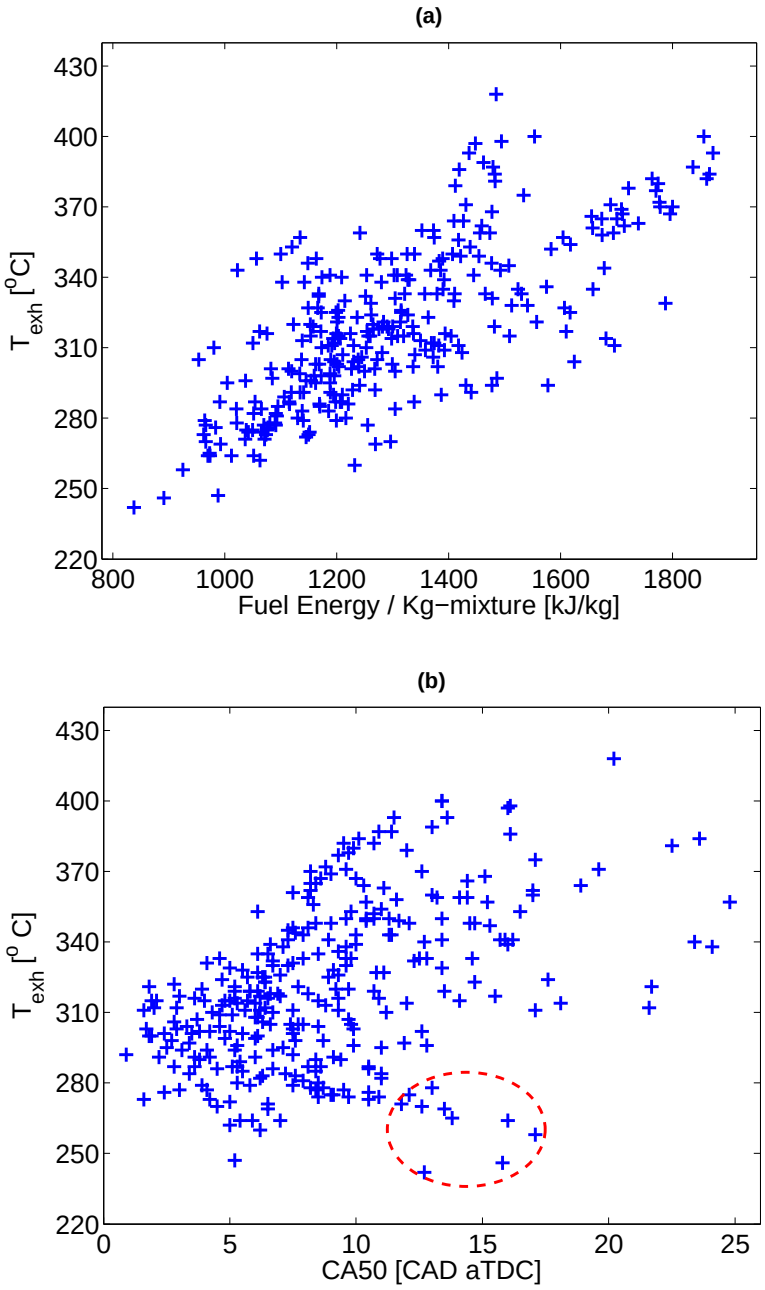

Figure 2.34: Variations in HCCI exhaust temperature versus CA50 and mixture specific fuel energy.

Table 2.9 summarizes the results of comparing the effects of changing six engine variables on T_{exh} in HCCI conditions. The first group are the primary inputs for which the location of ignition timing is the main factor that influences

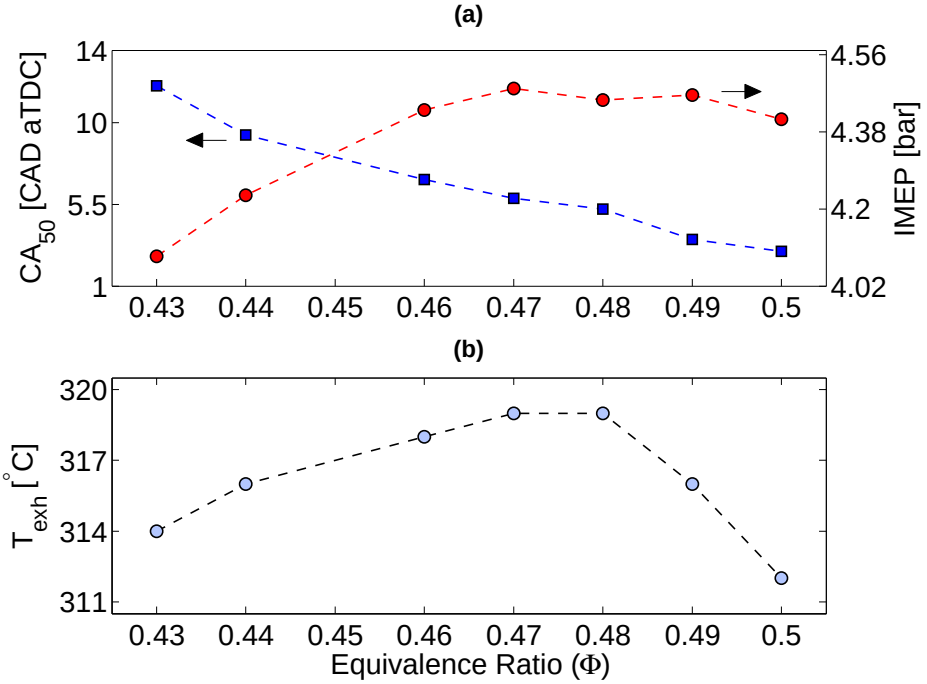

Figure 2.35: Variations in HCCI exhaust temperature with changing equivalence ratio. (Fuel: PRF0, N = 900 rpm, T_{man} = 89°C, P_{man} = 100 kPa − data points 44-50 in Appendix B)

Table 2.9: Trend of variation in HCCI exhaust temperature with changing six main engine variables.

Variable	$\mathbf{T_{exh}}$	**Main effects**	**Slope** ($\Delta T_{exh}/\Delta x$)
Intake Pressure (P_m) ↑	↓	One	- 2.1 °C/kPa
Octane Number (ON) ↑	↑	One	+1.1 °C/ON
Engine Speed (N) ↑	↑	Two parallel	+4.3 °C/10rpm
Coolant Temperature (T_c) ↑	↑ / ↓	Two opposing	+0.3 °C/°C
Intake Temperature (T_m) ↑	↑ / ↓	Two opposing	−0.3 °C/°C
Equivalence Ratio (Φ) ↑	↑ / ↓	Two opposing	variable

T_{exh}. This group includes the intake pressure and the fuel octane number. As discussed, later and longer ignitions after TDC result in hotter exhaust gases. The second group are compounding inputs that include the engine speed. Variation in heat loss of exhaust gases is the second main factor which is coupled with the factor of ignition timing location to amplify the influence of engine speed variations on T_{exh}. The third group are inputs that cause opposing effects. The coolant temperature, intake temperature and the equivalence ratio are in this group. In this case, the final trend of T_{exh} variation depends whether the influence of ignition timing location is stronger/weaker than the second main factor (heat loss or energy input air or energy input fuel).

The steady-state experimental data is used to find an empirical correlation to provide understanding of variations in T_{exh}. To simplify the correlation, constant engine speed and coolant/oil temperatures are assumed. Three main parameters are selected to characterize T_{exh}: specific energy input fuel (magnitude parameter), CA_{50} (location parameter) and BD (dispersion parameter). The following correlation is found to work well on the experimental data:

$$T_{exh} = \left[A_T + B_T \frac{\ln(q_f)}{q_f^2} + C_T \left[\ln(CA_{50})\right]^2 \right] . BD^{D_T} \tag{2.2}$$

where, q_f is specific energy input fuel in kJ/kg, CA_{50} is presented in CAD aTDC and BD is in CAD. Half of the 304 HCCI experimental data is used to parameterize the correlation (2.2) and the resulting values of constants are $A_T = 375.24$, $B_T = -1.96\times10^7$, $C_T = 5.26$, and $D_T = 0.02$. Predicted T_{exh} are compared with those from experiments in Figure 2.36 for all 304 HCCI operating conditions used in this study. The results indicate the simple correlation captures the trend of T_{exh} variations with a good agreement with the experimental data for the ma-

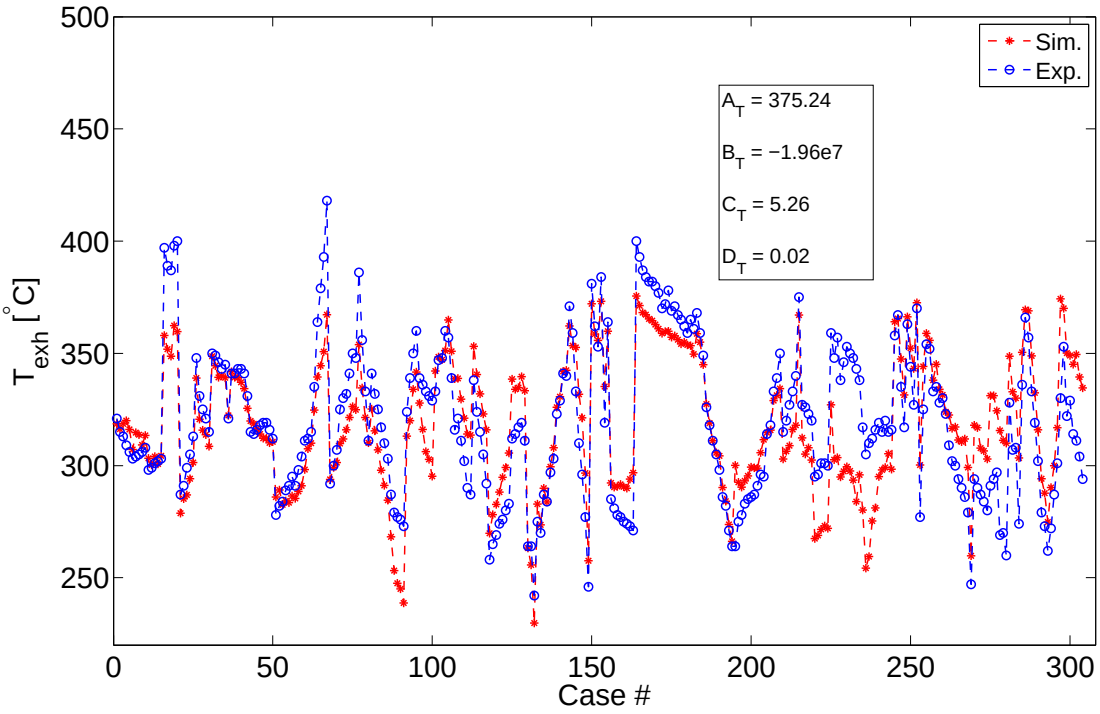

Figure 2.36: Comparison between predicted and experimental T_{exh} for four PRF blends at different HCCI steady-state engine conditions.

jority of operating conditions. An uncertainty[9] of ±25 °C is found in predictions from the correlation (2.2). The main source of error in Figure 2.36 comes from ignoring heat loss variations in the correlation (2.2) for the data points with variable engine speeds or variable coolant temperatures (see Table 2.8). Examining the values of constants in the correlation (2.2) indicates BD has significantly lower impact on T_{exh} compared to CA_{50} and q_f. Variation in T_{exh} as a function of q_f and CA_{50} is simulated in Figure 2.37 for an average BD at a range of HCCI operating conditions from Table 2.8. As expected T_{exh} drops with reducing q_f or advancing ignition. The simulation results show q_f impacts T_{exh} more strongly than that of CA_{50} for the operating range indicated in Figure 2.37.

[9]The uncertainty is determined by 2σ, where σ is the standard deviation of residual errors. This means that the true value, with 95% confidence, lies within $\pm 2\sigma$ of the estimated value. [102]

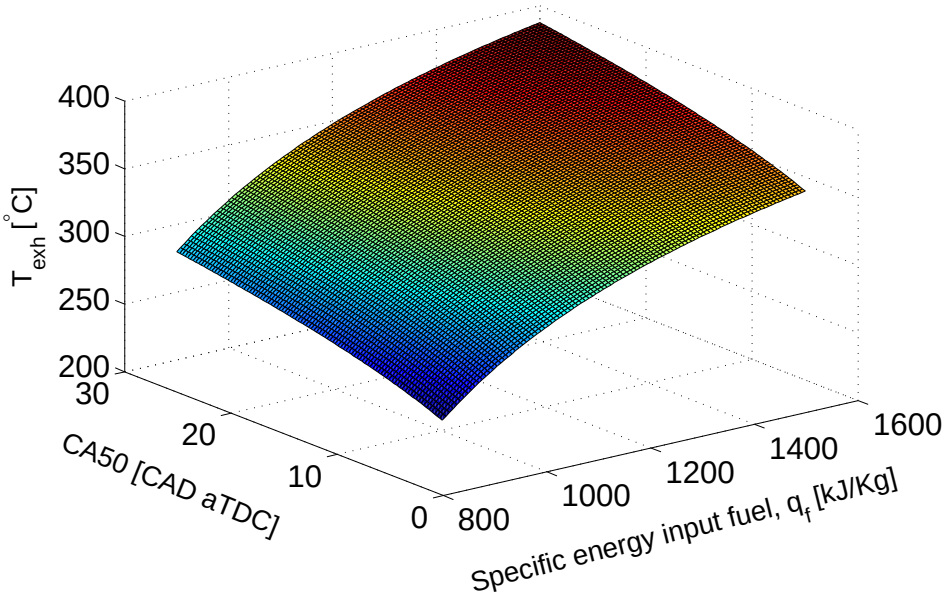

Figure 2.37: Simulated exhaust temperature using the correlation (2.2) for HCCI operation range in Table 2.8. (An average BD of 4.4 CAD is used to generate this plot.)

Comparing the trend of variations in T_{exh} with changing engine load (IMEP) in Figure 2.28, Figures 2.30-2.33, and Figure 2.35 indicate that T_{exh} is not necessarily a function of engine load in HCCI. In Figure 2.28, T_{exh} decreases by increasing engine load, but T_{exh} increases by increasing engine load in Figure 2.32. Similarly, T_{exh} increases in Figures 2.30-2.31 no matter if engine load increases or decreases. This is because T_{exh} is mainly function of other discussed variables that may also influence engine load. But IMEP in HCCI mode mainly depends on the fueling rate rather than the ignition timing; however, IMEP becomes strongly dependant on the ignition timing for the conditions that have a constant fueling rate [80]. This explains why IMEP increases in Figure 2.28 and Figure 2.32 by either increasing intake pressure or decreasing intake temperature. Since Φ is kept constant in Figure 2.28 and Figure 2.32, higher intake pressure and lower intake temperature require more fuel mass flow rates. However, IMEP decreases

for late ignition even if fueling rate is increased. This is evident in data point at 1113 rpm (#67 in Appendix B) in Figure 2.30 with CA_{50} =20.2 CAD aTDC for which the IMEP drops despite increasing fueling rate[10].

CO and HC emissions for the data points from P_m sweep (Figure 2.28), RPM sweep (Figure 2.30), T_m sweep (Figure 2.32), and Φ sweep (Figure 2.35) are shown in Figure 2.38. A strong relation is observed between CA_{50} and amounts of CO and HC emissions. This relation holds for all the four engine inputs variable. Both CO and HC emissions increase with increasing CA_{50}. Higher in-cylinder temperature during HCCI combustion tends to occur at earlier ignitions as shown in Figure 2.28-a and Figure 2.32-a. High combustion temperature which is well characterized by the peak cylinder cycle temperature is the main requirement for CO and HC oxidation in HCCI engines [6, 3, 64]. However, higher peak combustion temperature at earlier ignitions also causes higher NOx emissions. This is evident in NOx values in RPM sweep data points (#62−67 in Appendix B) where NOx increases from 0 ppm to 144 ppm when CA_{50} advances from 20.2 CAD aTDC to 1.9 CAD aTDC.

2.3.2.2 T_{exh} Variations in SI Mode vs. HCCI Mode

Switching between HCCI and SI modes is a technique to increase limited engine output power in HCCI by switching to SI mode to get full power. These two combustion modes have different T_{exh} characteristics due to the different combustion principles. Ignition timing location is an important factor in both combustion modes. Ignition timing in an SI engine is adjusted by spark timing, while engine operating conditions determine ignition timing (CA_{50}) in HCCI mode. This leads to having less complicated behavior in T_{exh} variations in SI mode compared to

[10]To keep Φ constant by increasing engine speed, the fueling rate is increased in proportion to the increased air into the engine. Air mass flow rate for the data points in Figure 2.30 increases from 2.3 g/sec to 3.2 g/sec by increasing engine speed from 813 rpm to 1113 rpm.

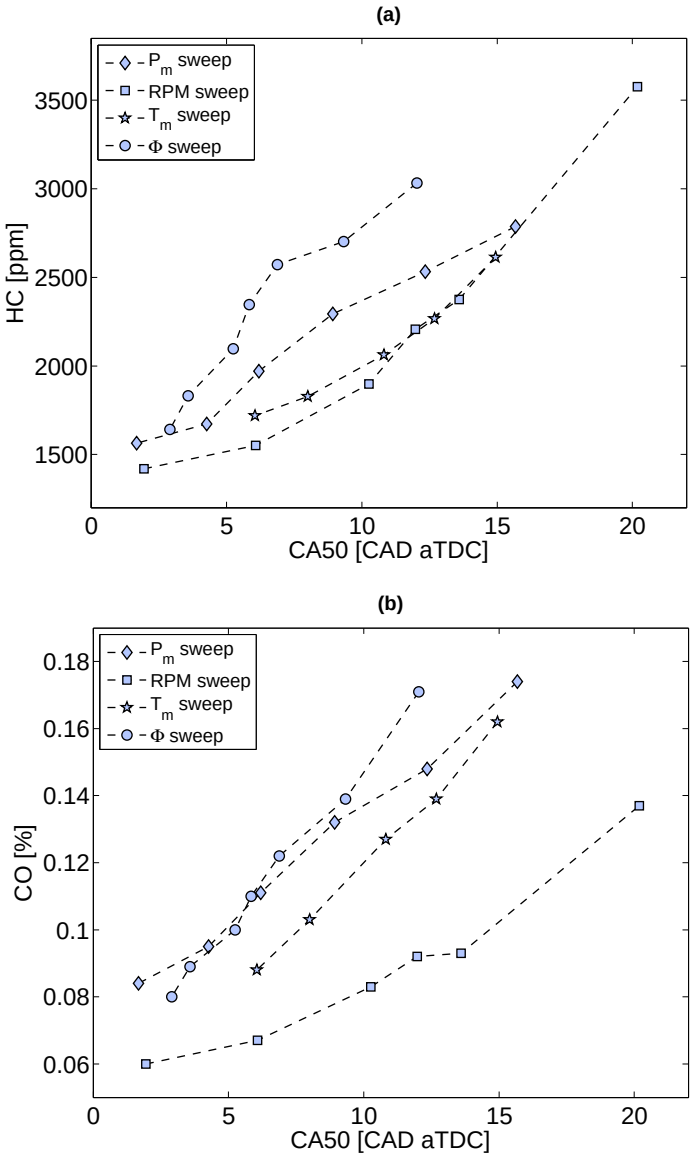

Figure 2.38: Variations in HC and CO emissions with changing four engine variables: (1) P_m sweep from Figure 2.23, (2) RPM sweep from Figure 2.24, (3) T_m sweep from Figure 2.32, (4) Φ sweep from Figure 2.35.

that of HCCI mode. Spark timing, engine speed and load are three main factors that influence T_{exh} in SI mode [101]. Similar to HCCI, later ignitions result in higher exhaust temperature which is also used as a technique to reduce catalyst light-off time during cold start [127]. Experimental results for SI mode at a fixed ignition timing (CA_{50}) condition as engine speed and intake pressure are varied

for stoichiometric operation are shown in Figure 2.39-a. Similar to the results in Figure 2.30, T_{exh} also increases in SI mode when engine speed increases. But opposite to what is observed in HCCI mode (Figure 2.28), T_{exh} increases with increasing the intake pressure. As shown in Figure 2.39-b, increasing the engine load in SI mode by boosting intake pressure leads to increasing T_{exh}. This is different than that of HCCI mode for which engine load is not a main factor to affect T_{exh}. In addition, results from 36 different operating points in Figure 2.39 show the engine speed has a larger impact on T_{exh} in SI mode compared to that of intake pressure or engine load ($\Delta T_{exh}/\Delta rpm$ = 1.2-1.3°C/10rpm, $\Delta T_{exh}/\Delta P_m$ = 0.5-0.7°C/kPa, $\Delta T_{exh}/\Delta IMEP$ = 0.04-0.07°C/kPa). The impact from changing engine speed on T_{exh} in SI mode can be significantly larger than that of engine load, comparing the typical range of variations in engine speed with that of engine load or intake pressure in SI engines. A similar trend is also observed in HCCI mode where the engine speed is more influential on T_{exh} than the intake pressure.

Finally, transient exhaust temperature (T_{exh}) during HCCI-SI mode switch at nearly constant load is shown in Figure 2.40. The exhaust gas temperature is substantially higher in SI mode compared to that of HCCI mode for constant load condition. The BD in SI mode is five times longer than that of HCCI mode for the test condition in Figure 2.40 (BD_{HCCI}=4 CAD, BD_{SI}=20 CAD). Longer combustion in SI results in releasing more energy at later crank angles compared to that of HCCI and results in higher T_{exh} in SI mode. In addition, SI mode typically runs with significantly richer intake charge than that of HCCI mode − note that fuel conversion efficiency in SI mode is lower than that of HCCI. For instance the value of Φ changes from 0.45 to 0.95 when the Ricardo engine is switched from HCCI to SI mode in Figure 2.40. The richer mixture requirement in SI mode can cause a substantial increase in T_{exh} as more heat is released

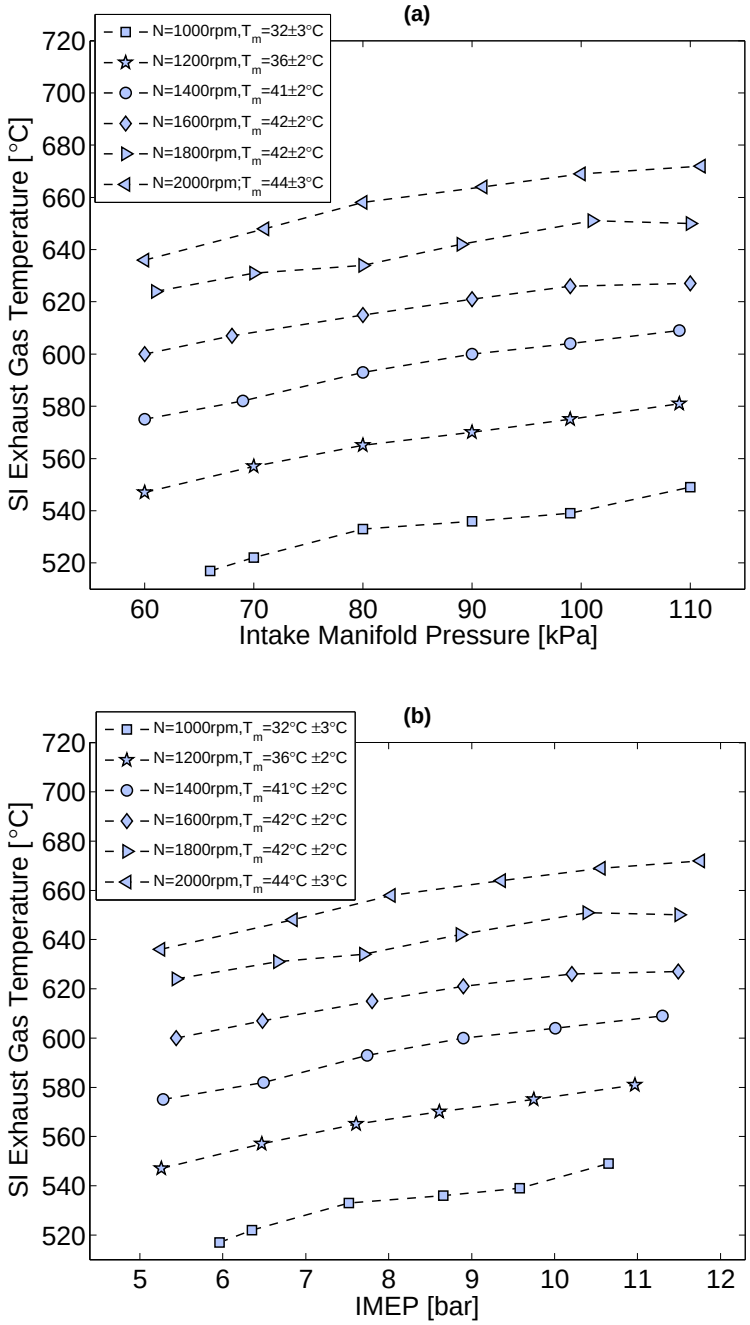

Figure 2.39: Variations in the exhaust temperature in SI mode as a function of engine load and engine speed.

compared to that of HCCI. For almost the same load condition in Figure 2.40 the amount of heat released increases by about 50J when the Ricardo engine

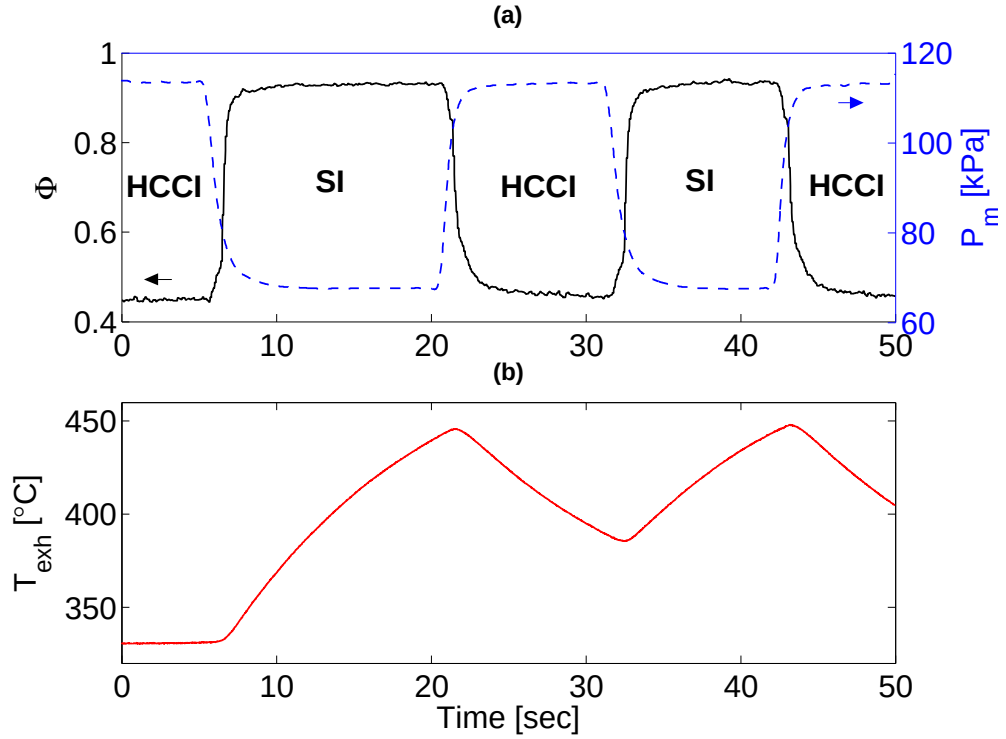

Figure 2.40: Variation in the exhaust gas temperature in HCCI-SI mode switch with similar steady state loads (IMEP= 4.8bar±0.4bar, CA50 = 7.4±2.2 CAD aTDC, N= 1000 rpm, T_m= 98.3±1.2°C.)

switches from HCCI mode to SI mode. Higher heat released (460J) in SI mode in Figure 2.40 contributes to have a higher T_{exh} in SI mode than that of HCCI mode. Since mode switching from HCCI to SI is usually done from a medium load to a full load condition in order to extend HCCI operating range, T_{exh} should substantially increase during the mode switch from HCCI to the SI in a higher engine load. This is also evident from comparing the results in Figure 2.28 with those of Figure 2.39 where a significantly higher T_{exh} is observed at high-load SI conditions in Figure 2.39 compared to the medium-load HCCI conditions in Figure 2.28.

2.4 SUMMARY

Understanding cyclic variation of ignition timing and exhaust temperature variation is examined as this is an essential step for being able to implement future effective control algorithms. This work systematically studies variation in HCCI ignition timing and exhaust temperature to get a physical understanding and to examine the complex behavior. Cyclic variation in HCCI ignition timing is experimentally investigated using over 430 operating points from two different HCCI engines and over 340 steady-state and transient experimental operating points from Ricardo engine are used to investigate T_{exh} as a function of several main engine variables. The analysis of experimental measurements results in the following findings for the engines studied.

Cyclic variation of HCCI ignition timing:

1. Although known for low cyclic variation, HCCI engines can have very high cyclic variation particularly in ultra-lean highly-diluted or low coolant temperature conditions. At such a condition, cyclic variation (STD) of CA50 can be as high as 4 CAD. HCCI combustion is susceptible to cyclic variations and the COV_{IMEP} threshold of 5% is found as the misfire/partial burn limit for the Ricardo engine.

2. Cyclic variation of SOC is generally increased by decreasing the intake temperature or decreasing the coolant temperature. HCCI combustion is more sensitive to varying intake temperature compared to that of coolant temperature in terms of cyclic variation of SOC. However, it is more sensitive to coolant temperature compared to the intake temperature in terms of cyclic variation of BD. This is attributed to the higher coolant temperature influence on thermal stratification and hence on BD, but intake tempera-

ture has more influence on the core gas thermal state compared to coolant temperature.

3. Cyclic variation of SOC, which is related with that of CA50, is generally reduced by increasing the mixture equivalence ratio, but it is elevated with increasing the EGR rate in the HCCI range studied. The intake pressure and engine speed mainly influence the cyclic variations of HCCI combustion by changing the location of SOC. SOC retards with increasing the engine speed, but it advances with increasing the intake pressure.

4. HCCI cyclic variation depends on the dynamic of charge cyclic variation and the physics occurring inside the cylinder and three patterns are observed: normal, periodic, and weak/misfired. To have HCCI with low cyclic variation, periodic and misfired oscillation patterns should be prevented and the magnitude of variation in the normal pattern should be maintained low.

5. Individually plotting cyclic variation of P_{max}, BD and CA50 versus cyclic variation of SOC allows 5 regions of HCCI combustion to be recognized. These regions differ in operating conditions and average SOC. They range from knocking region with average SOC of 1.9 CAD aTDC to unstable-misfire region with average SOC of 11.8 CAD aTDC. Due to different observed interrelation between cyclic variation of SOC and BD, different regions require a different control approach to minimize both cyclic variations of SOC and BD. For instance control of SOC might suffice for controlling both SOC and BD cyclic variation in region-I, but it is less successful for region-IV and region-V. A good correlation exists between the cyclic variations of SOC with those of BD, CA50, $\theta_{HRR_{max}}$, $\theta_{P_{max}}$, P_{max} at the conditions when the cyclic variation of SOC is low – region-I ($STD_{SOC} \leq$ 1.5 CAD). This introduces an appropriate working region for the controller

of HCCI ignition timing as cyclic control of SOC (to near TDC) can be utilized to control the cyclic variations of HCCI combustion.

6. A distinct operating region is noted for the points with knocking cycles. In this region, cyclic variation of SOC, CA50, and P_{max} is low, but cyclic variation of BD is high.

7. For the PRF fuels studied, the first stage of HCCI combustion has less cyclic variation compared to that of the second (main) stage and no correlation is seen between the cyclic variations of these two stages. HTR is much more sensitive than LTR to the variations of intake temperature, intake pressure, equivalence ratio and coolant temperature. Equivalence ratio and intake pressure are less influential on LTR compared to intake temperature and coolant temperature, but HTR exhibits strong sensitivity to all these four variables.

8. $\theta_{HRR_{max}}$ coincides with CA50 and a strong linear correlation exists between CA50 and $\theta_{P_{max}}$. Cyclic variation of $\theta_{HRR_{max}}$ and $\theta_{P_{max}}$ also correlates well with that of CA50 for the conditions when the cyclic variation of CA50 is low ($STD_{CA50} \leq 1.7\ CAD$).

9. Faster HCCI combustion (short BD) is more likely to have smaller cyclic variations of ignition timing – particularly burn duration. HCCI operation with higher PRFs (higher octane numbers) for same charge conditions produces a higher level of cyclic variation in BD. At a constant operating point, higher IMEP is generally produced for faster HCCI combustion.

10. Cyclic variation of HCCI combustion is highly dependent on the location of the start of combustion. When HCCI combustion occurs immediately after TDC, it is more likely to have low cyclic variations of SOC, IMEP,

P_{max}, and BD compared to HCCI combustion occurring late after TDC where high cyclic variations are seen. The most stable operating region is found to be where SOC occurs in an 5 degree window, between 0 – 5 CAD aTDC and operating conditions that can generally provide low HCCI cyclic variations are: fully warmed-up conditions, low EGR, equivalence ratio as high as possible, without knock, and high intake charge temperature.

Variation of HCCI exhaust temperature:

1. A large number (92 points) of HCCI operating conditions has T_{exh} lower than typical catalyst light-off temperature (300 °C). All of points with the low T_{exh} have negligible NOx emission while having a minimum IMEP of about 4 bar. These data points represent potential desirable HCCI points but the low T_{exh} is detrimental to affect catalyst operation for converting HC and CO emission in these conditions.

2. Variation of T_{exh} in HCCI can be explained by a combination of different factors as summarized in Figure 2.41. T_{exh} in HCCI mode depends on the location of ignition timing which is determined by a combination of factors from changing different engine variables as seen in Figure 2.41. In addition to ignition timing (main factor), T_{exh} is influenced by other secondary factors including heat loss, energy input air, energy input fuel, and BD. A conflict between the primary factor and secondary factors leads to a complex behavior in T_{exh} variations in HCCI mode. Three different groups of engine variables are distinguished: primary, compounding, and opposing. Intake pressure and fuel octane number are grouped into primary variables for which location of ignition timing (CA_{50}) is the dominant factor. For these variables T_{exh} increases by increasing CA_{50}. Engine speed is grouped into compounding variables, but coolant temperature, intake temperature

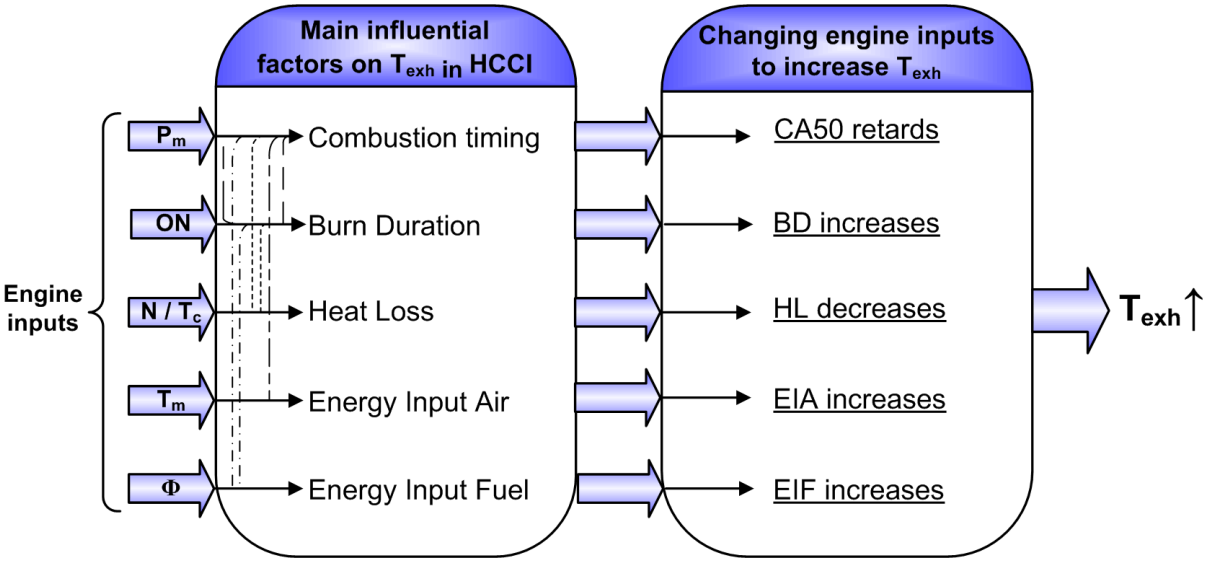

Figure 2.41: Schematic diagram of different factors influencing HCCI exhaust temperature.

and equivalence ratio are grouped into opposing variables. T_{exh} increases substantially by increasing engine speed since both CA_{50} is increased (factor 1) and engine heat loss is reduced (factor 2). But T_{exh} can either increase or decrease when Φ increases. This depends on the competition between changing the location of heat release by advancing CA_{50} (factor 1 − decreasing T_{exh}) and increasing amount of heat released by increasing energy input fuel (factor 2 − increasing T_{exh}) when Φ increases.

3. Variations in T_{exh} can be predicted for constant engine speed and coolant temperature conditions by using a simple empirical correlation that incorporates three input parameters: s*pecific energy input fuel* (magnitude parameter), CA_{50} (location parameter) and *BD* (dispersion parameter). Simulation results from comparing these three parameters indicate the *specific energy input fuel* has the strongest impact on T_{exh} at these conditions. In contrast, *BD* variations cause the least impact on T_{exh}.

4. CO and HC emissions in HCCI are strongly dependant on the location of ignition timing (CA_{50}). This relation appears to be independent of the four engine variables (P_m, RPM, T_m, Φ) studied. Higher CO and HC emissions are observed when shifting CA_{50} from early ignitions to late ignitions after TDC. This is due to having higher peak in-cylinder temperature during combustion when ignition occurs close to TDC. NOx emission shows an opposite trend where NOx increases when CA_{50} is advanced towards TDC.

5. T_{exh} in HCCI mode is not a main function of engine load. This is different from SI mode where engine load is one of the three main factors affecting T_{exh}.

6. Similar to HCCI mode, T_{exh} in SI mode increases by increasing engine speed. But opposite to HCCI mode, T_{exh} in SI mode decreases by decreasing intake pressure. In both modes, variation in engine speed has a larger impact on T_{exh} compared to that of intake pressure.

7. T_{exh} in SI mode is significantly higher than that of HCCI for a similar engine load condition. Longer burn duration and higher fuel energy content in SI mode lead to a higher T_{exh} comparing to that of HCCI mode.

Chapter 3

Thermo-kinetic Modeling and Sensitivity Analysis of HCCI Combustion[1]

Ignition timing in HCCI engines is dominated by thermo-kinetic reactions that are dependant on the charge properties. To predict and control ignition timing in HCCI engines, combustion simulation models are useful to understand the effect of modifying the properties of the engine charge on ignition timing. The HCCI combustion model serves as a qualitative tool for ignition timing sensitivity analysis for different variables of an HCCI engine and for simulating parameter variations needed for development of a control-oriented HCCI model.

In this chapter, a single zone thermodynamic model, coupled to a kinetic mechanism, is developed to predict the ignition timing of Primary Reference Fuels (PRFs) in an HCCI engine. The model, consisting of 120 chemical reactions and 58 species, is validated against the experimental data from the Ricardo engine for various operating conditions. Then, the resulting model is used to perform a sensitivity analysis of HCCI ignition timing to the variations of engine charge properties in order to examine the relative importance of different charge properties for control applications.

[1]The results of this chapter are partially based on [105, 128].

3.1 INTRODUCTION

There are a wide range of HCCI combustion models in the literature that are mainly different in the level of complexity and the level of details in the applied kinetic mechanism. There are four main categories of Thermo-Kinetic Models (TKM) for modeling of HCCI combustion:

1. Zero dimensional TKMs [105]
2. Multi-zone TKMs [129]
3. Sequential CFD based multi-zone TKMs [130]
4. Coupled CFD-kinetic TKMs [131].

Each type of these models is intended for a different purpose. Single zone TKMs, with low computational requirements, are useful tools for predicting SOC [105, 130] and performance studies [132], but single zone TKMs lack the accuracy for predicting combustion peak pressure and combustion duration. Multi-zone TKMs address this problem by accurately predicting combustion peak pressure and combustion duration, but they don't seem accurate for predicting HC and CO emissions. Predictions of HC and CO can be improved by sequentially coupling multi-zone TKMs with a CFD code to determine temperature and mass distribution at the beginning of the engine closed cycle. Furthermore, more accurate prediction of emissions can be obtained by using coupled CFD-kinetic TKMs, but require extensive computation.

This study is an extension to the previous work [133] where an HCCI thermokinetic model is developed for a CFR engine. Here, the main target is modeling HCCI combustion to analyze ignition timing (SOC) for eventual control of SOC. To do this, the HCCI combustion model from [133] is extended using a modified Woschni heat transfer correlation adopted for HCCI engines. The resulting

model is parameterized for the Ricardo engine and then validated against ignition timing from cylinder pressure data taken from the experimental engine for four different PRF fuels over a range of HCCI operating conditions.

3.2 COMBUSTION MODEL

This section details the energy balance for modeling of the combustion zone, kinetic mechanism and solution methodology of the developed model to describe the in-cylinder thermo-kinetic state of an HCCI engine from IVC to exhaust valve opening.

3.2.1 Energy Balance

The combustion chamber of an HCCI engine is considered as a single thermodynamic zone with the assumption of a uniform thermodynamic state within the zone. It is assumed that all species in the zone can be treated as ideal gases and blow-by is negligible and mass of in-cylinder mixture is constant. Evaporation of fuel in the intake port and combustion chamber is also neglected and it is assumed that the entire mixture is in the gas phase. Furthermore, an average temperature of combustion chamber walls is used to consider the convective heat transfer between the zone and its surroundings. The first law analysis of the system is used to determine the variation of the thermodynamic state of the mixture with time. This results in the following equation to calculate the rate of change of the mixture temperature (T) [105]:

$$\frac{dT}{dt} = \frac{-P\frac{dV}{dt} - \frac{dQ_w}{dt} - \sum_i \frac{dN_i}{dt}\overline{h}_i + \mathrm{R_u}T\sum_i \frac{dN_i}{dt}}{\sum_i N_i \overline{c}_{p,i} - N_{mix}\mathrm{R_u}} \tag{3.1}$$

where, P is the in-cylinder gas pressure, N_i and $\overline{c}_{p,i}$ are the number of moles and the molar specific heat of the i^{th} specie. $\mathrm{R_u}$ is the universal gas constant and V is the cylinder volume which is calculated at any crank angle from engine geometry

by using crank-slider mechanism equations [101]. Q_w is the heat transfer between the in-cylinder gas and the surrounding walls. More details of the model can be found in [105].

$\dot{Q_w}$ is modeled using the Modified Woschni heat transfer correlation that is adopted for HCCI engines [134]:

$$\dot{Q_w}(t) = -h_c(t)\, A_s\, (T_g - T_w) \tag{3.2}$$

where, A_s is the in-cylinder surface area; T_g and T_w are gas temperature and average wall temperature; h_c is the convective heat transfer coefficient that is given by:

$$h_c(t) = \alpha_{\text{scaling}} \times L(t)^{-0.2} \times P(t)^{0.8} \times T(t)^{-0.73} \times \omega(t)^{0.8} \tag{3.3}$$

$$\omega(t) = \mathrm{C}_1 S_p + \frac{\mathrm{C}_2}{6}\, \frac{V_d\, T_r}{P_r\, V_r}(P - P_{mot}) \tag{3.4}$$

where, L is the instantaneous cylinder height, P and T are the gas temperature and pressure, ω is the local gas velocity, S_p is the average piston speed, T_r, P_r and V_r are temperature, pressure and volume at the IVC moment, V_d is the displacement volume and P and P_{mot} are instantaneous pressure and the corresponding motoring pressure at the same firing condition. C_1 and C_2 are constant values and α_{scaling} is the scaling factor for different engine geometries.

The developed TKM requires the mixture temperature at IVC (T_{ivc}). But experimentally measuring the T_{ivc} is difficult and using the gas temperature in the intake manifold (T_m) as T_{ivc} yields erroneous SOC from the TKM. Thus the following semi-empirical correlation is used to predict T_{ivc} from the manifold values:

$$T_{ivc} = \left(\mathrm{a}\ T_m^2 + \mathrm{b}\ T_m + \mathrm{c}\right) \frac{\phi^{\mathrm{d}}\ .\ N^{\mathrm{e}}}{(1 + EGR)^{\mathrm{f}}} \tag{3.5}$$

where a, b, c, d, e and f are the parameters of the correlation that are determined from comparing experimental and TKM simulated pressure traces. ϕ represents equivalence ratio of the air-fuel mixture and EGR is the percentage of the total intake mixture which is recycled.

3.2.2 Kinetic Mechanism

The chemical kinetic mechanism consists of 58 species and 102 reactions for describing the combustion of arbitrary PRF blends. The chemical kinetic mechanism is composed of several sub-mechanisms. The ignition, large molecule decomposition, high temperature sub-mechanisms are from Zheng *et al.* [135], with fuel specific rate constants from Li *et al.* [136]. The interaction between the two reference fuels is described using the reaction presented by Tanaka *et al.* [137].

3.2.3 Solution Methodology

The mathematical model results in a set of stiff ordinary differential equations that are integrated with the ode15 solver in Matlab. The tolerances for this multi-step numerical solver was determined heuristically to provide a compromise between calculation speed and solution convergence.

3.3 MODEL VALIDATION

The developed thermokinetic model is validated based on its ability to predict SOC for the Ricardo engine running in the HCCI mode. Collected experimental data from Section 2.2.2 is used in this section and the TKM model is tested for the Ricardo engine experimental conditions given in Table 3.1. Four different PRF fuels are used to validate the ability of the TKM model to predict ignition timing for different octane numbers. In order to cover the operating region of the Ricardo engine, each of the 14 points in Table 3.1 corresponds to the conditions close to the limits for which HCCI operation with reasonable cyclic variations is

possible at the PRF blend used. The mixture pressure at IVC, P_{ivc}, is taken from the experimental pressure trace.

The comparison of experimental and simulated ignition timings in Table 3.1 indicates that the TKM model is capable of predicting SOC for different PRF blends over a range of equivalence ratios, intake temperatures, intake pressures,

Table 3.1: Comparison of HCCI experimental and simulated SOC. (Values on the top of the vectors are the average values from all individual cycles for each experiment.)

#	Fuel [PRF]	N [rpm]	ϕ	EGR [%]	T_m [^{o}C]	P_{ivc} [kPa]	SOC [CAD aTDC]	
							Experiment	Simulation
1	0	800	0.49	0	140	107	2.3 $\xrightarrow{3.7}$ 5.2	4.4
2	0	800	0.72	17	80	107	2.9 $\xrightarrow{3.8}$ 4.8	4.9
3	0	1000	0.58	9	100	110	5.1 $\xrightarrow{7.7}$ 12.4	6.2
4	0	1000	0.67	18	100	112	3.8 $\xrightarrow{6.5}$ 10.5	5
5	10	800	0.57	0	60	109	2.5 $\xrightarrow{5.5}$ 8.4	6.4
6	10	800	0.66	15	90	107	5.1 $\xrightarrow{8.1}$ 12.6	8.3
7	10	1000	0.52	0	110	109	4.6 $\xrightarrow{6.6}$ 10	8
8	10	1000	0.68	16	100	110	6.5 $\xrightarrow{11.4}$ 23.2	10.8
9	20	800	0.53	0	90	106	4.2 $\xrightarrow{6.9}$ 11.1	6
10	20	800	0.38	0	120	125	5.6 $\xrightarrow{6.8}$ 8	6.9
11	20	1000	0.42	0	129	128	4.6 $\xrightarrow{6.2}$ 7.6	6.4
12	20	1000	0.75	11	100	111	5.7 $\xrightarrow{6.7}$ 7.9	7.1
13	40	810	0.45	0	110	147	-0.1 $\xrightarrow{0.8}$ 1.7	1.5
14	40	810	0.72	0	90	101	4.8 $\xrightarrow{5.9}$ 7.1	6.8

EGR rates, and engine speeds. Comparing SOC from the TKM with average values from 200 cycles for different operating points, the TKM predicts SOC for the Ricardo engine with an uncertainty of ± 1 CAD.

3.4 SENSITIVITY ANALYSIS

The developed TKM is used to perform a sensitivity analysis of SOC to initial temperature, initial pressure, EGR rate, equivalence ratio, and Octane Number (ON). This analysis can be applied to analyze ignition timing for control applications. In particular, the sensitivity analysis can be used for three different purposes. First, it helps to evaluate the relative importance of different charge properties for HCCI control-oriented modeling where a compromise among accuracy, computational time, and number of necessary measurements is required. Second, the sensitivity analysis can be used to choose an effective actuator to control ignition timing for different operating regions of an HCCI engine. Third, the sensitivity analysis is useful to determine the minimum and maximum possible incremental change of ignition timing for different actuators when defining control targets for an HCCI engine.

Table 3.2 indicates the base points chosen for the sensitivity analysis. These base points are selected to represent the conditions in the middle of the operating region for the two ranges of PRF blends the Ricardo engine could be run. A range of ϕ is used to examine the sensitivity analysis for different SOC positions.

Table 3.2: Base line points used for the sensitivity analysis

No.	PRF	N [rpm]	T_{ivc} [^oC]	P_{ivc} [kPa]	ϕ	EGR [%]
1	0	800	110	110	0.46, 0.57, 0.75	10
2	40	800	130	130	0.38, 0.58, 0.75	10

Table 3.3 quantifies the sensitivity or slope of SOC with the change in the charge properties. Results are shown for three different positions of SOC. Early ignitions ($\cong$ 4 CAD bTDC) are achieved with the richest ϕ limit of Table 3.2 and late ignitions ($\cong$ 10 CAD aTDC) are obtained with the leanest ϕ limit of

Table 3.2 for both PRF0 and PRF40 cases. Examining the sign of values in Table 3.3 shows that SOC advances with an increase in IVC temperature, equivalence ratio and IVC pressure, but SOC retards with an increase in EGR rate and octane number. Minimum and maximum possible changes of SOC on a real engine are bounded with actuators' limitations. Knowing the resolution of the engine's actuators in combination with the information from Table 3.3, minimum and maximum possible changes of SOC on the Ricardo engine can be determined. For instance, the resolutions of the supercharger and EGR valve in the Ricardo engine for changing intake pressure and EGR rate are 1 kPa and 4% respectively. Thus from Table 3.3 for PRF40 in TDC firing conditions, increasing the intake pressure causes SOC to change only 0.15 CAD (advance), but a minimum change of SOC with increasing EGR rate is 2.75 CAD (retard).

Table 3.3: Rate of the change of SOC with the change in the charge properties for the base points of Table 3.2 . (bTDC: before Top Dead Center; aTDC: after Top Dead Center)

	PRF0			PRF40		
SOC Position	bTDC	TDC	aTDC	bTDC	TDC	aTDC
$\Delta SOC/\Delta T_{ivc}$ [CAD/K]	-0.42	-0.6	-1.05	-0.5	-0.5	-0.9
$\Delta SOC/\Delta Phi$ [CAD/0.01Phi]	-0.1	-1.17	-1.2	0.02	-1.15	-1.4
$\Delta SOC/\Delta EGR$ [CAD/%EGR]	0.17	1.02	0.57	0.2	0.69	0.45
$\Delta SOC/\Delta P_{ivc}$ [CAD/kPa]	-0.2	-0.15	-0.5	-0.2	-0.15	-0.35
$\Delta SOC/\Delta ON$ [CAD/ 1ON]	0.8	0.75	1.35	0.22	0.17	0.3

To examine the relative importance of different charge properties on SOC, a normalized sensitivity function ($S_x = |\frac{\partial SOC}{\partial X}| \times \frac{X_b}{SOC_b} \times 100$) is used, where X is the variable and index b denotes for the base point. Sensitivity analysis is performed around the operating points in Table 3.2 and each variable (X) is separately

changed in a small range around the base points. The variation range of X is determined based on the minimum possible change of a variable on the Ricardo engine. As using the base values of EGR and ON when they are zero gives a false

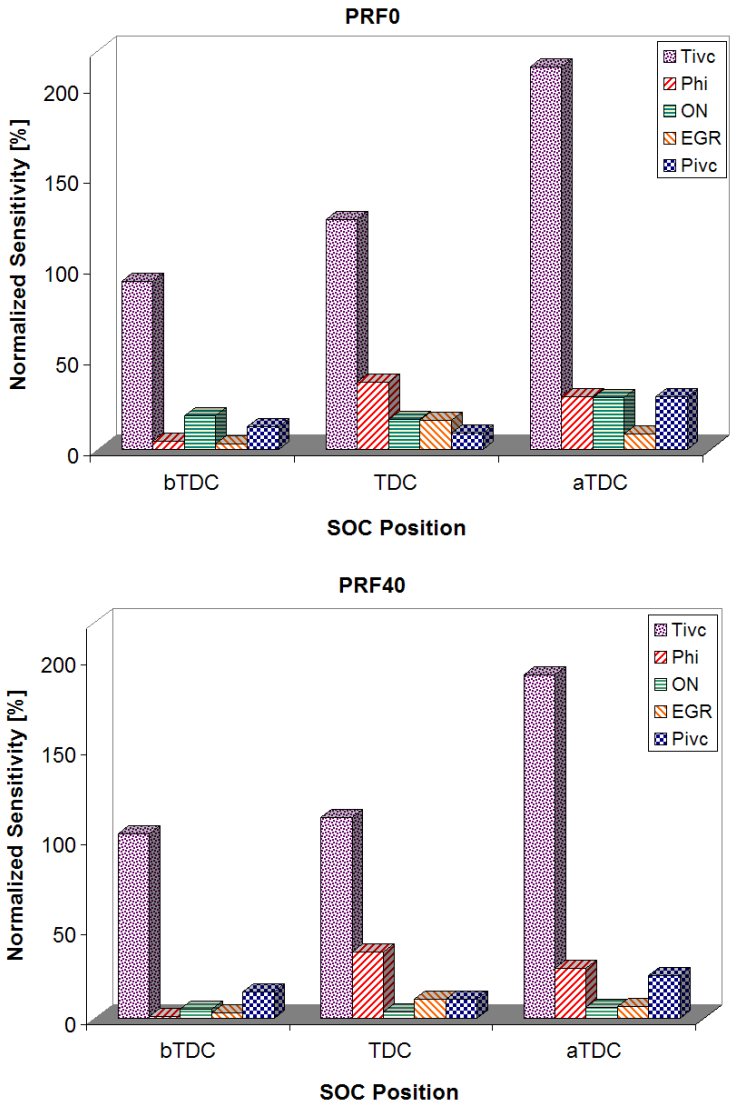

Figure 3.1: Normalized sensitivity results for SOC using TKM simulations and base points of Table 3.2.

sensitivity interpretation, their maximum possible values for the Ricardo engine are used for X_b. Figure 3.1 shows the simulation results.

Figure 3.1 shows that the sensitivity of SOC to the variations of charge properties is dependant on the position of SOC with less sensitivity being observed

for early ignitions. SOC shows the most sensitivity to the variations of the intake charge temperature, regardless of SOC position. The influence of equivalence ratio is pronounced for combustion happening around TDC and also late combustion, but less pronounced for early combustion. For both PRF0 and PRF40, a similar trend of change in sensitivity with respect to SOC position is seen for all charge properties except for the octane number of the charge. PRF40 shows less sensitivity to the changes in the octane number compared to that of PRF0.

3.5 SUMMARY

A one zone thermokinetic model using a chemical kinetic mechanism for primary reference fuels is extended and validated against the experimental data from a single cylinder engine. Then, the sensitivity analysis is done for these main charge variables: initial temperature, initial pressure, Exhaust Gas Recirculation (EGR) rate, equivalence ratio, and octane number. The analysis of results lead to the following conclusions:

1. The developed model can predict SOC for the studied engine running in HCCI mode with an uncertainty of ± 1 CAD over a range of equivalence ratios, intake temperatures, intake pressures, EGR rates, PRF blends, and engine speeds.

2. SOC shows a different order of sensitivity to the variation of charge properties when the position of SOC varies. While SOC is the most sensitive to the charge temperature variations and ϕ variations for the combustion occurs around TDC or a late combustion, SOC shows a small sensitivity to ϕ for an early combustion.

3. More sensitivity is observed in SOC to the variation of octane number when an HCCI engine runs with a PRF blend at a low octane number.

Chapter 4

Mean-Value Modeling of HCCI Combustion[1]

Extensive computation time in the TKMs makes them impractical for direct control applications on engines. For control design purposes low-order models with short computation time are needed. The purpose of this chapter is to develop a realtime model for predicting mean-value of HCCI combustion timing.

4.1 INTRODUCTION

A variety of models has been used to simulate the ignition timing of HCCI engines. They differ in the complexity and required input data. These models range from multi-dimensional CFD models [131, 140] and multi-zone models [141, 142], to simple control-oriented models [143, 144]. For real-time control, a compromise between the computation time and accuracy of the model is required. Low-order control oriented models can predict ignition timing of HCCI engines with a reasonable accuracy while having short computational time [145]. The main approaches of the control oriented models used to predict combustion timing for HCCI engines are shown in Figure 4.1. Control oriented models are categorized into two main groups of models. The first group is intended to predict HCCI combustion timing for steady-state operation. The output of these models provides mean-value combustion timing. The second group of the models, shown in the

[1]The results of this chapter are partially based on [138, 139].

right column of Figure 4.1, considers cyclic transition dynamics from one cycle to the next cycle. This group of the models are used for cycle-to-cycle control of HCCI combustion to manage the transition between different load-speed regions and also mode transition between HCCI operation and SI or CI operation. In this chapter, a control-oriented model for steady-state HCCI operation is detailed and in the next chapter a model for transient HCCI operation is described.

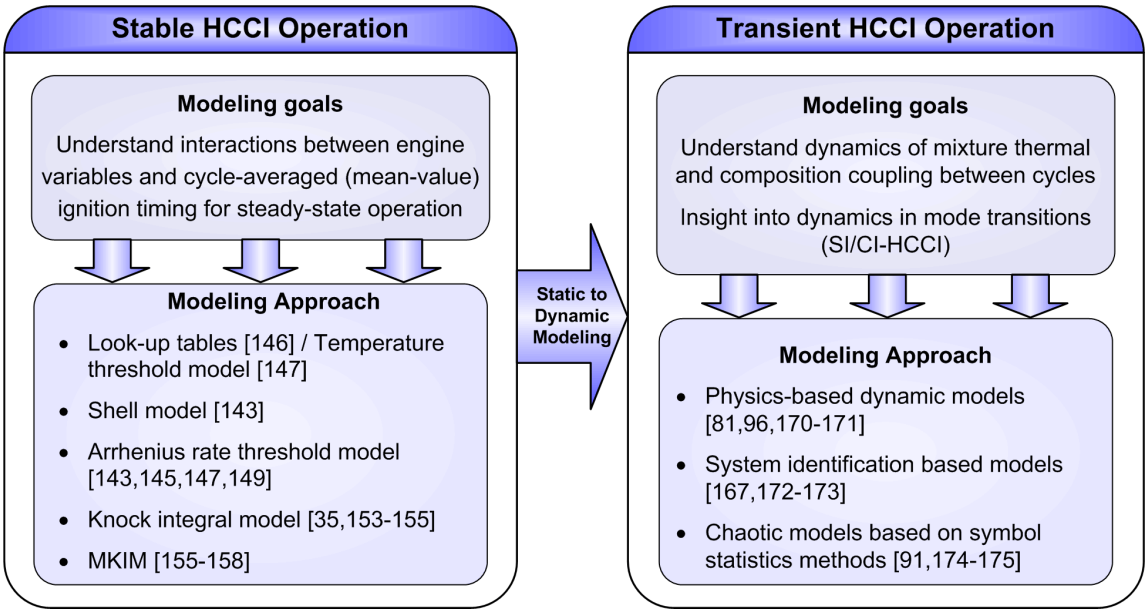

Figure 4.1: Main modeling approaches to predict HCCI combustion timing for control applications.

Steady-state control oriented modeling of HCCI combustion timing is grouped into the five categories of models as shown in Figure 4.1. In the simplest approach, HCCI combustion timing is mapped into look-up tables as a function of the engine variables which have been experimentally found to predominantly affect HCCI combustion [146]. This requires a large number of experiments, and may not work outside the region the engine has been mapped. The second simplest model defines a temperature threshold to find the start of combustion [147]. The basis of this model is that the mixture temperature has the most dominant effect on

the reaction rate of reactions that control HCCI auto-ignition delay. This model fails to capture combustion phasing at different operating conditions, which is due to the dependance of the initiation of the combustion reaction on not only the temperature but also on the concentration of species present in the cylinder. The Shell model [148] is another model used in [143] to predict HCCI auto-ignition timing. The results from the Shell model show an accurate estimation of the HCCI auto-ignition timing for a temperature and engine speed sweep, but less accurate results when changing the load. In [143, 145, 149], models based on Arrhenius-type reaction rate [150] are used. Here the integration of the Arrhenius global reaction rate for the fuel is tracked until it reaches a threshold value defined from experimental data. To parameterize the model, the values of the constants are taken from tabulated values for hydrocarbons [150]. This model type is accurate, but depends on having instantaneous fuel and oxygen concentrations as well as in-cylinder gas temperature which is impractical for on-board control of ignition timing.

To remove the need for in-cylinder composition data, some researches [151, 152] omitted the mixture composition term from the Arrhenius reaction rate. This simplified Arrhenius based model uses the idea that the composition term in Arrhenius reaction rate is in the secondary importance compared to other terms. Their results seem accurate in the studied HCCI range, but the model should be validated for a wide range of HCCI operation. The Knock-Integral Model (KIM) [153] is another category in control-oriented modeling of HCCI combustion timing. This model is based on an exponential correlation which includes the elements of in-cylinder gas pressure and temperature to predict the auto-ignition of a homogeneous mixture [35, 154, 155]. Although this model produces accurate results, again there is a need for some parameters which are difficult and expensive to measure. This limits using this model for real-time

control. To make more accurate and more practical models, a category of models has been defined and are denoted as Modified Knock Integral Model (MKIM). Two examples from this category are the models in [156] and [157] in which the compression process is considered a polytropic process to remove model's requirement for instantaneous in-cylinder gas temperature and pressure. Other example includes the model presented in [158] where the effects of residual gas and AFR have been added to the knock-integral model and also another model [155] in which a pressure term has been added to the knock-integral model to benefit from the physics of Arrhenius reaction rate based models.

Despite the extensive work done on control-oriented modeling of ignition timing for HCCI engines, improved models that work with easily measurable inputs and models that include variable working conditions are still needed. The model proposed in this chapter addresses some of the compromises of existing models. In particular, it is designed to be a control-oriented model which also works for different conditions including variable load, air temperature, engine speed, AFR, and EGR. Instantaneous in-cylinder gas temperature, pressure or the concentrations of fuel and oxygen are not required, instead measured EGR rate, AFR and intake manifold temperature and pressure are required.

4.2 MODEL DESCRIPTION

An HCCI combustion model incorporating a combination of physical and empirical models to predict CA_{50} is proposed. CA_{50} is chosen because it is a good and robust indicator of HCCI combustion [159] and CA_{50} can be reliably used for feedback control of HCCI combustion [160]. The structure of the model is illustrated in Figure 4.2. The model has three main parts: *Gas Exchange Process Model*, *Auto-ignition Model*, and *Fuel Burn Rate Model*. Inputs of the model are intake pressure, intake temperature, EGR rate, equivalence ratio and engine

speed. Using these inputs, the model's outputs are CA_{50}. The submodels shown as blocks in Figure 4.2 are described in detail in the following sections.

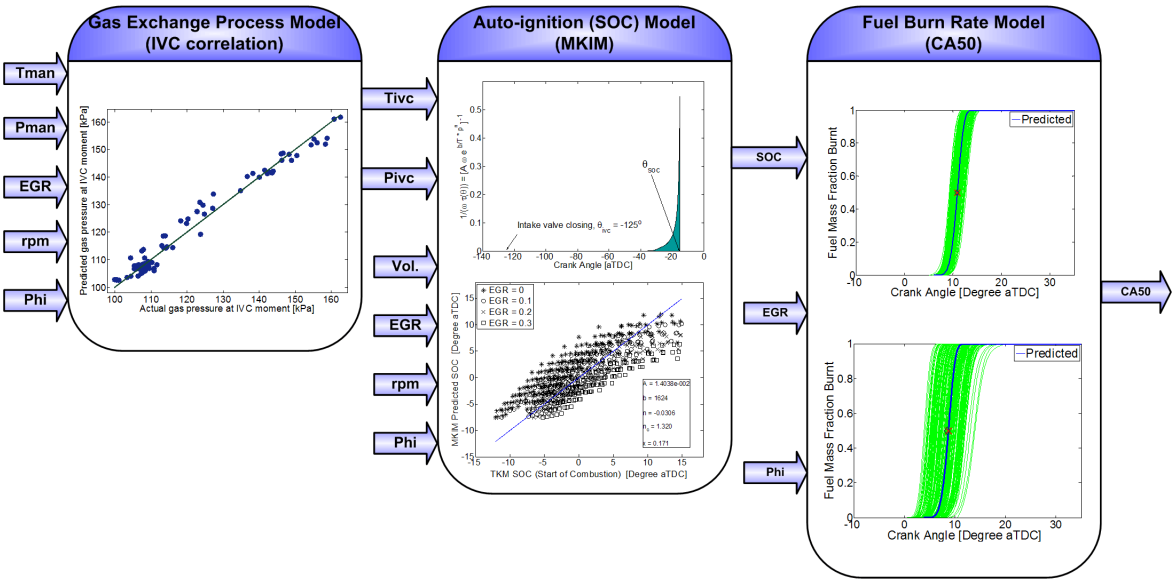

Figure 4.2: Schematic of the mean-value model to predict CA_{50}.

4.2.1 IVC temperature & pressure correlation

In a premixed HCCI engine only during the intake stroke can the combustion timing be directly influenced. Although the intake process commences by the intake valves opening, it is the mixture condition at Intake Valve Closing (IVC) moment that predominantly determines the HCCI combustion timing [161]. It is difficult and expensive to measure the mixture temperature and pressure at IVC moment, but the intake temperature and intake pressure are usually measured in the intake manifold in the production engines. Two simple semi-empirical correlations are used for the intake process to estimate the pressure and temperature of the mixture at IVC from the measured values of the intake manifold. Parameters of these correlations are estimated using the experimental and simulation data.

Table 4.1 shows how IVC gas pressure is expected to change when other parameters are changed within the HCCI operating range of the engine used in this study. The manifold gas pressure directly influences the gas pressure at IVC, P_{ivc}. When intake manifold temperature is increased or the equivalence ratio is decreased the mass of in-cylinder charge decrease, which that leads to a decrease in P_{ivc}. An increase in the engine speed results in less wall heat transfer which promotes an increase in P_{ivc}. EGR has a small influence on P_{ivc} that mainly comes from its dilution effect on changing the mass of in-cylinder charge.

Table 4.1: Expected trend of change in IVC gas pressure with other parameters

Parameter	$\mathbf{P_{ivc}}$
Engine Speed, N ↑	↑
EGR Fraction ↑	↓
Equivalence Ratio, ϕ ↑	↑
Manifold Pressure, P_{man} ↑	↑
Manifold Temperature, T_{man} ↑	↓

After trying different correlations based on the physics introduced in Table 4.1, the following correlation provided a good fit to the available experimental data. Conditions of the experimental data are detailed later in the section 4.3. One-third of the steady-state experimental data is used to parameterize the correlation and the other two-thirds of the experimental data is used to validate the correlation. The resulting correlation for the in-cylinder pressure at IVC (P_{ivc}) is:

$$P_{ivc} = \frac{N^{0.027}\ \phi^{0.046}}{T_m^{0.005}} P_m \tag{4.1}$$

where, N is the engine speed in RPM, and P_m and T_m are the gas pressure and temperature in the intake manifold in kiloPascals (kPa) and in Celsius (°C)

respectively and ϕ is the equivalence ratio. An uncertainty analysis on correlation (4.1) results in finding an uncertainty of ± 3.6 kPa when applying the correlation on the two-thirds of the steady-state experimental data that was not used to parameterize the correlation.

HCCI combustion is the most sensitive to T_{ivc} variations [152, 73] but it is very difficult and expensive to experimentally measure it. Here, T_{ivc} is estimated by using simulation results of the TKM developed in Chapter 3. Simulated T_{ivc} values that match experimental combustion timing are chosen as the correct T_{ivc}. Here, the TKM is run for the same experimental points used to parameterize correlation (4.1). The obtained values for T_{ivc} are used to parameterize the correlation (3.5) to predict the temperature of air-fuel mixture at IVC. Table 4.2 indicates the values of the estimated parameters. It should be noted that T_m is measured after the inclusion of EGR gases, so the charge heating effect of EGR is already included in the measured T_m (engine experimental setup in section 2.2.2).

Table 4.2: Values of parameters for the T_{ivc} correlation (3.5)

Parameter	**PRF0**	**PRF10**	**PRF20**	**PRF40**
a	-0.0073	-0.0017	-0.0017	-0.0007
b	1.4829	0.4073	0.5533	0.3470
c	110.3672	101.2723	113.4466	112.3506
d	-0.1488	-0.0431	-0.1164	-0.0051
e	-0.0850	-0.0162	-0.0426	-0.0175
f	0.0092	0.0024	0.0002	0.0012

An analysis of equation (3.5) indicates that T_{ivc} is most sensitive to the intake manifold temperature and engine speed compared to EGR and ϕ, with EGR having the least influence on T_{ivc}. As mentioned above the heating effect of EGR

is already included in the measured T_m and the EGR term in equation (3.5) includes other EGR effects (e.g. dilution/chemical) on T_{ivc}. The quadratic term for the influence of T_m on T_{ivc} results in a change in the direction of heat transfer between the in-cylinder gases and the cylinder wall when the in-cylinder gas temperature becomes higher than that of the cylinder wall [162]. For a constant T_m, ϕ and cylinder wall temperature (T_w), correlation (3.5) suggests that T_{ivc} decreases with increasing engine speed and increasing EGR rate. This can be explained by less available heating time (from the cylinder wall to the charge) at higher engine speeds. Also when EGR rate increases the total heat capacity of the charge increases[2][163]. This higher heat capacity reduces the amount of possible increase in the charge temperature during the heat transfer process between the charge and the cylinder wall with a constant T_w. Correlation (3.5) is cross-validated using the same data points used to test correlation (4.1) with the two-thirds of the data that is not used to parameterize the correlation. The results show an uncertainty of $\pm 3.8\,^{\circ}\mathrm{C}$.

4.2.2 Auto-ignition timing model

In this section, the original Knock Internal Model is introduced and its extension into the Modified Knock Integral Model is explained.

4.2.2.1 Knock Integral Model (KIM)

Kinetics of HCCI combustion are very similar to the chemical kinetics of knock in SI engines [152]. Knock (premature auto-ignition) in SI engines has been investigated for decades [153, 164]. To predict the conditions under which knock would occur for various fuels, Livengood and Wu [153] developed the first correlation to predict the auto-ignition of a homogeneous mixture, it was later termed the

[2]This heat capacity effect also delays HCCI auto-ignition timing and prolongs the combustion duration when EGR is increased. [163]

Knock-Integral Method (KIM) [101]. The basis of the correlation stems from the ignition delay of various fuels using a rapid compression testing machine. The resulting empirical relationship in the general form is:

$$\tau = \mathrm{A}e^{(\mathrm{b}/T)p^{\mathrm{n}}} \tag{4.2}$$

where, τ is the ignition delay, T is the mixture temperature as a function of time, p is the mixture pressure as a function of time, and A, b, and n are empirical constants. The constants are the model parameters which are determined for each engine.

Livengood and Wu proposed that there is a functional relationship between the concentration ratio, $(x)/(x)_c$, of the significant species in the reaction and the relative time, t/τ. The critical concentration ratio, $(x)_c$, is the concentration of the species at the end of the reaction being studied. Using the crank angle instead of time, the ignition correlation of Livengood and Wu becomes:

$$\frac{(x)}{(x)_c} = \int_{\theta_o=0}^{\theta=\theta_e} \frac{1}{\omega\tau}\, d\theta = \int_{\theta_o=0}^{\theta=\theta_e} \frac{1}{A\omega e^{(b/T)p^n}}\, d\theta = 1.0 \tag{4.3}$$

where, θ_e is the crank angle that auto-ignition or knock occurs and θ_o is the initial crank angle where the integration begins. The engine speed (ω) is represented in revolutions per minute (RPM), the pressure in kiloPascals (kPa), and the temperature in Kelvin (K). The value of θ_o is selected to be the crank angle of IVC timing where no appreciable reaction has begun ($\theta_o = \theta_{IVC}$). The value of the expression being integrated ($1/(\omega\tau)$) increases as the point of auto-ignition is approached as shown in Figure 4.3.

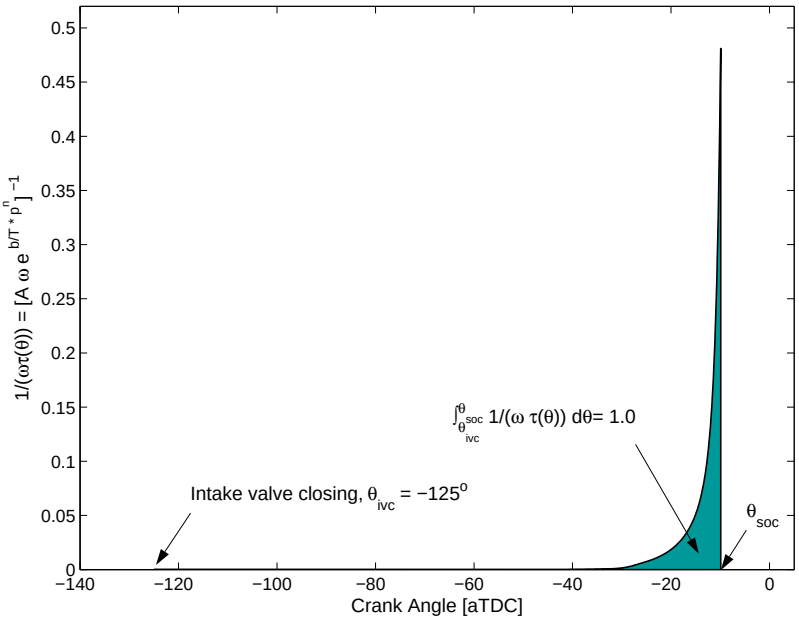

Figure 4.3: Graphical integration of $1/(\omega\tau)$ from the intake valve closing to the start of combustion.

4.2.2.2 Modified Knock-Integral Model (MKIM)

Although the KIM can predict HCCI auto-ignition, it is impractical for a real engine operation. Engine conditions, such as temperature, pressure must be available during compression. This is possible in simulations but it is not practical on an engine. Furthermore, the KIM is for an engine operating at a constant AFR with no EGR. To adapt this correlation to a typical HCCI engine with varying AFR rates and EGR, the KIM is enhanced with the following three modifications:

1. Polytropic compression – The requirement of crank angle measurements of temperature and pressure during the engine compression is avoided by assuming a polytropic process for the temperature and pressure rise in the cylinder during the compression [151]. This assumption ignores any pre-ignition heating caused by the reactions that occur before the SOC.

2. Variable AFR – The SOC changes as the concentrations of the fuel and oxygen are varied [67, 104]. To account for the AFR changes, crank angle

measurement of fuel and oxygen concentrations can be used in a modified KIM. However, this information is available in a TKM simulation but not in a real engine. As the equivalence ratio is indicative of the concentrations of the fuel and oxygen [143], the equivalence ratio can replace the fuel and oxygen concentration terms and can still be easily measured on an operating engine using a broadband oxygen sensor. Therefore, an equivalence ratio term is added to the KIM to account for the variable AFR conditions in the engine.

3. Variable EGR – SOC in HCCI combustion is affected by EGR [67]. To generalize the correlation for variable EGR rates, one term is added to account for the effect of varying EGR rates on SOC.

Developing the KIM to MKIM with using the three above modifications is detailed in Appendix D. The resulting MKIM is:

$$\int_{\theta_{ivc}}^{\theta_{soc}} \frac{\phi^{\mathrm{B}}}{A\omega \; exp\left(\frac{\mathrm{C}\left(P_{ivc}\, v_c^{\mathrm{k_c}}\right)^{\mathrm{D}}}{T_{ivc}\, v_c^{\mathrm{k_c}-1}}\right)}\, d\theta = 1.0 \tag{4.4}$$

where, θ is the engine crank angle, B, C, and D are constant parameters. $\mathrm{k_c}$ represents the average polytropic coefficient that is determined by using TKM simulations (see Appendix D). The value of the expression being integrated increases as the point of SOC is approached. A and v_c are determined by:

$$v_c(\theta) = \frac{V_{ivc}}{V(\theta)} \;\; , \;\; A = \mathrm{E}_1\, EGR + \mathrm{E}_2 \tag{4.5}$$

where, E_1 and E_2 are constant parameters and the cylinder volume, $V(\theta)$, is calculated at any crank angle using slider crank mechanism [101].

4.2.2.3 MKIM Setup

Parameters E_1, E_2, B, C, D, and k_c need to be determined to be able to use the MKIM to predict SOC. To parameterize the MKIM, three steps are required. First, simulation data covering a diverse range of the engine operation is collected and this data is used as the estimation data to parameterize the MKIM. Second, the polytropic parameter (k_c) is determined using a best-fit methodology over the compression part of the simulation data. Third, an optimization is used to find the best values for the parameters of the MKIM. These three steps are detailed below.

Thermokinetic Model Simulations

For accurate parameter estimation, the MKIM requires a large amount of the data from the engine at different working conditions. Due to cost limitations and potential hazard of damaging the engine by intense knocking when running the engine at the extreme operating points, it may not be possible to run the engine for a large number of experiments over a wide range of conditions. TKM from Chapter 3 is used as a virtual engine to provide the required data to parameterize the MKIM.

The TKM, used to explore the engine variable parameter space, is run over a wide range of engine variables including the engine speed, initial mixture temperature and pressure, EGR rate for the operating conditions listed in Table 4.3. The input ranges given in Table 4.3 are chosen to represent typical HCCI operation of the Ricardo single-cylinder engine. TKM simulations are done for the engine using four different PRF blends.

From the resulting 10880 simulations, complete combustion occurred in 6554

Table 4.3: Parameter variations carried out using the TKM

Variables	**Values**
Engine Speed	800, 1000 rpm
Initial Temperature	80, 85,..., 155, 160 ^{o}C
EGR(%)	0, 10, 20, 30
Equivalence Ratio	0.5, 0.6, 0.7, 0.8
Initial Pressure	95, 100, 105, 110, 115 kPa
Fuel	PRF0, PRF10, PRF20, PRF40
Wall temperature	390 K

simulations. Late ignited[3] TKM simulations are excluded since near TDC firing conditions are of practical interest. This results in 5534 TKM simulations (Table 4.4) that are used to parameterize the MKIM.

Table 4.4: Number of TKM simulations with an appropriate HCCI combustion

Fuel	**Engine speed**	
(PRF)	800 rpm	1000 rpm
0	937	853
10	769	700
20	685	611
40	521	458

As Table 4.4 shows, the number of HCCI auto-ignition points decreases with an increase in engine speed and PRF (octane) number. This is expected as: 1) HCCI combustion is a time-based process and there is less time available when engine speed is increased; and, 2) the chance of auto-ignition increases

[3]TKM simulations in which the second stage of HCCI combustion occurs at the crank angle higher than 10 degrees after Top Dead Center (TDC).

with a decrease in octane number particularly in this engine with a relatively low compression ratio.

Finding the Polytropic Parameter

Using the engine parameter variations for the applied PRF fuels, the values of k_c can be determined by fitting a polytropic relation between the temperature or pressure at IVC and SOC of the simulations. The value of $k_c = 1.32$ is chosen using the simulation results in Appendix D.2.4.1.

Optimizing the MKIM Parameters

The parameters of the MKIM equation (4.4) are fit to minimize the error of the integration, where the target value is 1.0. The Nelder-Mead simplex minimization method [165] is used as an off-line optimization technique to parameterize the MKIM using the 5534 TKM simulations. The integration is carried out numerically with the rectangular method with a step size of 0.1 CAD. The program then uses the optimized parameters and computes the predicted auto-ignition point by integrating (4.4) until it equals 1.0. The resulting crank angle is taken as the predicted angle of auto-ignition.

First, parameters B, C, D, and A are determined by applying the estimation code on all the TKM simulation results with four different EGR rates. Then, the parameter A is determined for each group of TKM simulations with the same EGR rate, keeping the values of B, C, and D constant from the first stage. This process is done for each of the 8 individual cases in Table 4.4. Figure 4.4 indicates one sample estimation result for the predicted SOC before (a) and after (b) including the EGR level in the parameter A. As seen in Figure 4.4, the prediction are substantially reduced when EGR level is considered in the MKIM. For all 5534 TKM simulations, the range of uncertainty in model prediction

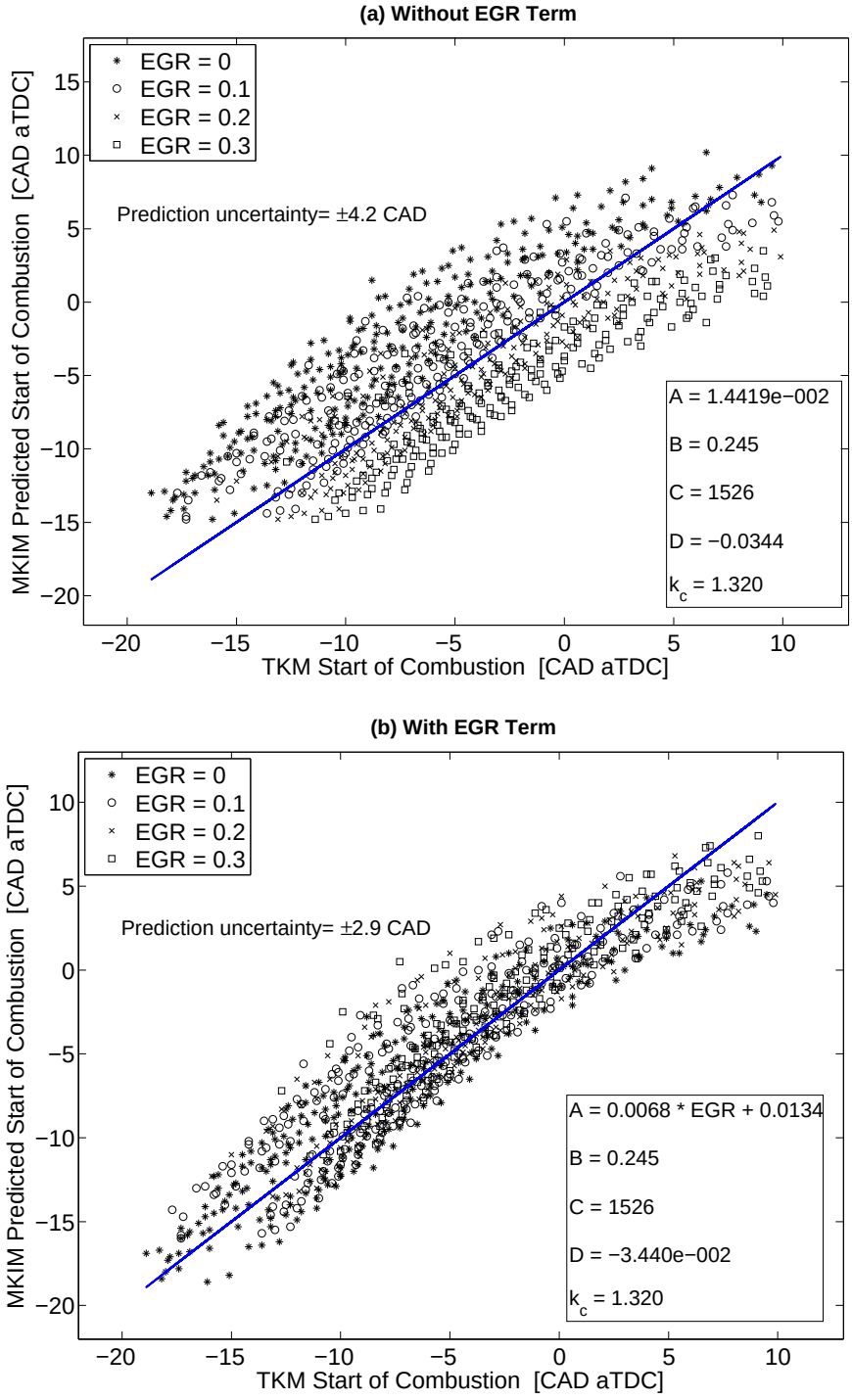

Figure 4.4: MKIM predicted SOC versus TKM simulations at various engine conditions at 800 rpm using PRF0 as the fuel. The line represents where SOC from MKIM and that of TKM are the same.

results is from ±3 to ±4 CAD.

Sample values of parameters A, B, C, D, and k_c in equation (4.4) determined for the PRF blends are shown in Figure 4.4. The order and sign of these parameters are the same for other cases of Table 4.4. By examining these parameters it can be seen that for the four PRF blends the SOC advances by increasing the initial temperature and initial pressure, while it retards with an increase in the engine speed. This trend has been also observed in [143]. Furthermore for all four PRF blends studied, SOC occurs earlier when equivalence ratio increases, while SOC is delayed when EGR level increases. The same trend has been also reported in [67].

4.2.3 Fuel burn rate model

Fuel burning rate influences HCCI combustion in terms of efficiency, stability and cyclic variability [72, 73] and should be controlled to achieve desirable HCCI performance. Prediction of SOC is necessary but not sufficient for a model-based control of HCCI combustion since different combustion durations can occur with a same SOC. As the main stage of HCCI combustion has a steep heat release slope, CA_{50} (the crank angle of 50% fuel burned) is a robust feedback indicator of an HCCI combustion [159] and is chosen as the main output of the mean-value model in this study. A modified Wiebe function is used to predict fuel mass fraction burned (x_b) and to calculate CA_{50}:

$$x_b(\theta) = 1 - exp\left(-\mathrm{A}\left[\frac{\theta - \theta_{soc}}{\theta_d}\right]^{\mathrm{B}}\right) \tag{4.6}$$

where, A and B are constant parameters and θ_{soc} is SOC crank angle and θ_d is the combustion duration determined by:

$$\theta_d = \mathrm{C}\,(1 + X_d)^{\mathrm{D}}\ \phi^{\mathrm{E}} \tag{4.7}$$

where, C, D, and E are constant parameters. The fuel burn rate model requires the parameter values of A, B, C, D, and E in order to predict CA_{50} ($x_b = 0.5$) and the method in [166] is used to parameterize the model. Nelder-Mead simplex minimization method [165] is applied on one-third of the steady-state experimental data points to determine the model parameters. The data points are the same as the points used to parameterize the IVC correlations (4.2.1) and conditions of these points are detailed in Section 4.3. The resulting parameters are A= 2.02, B= 5.08, C= 5.98, D= 0.01, and E= -0.02. By examining these parameters it can be seen that the model predicts CA_{50} advances and θ_d shortens with an increase in equivalence ratio, but the combustion is prolonged by increasing the dilution rate. This trend is consistent with observations from experimental studies [67, 72].

4.3 MODEL VALIDATION

Ricardo steady-state experimental test points are used to validate the final model. CA_{50} as the main output of the model is tested with experimental CA_{50} values processed from the recorded pressure trace data. Table 4.5 details the steady-state experimental points used to validate the proposed model and to parameterize empirical correlations.

The three sub-models in Figure 4.2 are linked together to generate a model which predicts the mean CA_{50}. A comparison between predicted CA_{50} with those of experiments is shown in Figure 4.5 for four different fuels at various operating conditions. As the experimental HCCI data has cyclic variations in CA_{50}, the range of CA_{50} variation from 200 consecutive cycles for each operating point is also shown in Figure 4.5. The diamond symbol indicates the average experimental CA_{50} calculated from averaging the CA_{50} from 200 cycles and the round symbol

Table 4.5: Steady-state engine operating conditions for the data points used to validate (213 points) the final CA_{50} model and to parameterize (74 points) the empirical models in equations (4.1), (3.5), and (4.6).

Variables	**whole data**	**empirical models**
Fuel (PRF)	0, 10, 20, 40	
N [rpm]	800 - 1017	
T_m $[^oC]$	41 - 152	70 - 152
EGR [%]	0 - 28.5	0 - 27
ϕ	0.29 - 0.94	0.29 - 0.94
P_m [kPa]	89 - 145	89 - 145
$T_{coolant}$ / T_{oil} $[^oC]$	61 - 83	

shows the predicted CA_{50} from the model for using the average experimental conditions over 200 cycles for each test point. A good agreement between the model prediction and the measured experimental CA_{50} is observed in Figure 4.5. The model uncertainty is determined by calculating 2σ, where σ is the standard deviation of residual error between diamond symbols and round symbols. The model prediction uncertainty for 213 steady-state operating points in Figure 4.5 is ± 2 CAD and the model predictions are usually within the CA_{50} experimental range.

Figure 4.5 also shows that cyclic variations of CA_{50} are higher when CA_{50} occurs late. This is consistent with the experimental observations in Chapter 2. The position of CA_{50} highly affects cyclic variations of IMEP and CA_{50} also influences maximum pressure rise rate characterizing the knock limit [72]. Too late ignitions can misfire while too early ignitions can knock. Therefore only an appropriate window of CA_{50} provides acceptable HCCI operation. The experimental data for the Ricardo engine shows that acceptable operation in terms of cyclic variations, IMEP and knocking level occurs when CA_{50} is between 4 and 12 CAD aTDC .

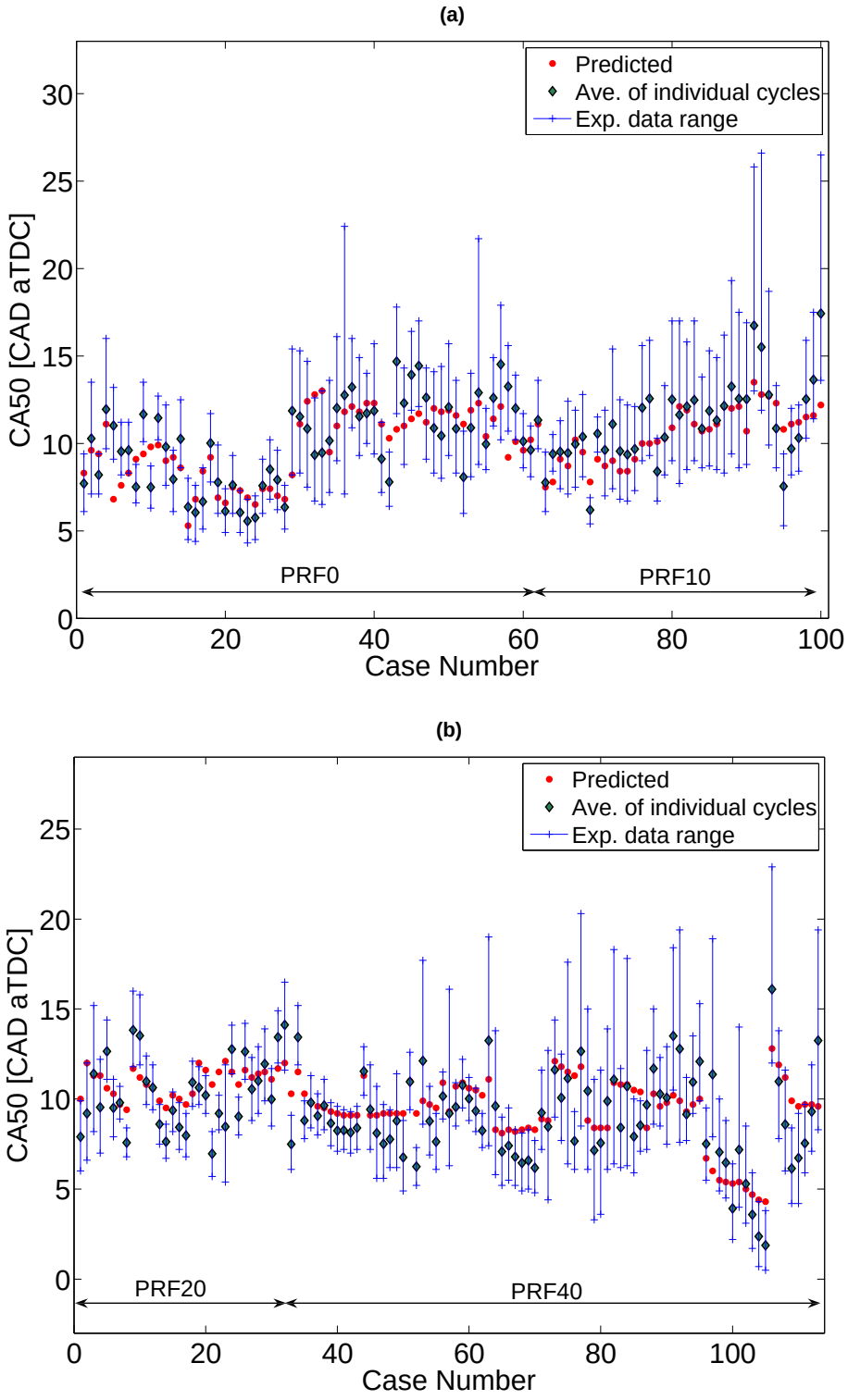

Figure 4.5: Comparison between predicted and experimental CA_{50} for four PRF blends at 213 different steady-state engine conditions.

Steady-state CA_{50} predictions agree well with experimental CA_{50} measurements considering that SOC model was parameterized using the TKM simulation model and then validated with HCCI experiments of which only 1% of them are used to calibrate the TKM. As the TKM does not exactly represent the real engine, the uncertainty in TKM can be one possible source of uncertainty. Other possible sources of uncertainty are the inherent uncertainty of the applied semi-empirical correlations and neglecting the variation of coolant temperature in the TKM since a constant wall temperature is assumed despite the variation in coolant temperature (Table 4.5) in the HCCI experiments.

4.4 SUMMARY

A Modified Knock Integral Model (MKIM) for HCCI combustion has been developed with semi-empirical correlations for gas exchange process and fuel burn rate to predict mean-value combustion timing (CA_{50}). The parameters of the model are identified with a minimization method using simulation/experimental data. Over a wide range of conditions a more complex and computationally intensive TKM model is used to parameterize the MKIM. Experimental data from Ricardo engine is used to parameterize the semi-empirical correlations. The resulting model doesn't require instantaneous in-cylinder parameters but only intake manifold temperature and pressure, EGR rate, engine speed and equivalence ratio to predict CA_{50}.

The model has been tested for a large number of TKM simulations (5534 points) and HCCI experiments (213 points). The MKIM model is able to predict combustion phasing for the experimental HCCI engine with an uncertainty of ± 2 CAD. This uncertainty level seems an acceptable compromise between accuracy and computational load. The validation results of the model cover a large range of engine inputs (initial temperatures, equivalence ratios, EGR rates, and

initial pressures). These results extend previous works [151, 143, 147, 155, 158] on control-oriented modeling of HCCI ignition timing by predicting CA_{50} over a range of engine inputs.

Chapter 5

Dynamic Modeling of HCCI Combustion[1]

The dynamics of thermal coupling between cycles and the dynamics of the control's actuator are investigated for future control of HCCI. To do this, the mean-value HCCI ignition timing model from Chapter 4 is extended into a dynamic full-cycle physics based control oriented HCCI model. The new model predicts cycle-to-cycle combustion timing in transient fueling conditions for HCCI engines. The model simulates the engine cycle from the intake stroke to the exhaust stroke and includes the thermal coupling dynamics caused by the residual gases from one cycle to the next cycle. In addition, the dynamics of fuel transport from the intake port into the cylinder is described using a fuel dynamic model. The resulting HCCI model is parameterized with TKM simulations and Ricardo experimental data. Finally, the model is validated with the experimental data in transient HCCI operation.

5.1 INTRODUCTION

Influential charge properties on HCCI are gas thermodynamic properties (temperature and pressure), mixture AFR, EGR rate, fuel composition/octane number, compression ratio, thermal and compositional inhomogeneities and the residual gas from the previous cycles [74, 80]. Changes in any of these factors can disturb the HCCI ignition timing. HCCI becomes even more sensitive to these distur-

[1]The results of this chapter are partially based on [126, 138].

bances for the late ignitions [75, 89]. If one of the charge variables is used as the parameter to control ignition timing, both the dynamics of changing the charge variable on combustion timing and the actuator dynamics should be considered. Three main techniques to control HCCI ignition timing during transients are: 1) Variable Valve Actuation (VVA) by changing the amount of retained residual gas and by changing the effective compression ratio [167, 31]; 2) Variable Compression Ratio (VCR) to change compression temperature and pressure [37, 168]; 3) Dual Fuel Modulation (DFM) for changing the fuel octane number and the fuel composition [26, 169]. To apply each of these methods, the corresponding dynamics should be considered. For instance, the dynamics of thermal coupling between cycles by the residual gases from one cycle to the next cycle becomes important for the residual affected HCCI using VVA. DFM is another means for control of HCCI combustion and the problem of carrying two fuel tanks can be solved by generating two fuels from one fuel using a reformer [78]. Applying DFM to control ignition timing requires the consideration of fueling transient dynamics.

This study focuses on modeling the dynamics affecting the combustion timing particularly for transient fueling conditions where AFR and fuel octane number are changed to control HCCI ignition timing. Model-based control of HCCI requires computationally efficient control models of the dynamics affecting the combustion timing. These models can also be used in an off-line simulation bed to design and evaluate the combustion timing controller.

As explained previously in Figure 4.1, the two main categories of control-oriented models used to predict combustion timing for HCCI engines are: I) steady-state models, II) cycle-to-cycle (transient) models. The first category, discussed before in Chapter 4, includes the models that provide mean-value combustion timing for steady-state HCCI operation. These models lack cyclic transition dy-

namics from one cycle to the next cycle. However, they can be augmented with other models to consider cycle-to-cycle interactions. This raises these models to the second category of the models that are appropriate not only for steady-state operation but also for transient operation. The second category of models are intended for cycle-to-cycle control of HCCI combustion to manage the transition between different load-speed regions. These models can be based on the category-I (steady-state) models but incorporate the cyclic transition dynamics from one cycle to the next cycle. The three main approaches in the literature for the category-II (transient) models are illustrated in Figure 5.1. The first group are the physic-based models [81, 96, 170, 171] which are mainly thermodynamic models that include exhaust/residual thermal feedback dynamics from one cycle to the next cycle.

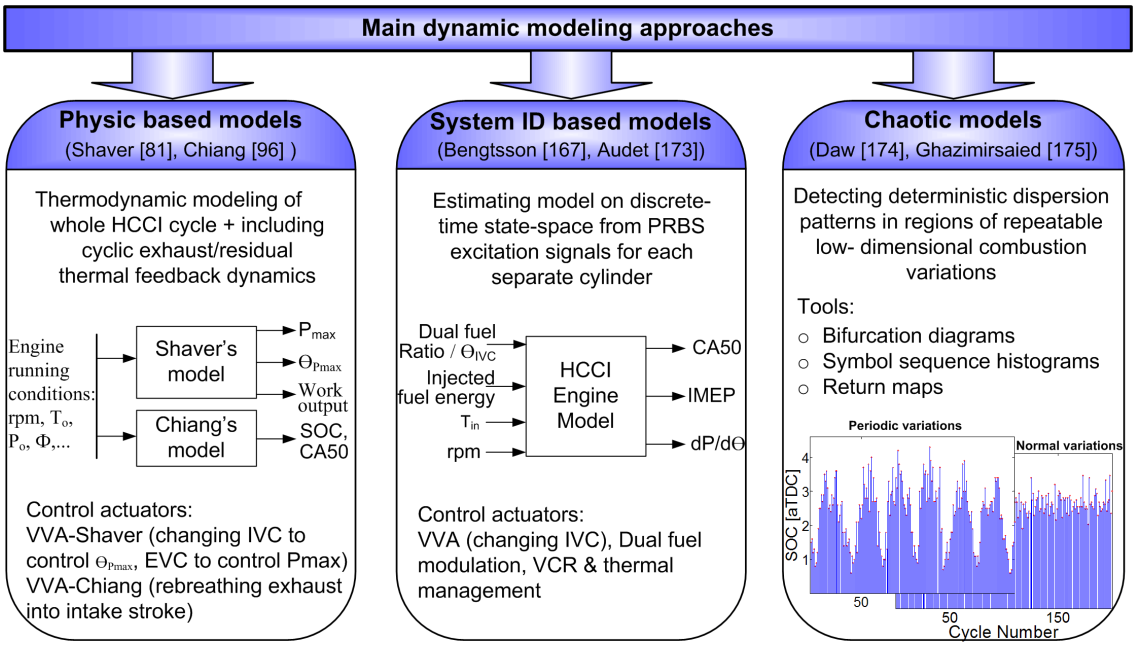

Figure 5.1: Main modeling approaches to predict HCCI cycle-to-cycle combustion timing for control applications.

The physic-based models in category-II are developed based on the category-I

models and they can predict HCCI ignition timing, the engine output work and the peak pressure. The second group are the estimated discrete-time state-space models [167, 172, 173] obtained from applying system identification methods for different load ranges. In these works, Pseudo-Random Binary Sequence (PRBS) excitation signals using both VVA and DFM are used to find the Multi-Input Multi-Output (MIMO) models to predict ignition timing and IMEP. Inputs for these models include the injected fuel energy, dual fuel ratio / valve timing and charge properties. The third group are chaotic models [91, 174, 175] that are based on the recognition of the deterministic dynamics of cyclic oscillations. Results of these models show that consecutive heat release values can be approximated by a sequence of non-linear patterns in a low-dimensional dynamic map.

A new dynamic physics-based control-oriented model is developed in this study to capture the key dynamics for HCCI combustion in transient fueling operation. The model predicts cycle-to-cycle combustion phasing for an HCCI engine without requiring large computation time and doesn't require inputs that are difficult to measure real-time on an engine. Simulated CA50 is experimentally validated with transient fueling tests where n-Heptane and iso-Octane fuels are modulated to provide fuels at different octane numbers and different equivalence ratios.

The following two sections describe the structure of the *HCCI Dynamic Model* and the *Fuel Transport Model*. The governing equations of these two main models are introduced and the methodology to parameterize them is discussed. Next, the details of transient experimental data are explained. Finally, the model is experimentally validated with transient tests.

5.2 HCCI DYNAMIC MODEL

An HCCI operating cycle is broken down into a sequence of valve events that include: intake stroke, compression stroke, combustion, expansion stroke, and exhaust stroke. The complete cycle simulation of an HCCI engine is done by building and linking the models for each part. The whole combustion chamber is assumed as a single zone with a uniformly distributed mixture. The models used to simulate each part of the process are explained in this section.

5.2.1 Intake Stroke (IVO → IVC)

The initial temperature and the pressure of the air-fuel mixture at IVC are calculated by using equation (4.1) and equation (3.5) from the mean-value model in Chapter 4. The effect from residual gas is not included in the mean-value model, thus the mass fraction and temperature of the residual gas should be calculated since this information is required to determine the gas state at IVC by including the mixing of the residual gas with the fresh air-fuel charge.

5.2.1.1 Residual gas model (initial value)

Residual gas from the previous cycles influence the mixture conditions at IVC in terms of the temperature, composition and the dilution level. The residual gas causes thermal cycle-to-cycle dynamics due to the coupling of cycles. These dynamics are important when designing HCCI transition particularly when the amount of internal EGR is altered by variable valve timing [96]. The thermal cyclic interaction is even more important for HCCI/SI or HCCI/CI modal transitions due to different residual gas temperatures when switching from one mode to the other [81].

In this study, the composition of the residual gas is considered to be a combination of combustion products for a complete, lean combustion that consists of

H_2O, CO_2, N_2 and O_2 gases. Residual gas mass fraction (X_r) is defined as:

$$X_r = \frac{m_r}{m_t} \qquad ; \qquad m_t = m_a + m_{egr} + m_f + m_r \tag{5.1}$$

where, m presents the mass and indexes of a, egr, f, r and t respectively stand for air, EGR, fuel, residual gas and total when the intake valves are closed. Two major sources of residual gas are: 1) the trapped exhaust gas before Intake Valve Opening (IVO) and 2) the back-flow of the exhaust gas into the cylinder during the valve overlap period. In HCCI engines, X_r is mainly dependant on valve timing, engine speed, fuel amount, intake manifold pressure and exhaust manifold pressure [176]. A model [177] is used to get a starting value for the value of X_r:

$$X_r = \overbrace{\sqrt{\frac{1}{C}}\,\frac{\pi\sqrt{2}}{360}\,\frac{r_c-1}{r_c}\,\frac{OF}{N}\sqrt{\frac{\mathrm{R}\,T_m|P_{exh}-P_m|}{P_{exh}}}\,\left(\frac{P_{exh}}{P_m}\right)^{\frac{k+1}{2k}}}^{\alpha} + \overbrace{\frac{1}{C}\,\frac{r_c-1}{r_c}\,\phi\,\frac{V_{ivo}}{V_{dis}}\,\left(\frac{P_{exh}}{P_m}\right)^{\frac{1}{k}}}^{\beta} \tag{5.2}$$

where, r_c indicates the compression ratio; P_{exh} is the exhaust pressure; R is the gas constant, and k is the ratio of specific heats. V_{ivo} is the cylinder volume at IVO moment and V_{dis} is the displacement volume. OF is the valve overlap factor that is calculated by using geometry and timing of both intake and exhaust valves. The parameter C is calculated as:

$$C = \left[1 + \frac{LHV}{c_v\,T_m\left(\frac{m_t}{m_f}\right)r_c^{k-1}}\right]^{\frac{1}{k}} \tag{5.3}$$

where, LHV represents the lower heating value of the fuel and c_v is the constant-volume specific heat capacity of the in-cylinder gas at the IVC moment. LHV for an arbitrary blend of PRF fuels ($\%V_{_n}+\%V_{_{iso}}$; iso for iso-Octane, n for n-Heptane) is evaluated by:

$$LHV = \frac{\%V_n \, \rho_n \, LHV_n \; + \; \%V_{iso} \, \rho_{iso} \, LHV_{iso}}{\%V_n \, \rho_n \; + \; \%V_{iso} \, \rho_{iso}} \tag{5.4}$$

where, $\%V$ is the volume percentage and ρ is the density of the fuel.

The first term (α) in equation (5.2) is attributed to the portion of the residual gas caused by the back-flow during the valve overlap period and the second term (β) accounts for the trapped exhaust gases before IVO [177]. As the engine used in this study has a valve overlap period of zero degrees, the first term in equation (5.2) is assumed to be zero[2]. The value of X_r obtained from equation (5.2) is used as the starting value to initialize the *HCCI Dynamic Model* to solve the thermodynamic equations. The value of X_r is then determined at the end of the simulation cycle based on the amount of mass retained inside the cylinder at the moment of Exhaust Valve Closing (EVC). Then an iterative process is performed with the new X_r until it converges to the X_r obtained at the end of the cycle.

5.2.1.2 Mixing temperature equation

Mixing of the fresh charge with the residual gas from the previous cycles affects the mixture temperature at IVC, but the T_{ivc} values obtained from equation (3.5) don't consider this effect. A modified temperature for IVC moment (T_{mix}) is calculated to account for the mixing process. In-cylinder gases are considered as ideal gases and assuming energy is conserved in the mixing process of the residual gas and fresh charge yields:

$$T_{mix}(i) = (1 - X_r) \left(\frac{c_{v,ch}}{c_{v,t}} \right) T_{ivc}(i) + X_r \left(\frac{c_{v,r}}{c_{v,t}} \right) T_r(i-1) \tag{5.5}$$

where, i is the cycle number index and subscripts r, ch and t represent the

[2]This term (α) should not be ignored if an engine uses a typical SI valve timing with a positive valve overlap. The model is not sensitive to the term α in relation to stability, thus the model is expected to work for engines with positive valve overlap.

residual gas, the charge (air+fuel+EGR), and the total in-cylinder gas at IVC respectively. Equation (5.5) suggests a thermal coupling between the cycle (i) and the previous cycle ($i-1$) introduced by residual gases. The c_v properties of different gas components of the in-cylinder mixture are determined by using the NASA polynomials database [178].

5.2.1.3 Dilution fraction equation

The amount of residual gas changes the properties and the dilution level of the charge at IVC. This subsequently influences the combustion timing and the fuel burn rate. A parameter is defined as the mixture dilution fraction (X_d) that accounts for the dilution caused by (external) EGR contained in the fresh charge and the dilution caused by the residual gases (internal EGR):

$$X_d = EGR + \frac{X_r}{1 - X_r} \tag{5.6}$$

both influence the combustion timing and the fuel burn rate.

5.2.2 Compression Stroke (IVC → SOC)

The location of SOC is determined using the MKIM (Section 4.2.2.2) and pressure and temperature at SOC are determined using polytropic relation.

5.2.2.1 Polytropic compression

Extensive studies of the compression process show that compression of the unburned mixture prior to combustion is accurately fitted by a polytropic relation ($PV^k = constant$) [101]. Here, blow by is ignored and a polytropic relation is used to calculate the temperature and pressure of the in-cylinder mixture at SOC using the available data at IVC:

$$T_{soc} = T_{mix} \cdot \left(\frac{V_{ivc}}{V_{soc}}\right)^{k_c - 1} \tag{5.7}$$

$$P_{soc} = P_{ivc} \cdot \left(\frac{V_{ivc}}{V_{soc}}\right)^{k_c} \tag{5.8}$$

where, V is the cylinder volume and k_c is the average specific heat capacity ratio for the compression process. The constant $k_c = 1.32$ is chosen based on a best fit on TKM simulated compression results shown in Appendix D.2.4.1. $k_c = 1.32$ is only valid for PRF blend fuels used in this study and it should be calculated for each particular fuel since k_c depends on the type of fuel.

5.2.3 Combustion Period (SOC → EOC)

End of Combustion (θ_{eoc}) is defined as the crank angle where 99% of the fuel mass is burned. The modified Wiebe function from Section 4.2.3 is used to predict fuel mass fraction burned (x_b) and to calculate CA50 and θ_{eoc}. Temperature and pressure at EOC are determined using EOC state equations.

5.2.3.1 EOC state equations

During combustion, the combustion chamber is considered as a closed system and the first law of thermodynamics is applied on the system between SOC and EOC to obtain the temperature and pressure of in-cylinder gas at EOC using available properties at SOC:

$$U_{eoc} = U_{soc} + Q_{fuel} - Q_w - W_{soc-eoc} \tag{5.9}$$

where, U is the internal energy; Q_{fuel} is the energy released from burning fuel; Q_w is the heat loss from the in-cylinder gas to the surrounding walls and $W_{soc-eoc}$ is the work produced during the crank angle interval between SOC and EOC. Q_w is assumed negligible in equation (5.9) because HCCI combustion is very fast and little time is available for heat transfer and the surface area for heat transfer is also small by having a desirable HCCI combustion occur at crank angles close to

TDC [73]. An empirical correlation is obtained from experimental measurements to predict the $W_{soc-eoc}$:

$$W_{soc-eoc} = m_f \; LHV \overbrace{\frac{P_m^{\mathrm{A}} \; N^{\mathrm{B}}}{(1+EGR)^{\mathrm{C}}} \left(\mathrm{D}_1 \, \theta_{soc}^2 + \mathrm{D}_2 \, \theta_{soc} + \mathrm{D}_3\right)}^{\mathbb{W}} \tag{5.10}$$

where, m_f is the mass of the fuel injected per cycle and A, B, C, D_1, D_2, D_3 are the constant parameters that are determined by applying the Nelder-Mead optimization technique on the one-third of the steady-state experimental data detailed in the section 4.3. The resulting parameters are A= 2.629, B= -2.860, C= -0.056, D_1= 0.021, D_2= -3.711, D_3= 0.010. Correlation (5.10) predicts that ignition timing (θ_{soc}) influences the amount of the work produced from an HCCI combustion. This is also observed in the experimental study in Chapter 2 where it is shown that ignition timing influences IMEP in HCCI combustion.

In comparison to the $W_{soc-eoc}$ term in equation (5.9), the Q_{fuel} term is much larger in magnitude. The energy released from the fuel, Q_{fuel}, is given by:

$$Q_{fuel} = m_f \; . \; CoC \; . \; LHV \tag{5.11}$$

where, CoC is the Completeness of Combustion and is calculated by the following empirical correlation that is parameterized with the same experimental data used for correlation (5.10):

$$CoC = \frac{\Phi^{\mathrm{A}} \; P_m^{\mathrm{B}}}{(1+EGR)^{\mathrm{C}}} \left(\mathrm{D}_1 \, \theta_{soc}^2 + \mathrm{D}_2 \, \theta_{soc} + \mathrm{D}_3\right) \tag{5.12}$$

where, A= 0.169, B= 0.165, C= 0.053, D_1= -0.001, D_2= 0.458, D_3= 1.390. The CoC correlation suggests a higher CoC when θ_{soc} occurs at TDC or slightly after TDC, but CoC drops for early and late ignitions. This is consistent with the observation in [89] where the possibility of partial-burn cycles or misfired cycles in HCCI combustion increases when ignition is late. Furthermore, experimental

results in [73] show that cyclic variability of HCCI combustion increases for ignitions that are too early or too late. Cyclic variability influences the instability or misfire limit of an HCCI engine.

Mass fractions (y) for each of the combustion reactants are determined using equations (5.13) to (5.15) and the mass fractions of the combustion products are calculated using general reaction equations of PRF blends for a complete, lean combustion [150].

$$y_{a} = \frac{m_{a}}{m_{t}} = \frac{AFR\,(1 - X_{r})\,(1 - EGR)}{AFR + 1} \tag{5.13}$$

$$y_{egr} = \frac{m_{egr}}{m_{t}} = EGR\;(1 - X_{r}) \tag{5.14}$$

$$y_{f} = \frac{m_{f}}{m_{t}} = \frac{(1 - X_{r})\,(1 - EGR)}{AFR + 1} \tag{5.15}$$

where, AFR is the air fuel ratio of the charge. Combustion reactants (PRF blend fuel, air, EGR, residual gas) and combustion products (H_2O, CO_2, N_2, O_2) are assumed to be ideal gases. Using this assumption, equations (5.9) and (5.10) are combined and rearranged to give the in-cylinder gas temperature at EOC:

$$T_{eoc} = \frac{\left(\sum_{i} c_{v,i}\; y_{i}\right)_{R} .\; T_{soc} + \frac{m_{f}}{m_{t}} .\; LHV\,(CoC - \mathbb{W})}{\left(\sum_{i} c_{v,i}\; y_{i}\right)_{P}} \tag{5.16}$$

where, symbols R and P stand for Reactants and Products respectively ($\mathbb{W}$ from equation 5.10). Finally, pressure at EOC is calculated by using the ideal gas state equation for EOC and IVC conditions assuming constant mass (no blow-by):

$$P_{eoc} = P_{ivc} \cdot \frac{V_{ivc}}{V_{eoc}} \cdot \frac{T_{eoc}}{T_{mix}} \cdot \frac{R_{eoc}}{R_{ivc}} \tag{5.17}$$

5.2.4 Expansion Stroke (EOC → EVO)

5.2.4.1 Polytropic expansion

Similar to the compression stroke, the expansion of burned gases after EOC can be characterized by a polytropic relation [101]. Here, temperature and pressure of the burned gas at Exhaust Valve Opening (EVO) are calculated based on available data from EOC by using a polytropic relation:

$$T_{evo} = T_{eoc} \cdot \left(\frac{V_{eoc}}{V_{evo}}\right)^{\mathrm{k_e}-1} \tag{5.18}$$

$$P_{evo} = P_{eoc} \cdot \left(\frac{V_{eoc}}{V_{evo}}\right)^{\mathrm{k_e}} \tag{5.19}$$

where, $\mathrm{k_e}$ is the average specific heat capacity ratio for the expansion process that can be determined with a similar approach to section 5.2.2.1.

5.2.5 Exhaust Stroke (EVO → EVC)

5.2.5.1 Exhaust gas model

When the exhaust valves open, the in-cylinder gas goes through a blow-down phase to a gas displacement phase from the moving piston. A single zone crank-angle resolved model is developed to predict the gas state (temperature, pressure, mass) at the EVC moment. A quasi-steady assumption is used and the properties of the gas including the gas leaving or entering into the cylinder are assumed steady and homogeneous. Furthermore, the change in the kinetic and potential energies of the gas are ignored. Using these assumptions, the first law of thermodynamics for the exhaust gas as an open Control Volume (CV) between the state "1" and the state "2" yields:

$$\dot{Q}_w - \dot{W} = \sum \dot{m}_{ce} h_{ce} + \left[\frac{(m_2 u_2 - m_1 u_1)_{CV}}{\Delta t}\right] - \sum \dot{m}_{ec} h_{ec} \tag{5.20}$$

where, h is the enthalpy of the gas and Δt is the time span between states "1" and "2". Index "ce" refers to the exhaust flow from the cylinder to the exhaust manifold and "ec" refers to the backflow from the exhaust manifold to the cylinder. As the Ricardo engine has a zero valve overlap period, small exhaust backflow is expected and no flow between the intake manifold and the cylinder is considered during the exhaust stroke. The heat transfer to the cylinder walls is modeled using the Modified Woschni heat transfer correlation, previously explained in Section 3.3.

Equation (5.20) is rearranged by using the ideal gas assumption and generated work equation ($\dot{W} = -P\dot{V}$). T_{evc} is determined from EVO to EVC using the following equation in the combination with ideal gas state equation and exhaust valve flow model.

$$T_2 = \frac{T_1 \left(\sum_i m_{i,1}\ c_{v_i,1} - \sum_i c_{p_i,1} \left(m_{i,ce} + m_{i,ec}\right)\right) + Q_w + P_1\, dV}{\sum_i m_{i,2}\ c_{v_i,2}} \tag{5.21}$$

The ideal gas state equation is used to calculate the gas pressure (P_1) in equation (5.21) and the exhaust valve flow model is used to calculate the mass of the gas inside the cylinder ($m_{i,1}, m_{i,2}$) and also the flow across the exhaust valves ($m_{i,ce}, m_{i,ec}$).

5.2.5.2 Exhaust valve flow model

Dynamics of the gas flow across the exhaust valves are modeled by using the orifice equation for one-dimensional, steady-state, compressible, isentropic flow [101]:

if $P_T/P_o > [2/(\mathrm{k}+1)]^{\mathrm{k}/(\mathrm{k}-1)}$],

$$\dot{m} = \frac{C_D\, A_R\, P_o}{\sqrt{\mathrm{R}\, T_o}} \left(\frac{P_T}{P_o}\right)^{\frac{1}{\mathrm{k}}} \left\{\frac{2\,\mathrm{k}}{\mathrm{k}-1}\left[1 - \left(\frac{P_T}{P_o}\right)^{\frac{\mathrm{k}-1}{\mathrm{k}}}\right]\right\}^{\frac{1}{2}} \tag{5.22}$$

otherwise,

$$\dot{m} = \frac{C_D\, A_R\, P_o}{\sqrt{\mathrm{R}\, T_o}}\ \mathrm{k}^{\frac{1}{2}} \left(\frac{2}{\mathrm{k}+1}\right)^{\frac{\mathrm{k}+1}{2(\mathrm{k}-1)}} \tag{5.23}$$

where, C_D is the discharge coefficient; subscripts "$_o$" and "$_T$" refer to the gas properties at the upstream and the downstream of the exhaust valves. A_R is a reference area (called curtain area) which is calculated by:

$$A_R = \pi\, d_v\, L_v \tag{5.24}$$

where, d_v is the diameter of the exhaust valves ($d_v = 27mm$) and L_v is the axial valve lift that is measured off-line. Figure 5.2 shows the measured lift profile for the valves. C_D is experimentally determined using flow measurements from [173]

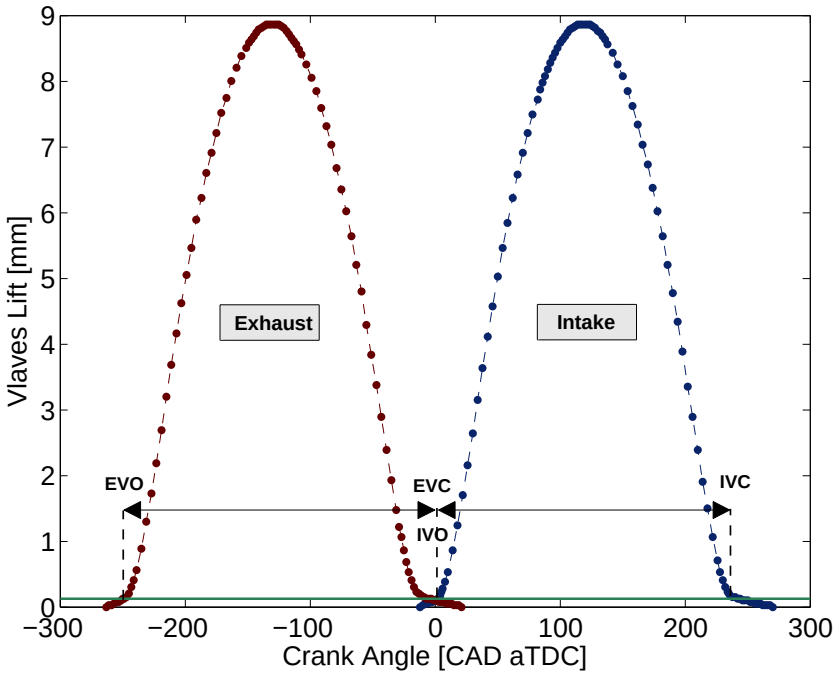

Figure 5.2: Measured lift profile for the valves used in this study. [The solid horizontal line shows the defined threshold ($\simeq$ 0.15 mm) for opening/closing point of valves.]

on a flow-bench apparatus for a similar cylinder-head (see Appendix E.2). Flow measurements are at 45 different valve lifts and pressure ratios (P_T/P_o) while

sweeping from choked-flow conditions ($P_T/P_o \leq [2/(\mathrm{k}+1)]^{\mathrm{k}/(\mathrm{k}-1)}$) to the un-choked-flow conditions. The following correlation is found to work well on the available data:

$$C_D = \mathrm{A} + \mathrm{B}\ \ln\left(\frac{L_v}{d_v}\right) + \mathrm{C}\ \left(\ln\left(\frac{L_v}{d_v}\right)\right)^2 + \mathrm{D}\ \ln\left(\frac{P_o}{P_T}\right) \tag{5.25}$$

where, A = -0.152, B = -0.577, C = -0.082, and D = 0.294. For the 45 flow measurements, the uncertainty in predicted C_D from correlation (5.25) is ± 0.06.

Figure 5.3 shows the simulation results of the model for mass of the gas inside the cylinder from the EVO moment to the EVC moment. As expected mass of the gas inside the cylinder substantially drops during the blow-down phase until the cylinder pressure reaches the exhaust pressure. Next, pressure

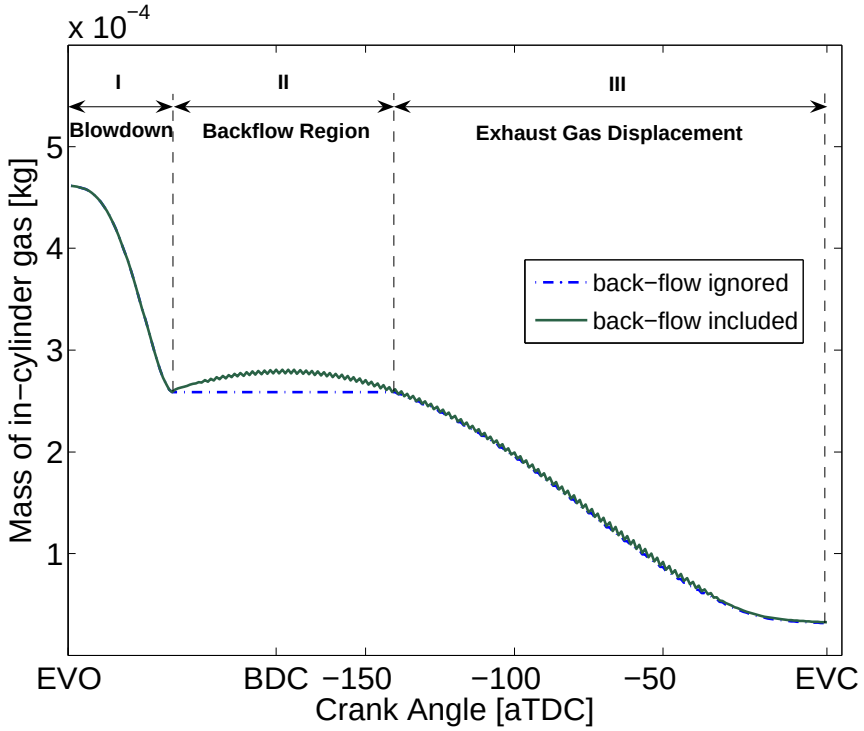

Figure 5.3: Simulated mass of the gas inside the cylinder during the exhaust period for a sample operating point. (Fuel = PRF0, N = 813 rpm, $\Phi = 0.36$, P_m = 110 kPa, $T_m = 91°$C)

drops more inside the cylinder due to further expansion by moving the piston downwards to BDC (Bottom Dead Center). This is enough to commence the backflow from the exhaust into the cylinder. This causes an increase in the cylinder mass as indicated in Figure 5.3. But this trend does not last long and in the gas displacement phase the cylinder pressure rises again higher than the exhaust pressure by moving the piston upwards through the exhaust stroke. Thus the mass of the in-cylinder gas continues to drop until the exhaust valves are closed (EVC). Figure 5.3 also shows the simulation results when the backflow is ignored. It indicates that for this engine the backflow does not significantly influence the final mass of the retained gas inside the cylinder at the moment of EVC.

5.2.5.3 Residual gas state

In-cylinder gas temperature and the retained mass inside the cylinder at the moment of EVC determine the temperature of residual gas (T_r) and the mass fraction of the residual gas (X_r).

5.2.6 Model Layout

A structure of a dynamic full-cycle simulation model has been formed that includes thermal coupling from one cycle to the next cycle through mass and thermal properties of residual gases. Figure 5.4 shows an overall schematic of the model programmed in Matlab computing environment. The model requires these seven measurable inputs: intake manifold temperature, intake manifold pressure, EGR, engine speed, equivalence ratio, mass of injected fuel, and pressure in the exhaust port.

Three iteration loops are needed in the model (see Figure 5.4). The first loop is used to get the initial X_r in the intake stroke and it runs only one time. The second loop is used to get T_{eoc} in the combustion stroke and it runs every

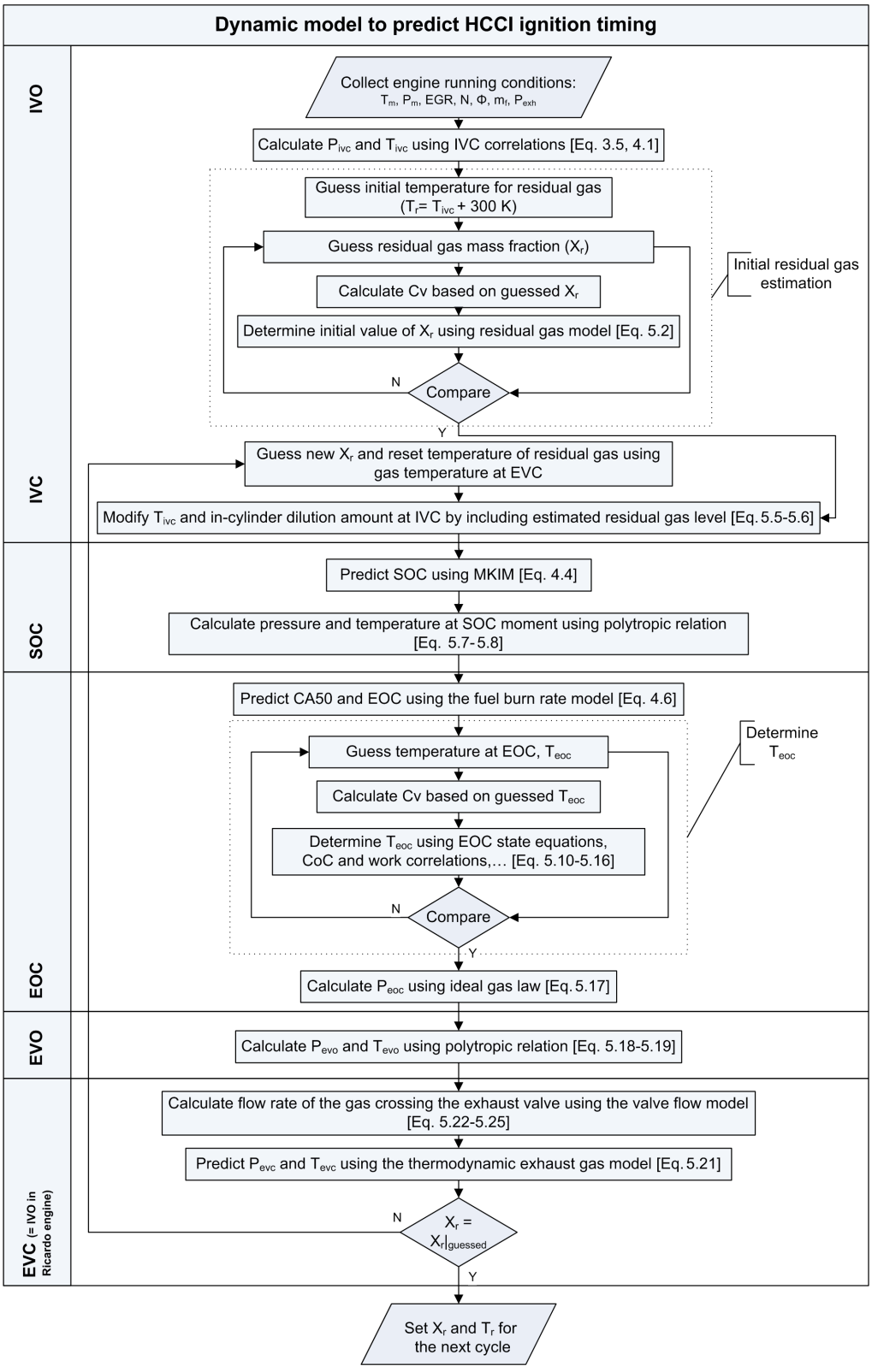

Figure 5.4: Schematic of the developed model.

cycle. These two loops are present due to the dependance of the gas specific heat capacity (c_v) on X_r and gas temperature, but X_r and T_{eoc} depend on c_v in equation (5.3) and equation (5.16). Figure 5.5 shows a sample simulation

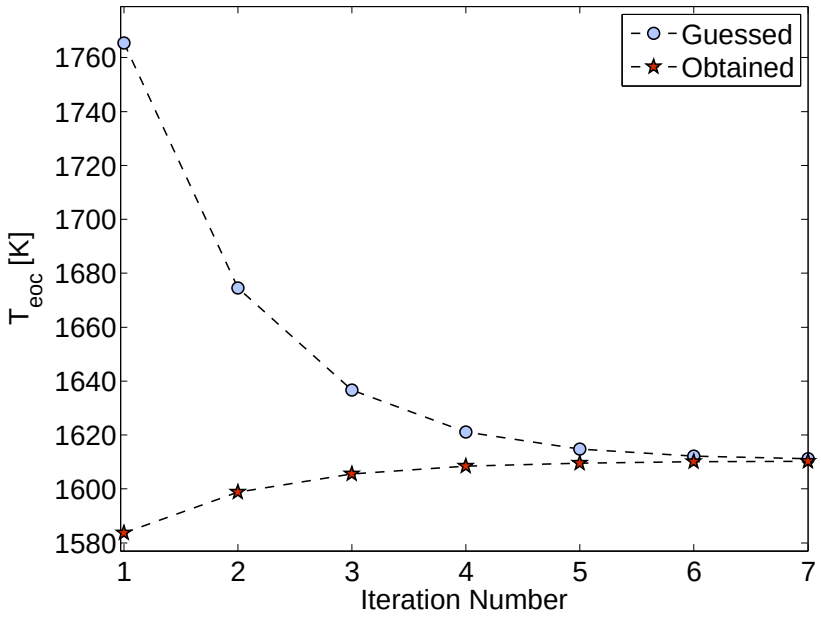

Figure 5.5: Simulation conversion rate for the T_{eoc} for a sample operating point. (Fuel = PRF0, N = 810 rpm, $\Phi = 0.44$, $P_m = 101$ kPa, $T_m = 102$°C)

result of the iterative process in the model to predict T_{eoc}. It can be seen the simulation converges to a constant value with a small error (< 1°C) within seven iterations. Four to six iterations are typically required to get T_{eoc} within 5°C resolution for different simulation conditions. The third iteration loop in the model (Figure 5.4) calculates X_r and it runs only at the start of simulation. The initial X_r value from equation (5.2) is tested at the end of simulation cycle (EVC) and then based on the difference between the initial and calculated values, iteration is performed by repeating the simulation from IVC to EVC. This process continues until consecutive values of X_r converge within a tolerance. However, for each operating point this iterative process is run only once for the first cycle to get the correct X_r, then the values of X_r for the next cycle is always determined

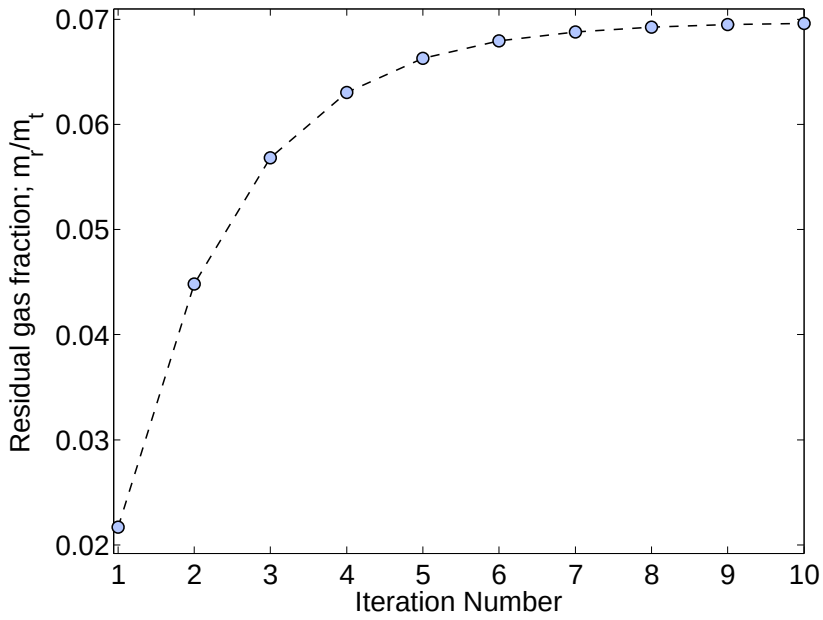

Figure 5.6: Conversion rate of the simulated residual gas mass fraction for a sample operating point. (Fuel = PRF0, N = 810 rpm, $\Phi = 0.44$, $P_m = 101$ kPa, $T_m = 102°$C)

from calculated X_r of the previous cycle. Figure 5.6 indicates a sample simulation result of the iterative process to get correct X_r for the first cycle of a new operating point. As seen in the figure, X_r converges to 6.7% $\pm$ 0.01% within 10 iterations from the starting value of 2.2% obtained from equation (5.2). Typically five to seven iterations are required to obtain X_r with a convergence error of 0.001 for different simulation conditions.

5.3 FUEL TRANSPORT MODEL

Dynamics of transporting the fuel into the cylinder is one of the main charge dynamics involved in an HCCI operation during transient fueling. Fuel transport dynamics is described using the approach known as $x - \tau_f$ model [179]. $x - \tau_f$ model assumes that a fraction (x) of the fuel delivered to the intake system is deposited on the surfaces in the form of fuel film and enters the cylinder at a

rate proportional to the mass of fuel in the film and inversely proportional to a time constant (τ_f). The other fraction of the fuel $(1-x)$ is entrapped in the air flow as vapor. So for the case of a Port Fuel Injection (PFI), the injected fuel mass flow rate ($\dot{m}_{fi}$) divides into two portions including the vapor phase mass flow rate ($\dot{m}_{fv}$) and the liquid (fuel film) phase mass flow rate ($\dot{m}_{ff}$) as shown in Figure 5.7. These two portions determine the final fuel mass flow rate into the cylinder ($\dot{m}_f$) as expressed below [179]:

$$\dot{m}_f = \dot{m}_{fv} + \dot{m}_{ff} \tag{5.26}$$

$$\dot{m}_{fv} = (1-x)\ \dot{m}_{fi} \tag{5.27}$$

$$\dot{\dot{m}}_{ff} = \frac{x\,\dot{m}_{fi} - \dot{m}_{ff}}{\tau_f} \tag{5.28}$$

where, x with a value between 0 and 1 is the fuel split parameter and τ_f is the mean evaporation time for the fuel film flow from the intake ports. x and τ_f parameters must be identified, so the fuel transport dynamics can be included in the *HCCI Dynamic Model*.

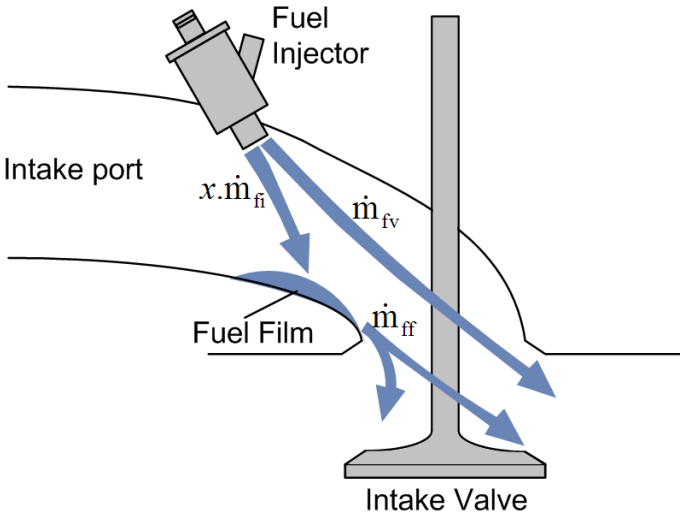

Figure 5.7: Fuel transport model

Other dynamics are also present in the path from injecting the fuel into the intake system until AFR is measured by an AFR sensor. These are the dynamic involved in transporting the exhaust gas to the AFR sensor and measurement dynamics in AFR sensor. These dynamics are important and should be considered in both AFR feedback control and the process of identifying x and τ_f. The dynamic of the exhaust gas transport is modeled as a pure delay [180, 181, 182] and is denoted as ΔT in this study. Similar to other studies [180, 182, 183, 184, 185] the dynamic in the response of the AFR sensor is considered as a first order lag element with a measurement time constant of τ_m.

The three main dynamics mentioned above can be put together into one transfer function to indicate the fuel transport dynamics from the injection in the intake ports until measurement by the AFR sensor in the exhaust pipe [186]:

$$\frac{\dot{m}_{fm}(s)}{\dot{m}_{fi}(s)} = \overbrace{\frac{1+\tau_f\,(1-x)\,S}{1+\tau_f S}}^{\alpha}\ \overbrace{e^{-S\Delta T}}^{\beta}\overbrace{\frac{1}{1+\tau_m S}}^{\gamma} \tag{5.29}$$

where, $\dot{m}_{fm}$ is the measured fuel mass flow rate. Term α represents the fuel transport dynamics and terms β and γ include the transport dynamics of the exhaust gas and the dynamics of the AFR sensor respectively.

5.3.1 Model parametrization

5.3.1.1 AFR sensor time constant – τ_m

AFR sensor used in this study is an ECM AFRecorder 1200 Universal Exhaust Gas Oxygen sensor (UEGO) that directly measures the oxygen content of the exhaust with a time constant of 150 msec [103]. ($\tau_m = 0.15$ sec)

5.3.1.2 Exhaust gas transport delay – ΔT

The fuel is injected 365 CAD before IVO and the AFR sensor is positioned approximately 25 cm downstream of the exhaust valve in the Ricardo engine. ΔT includes the fuel transport delay from the fuel injection moment until it reaches the AFR sensor. ΔT can be estimated by measuring the time that it takes a change in AFR in the intake system appears in the measurement by AFR sensor in the exhaust pipe. To do this a rectangular AFR excursion is made by rectangular injection rate at a constant air flow rate (constant throttle opening and engine speed) and then AFR variation is recorded by the AFR sensor. This process requires to include the dynamics of the AFR sensor as the measurement from the sensor is used. This becomes more important when a same method is used to identify x and τ_f. The AFR sensor dynamics ($\tau_m = 0.15$ sec) can be applied either on AFR sensor measurements or the AFR excursion from the injected fuel – see equation (5.29). An example of the data for the identification process is shown in Figure 5.8. Result of including τ_m dynamics on the injector Φ values is presented in the format of a dashed line and the solid line shows Φ measurements by the sensor. The modified Φ (dash line) and measured Φ (solid line) are used to determine ΔT using system identification methods [187].

ΔT is highly dependant on engine speeds and intake pressure [186]. Thus, different ΔT values are expected at different ranges of engine speed and intake pressures. Here, data points with similar engine speed and intake pressure are grouped together and ΔT is determined for each of these groups. The estimated ΔT for the operating point in Figure 5.8 is found 260 msec.

5.3.1.3 Fuel transport parameters – x, τ_f

The most common methods to determine x and τ_f for control applications are system identification methods [186]. In these methods, engine response to AFR

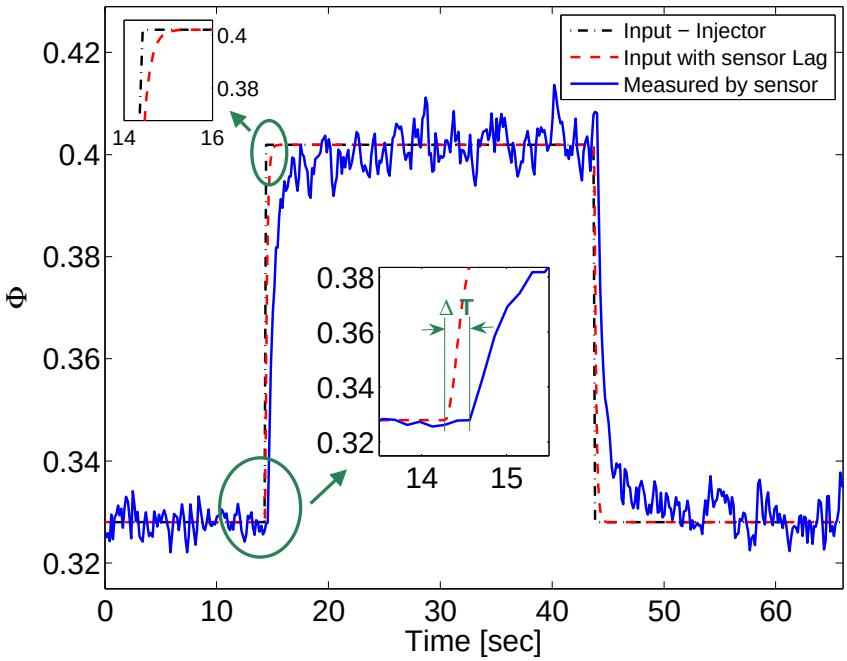

Figure 5.8: Processed AFR excursion data for the identification of fuel dynamics parameters. (PRF0, N = 815 rpm, P_m = 121 kPa, T_m = 67°C, $T_{coolant}$ = 72°C)

excursion, an excitation signal to the system, is recorded either by measuring engine torque [188] or by measuring exhaust AFR from a UEGO sensor [189]. Here, UEGO sensor measurements at sampling rate of 100Hz is used to record the engine response to a rectangular AFR excursion implemented in the intake ports by adjusting injection flow rate at a constant air mass flow rate. Rectangular excitation input is chosen because it is well capable to stimulate the system to identify x and τ_f as shown in [181, 186, 189]. System identification methods are applied to identify x and τ_f for each operating point.

The variables x and τ_f depend on the fuel type, coolant temperature, intake temperature, intake pressure and engine speed [186]. Changing each of these parameters can cause a variation in fuel transport parameters. Here, x and τ_f are estimated from the recorded AFR data for one operating point. Then, estimated x and τ_f are used to validate the model at another operating point with the conditions close to the test point used to find x and τ_f. The estimated

x and τ_f are 0.49 and 1.57 sec for the operating point in Figure 5.8. These values are tested by recorded AFR data for another test point with similar operating conditions in Figure 5.9-a. Similarly, x and τ_f are estimated 0.28 and 3.72 sec using the data for an operating point with a different octane number (PRF20, N

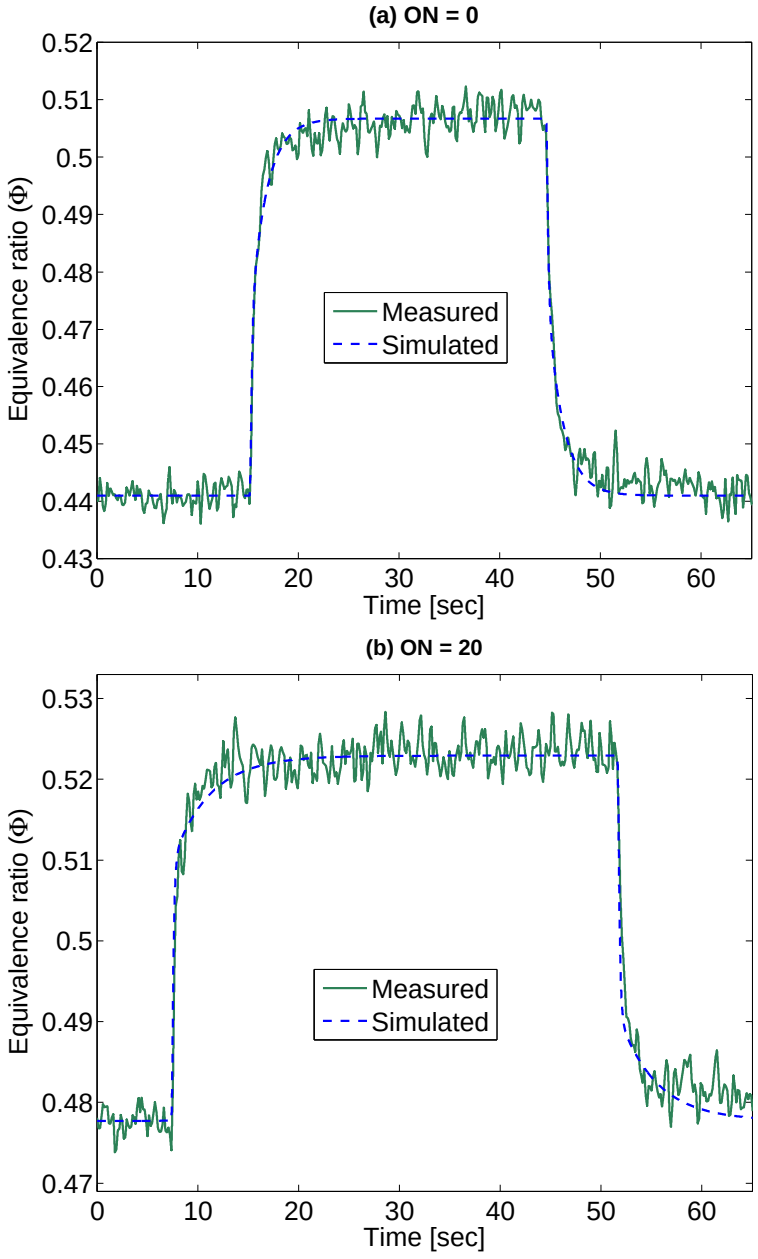

Figure 5.9: Measured and simulated equivalence ratio for two sample operating points. (a) N = 816 rpm, P_m = 100 kPa, T_m = 67°C, $T_{coolant}$ = 73°C; (b) N = 814 rpm, P_m = 100 kPa, T_m = 93°C, $T_{coolant}$ = 71°C.

= 814 rpm, P_m = 115 kPa, T_m = 95°C, $T_{coolant}$ = 71°C). The values of τ_f seem large and this is partly due to running the engine at a coolant temperature lower than that of a normal engine operation. The estimated parameters of x and τ_f are tested with the data for another test point with similar operating conditions in Figure 5.9-b. Simulation results in Figure 5.9 are in good agreement with those from the experimental measurements, though the operating conditions of the test points used to identify x and τ_f are not identical to those of the test points in Figure 5.9.

5.4 MODEL EXPERIMENTAL VALIDATION

Ricardo transient experimental test points are used to validate the final model that includes the dynamics from both HCCI combustion and transient fueling. Transient experiments are performed using the engine setup shown in Figure 2.26. Sensitivity analysis [128] for the current experimental setup suggests to use the octane number and equivalence ratio as the main variables to control HCCI combustion timing for the Ricardo engine. CA50 as the main output of the model is tested with experimental cyclic CA50 values processed from the recorded pressure trace data.

Transient experiments are performed by transient open loop fueling at a constant air flow rate. Fuel mass flow rate are first stepped up and then stepped down to the initial value to study the system dynamics in both directions of increasing and decreasing engine loads. During each transient test 450 cycles of cylinder pressure data are recorded at 0.1 CAD and other measured engine variables are recorded at 100Hz.

Both n-Heptane and iso-Octane injectors are aimed directly at the back of the intake valves and they are located respectively at the approximate position of 10 cm and 25 cm from the intake valves. A dSpace MicroAutobox 1401/1501

ECU is used to control the injection Pulse Width (PW) of n-Heptane and iso-Octane injectors to provide the desired AFR and Octane Number (ON). Injected fuel mass per cycle ($m_{f,i}$) for both injectors is estimated from the PW of the injectors [185]:

$$m_{f,inj}\left[\frac{g}{cycle}\right] = \mathrm{C_f}\ .\ PW_{inj}\,[ms] + \mathrm{C_{offset}} \tag{5.30}$$

where, $\mathrm{C_f}$ and $\mathrm{C_{offset}}$ are constant parameters that are determined by injector calibration from steady state fuel flow measurements at different operating conditions. The resulting $\mathrm{C_f}$ and $\mathrm{C_{offset}}$ are 3.30 $\left[\frac{g}{ms.cycle}\right]$ and -2.90 $\left[\frac{g}{cycle}\right]$ for iso-Octane injector and 2.95 $\left[\frac{g}{ms.cycle}\right]$ and -2.74 $\left[\frac{g}{cycle}\right]$ for n-Heptane injector. More details about the procedure to calculate these parameters are explained in the Appendix E.

The model requires seven measurable inputs that are: intake manifold temperature and pressure, EGR, engine speed, equivalence ratio, pressure in the exhaust port and mass of injected fuel which is calculated from injectors' pulse widths. The test points reported next have not been used before to parameterize the model. Processing time of the model in Matlab is about 61 sec for simulating 450 cycles using a 2.22 GHz AMD 64 X2 Dual Processor. This leads to an average simulation time $\sim$ 0.14 sec for each individual engine cycle. The processing time could be reduced for real time applications by optimizing the code and using specialized hardware such as Field-Programmable Gate Array (FPGA) [160].

Figures 5.10 and 5.11 show the transient response during the fuel and ON steps. As expected CA50 advances with increasing equivalence ratio, but it retards with increasing octane number. Values of fuel mass flow rate are calculated from injector pulse width from equation (5.30). Figure 5.10 compares the predicted system transient response with that of the experiment when equivalence ratio is changed. A Φ excursion is evident in Figure 5.10 though the injection

step change is done sharply. This indicates the significance of fuel transport dynamics in the Ricardo engine with the current setup that incorporates a closed valve injection timing. A limited range of Φ is possible at each constant EGR rate operating point and this range becomes smaller when switching to the fuels with higher octane numbers.

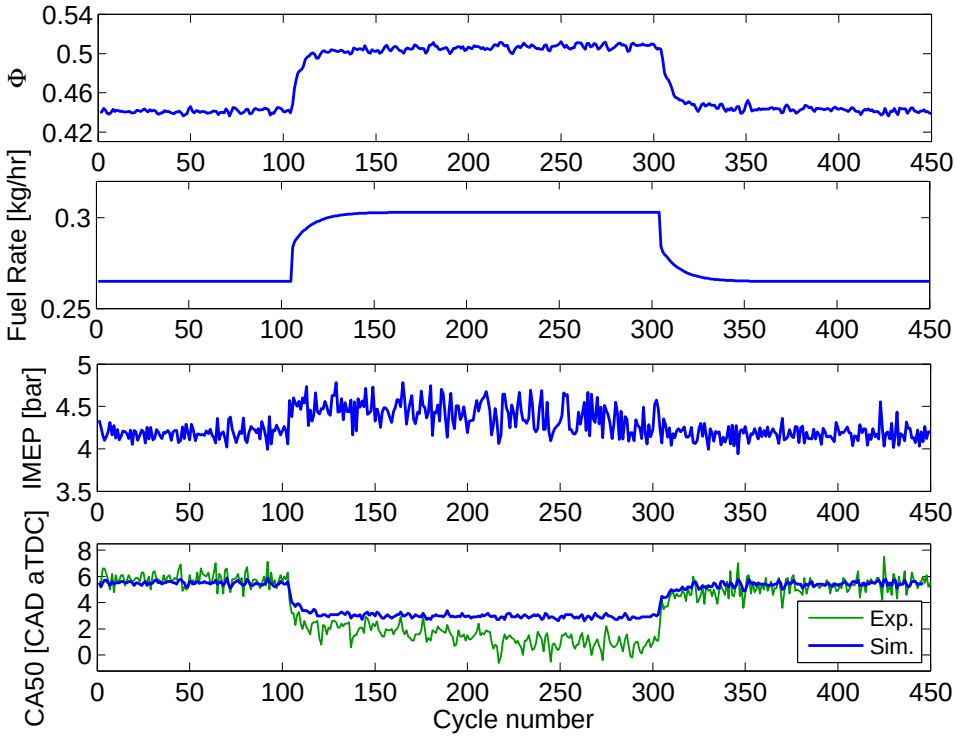

Figure 5.10: Equivalence ratio step: comparison between predicted and experimental cycle-to-cycle CA50. (ON = 0; P_m = 100 kPa, T_m = 67°C, EGR = 0%, P_{exh} = 97.3 kPa)

Predicted CA50 from the model is compared with those of the experiment in Figure 5.11 and Figure 5.12 when ON is switched from 0 to 20. Transient response of the engine is shown for: only ON change in Figure 5.11; and simultaneous change of ON with Φ in Figure 5.12. For the experimental conditions tested a step change of 20 in fuel octane number at a constant Φ often violated knock/misfire limits of HCCI combustion. The combination of ON and Φ is expectant to achieve the desirable ignition timing and is shown in Figure 5.12.

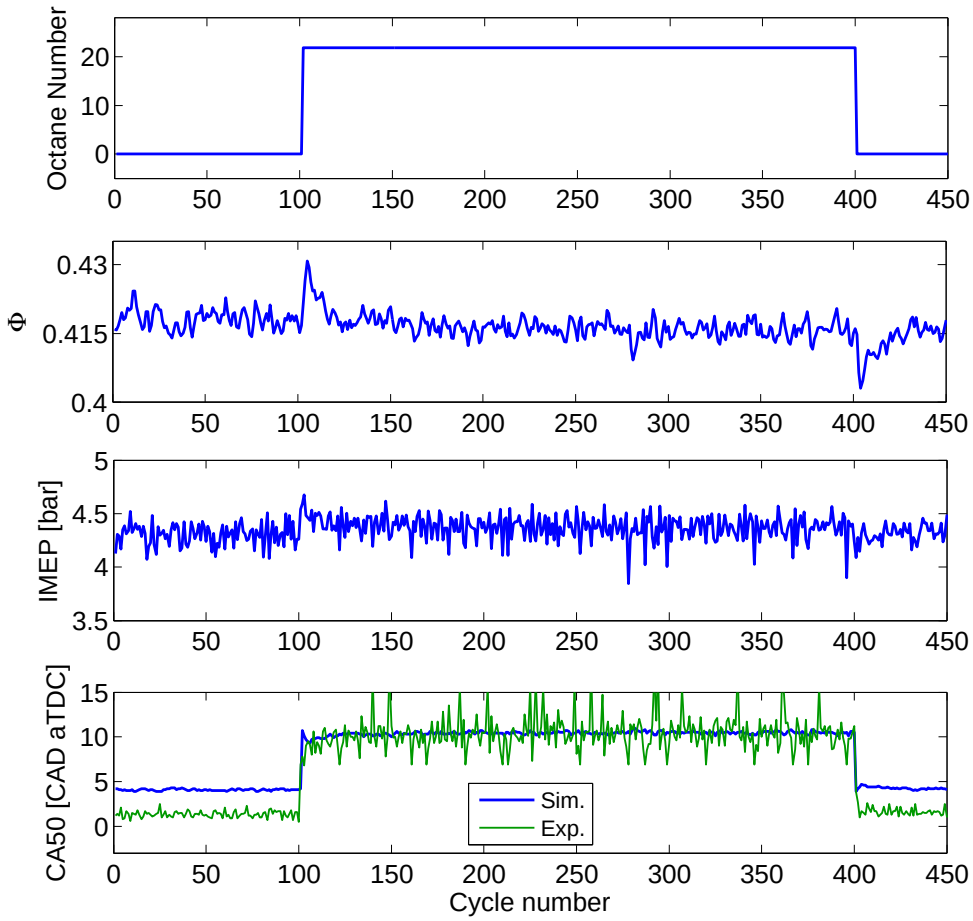

Figure 5.11: Octane number step: comparison between predicted and experimental cycle-to-cycle CA50. (P_m = 110 kPa, T_m = 91°C, $\Phi \cong 0.42$, EGR = 0%, P_{exh} = 99 kPa)

Predicted CA50 from the model is in good agreement with those of the experiments in Figures 5.10, 5.11, and 5.12 and the model captures the overall dynamic trend of changes and predicts CA50 within uncertainty of ±1.5 CAD to ±2.6 CAD from those of the experimental data. The trend of change in CA50 by increasing the equivalence ratio in Figure 5.10 is opposite to that in Figure 5.12. CA50 advances in Figure 5.10 but it retards in Figure 5.12 when the charge becomes richer. CA50 retards in Figure 5.12 as a result of increasing the octane number. This indicates that CA50 exhibits more dependance to the variation of octane number compared to that of Φ for the range indicated. Since predicted

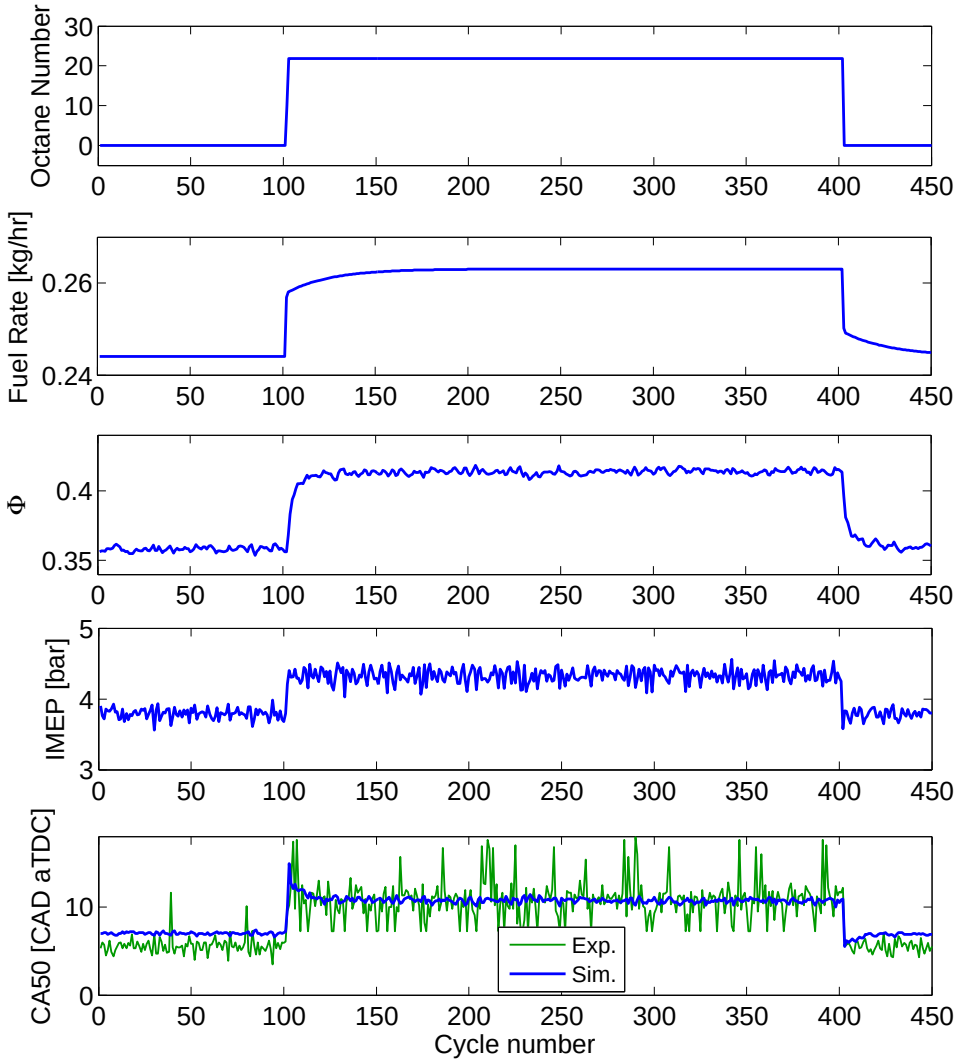

Figure 5.12: Octane number and equivalence ratio (Φ) step: comparison between predicted and experimental cycle-to-cycle CA50. (P_m = 110 kPa, T_m = 91°C, EGR = 0%, P_{exh} = 99 kPa)

CA50 from the model follows a trend similar to that of the experiment in Figure 5.12, this indicates that the model can capture the competing dynamics of simultaneous change of two different charge variables to affect the combustion timing.

5.5 SUMMARY

A dynamic full-cycle physics based Control Oriented Model (COM) has been developed that includes the fuel transport dynamics and thermal coupling between cycles through mass and thermal properties of residual gases. The model incorporates a combination of physical and empirical models to simulate an HCCI cycle in a sequence of valve events. Parameters of the model are determined by using a combination of system identification and optimization methods. To do this three different types of data are collected: experimental transient AFR excursions, steady-state HCCI experiments, and TKM simulations at an extensive range of operating conditions. Once the COM is parameterized it needs these seven inputs to predict HCCI ignition timing: intake manifold temperature, intake manifold pressure, EGR, engine speed, equivalence ratio, fuel injection pulse width, and pressure in the exhaust port. The COM predicts different ignition timing parameters such SOC, CA50, and EOC. However, the COM is mainly designed to predict CA50 as the best metric for HCCI ignition timing.

The COM is validated with rectangular fueling transient tests which are not used to parameterize the model. Transient change in equivalence ratio/octane number and simultaneous changing of equivalence ratio and octane number are used to test the model for HCCI in transient fueling conditions. The results indicate the COM can capture the main transient dynamics for both single and double (Φ and ON) transient fueling operations. CA50 predictions from the COM have an uncertainty of ± 2.6 CAD.

Results from this work indicate the COM is capable of simulating the key dynamics in HCCI ignition timing with sufficient accuracy for control applications. The model is computationally efficient with an average processing time of about 0.14 sec to simulate a whole HCCI cycle on a 2.22 GHz AMD 64 X2

Dual Processor. In addition, all inputs of the model can be readily measured or estimated on a real engine. These make the COM simple and fast enough for using in the synthesis of strategies for physics-based control of HCCI engines.

Chapter 6

Modeling the Distribution of HCCI Combustion Timing Ensemble[1]

Combustion timing for consecutive cycles at each operating point makes an ensemble of combustion timing which can exhibit different shapes of probability distributions depending on the random and physical patterns existing in the data. A combined physical-statistical control-oriented model is developed to predict the distribution of HCCI combustion timing for a range of operating conditions. The main output of the model is the Probability Density Function (PDF) metric of CA_{50} distribution. HCCI control can benefit from knowing PDF of CA_{50} ensemble in order to avoid the unstable HCCI operating regions which exhibit high cyclic variations.

In this chapter, after introducing the combustion timing ensemble and its application in HCCI, experimental data at 338 different operating conditions is examined to investigate the existence of a normal distribution in Ricardo HCCI data. Next a physical-statistical model is designed to predict PDF of CA_{50} ensemble and finally the resulting model is experimentally validated.

6.1 INTRODUCTION

Cyclic variation in HCCI combustion can occur with a variety of patterns depending on the physics occurring inside the cylinder and the pattern of charge

[1]The results of this chapter are partially based on [190] and [92].

variations [80, 73]. One method to understand these patterns is to analyze the ignition timing ensemble − formed by a large number of consecutive ignition timings. This ensemble exhibits various distribution shapes for different operating conditions. A sample of a CA_{50} ensemble distribution is shown in Figure 6.1 where the shape of the distribution about the mean is shown. For a normal distribution as in Figure 6.1, the mean CA_{50} ignition timing occurs with the highest probability. However, the CA_{50} ensemble of HCCI combustion is not usually normally distributed as will be discussed in this chapter and other possible distributions are studied. The CA_{50} distribution plot shows the dispersion level of the data (distance from the mean) and indicates the extremes of CA_{50} variations. In addition, skewness of the data and presence of multiple modes in the data

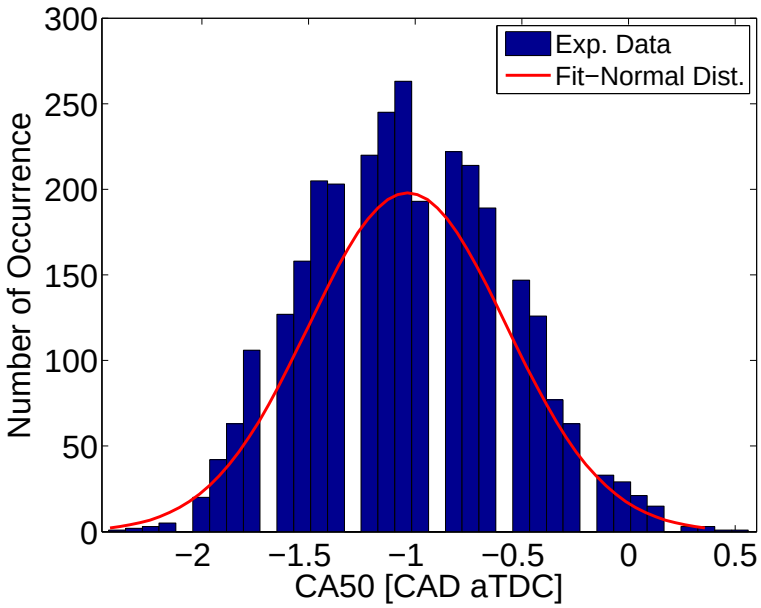

Figure 6.1: Histogram of CA_{50} distribution for a sample operating point. (Fuel= PRF0, N= 1000 rpm, Φ= 0.33, EGR= 0%, T_m= 145 ^oC, P_m= 132 kPa.)

can be found by examining the distribution plot of sampled data [191]. Knowledge of the CA_{50} distribution can provide valuable information to find high cyclic variation operating regions for HCCI engines. In addition, having specific infor-

mation about the shape of distribution could be of utility for designing a HCCI combustion controller.

Only a few studies [80, 89, 87] in the literature have investigated cyclic variations of ignition timing in HCCI engines. However, none of these researches have studied the distribution shape of HCCI ignition timing. This study examines the distribution shapes of HCCI ignition timing at steady-state conditions for an HCCI engine. A model is developed to predict PDF of CA_{50} ensemble for a range of HCCI operating conditions. The PDF explains the occurrence probability associated with every crank angle in CA_{50} ensemble.

6.2 NORMAL DISTRIBUTION ANALYSIS

A novel approach for analyzing the cycle to cycle combustion timing is using statistical methods. The population of consecutive ignitions at a constant operating point can be used to form a probability distribution for cycle-to-cycle combustion timing. Normal distribution is the most common probability distribution used to characterize experimental data [191]. Experimental data at 338[2] different points collected from the Ricardo engine are analyzed to determine which conditions have a normal distribution for CA_{50}. Two common testing methods for normal distributions are used. The first method is the *Lilliefors* test that evaluates the input data and returns the result of the hypothesis test for the goodness of fit to the normal distribution [193]. The second method is the *Kolmogorov-Smirnov* test that compares the values in the data with a standard normal distribution and checks the hypothesis that the data has a standard normal distribution [193]. These two methods are applied on the CA_{50} data sets from 338 points. Points that

[2]This includes 329 experimental data points from Section 2.2.2 and 9 new data points from [192].

successfully pass these two tests are then visually evaluated with normal probability plot. The normal probability plot is a graphical tool to assess whether or not a data set follows a pattern of a normal distribution [191]. Data from the experimental points are plotted against a theoretical normal distribution and if data is normally distributed, it forms an approximate straight line. The level of departures from normality is judged by how far the points vary from the straight line. Figure 6.2 shows a normal probability plot for a sample experimental point that exhibits a normal distribution. CA_{50} data sets for all experimental points are processed using the procedure mentioned above and 19 points out of 338 points are judged to have a normal distribution. The range of ignition timing parameters for cases with normal distribution are compared with those of the whole data set in Table 6.1.

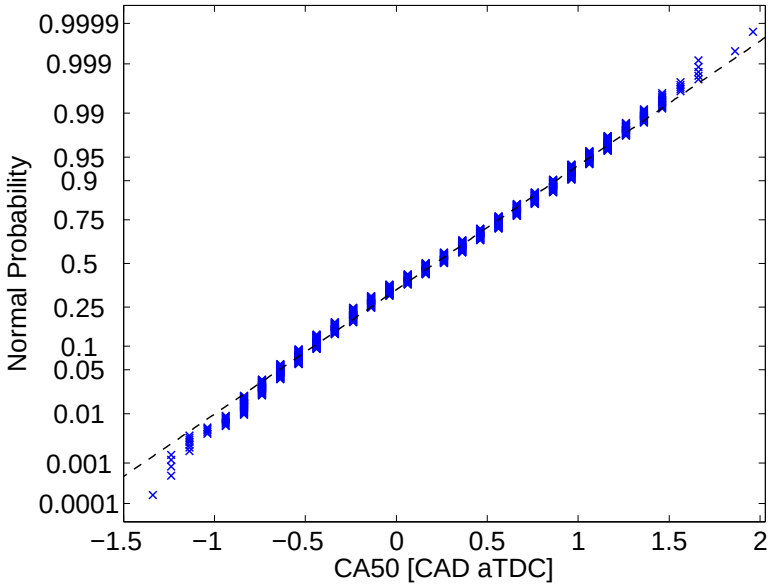

Figure 6.2: Sample normal probability plot. (Operating condition is the same as that in Figure 6.1.)

Table 6.1 shows that normal distribution of CA_{50} is more likely to occur in HCCI ignitions occurring for a window immediately after TDC ($0.8 \leq$ SOC $\leq$7.7 CAD aTDC). In those conditions, cyclic variations of CA_{50} is typically low

($0.5 \leq \ STD_{CA50} \leq$1.4 CAD) and the burn duration is short ($2.5 \leq$ BD $\leq$ 4.3 CAD). A large deviation from the straight line is observed in normal probability plots of the operating points which have mean CA_{50} occurring after 15 CAD aTDC.

Table 6.1: Comparing the range of ignition timing parameters for cases with Normal Distribution (ND) with those from the whole 338 HCCI experiments.

Parameter	**SOC**	**CA_{50}**	**BD**	**$STD_{CA_{50}}$**
Whole Exp. Data	-4.6 $\rightarrow$ 21.9	1.8 $\rightarrow$ 24.9	2.4 $\rightarrow$ 13.1	0.4 $\rightarrow$ 4.4
ND cases	0.8 $\rightarrow$ 7.7	4.5 $\rightarrow$ 11.5	2.5 $\rightarrow$ 4.3	0.5 $\rightarrow$ 1.4

Furthermore, all the 19 test points are for fully warmed up conditions and none of the points which have low coolant temperature show a normal distribution for CA_{50}. No direct preference for normal distribution is seen in operating conditions in terms of octane number, engine speed, equivalence ratio and intake conditions. However, a combination of these conditions determine the location of SOC.

6.3 HCCI ENSEMBLE DISTRIBUTION MODEL

An HCCI combustion model incorporating a combination of physical and statistical models to predict probability distribution function of CA_{50} ensemble is proposed. The physical model predicts the mean value and the Standard Deviation (STD) of CA_{50} and the statistical model predicts the shape of probability distribution of CA_{50} ensemble. The structure of the model is illustrated in Figure 6.3. The physical model has two main parts: *Combustion Model* (I-III) and *Ignition Timing Dispersion Model* (IV). Outputs from the physical model are given to a statistical model (V) to determine the probability distribution of CA_{50} ensemble. Inputs of the resulting model are intake manifold pressure, intake manifold temperature, EGR rate, equivalence ratio and engine speed. Using these inputs, the

model's output is probability distribution functions of the CA_{50} ensemble in the forms of PDF or Cumulative Distribution Functions (CDF).

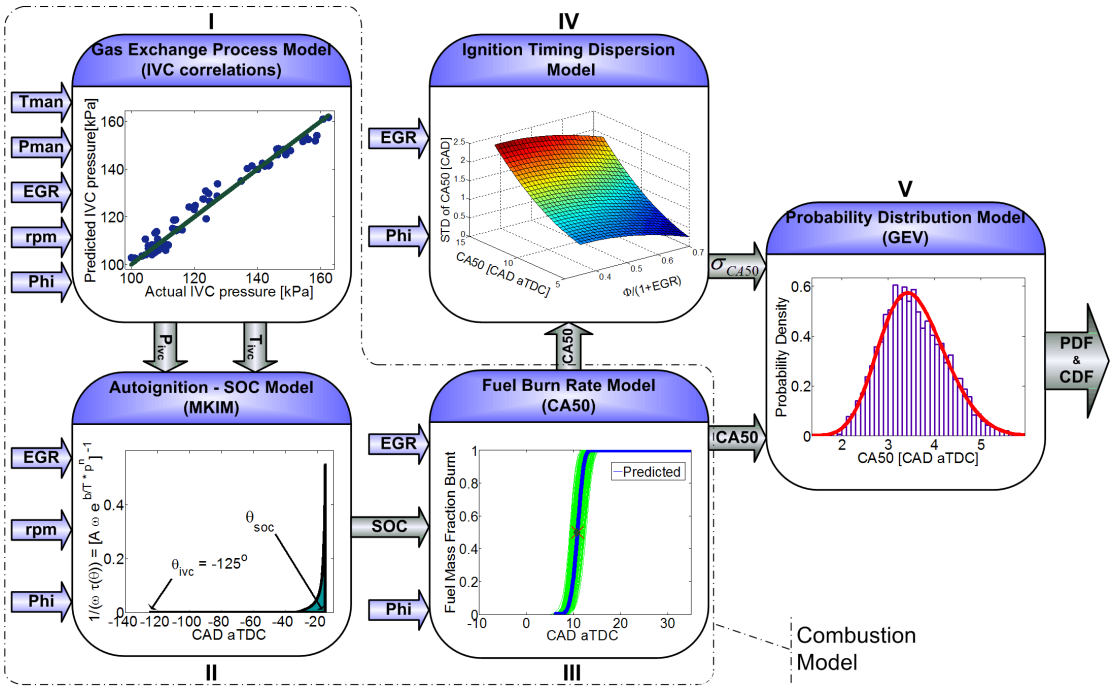

Figure 6.3: Schematic of the model.

The Mean-value HCCI model from Chapter 4 is used as the *Combustion Model* to predict CA_{50}. The two other submodels shown as blocks IV and V in Figure 6.3 are detailed below:

6.3.1 Ignition Timing Dispersion Model (Block IV)

Experimental results in Chapter 2 indicate that HCCI combustion exhibits different levels of cyclic variation depending on an engine's operating condition. HCCI cyclic variations highly depend on the location of ignition timing and HCCI ignitions close to TDC are more likely to have low cyclic variations compared to the late ignitions. In this study HCCI ignition timing (CA_{50}) was always after TDC.

STD is the square root of the second central moment of sampled data set and

is a common measure of cyclic variability for crank angle based parameters like CA_{50} [75, 109, 110]. Here, an empirical correlation is used to estimate the STD of CA_{50} ($\sigma_{CA_{50}}$) for a given operating condition. The experimental data is used to find an empirical correlation that predicts $\sigma_{CA_{50}}$ with the inputs that can be measured real-time on an engine. The following correlation is found to work well on the available data:

$$\sigma_{CA_{50}} = A_D + B_D \,.\, CA_{50}^2 \ln(CA_{50}) + C_D \,.\, D_f \ln(D_f) \qquad (6.1)$$
$$where,\ D_f = \frac{\phi}{1 + EGR}$$

D_f represents the dilution factor and A_D, B_D, and C_D are the dispersion constants that need to be determined. Equation (6.1) is parameterized using about 35% of the experimental data − see Table 4.5. This yields A_D= - 1.076, B_D= 0.003 and C_D= −4.768. The resulting correlation is cross-validated by all the experimental data points listed in Table 4.5. An uncertainty analysis for predicting $\sigma_{CA_{50}}$ indicates an uncertainty of ±0.8 CAD.

CA_{50} , ϕ, and EGR rate are the three variables used in correlation (6.1) because they have the highest influence on $\sigma_{CA_{50}}$ for an HCCI engine operating at fully warmed-up conditions. Simulated $\sigma_{CA_{50}}$ over a range of engine variables for the Ricardo engine is shown in Figure 6.4. $\sigma_{CA_{50}}$ increases with: decreasing equivalence ratio or increasing EGR rate. In addition, correlation (6.1) predicts that $\sigma_{CA_{50}}$ increases when CA_{50} is further retarded for late ignitions. Results from experimental studies [80, 73] for the Ricardo engine confirm these simulation results. $\sigma_{CA_{50}}$ is more sensitive to the location of CA_{50} in Figure 6.4 compared to the ϕ-EGR ratio. Intake pressure, intake temperature, and fuel octane number are the other engine variables that changed causing CA_{50} to vary at fixed ϕ and

EGR rate.

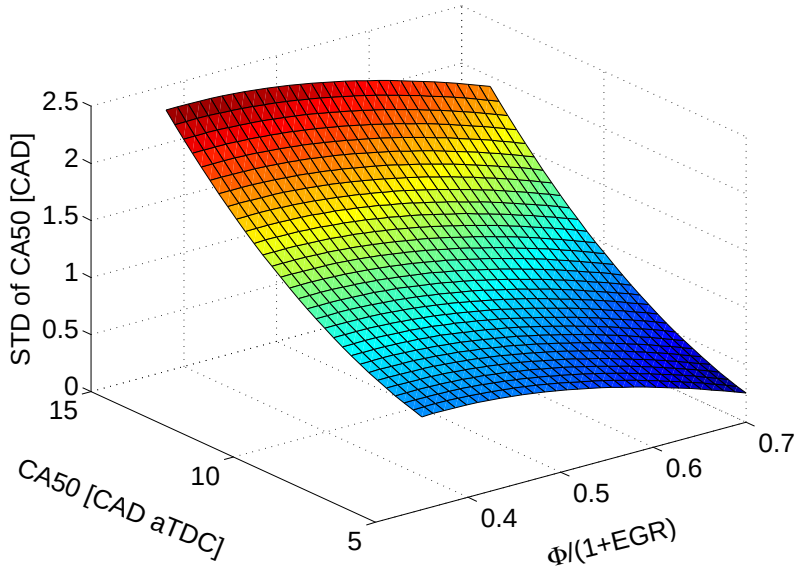

Figure 6.4: Simulated standard deviation of CA_{50} using equation (6.1) for HCCI operation range in Table 4.5.

6.3.2 Probability Distribution Model (Block V)

Mean and STD of CA_{50} are valuable metrics for normal distributions, but they are not enough to characterize the distribution shape if the distribution of CA_{50} ensemble is not normal. Experimental results from Section 6.2 on the Ricardo engine show that a normal distribution is observed in only less than 1% of the 338 collected data points for a range of HCCI operating conditions.

The population of consecutive ignitions for a constant operating point can be used to form a probability distribution for CA_{50} ensemble. A normal distribution is widely used to characterize experimental data[191]. The normal probability plot depicts the shape and pattern of deviation from the normal distribution (e.g. it shows if the data is skewed or has short/long tails). Here, normal probability plot is only used to indicate the shape of deviation from normal distribution by

varying engine conditions and more detailed analysis of the data is done by using PDF and CDF plots.

The normal probability plots obtained at misfire limit (Fig. 6.5-a) and knock limit (Fig. 6.5-b) by varying intake manifold temperature show a significant difference. The large deviation from the normal distribution near the misfire vicinity decreases substantially at knock vicinity. Assuming a normal distribution for the random component of the data, deviations from a normal distribution are indicative of deterministic component in the data [191]. This suggests more deterministic patterns in the data at misfire limit compared to that of the knock limit in Figure 6.5. This observation is consistent with the results in a previous study [192] which uses chaotic methods to characterize CA_{50} ensembles from the Ricardo engine. Having more deterministic patterns near the misfire limit might be explained by the experimental observations in [80, 73]. These experimental studies indicate that in the misfire operating conditions there is a high possibility that a weak misfired cycle is followed by a strong cycle. This coupling between consecutive ignition timings causes deterministic structure. In addition, misfire points occur at later crank angles compared to the points in the knock limit. This exposes the combustion to more physical sources of cycle variations such as higher thermal stratifications for later ignitions and increased sensitivity to the fluctuations of the charge temperature when the combustion is retarded [75, 111]. Retarded ignition for misfire points is also evident in Figure 6.5 where mean CA_{50} in Fig. 6.5-a is over 10 CAD retarded compared to that of Fig. 6.5-b (knock limit). Results from [192] also show that the ignitions with normal distribution had CA_{50} close to TDC and they never occur at late ignitions ($CA_{50} > 12$ CAD aTDC). In addition, points at the knock limit have typically strong combustion and they exhibit less variation between cycles [80]. This is also evident in Figure 6.5 where the range of CA_{50} variation in Fig. 6.5-a

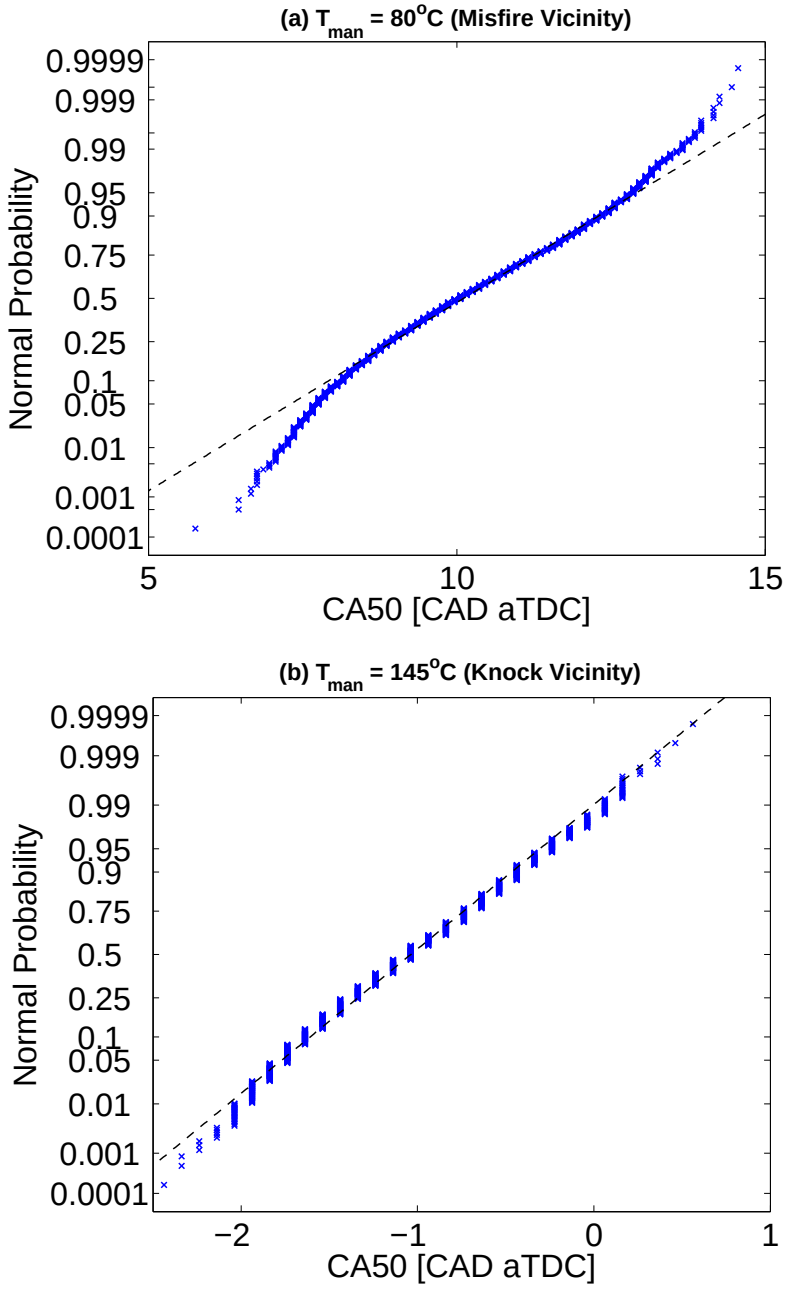

Figure 6.5: Normal probability plot: moving from misfire limit to knock limit by varying the intake temperature with the base operating conditions of PRF0, N= 1000 rpm, Φ= 0.33, EGR= 0%, P_m= 132 kPa. (Data point (b) is the same as that in Figure 6.1.)

is almost three times larger than that of the knocking point in Fig. 6.5-b. This can be because physical sources of cyclic variation [80] are not strong enough

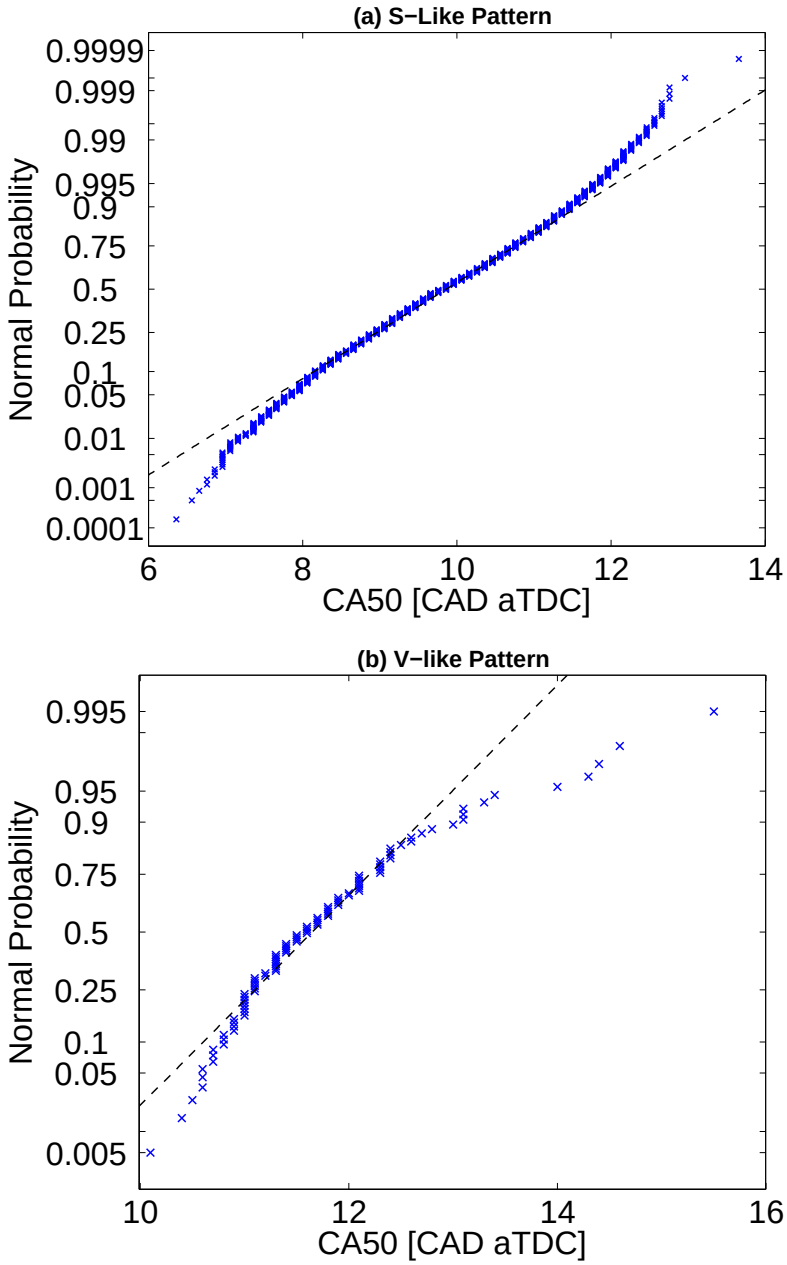

Figure 6.6: Two main common normal probability patterns observed in unknocking data points. (Data point (a): EGR = 16%, $\Phi = 0.39$, $T_m = 114$ ^{o}C, $P_m = 133$ kPa; Data point (b): EGR = 21%, $\Phi = 0.79$, $T_m = 80$ C, $P_m = 92$ kPa.)

to affect CA_{50} significantly for the points at the knock limit, but for the weak ignitions at the misfire limit any small source of cyclic variation is strong enough to influence cyclic variation of CA_{50}.

CA_{50} data sets for over 200 experimental points described in Table 4.5 are studied to observe variations in normal probability plots. Points close to knock limit usually show the minimum deviation from the straight line in the normal probability plot, but the majority of the other points particularly those in the vicinity of misfire limit have either a S-like pattern or a V-like pattern shown in Figure 6.6. In both patterns, plots show a reasonable straight pattern in the center of the data. But the deviation from the straight line is intensified at the tails of the data set in both patterns. The S-like pattern shows increasing marked departure above the reference line for CA50's higher than the mean CA_{50}. In an opposite trend, the V-like pattern shows the departure trend below the reference line. If these patterns are predicted, they can be used to find the distribution shape of CA_{50} ensemble at different operating conditions.

Sixteen different common distribution models [193] are studied. Figures 6.7 and 6.8 show the four distribution models that produce best fitting results for normal probability and PDF plots. These figures indicate Generalized Extreme Value (GEV) distribution generates the best agreement between simulated and experimental distributions for both S-pattern and V-pattern distributions. This is also confirmed using maximum likelihood criteria [194].

The GEV distribution provides a continuous range of shapes by combining three simpler distributions into a single form. The probability density function for this model is based on three main parameters including a location parameter (mean), a scale parameter (standard deviation), and a shape parameter. The

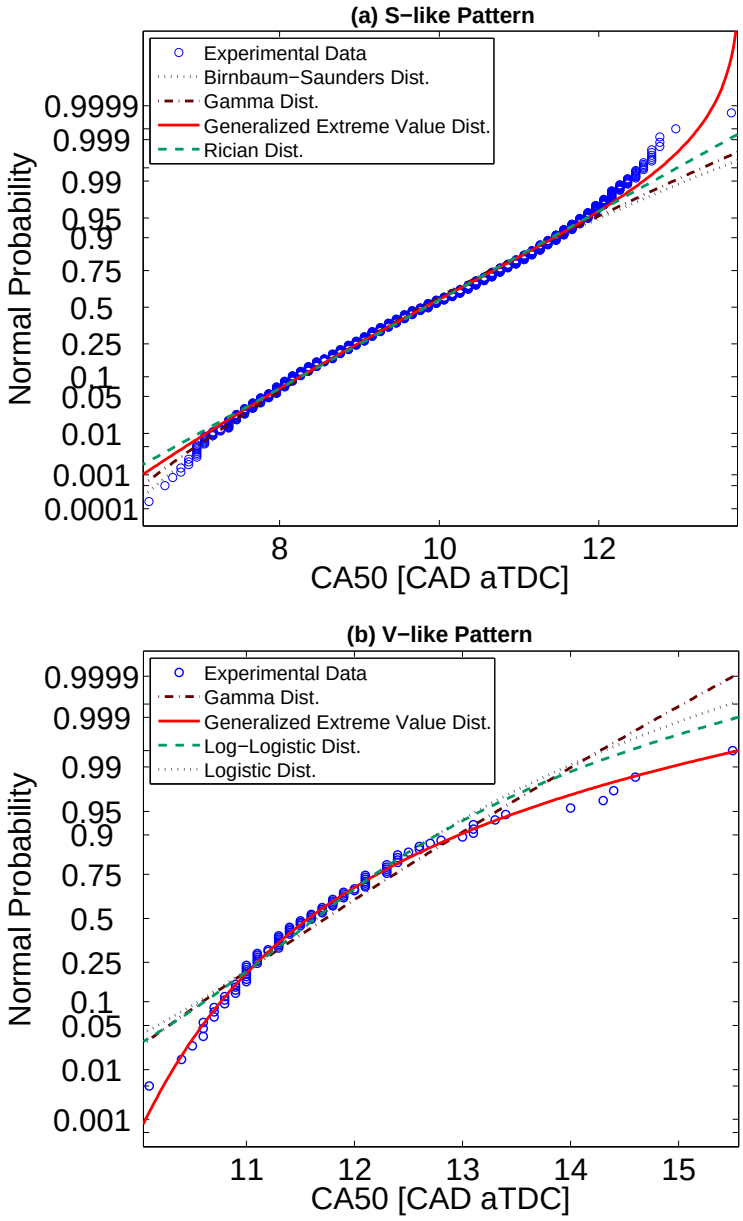

Figure 6.7: Fitted distribution models for the normal probability plot. Operating conditions are the same as those in Figure 6.6.

probability density function for the GEV distribution is given by [194]:

$$P(x) = \begin{cases} \frac{1}{\sigma} \exp\left[-\left[1-k\frac{(x-\mu)}{\sigma}\right]^{\frac{1}{k}}\right]\left[1-k\frac{(x-\mu)}{\sigma}\right]^{\frac{1}{k-1}} & (a) \\ \\ \frac{1}{\sigma}\exp\left[-\exp\left(\frac{\mu-x}{\sigma}\right)\right]\exp\left(\frac{\mu-x}{\sigma}\right), \quad k=0 & (b) \end{cases} \tag{6.2}$$

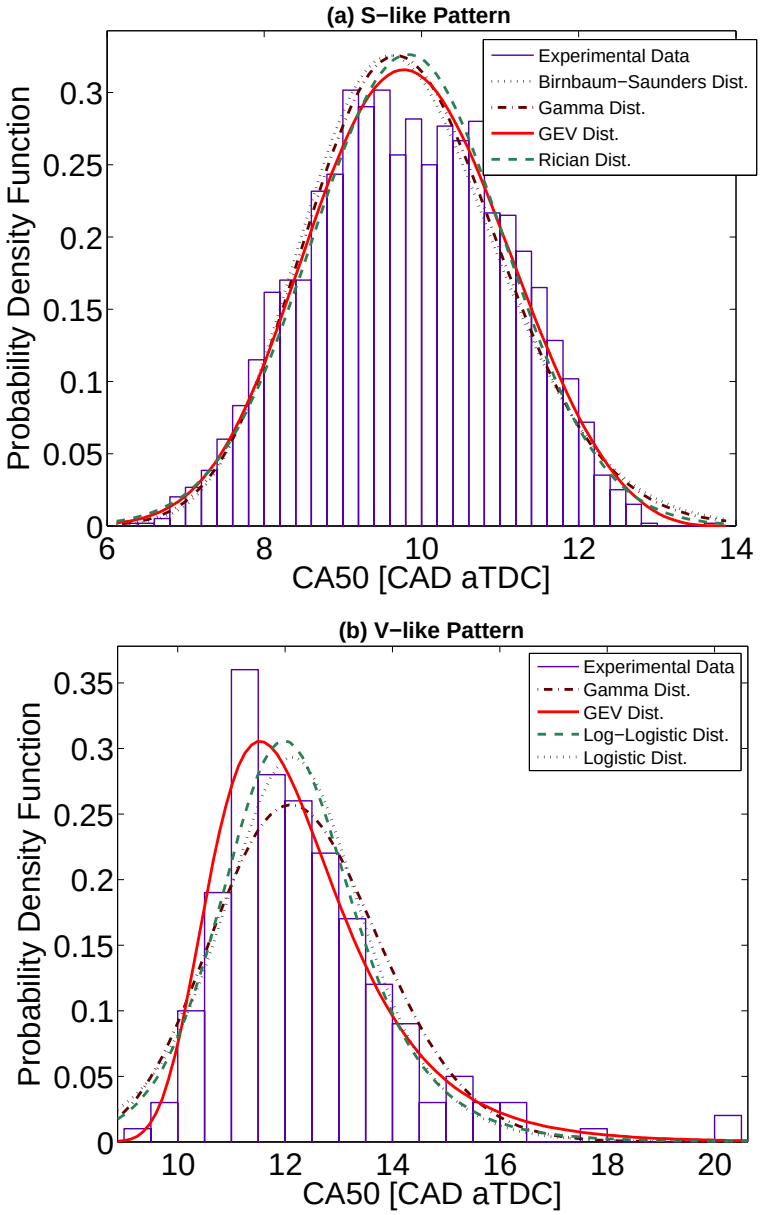

Figure 6.8: Fitted distribution models for the PDF plot. Operating conditions are the same as those in Figure 6.7.

where, μ is a location parameter σ and k are a scale parameter and a shape

parameter respectively. The CDF for the GEV distribution is [194]:

$$F(x) = \begin{cases} \exp\left[-\left[1-k\left(\frac{x-\mu}{\sigma}\right)\right]^{\frac{1}{k}}\right], \quad 1-k\left(\frac{x-\mu}{\sigma}\right) \geq 0 \quad (a) \\ \\ \exp\left[-\exp\left(\frac{x-\mu}{\sigma}\right)\right], \qquad\qquad k=0 \qquad\qquad (b) \end{cases} \tag{6.3}$$

For each x (CA_{50}) in equation (6.3), CDF indicates the probability of CA_{50} taking on values less than or equal to a particular CA_{50}. More details about GEV distribution can be found in [195, 196].

The mean of CA_{50} is used as the location parameter and STD of CA_{50} ensemble is chosen as the scale parameter. Mean CA_{50} is taken from *Combustion Model* and STD of CA_{50} is provided by *Ignition Timing Dispersion Model*. The shape parameter k is selected -0.33 using the results from applying the methods of distribution fitting [193].

6.3.3 Experimental Validation

The five sub-models in Figure 6.3 are linked together to generate a model which predicts both mean CA_{50} and the distribution shape of CA_{50} ensemble. Experimental data from Ricardo engine is used to validate the model. To characterize the distribution shape of CA_{50} ensemble the PDF and the CDF are the outputs of the model. Predicted PDF and CDF from the model are compared with those of the experiments in Figures 6.9 and 6.10. The two sample operating points in these figures use different fuels and they have not been used to parameterize the model. Predicted probability distributions in Figures 6.9 and 6.10 are consistent with those of the experimental measurements. The uncertainty of predictions in Figure 6.10 is determined ± 0.04. The model captures the main trend of variation in CA_{50} probability values. However, a discrepancy between the simulation and the experiment is observed at the minimum and maximum of CA_{50} ensemble in

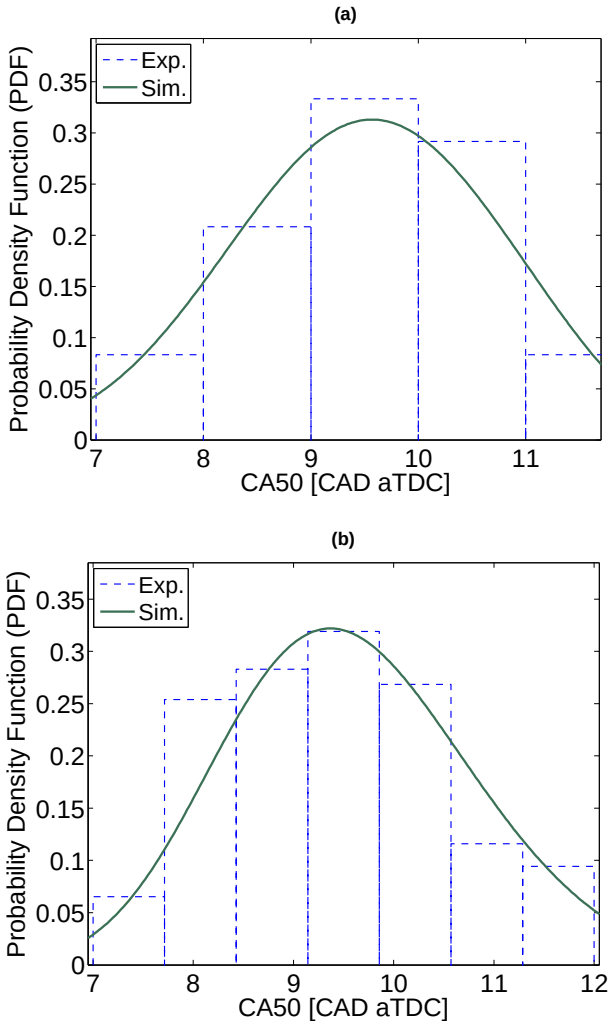

Figure 6.9: Empirical and predicted probability density function in two different conditions operated with different fuels. (Data point (a): Fuel= PRF10, N= 800 rpm, $\Phi = 0.48$, EGR = 1%, $T_m = 120$ C, $P_m = 93$ kPa - point #65 in Figure 4.5-a; Data point (b): Fuel= PRF40, N= 810 rpm, $\Phi = 0.52$, EGR = 0%, $T_m = 116$ C, $P_m = 111$ kPa - point #45 in Figure 4.5-b.)

CDF plots. This might be due to not recording enough number of cycles for the experimental CA_{50} ensemble. The chance for letting all potential crank angles appear in a CA_{50} ensemble generally increases by recording a higher number of consecutive cycles at each test point.

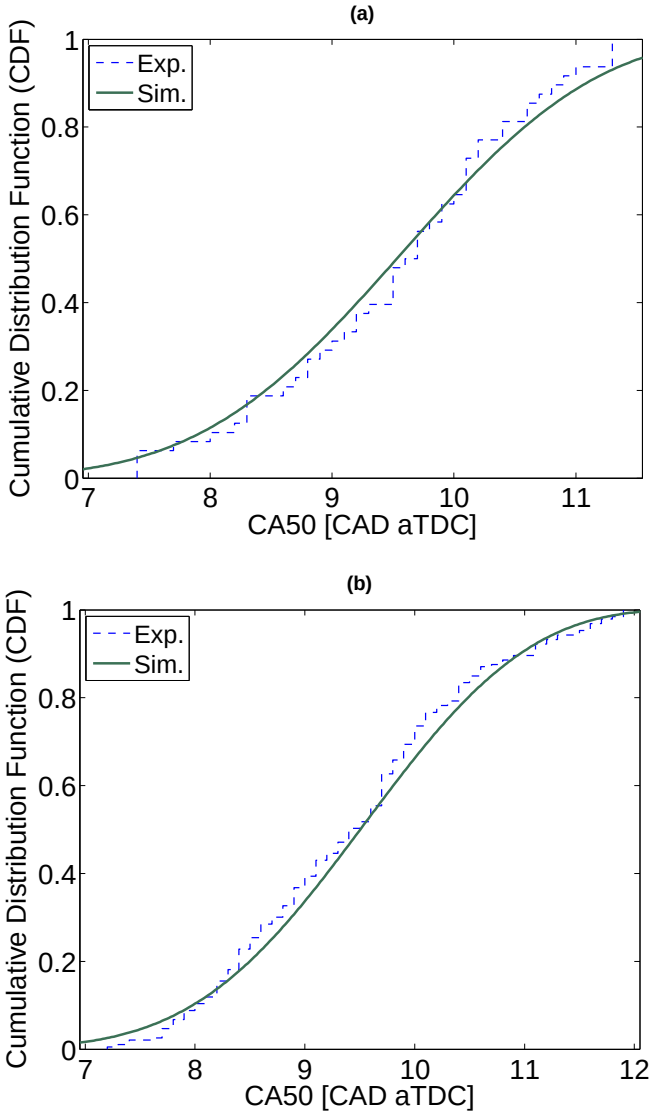

Figure 6.10: Empirical and predicted cumulative distribution function for the operating points in Figure 6.9.

6.3.4 Predicting Ranges of Cyclic Variation

Predicting ranges of ignition timing cyclic variability is useful for determining HCCI operating regions which have high cyclic variability. The developed model is used to determine ranges of CA_{50} cyclic variability at different HCCI operating conditions. Predicted contours of $STD_{CA_{50}}$ versus variations of intake manifold pressure and equivalence ratio are shown in Figures 6.11-6.12 for PRF0 and

PRF40 fuels.

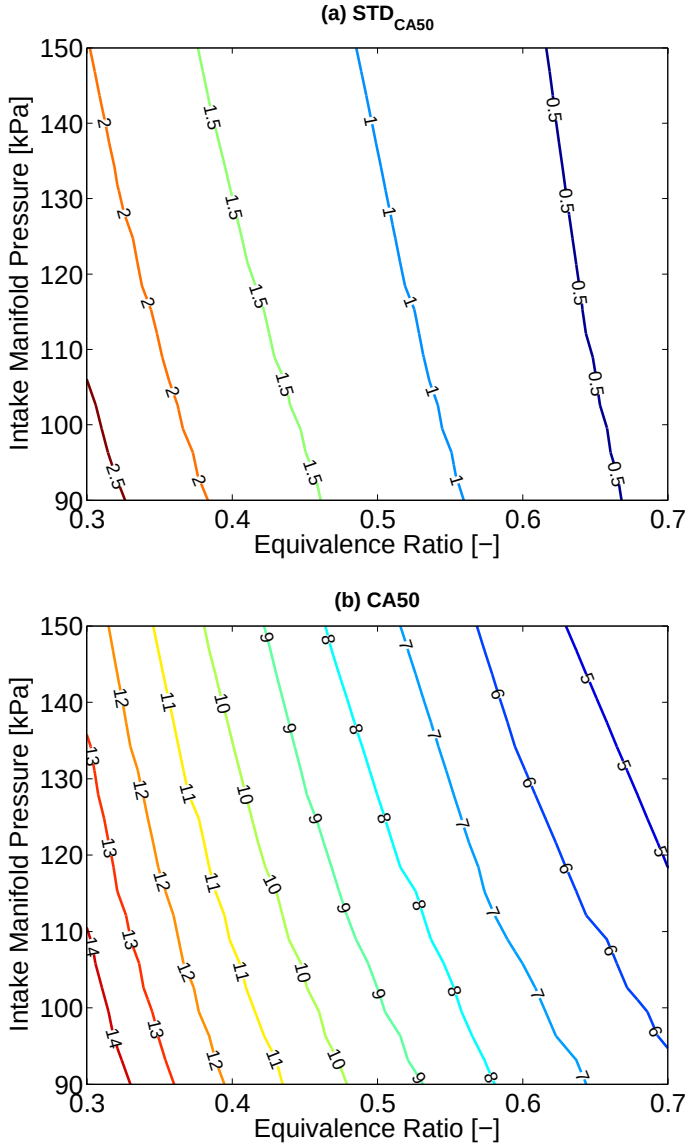

Figure 6.11: Predicted CA_{50} and STD of CA_{50} for HCCI operation with PRF0 fuel. (N= 800 rpm, T_m= 50 ^oC, EGR= 0%)

The experimental results in Section 2.2.3.3 indicate that the data points with a $STD_{CA_{50}}$ higher than 1.7 CAD are located outside of the desirable HCCI region-I (which is characterized by low cyclic variation and correlated ignition timing metrics). Thus the HCCI operating region that result in an HCCI combustion with a low cyclic variability are easily determined in Figures 6.11-6.12. A higher

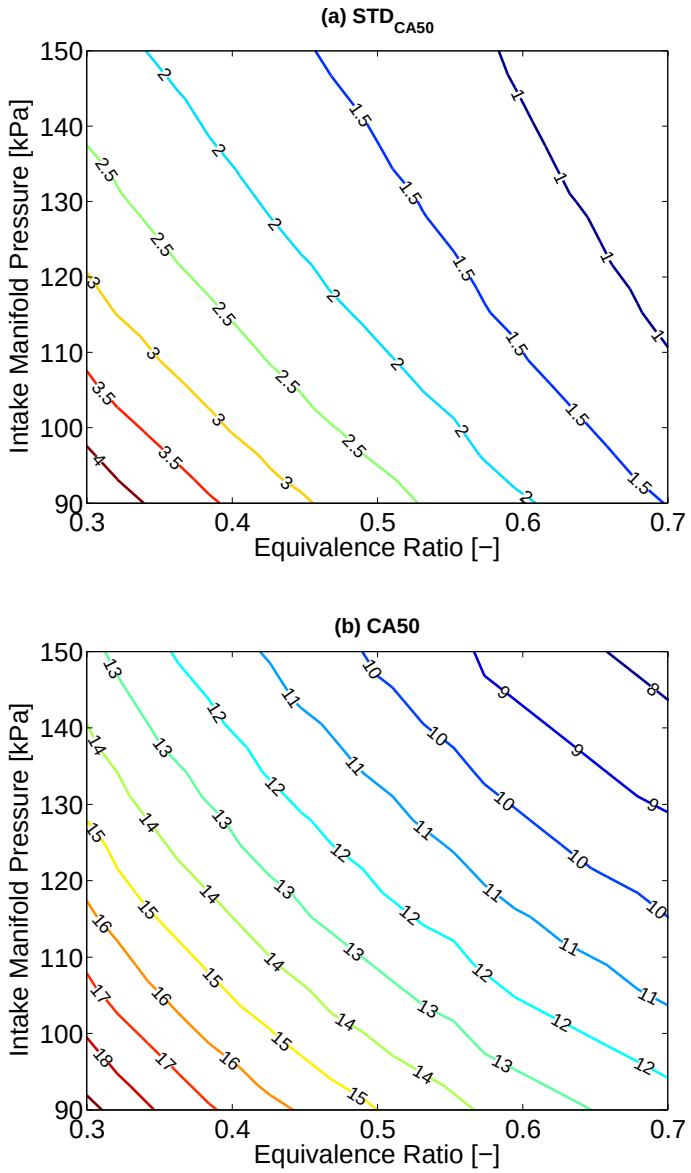

Figure 6.12: Predicted CA_{50} and STD of CA_{50} for HCCI operation with PRF40 fuel. (N= 800 rpm, T_m= 50 ^oC, EGR= 0%)

cyclic variation of CA_{50} is observed in Figures 6.11-6.12 for operating conditions with leaner mixtures at lower intake pressures. In addition, the low cyclic variation region is larger in Figure 6.11-a compared to that of Figure 6.12-a. This is attributed to a more delayed CA_{50} at the higher octane number – as seen by comparing CA_{50} in Figure 6.11-b with that of Figure 6.12-b.

6.4 SUMMARY

Experimental data at a large number of operating conditions are used to study the shapes of CA_{50} distribution for an HCCI engine. A model based on this experimental data is developed to predict the shape of CA_{50} probability distributions. The results show that different patterns such as straight, V-like and S-like can occur in normal probability plots depending on the HCCI operating conditions. HCCI ignitions occurring immediately after TDC are more likely to have normal distribution. Normal distributions have a higher tendency to appear in the points at the knock vicinity while misfire operating points have the highest deviation from the normal distribution. GEV distribution seems promising to cover the range of distribution shapes observed for CA_{50} ensembles.

The proposed model embodies different components obtained from physical and statistical studies of ignition timing in HCCI engines. The model requires intake manifold pressure, intake manifold temperature, EGR rate, equivalence ratio and engine speed in order to predict PDF and CDF of CA_{50} distribution. The results of validating the model with experimental data show predictions of PDF / CDF follow the experimental trends with a good agreement for the two different PRF fuels tested. Finally, the resulting model is utilized to predict HCCI operating regions which have high combustion cyclic variability.

Chapter 7

Conclusions and Future Work

Experimental and simulation study has been conducted to characterize HCCI ignition timing and develop a useful physic-based model for control applications. Major results and contributions from this thesis are summarized in this chapter and recommendations for further work are outlined.

7.1 CONCLUSIONS

The analysis of the results in this study leads to the following findings and conclusions:

7.1.1 Experimental Study of HCCI

- Cyclic variations of HCCI engines can be very large under certain operating conditions. The dynamic of charge cyclic variation and the physics occurring inside the cylinder influence HCCI cyclic variation. Three distinct patterns of cyclic variation for the SOC, combustion peak pressure, and IMEP are observed. These patterns are normal cyclic variations, periodic cyclic variations and cyclic variations with weak/misfired ignitions. For providing stable HCCI operation, the combustion controller should remove periodic and misfired oscillation patterns and the magnitude of variation in the normal pattern should be maintained low.

  The location of SOC plays an important role on cyclic variations of HCCI

combustion with less variation observed when SOC occurs immediately after TDC. The most stable operating region is found to be where SOC occurs in an 5 degree window, between 0 – 5 CAD aTDC. Higher levels of cyclic variations are observed in the main (second) stage of HCCI combustion compared to that of the first stage for the PRF fuels studied. The sensitivity of SOC to different charge properties varies. Cyclic variation of SOC increases with an increase in EGR rate, but it decreases with an increase in equivalence ratio, intake manifold temperature and coolant temperature.

Five regions are recognized to exhibit different interrelations between cyclic variation of SOC and BD. Each of these regions requires a different control approach to minimize both cyclic variations of SOC and BD. Control of SOC might suffice for controlling both SOC and BD cyclic variation in region-I which has low SOC cyclic variation, but this approach is less successful for region-IV and region-V which include partial burning or misfiring points.

- For the 340 HCCI conditions tested, a significant number have an exhaust gas temperature below 300 °C which is below the light-off temperature of typical catalytic converters in the market. The low exhaust gas temperature in certain operating conditions can limit the operating range in HCCI engines. Three different categories of engine variables are recognized and classified by how the exhaust temperature is affected by changing that variable. The first category is defined as primary variables (e.g. intake pressure and fuel octane number) for which location of ignition timing is the dominant factor to influence exhaust temperature. The other groups include compounding variables like engine speed, and opposing variables like intake temperature, coolant temperature and equivalence ratio. For these

two groups, in addition to the main factor of ignition timing, exhaust temperature is influenced by other secondary factors like heat loss, energy input air, energy input fuel, and burn duration. Energy input fuel is found the most influential secondary factor on HCCI exhaust temperature.

- The exhaust gas temperature in the HCCI mode differs significantly from that of the SI mode. For the same engine load, a substantially higher exhaust temperature is observed in SI mode compared to that of HCCI mode – this is primarily caused by higher fuel energy content in SI mode. Unlike SI engines where engine load is a main factor for determining exhaust temperature, the exhaust temperature in HCCI is not strongly dependant on engine load. Opposite to the SI mode, exhaust temperature in HCCI mode increases by decreasing the intake pressure at a constant equivalence ratio.

- Experimental study of the shape of probability distributions for HCCI ignition timing ensemble results in different patterns of straight, V-like and S-like in normal probability plots depending on the HCCI operating conditions. The straight pattern is more likely to occur in the points at the knock vicinity and V-like and S-like patterns have more tendency to appear in the operating points at the misfire vicinity.

7.1.2 Modeling of HCCI Ignition Timing

- A Thermo-Kinetic Model (TKM) for primary reference fuels has been extended and validated for predicting the auto-ignition in an HCCI engine. The TKM is able to predict the SOC with an uncertainty of ± 1.0 CAD over a range of HCCI operating conditions. Results of sensitivity analysis from using the TKM indicate the HCCI combustion timing exhibits different levels of sensitivity to the charge properties depending on the location

of SOC. SOC is the most sensitive to the charge temperature variations and Φ variations for late ignitions, but a lower level of sensitivity in SOC with varying Φ is observed for an early ignition.

- A dynamic physics based Control Oriented Model (COM) having HCCI combustion timing (CA_{50}) as the output has been developed. The model captures key HCCI dynamics and can be used for both steady-state and transient HCCI operations. The COM has been cross validated with transient and steady-state experimental measurements. The uncertainty in the model predictions is ± 2.6 CAD. The average processing time of COM is about 0.14 sec to simulate a whole HCCI cycle on a 2.22 GHz AMD 64 X2 dual processor. The seven inputs of the model are: engine speed, intake manifold pressure, intake manifold temperature, EGR rate, equivalence ratio, exhaust pressure and amount of fuel injected. All of these inputs can be easily measured or estimated on an engine. Low computation time, a simple structure, and inputs that are easily measurable make the COM promising to use to design and implement an HCCI combustion controller.

- Generalized Extreme Value (GEV) distribution is found to cover the range of distribution shapes observed in combustion timing ensembles at different HCCI operating conditions. An HCCI ensemble distribution model has been developed to predict PDF / CDF of CA_{50} ensemble for an HCCI engine. The model incorporates the GEV statistical model in combination with an empirical ignition timing dispersion model and a mean-value combustion model. The resulting model has been validated with experimental data and predicted CDF from the model has an uncertainty of ± 0.04.

- An empirical correlation has been developed to predict HCCI exhaust temperature variations for constant engine speed and coolant temperature con-

ditions. The correlation incorporates three input parameters: specific energy input fuel (magnitude parameter), CA_{50} (location parameter) and burn duration (dispersion parameter). The correlation has been validated with experimental measurements and the comparison results show an uncertainty of $\pm 25\,^{\circ}\mathrm{C}$ in model predictions for 304 steady-state HCCI operating points tested.

7.2 MAJOR THESIS CONTRIBUTIONS

The major contributions of this thesis are outlined below:

- investigated cyclic variation of HCCI ignition timing; identified cyclic variation patterns as well as regions with distinct cyclic variation properties; characterized the factors influencing HCCI cyclic variation;
- determined the main influential parameters on HCCI exhaust temperature; illustrated the necessity to control both ignition timing and exhaust temperature to extend HCCI operating range; identified the differences between the properties of HCCI and SI exhaust temperatures which is critical for HCCI-SI mode switching;
- studied the probability distributions of HCCI ignition timing ensemble; used the information from ignition timing ensemble to determine regions with high cyclic variation in HCCI operating range;
- developed and validated a full-cycle physics based control oriented model to predict HCCI ignition timing for both steady-state and transient operations.

7.3 FUTURE WORK

The COM and HCCI ensemble distribution model in this work are useful tools for both understanding HCCI combustion and future HCCI control applications.

However, there are still many avenues that could be further pursued to improve the quality of modeling and to take further steps to implement the results from this work.

7.3.1 Further Improving the HCCI Modeling

- The COM could be improved by including the thermal transient dynamics for the conditions with variable coolant temperatures. This would enable the COM to work for cold start and warmup conditions.

- The gas exchange model could be modified with a more detailed model for the residual affected HCCI. This would help the COM to work for variable valve timing conditions, so that the COM could be applied to design the HCCI controller which uses a VVT actuator such as [197].

- Predictions from the COM do not capture some of the large cyclic experimentally observed fluctuations in the late HCCI cycles. Incorporating the dynamics/cyclic pattern for the points close to partially burn/misfire limit could improve the accuracy of the model.

- The HCCI ensemble distribution model could be used to find high cyclic variation operating regions. This information could help to predict the misfire/partial burn limit of the HCCI engine by using the results in [198].

7.3.2 HCCI Control Using the COM

- The COM could be used as a simulation model to design the HCCI combustion controller. Future work includes utilizing the COM for controller design. Subsequently, the COM could be then ported for on-line model-based HCCI control.

- Since CA_{50} influences T_{exh}, engine-out emissions and output power the

optimal control of CA_{50} to adjust exhaust temperature and engine output power would be beneficial for providing a larger HCCI operating range for which the catalyst would have sufficient exhaust temperature.

7.3.3 Reducing HCCI Exhaust Aftertreatment Light-off period

- Since the oxidation process particularly CO-CO_2 reactions in catalytic converters are exothermic. It would be useful to study HCCI conditions that promote higher CO-CO_2 reactions in catalyst so that the heat generated by exothermic oxidation reactions in the catalyst can help the catalyst to reach the light-off temperature and maintain sufficiently high temperature for high efficiency.

- Phase-Change Materials (PCM) with a transition temperature of about 300-350°C, which is slightly above the light-off temperature of typical catalysts, has been used in catalyst in other works [199] to reduce catalyst light-off time during cold start. A PCM is particularly useful for conditions that a vehicle has short stops before starting again. Using PCM could be of extra benefits for dual-mode (HCCI-SI) engines, since it can keep catalyst warm during mode switch provided an engine starts in SI mode. This could be an interesting avenue to study.

Bibliography

[1] Environment Canada National Inventory Report. "Canada's Greenhouse Gas Inventory: 1990-2003". Technical report, October 2005.

[2] F. Zhao, T. W. Asmus, D. N. Assanis, J. E. Dec, J. A. Eng, and P. M. Najt. *Homogeneous Charge Compression Ignition (HCCI) Engines*. SAE Publication PT-94, 2003.

[3] R. H. Stanglmaier and C. E. Roberts. "Homogeneous Charge Compression Ignition (HCCI): Benefits, Compromises, and Future Engine Applications". *SAE Paper No. 1999-01-3682*, 1999.

[4] J. Marshall. "Clean-burn Engine Dodges Ever Tighter Regulations". In *New Scientist magazine*. January 2006.

[5] P. Price, R. Stone, J. Misztal, H. Xu, M. Wyszynski, T. Wilson, and J. Qiao. "Particulate Emissions From a Gasoline Homogeneous Charge Compression Ignition Engine". SAE Paper No. 2007-01-0209, 2007.

[6] H. Zhao. *Homogeneous Charge Compression Ignition (HCCI) and Controlled Auto Ignition (CAI) Engines for the Automotive Industry*. Woodhead Publishing Ltd., Brunel University UK, 2007.

[7] O. Erlandsson. "Early Swedish Hot-Bulb Engines - Efficiency and Performance Compared to Contemporary Gasoline and Diesel Engines". SAE Paper No. 2002-01-0115, 2002.

[8] L. A. Gussak. "High Chemical Activity of Incomplete Combustion Products and a Method of Prechamber Torch Ignition for Avalanche Activation of Combustion in Internal Combustion Engines". SAE Paper No. 750890, 1975.

[9] S. Onishi, S. H. Jo, K. Shoda, P. D. Jo, and S. Kato. "Active Thermo-Atmosphere Combustion (ATAC) A New Combustion Process for Internal Combustion Engines". *SAE Paper No. 790501*, 1979.

[10] M. Noguchi, Y. Tanaka, T. Tanaka, and Y. Takeuchi. "A Study on Gasoline Engine Combustion by Observation of Intermediate Reactive Products during Combustion". *SAE Paper No. 790840*, 1979.

[11] P.M. Najt and D.E. Foster. "Compression-Ignited Homogeneous Charge Combustion". *SAE Paper No. 830264*, 1983.

[12] R. H. Thring. "Homogeneous Charge Compression Ignition (HCCI) Engines". SAE Paper No. 892068, 1989.

[13] T. Aoyama, Y. Hattori, J. Mizuta, and Y. Sato. "An Experimental Study on Premixed-Charge Compression Ignition Gasoline Engine". SAE Paper No. 1996-01-960081, 1996.

[14] T.W. Ryan and T.J. Callahan. "Homogeneous Charge Compression Ignition of Diesel Fuel". *SAE Paper No. 961160*, 1996.

[15] M. Christensen, A. Hultqvist, and B. Johansson. "Demonstarting the Multi Fuel Capability of a Homogenous Charge Compression Ignition Engine with Variable Compression Ratio". SAE Paper No. 1999-01-3679, 1999.

[16] European Federation for Transport and Environment. "Waiting for Euro 5 and Euro 6 New Emission Standards for Passenger Cars, Vans and Lorries". http://www.t-e.nu/, 2004.

[17] US Environmental Protection Agency. "2007 Emission Standard for Heavy Duty Truck and Bus Engines". http://www.epa.gov/, 2000.

[18] S. B. Fiveland, R. Agama, M. Christensen, B. Johansson, J. Hiltner, F. Mauss, and D. N. Assanis. "Experimental and Simulated Results Detailing the Sensitivity of Natural Gas HCCI Engines to Fuel Composition". SAE Paper No. 20001-01-3609, 2001.

[19] J. Arrafgle, B. Tormos, J. J. Laopez, and A. Garcia. "Analysis of the Potential of Biodiesel as an Alternative Fuel for Current and Future HSDI Engines". SAE Paper No. 2009-01-0480, 2009.

[20] A. Tsolakisa, A. Megaritisb, and D. Yap. "Application of Exhaust Gas Fuel Reforming in Diesel and Homogeneous Charge Compression Ignition (HCCI) Engines Fuelled with Biofuels". *Energy*, 33:462–470, 2008.

[21] R.F. Cracknell, D.J. Rickeard, J. Ariztegui, K.D. Rose, M. Muether, M. Lamping, and A. Kolbeck. "Advanced Combustion for Low Emissions and High Efficiency Part 2: Impact of Fuel Properties on HCCI Combustion". SAE Paper No. 2008-01-2404, 2008.

[22] M. Yao, Z. Zheng, and H. Liu. "Progress and Recent Trends in Homogeneous Charge Compression Ignition (HCCI) Engines". *Progress in Energy and Combustion Science*, in press, 2009.

[23] V. Hosseini and M.D. Checkel. "Reformer Gas Composition Effect on HCCI Combustion of n-Heptane, Iso-Octane, and Natural Gas". SAE Paper No. 2008-01-0049, 2008.

[24] O. Stenlåås, M. Christensen, R. Egnell, P. Tunestål, B. Johansson, and F. Mauss. "Reformed Methanol Gas as Homogeneous Charge Compression Ignition Engine Fuel". SAE Paper No. 2004-01-2991, 2004.

[25] P. Kongsereeparp and M. D. Checkel. "Study of Reformer Gas Effects on n-Heptane HCCI Combustion Using a Chemical Kinetic Mechanism Optimized by Genetic Algorithm". SAE Paper No. 2008-01-0039, 2008.

[26] J. Olsson, P. Tunestål, and B. Johansson. "Closed-Loop Control of an HCCI Engine". *SAE Paper No. 2001-01-1031*, 2001.

[27] V. Manente, P. Tunestål, and B. Johansson. "Mini High-Speed HCCI Engine Fueled with Ether: Load Range, Emission Characteristics and Optical Analysis". SAE Paper No. 2007-01-3606, 2007.

[28] U.S. Department of Energy. "Homogeneous Charge Compression Ignition Technology - A Report to the U.S. Congress". Technical report, April 2001.

[29] R. Yu, X. S. Bai, H. Lehtiniemi, S. S. Ahmed, F. Mauss, M. Richter, M. Aldn, L. Hildingsson, B. Johansson, and A. Hultqvist. "Effect of Turbulence and Initial Temperature Inhomogeneity on Homogeneous Charge Compression Ignition Combustion". *SAE Paper No. 2006-01-3318*, 2006.

[30] A. Hultqvist, M. Christensen, B. Johansson, M. Richter, J. Nygren, J. Hult, and M. AldJn. "The Research About the Effects of Thermal Stratification on n-Heptane/iso-Octane-Air Mixture HCCI Combustion Using a Rapid Compression Machine". *SAE Paper No. 2006-01-3319*, 2006.

[31] D. Law, D. Kemp, J. Allen, G. Kirkpatrick, and T. Copland. "Controlled Combustion in an IC-Engine with a Fully Variable Valve Train". *SAE Paper No. 2000-01-0251*, 2000.

[32] M. Jennische. *"Closed-Loop Control of Start of Combustion in a Homogeneous Charge Compression Ignition Engine"*. M.Sc. Thesis, Lund Institute of Technology, 2003.

[33] P. Caton, A. Simon, J. C. Gerdes, and C. Edwards. "Residualeffected Homogeneous Charge Compression Ignition at Low Compression Ratio Using Exhaust Reinduction". *International Journal of Engine Research*, (4):163–177, 2003.

[34] S. Yamaoka, H. Kakuya, S. Nakagawa, T. Okada, A. Shimada, and Y. Kihara. "HCCI Operation Control in a Multi-Cylinder Gasoline Engine". SAE Paper No. 2005-01-0120, 2005.

[35] F. Agrell, H.E. Ångström, B. Eriksson, J. Wikander, and J. Linderyd. "Integrated Simulation and Engine Test of Closed-Loop HCCI Control by Aid of Variable Valve Timings". *SAE Paper No. 2003-01-0748*, 2003.

[36] J. Hyvönen, G. Haraldsson, and B. Johansson. "Supercharging HCCI to Extend the Operating Range in a Multi-Cylinder VCR HCCI Engine". *SAE Paper No. 2003-01-3214*, 2003.

[37] G. Haraldsson, P. Tunestål, B. Johansson, and J. Hyvönen. "HCCI Combustion Phasing with Closed-Loop Combustion Control Using Variable Compression Ratio in a Multi-Cylinder Engine". *SAE Paper No. 2003-01-1830*, 2003.

[38] R. Chen, N. Milovanovic, J. Turner, and D. Blundell. "The Thermal Effect of Internal Exhaust Gas Recirculation on Controlled Auto-Ignition". *SAE Paper No. 2003-01-0751*, 2003.

[39] Y. Takeda, N. Keiichi, and N. Keiichi. "Emission Characteristics of Premixed Lean Diesel Combustion with Extremely Early Staged Fuel Injection". SAE Paper No. 961163, 1996.

[40] D. I. Handford and M. D. Checkel. "Extending the Load Range of a Natural Gas HCCI Engine using Direct Injected Pilot Charge and External EGR". SAE Paper No. 2009-01-1884, 2009.

[41] K. Nakagome, N. Shimazaki, K. Niimura, and S. Kobayashi. "Combustion and Emission Characteristics of Premixed Lean Diesel Combustion Engine". SAE Paper No. 970898, 1997.

[42] S. M. Aceves, D.L. Flowers, J. Martinez-Frias, J. R. Smith, R. Dibble, M. Au, and J. Girard. "HCCI Combustion: Analysis and Experiments". SAE Paper No. 2001-01-2077, 2001.

[43] G. Haraldsson, P. Tunestål, B. Johansson, and J. Hyvönen. "HCCI Closed-Loop Combustion Control Using Fast Thermal Management". *SAE Paper No. 2004-01-0943*, 2004.

[44] M. Christensen and B. Johansson. "Homogeneous Charge Compression Ignition with Water Injection". SAE Paper No. 1999-01-0182, 1999.

[45] T. Milovanovic, D. Blundell, R. Pearson, J. Turner, and R. Chen. "Enlarging the Operational Range of a Gasoline HCCI Engine By Controlling the Coolant Temperature". SAE Paper No. 2005-01-0157, 2005.

[46] M. Furutani, Y. Ohta, M. Kovo, and M. Hasegawa. "An Ultra-Lean Premixed Compression Ignition Engine Concept and its Characteristics". Procedding of the fourth International Symposium COMODIA 98, 1998.

[47] H. Akagawa, T. Miyamoto, A. Harada, S. Sasaki, N. Shimazaki, T. Hashizume, and K. Tsujimura. "Approaches to Solve Problems of the Premixed Lean Diesel Combustion". SAE Paper No. 1999-01-0183, 1999.

[48] P. Tunestål, J.O. Olsson, and B. Johansson. "Closed Loop Control of HCCI Engines". In *Nonlinear and Hybrid Systems in Automotive Control*. Springer-Verlag, Lund, 2002.

[49] D. Yap, A. Megaritis, S. Peucheret, M.L. Wyszynski, and Hongming Xu. "Effect of Hydrogen Addition on Natural Gas HCCI Combustion". SAE Paper No. 2004-01-1972, 2004.

[50] H. Hu, T. Wilson, S. Richardson, M.L. Wyszynski, T. Megaritis, D. Yap, S. Golunski, and D. James. "Extension of the Boundary of HCCI Combustion Using Fuel Reforming Technology". SAE Paper No. 2004-08-0286, 2004.

[51] V. Hosseini, W. S. Neill, and M. D. Checkel. "Controlling n-Heptane HCCI Combustion with Partial Reforming: Experimental Results and Modeling Analysis". *Journal of Engineering for Gas Turbines and Power Transactions*, to appear, 2009.

[52] J. Martinez-Frias, S.M. Aceves, D. Flowers, J.R. Smith, and R. Dibble. "Equivalence Ratio-EGR Control of HCCI Engine Operation and the Potential for Transition to Spark-ignited Operation". SAE Paper No. 2001-01-3613, 2001.

[53] M. Christensen, B. Johansson, P. Amneus, and F. Mauss. "Supercharged Homogeneous Charge Compression Ignition". SAE Paper No. 980787, 1998.

[54] Y. Iwabuchi, K. Kawai, T. Shoji, and Y. Takeda. "Trial of New Concept Diesel Combustion System Premixed Compression-Ignition Combustion". SAE Paper No. 1999-01-0185, 1999.

[55] R. Sun, R. Thomas, and C.L. Gray. "An HCCI Engine: Power Plant for a Hybrid Vehicle". SAE Paper No. 2004-01-0933, 2004.

[56] J.O. Olsson, P. Tunestål, and B. Johansson. "Boosting for High Load HCCI". SAE Paper No. 2004-01-0940, 2004.

[57] J.O. Olsson, P. Tunestal, G. Haraldsson, and B. Johansson. "A Turbo Charged Dual Fuel HCCI Engine". SAE Paper No. 2001-01-1896, 2001.

[58] L. Koopmans, H. Strom, S. Lundgren, O. Backlund, and I. Denbratt. "Demonstrating a SI-HCCI-SI Mode Change on a Volvo 5-Cylinder Electronic Valve Control Engine". SAE Paper No. 2003-01-0753, 2003.

[59] H. Santoso, J. Matthews, and W. K. Cheng. "Managing SI/HCCI Dual-Mode Engine Operation". SAE Paper No. 2005-01-0162, 2005.

[60] Y. Guezennec, C. Musardo, B. Staccia, S. Midlam-Mohler, E. Calo, P. Pisu, and G. Rizzoni. "Supervisory Control for NOx Reduction of an HEV With a Mixed-Mode HCCI/DI Engine". SAE Paper No. 2004-05-0123, 2004.

[61] S. Midlam-Mohler, S. Haas, Y. Guezennec, M. Bargende, and G. Rizzoni. "Mixed-Mode Diesel HCCI/DI With External Mixture Preparation". SAE Paper No. 2004-05-0446, 2004.

[62] Magnus Christensen, Bengt Johansson, and Patrick Einewall. "Homogeneous charge compression ignition (HCCI) using isooctane, ethanol and natural gas A comparison with spark-ignition operation". SAE Paper No. 972874, 1997.

[63] A. Harada, N. Shimazaki, S. Sasaki, T. Miyamoto, H. Akagawa, and K. Tsujimura. "The effects of Mixture Formation on Premixed Lean Diesel Combustion". SAE Paper No. 980533, 1998.

[64] M. Sjöberg and J. E. Dec. "An Investigation into Lowest Acceptable Combustion Temperatures for Hydrocarbon Fuels in HCCI Engines". *Proc. of the Combustion Institute*, 30:2719–2726, 2005.

[65] J. E. Dec. "A Computational Study of the Effects of Low Fuel Loading and EGR on Heat Release Rates and Combustion Limits in HCCI Engines". *SAE Paper No. 2002-01-1309*, 2002.

[66] S. Aceves, D. Flowers, F. Espinoza-Loza, J. Martinez-Frias, R. Dibble, M. Christensen, B. Johansson, and R. P. Hessel. "Piston-Liner Crevice Geometry Effect on HCCI Combustion by Multi-Zone Analysis". *SAE Paper No. 2002-01-2869*, 2002.

[67] X. Lu, W. Chen, Y. Hou, and Z. Huang. "Study on the Ignition, Combustion and Emissions of HCCI Combustion Engines Fueled With Primary Reference Fuels". *SAE Paper No. 2005-01-0155*, 2005.

[68] R. J. Wanker, J. C. Wurzenberger, and H. A. Schuemie. "Three-Way Catalyst Light-off During the NEDC Test Cycle: Fully Coupled 0D/1D Simulation of Gasoline Combustion, Pollutant Formation and Aftertreatment Systems". *SAE Paper No. 2008-01-1755*, 2008.

[69] M. Borland and F. Zhao. "Application of Secondary Air Injection for Simultaneously Reducing Converter-In Emissions and Improving Catalyst Light-Off Performance". *SAE Paper No. 2002-01-2803*, 2002.

[70] P. A. Konstantinidis and G. C. Koitsakis. "Computer Aided Assessment and Optimization of Catalyst Fast Light-Off Techniques". *IMechE ,Part D*, 211, 1997.

[71] H. Bauer, H.-G. Haldenwanger, P. Hirth, and R. Brück. "Thermal Management of Close Coupled Catalysts". *SAE Paper No. 1999-01-1231*, 1999.

[72] G. T. Kalghatgi and R. A. Head. "Combustion Limits and Efficiency in a Homogeneous Charge Compression Ignition Engine". *Int. Journal of Engine Research*, 7:215–236, 2006.

[73] M. Shahbakhti, R. Lupul, and C. R. Koch. "Cyclic Variations of Ignition Timing in an HCCI Engine". *Proceeding of ASME/IEEE Joint Rail Conference & Internal Combustion Engine Spring Technical Conference*, 2007.

[74] Z. Serinyel, L. Le Moyne, and P. Guibert. "Homogeneous Charge Compression Ignition as an Alternative Combustion Mode for the Future of Internal Combustion Engines". *International Journal of Vehicle Design*, 44(1-2):20 – 40, 2007.

[75] M. Sjöberg, J. E. Dec, A. Babajimopoulos, and D. Assanis. "Comparing Enhanced Natural Thermal Stratification Against Retarded Combustion Phasing for Smoothing of HCCI Heat-Release Rates". *SAE Paper No. 2004-01-2994*, 2004.

[76] J. Olsson, P. Tunestl, B. Johansson, S. Fiveland, R. Agama, M. Willi, and D. Assanis. "Compression Ratio Influence on Maximum Load of a Natural Gas Fueled HCCI Engine". *SAE Paper No. 2002-01-0111*, 2002.

[77] R. J. Iverson, R. E. Herold, R. Augusta, D. E. Foster, J. B. Ghandhi, J. A. Eng, and P. M. Najt. "The Effects of Intake Charge Preheating in a Gasoline-Fueled HCCI Engine". *SAE Paper No. 2005-01-3742*, 2005.

[78] B. Johansson. "Homogeneous Charge Compression Ignition: The Future of IC Engines?". *International Journal of Vehicle Design*, 44(1-2):1 – 19, 2007.

[79] M. Yao, Z. Zheng, B. Zhang, and Z. Chen. "The Effect of PRF Fuel Octane Number on HCCI Operation". *SAE Paper No. 2004-01-2992*, 2004.

[80] M. Shahbakhti and C. R. Koch. "Characterizing the Cyclic Variability of Ignition Timing in an HCCI Engine Fueled with n-Heptane/iso-Octane Blend Fuels". *International Journal of Engine Research*, 9:361–397, 2008.

[81] G. M. Shaver, M. J. Roelle, and J. C. Gerdes. "Modeling Cycle to Cycle Dynamics and Mode Transition in HCCI Engines with Variable Valve Actuation". *Journal of Control Engineering Practice*, 14:213–222, 2006.

[82] M. Atkins and C. R. Koch. "The Effect of Fuel Octane and Diluent on HCCI Combustion". *Proceeding of IMechE - Part D*, 219:665 – 675, 2005.

[83] S. Matsuoka, T. Yamaguchi, and Y. Umemura. "Factors Influencing the Cyclic Variation of Combustion of Spark Ignition Engine". SAE Paper No. 710586, 1971.

[84] M. A. Ceviz and F. Yuksel. "Cyclic Variations on LPG and Gasoline-Fuelled Lean Burn SI Engine". *Renewable Energy*, 32:1950–60, 2006.

[85] L. Xingcai, J. Libin, M. Junjun, and H. Zhen. "Experimental Study on the Cycle-by-Cycle Variations of Homogeneous Charge Compression Ignition Combustion Using Primary Reference Fuels and Their Mixtures". *Proceeding of IMechE - Part D*, 221:859 – 866, 2007.

[86] C. S. Daw, K. D. Edwards, R. M. Wagner, and J. B. Green. "Modeling Cyclic Variability in Spark-Assisted HCCI". *Journal of Engineering for Gas Turbines and Power*, 130, 2008.

[87] L. Koopmans, O. Backlund, and I. Denbratt. "Cycle to Cycle Variations: Their Influence on Cycle Resolved Gas Temperature and Unburned Hydrocarbons from a Camless Gasoline Compression Ignition Engine". SAE Paper No. 2002-01-0110, 2002.

[88] C. Liu, G. A. Karim, A. Sohrabi, and F. Xiao. "Combustion and Cyclic Variation for Lean Mixture Operation". *ASME Internal Combustion Engine Spring Technical Conference*, 2006.

[89] M. Sjöberg and J. E. Dec. "Comparing Late-Cycle Autoignition Stability for Single- and Two-Stage Ignition Fuels in HCCI Engines". *Proceedings of the Combustion Institute*, 31:2895–2902, 2007.

[90] C. S. Daw, R. M. Wagner, K. D. Edwards, and J. B. Green Jr. "Understanding the Transition Between Conventional Spark-Ignited Combustion and HCCI in a Gasoline Engine". *Proceedings of the Combustion Institute*, 31:2887 – 2894, 2007.

[91] R. M. Wagner, K. D. Edwards, C. S. Daw, J. B. Green Jr., and B. G. Bunting. "On the Nature of Cyclic Dispersion in Spark Assisted HCCI Combustion". *SAE Paper No. 2006-01-0418*, 2006.

[92] A. Ghazimirsaied, M. Shahbakhti, A. Audet, and C. R. Koch. "HCCI Engine Cyclic Variation Characterization Using Both Chaotic and Statistical Approach". *Proceeding of Combustion Institute/Canadian Section (CI/CS) Spring Technical Conference*, 2008.

[93] J. Pan, C. G. W. Sheppard, A. Tindall, M. Berzins, S. V. Pennington, and J. M. Ware. "End Gas Inhomogeneity, Autoignition and Knock". *SAE Paper No. 982616*, 1998.

[94] P. G. Aleiferis, A. G. Charalambides, Y. Hardalupas, A. M. K. P. Taylor, and Y. Urata. "Autoignition Initiation and Development of n-heptane HCCI Combustion Assisted by Inlet Air Heating, Internal EGR or Spark Discharge: An Optical Investigation". *SAE Paper No. 2006-01-3273*, 2006.

[95] A. Hultqvist, M. Christensen, B. Johansson, A. Franke, M. Richter, and M. Alden. "Study of Homogeneous Charge Compression Ignition Combustion Process by Chemiluminescence Imaging". *SAE Paper No. 1999-01-3680*, 1999.

[96] C. J. Chiang and A. G. Stefanopoulou. "Stability Analysis in Homogeneous Charge Compression Ignition (HCCI) Engines With High Dilution". *IEEE Transactions on Control Systems Technology*, 15:209–219, 2007.

[97] M. Richter, J. Engstrom, A. Franke, M. Alden, A. Hultqvist, and B. Johansson. "The Influence of Charge Inhomogeneity on the HCCI Combustion Process". *SAE Paper No. 2000-01-2868*, 2000.

[98] G. Grnefeld, V. Beushausen, P. Andresen, and W. Hentschel. "A Major Origin of Cyclic Energy Conversion Variations in SI Engines: Cycle-by-Cycle Variations of the Equivalence Ratio and Residual Gas of the Initial Charge". SAE Paper No. 941880, 1994.

[99] D. Yap, M. L. Wyszynski, A. Megaritis, and H. Xu. "Applying Boosting to Gasoline HCCI Operation With Residual Gas Trapping". *SAE Paper No. 2005-01-2121*, 2005.

[100] H. Zhao, Z. Peng, and N. Ladommatos. "Understanding of Controlled Autoignition Combustion in a Four-Stroke Gasoline Engine". *Proceedings of the IMechE Part D Journal of Automobile Engineering*, 215:1297–1310, 2001.

[101] John B. Heywood. *"Internal Combustion Engine Fundamentals"*. McGraw-Hill, New York, 1988.

[102] R.J. Moffat. "describing the uncertainties in experimental results". *Experimental Thermal and Fluid Science*, 1:3–17, 1988.

[103] R. Lupul. "Steady State and Transient Characterization of a HCCI Engine with Varying Octane Fuel". M.Sc. thesis, University of Alberta, 2008.

[104] S. Tanaka, F. Ayala, J. C. Keck, and J. B. Heywood. "Two-stage Ignition in HCCI Combustion and HCCI Control by Fuels and Additives". *Journal of Combustion and Flame*, 132:219–239, 2003.

[105] P. Kirchen, M. Shahbakhti, and C. R. Koch. "A Skeletal Kinetic Mechanism for PRF Combustion in HCCI Engines". *Journal of Combustion Science and Technology*, 179:1059–1083, 2007.

[106] G. M. Rassweiler and L. Withrow. "Motion Pictures of Engine Flames Correlated with Pressure Cards". *SAE Transaction*, 42(5):185–204, 1938.

[107] N. Ozdor, M. Dulger, and E. Sher. "Cyclic Variability in Spark Ignition Engines - A Literature Survey". *SAE Paper No. 940987*, 1994.

[108] M. Shahbakhti, R. Lupul, A. Audet, and C. R. Koch. "Experimental Study of HCCI Cyclic Variations for Low-Octane PRF Fuel Blends". *Proceeding of Combustion Institute/Canadian Section (CI/CS) Spring Technical Conference*, 2007.

[109] K. Kumano and N. Iida. "Analysis of the Effect of Charge Inhomogeneity on HCCI Combustion by Chemiluminescence Measurement". *SAE Paper No. 2004-01-1902*, 2004.

[110] B. Johansson. "Cycle to Cycle Variations in S.I. Engines - The Effects of Fluid Flow and Gas Composition in the Vicinity of the Spark Plug on Early Combustion". *SAE Paper No. 962084*, 1996.

[111] M. Sjöberg, J. E. Dec, and N. P. Cernansky. "Potential of Thermal Stratification and Combustion Retard for Reducing Pressure-Rise Rates in HCCI Engines, Based on Multi-Zone Modelling and Experiments". *SAE Paper No. 2005-01-0113*, 2005.

[112] D. Flowers, S. M. Aceves, J. Martinez-Frias, J. R. Smith, M. Au, J. Girard, and R. Dibble. "Operation of a Four-Cylinder 1.9L Propane Fueled Homogeneous Charge Compression Ignition Engine: Basic Operating Characteristics and Cylinder-to-Cylinder Effects". *SAE Paper No. 2001-01-1895*, 2001.

[113] F. Millo and C. V. Ferraro. "Knock in S.I. Engines: A Comparison between Different Techniques for Detection and Control. *SAE Paper No. 982477*, 1998.

[114] J. Chang, Z. Filipi, D. Assanis, T. Kuo, P. Najt, and R. Rask. "Characterizing the Thermal Sensitivity of a Gasoline Homogeneous Charge Compression Ignition Engine with Measurements of Instantaneous Wall Temperature and Heat Flux". *Int. J. of Engine Research*, 6, 2005.

[115] J. Bengtsson. *"Closed-Loop Control of HCCI Engine Dynamics"*. PhD. Thesis, Lund Institute of Technology, 2004.

[116] V. Ferrari, H. Rabinowitz, S. Siemund, T. Collinq, and B. Campbell. "Achieving EURO III and EURO IV with Ultra-Low Precious Metal Loadings". *SAE Paper No. 2007-01-2565*, 2007.

[117] E. Jean, V. Leroy, G. Montenegro, A. Onorati, and M. Laurell. "Impact of Ultra Low Thermal Inertia Manifolds on Emission Performance". *SAE Paper No. 2007-01-0935*, 2007.

[118] K. Tanikawa, T. Hirota, T. Yamada, M. Komori, G. Zhang, and H. Muraki. "Development of Advanced Three-Way Catalyst Technology". *SAE Paper No. 2008-01-1645*, 2008.

[119] W. B. Williamson, D. Dou, and H. J. Robota. "Development of Advanced Three-Way Catalyst Technology". *SAE Paper No. 1999-01-0776*, 1999.

[120] S. Zinola, J. Lavy, and A. Jaecker-Voirol. "Towards CO and HC Aftertreatment Devices for the Next Generation of Diesel Engines". *SAE Paper No. 2008-01-1543*, 2008.

[121] K. Bhaskar, S. Sendilvelan1, and K. Jeyachandran. "Experimental Investigation on Cold Start HC and CO Emission Control using Electrically Heated Pre-Catalyst (EHC) in Mark IV Ambassador SI engine". *SAE Paper No. 2004-28-0006*, 2004.

[122] P. Oeser, E. Mueller, and G. Haertel. "Novel Emission Technologies with Emphasis on Catalyst Cold Start Improvements Status Report on VW-Pierburg Burner/Catalyst Systems". *SAE Paper No. 940474*, 1994.

[123] A. Caraceni, V. Cioffi, F. Garofalo, C. Barberio, and G. Saroglia. "Emission Control Technologies for EU Stage IV + EOBD on Small Cars (Part I): Pre-screening of Potential Solutions". *SAE Paper No. 1999-01-0775*, 1999.

[124] S. Williams, L. Hu, T. Nakazono, H. Ohtsubo, and M. Uchida. "Oxidation Catalysts for Natural Gas Engine Operating under HCCI or SI Conditions". *SAE Paper No. 2008-01-0807*, 2008.

[125] R. S. Figliola and D. E. Beasley. *"Theory and Design for Mechanical Measurements"*. John Wiley & Sons, Inc., 2000.

[126] M. Shahbakhti and C. R. Koch. "Dynamic Modeling of HCCI Combustion Timing in Transient Fueling Operation". *SAE 2009 Transactions Journal of Engines*, SAE 2009-01-1136, to appear, accepted in Apr., 27, 2009.

[127] S. Russ, M. Thiel, and G. Lavoie. "SI Engine Operation with Retarded Ignition: Part 2 -HC Emissions and Oxidation". *SAE Paper No. 1999-01-3507*, 1999.

[128] M. Shahbakhti and C. R. Koch. "Thermo-Kinetic Combustion Modeling of an HCCI Engine to Analyze Ignition Timing for Control Applications". *Proceeding of Combustion Institute/Canadian Section (CI/CS) Spring Technical Conference*, 2007.

[129] P. Kongsereeparp, M. D. Checkel, and B. Kashani. "A Stand-alone Multi-Zone Model for Combustion in HCCI Engines". *ASME Internal Combustion Engine Division 2005 Fall Technical Conference*, ICEF2005-1241, 2005.

[130] S.M. Aceves, D.L. Flowers, C.K. Westbrook, J.R. Smith, W. Pitz, R. Dibble, M. Christensen, and B. Johansson. "A Multi-Zone Model for Prediction of HCCI Combustion and Emissions". SAE Paper No. 2000-01-0327, 2000.

[131] S. C. Kong and R. D. Reitz. "Numerical Study of Premixed HCCI Engine Combustion and its Sensitivity to Computational Mesh and Model Uncertainties". *Combustion Theory and Modeling*, pages 417–433, 2003.

[132] S.B. Fiveland and D.N. Assanis. "A Four-Stroke Homogeneous Charge Compression Ignition Engine Simulation for Combustion and Performance Studies". SAE Paper No. 2000-01-0332, 2000.

[133] P. Kirchen. *"Thermokinetic Modeling of the HCCI Cycle: Predicting the Ignition Timing"*. M.Sc. Thesis, University of Alberta, 2004.

[134] J. Chang, O. Guralp, Z. Filipi, D. Assanis, T. Kuo, P. Najt, and R. Rask. "New Heat Transfer Correlation for an HCCI Engine Derived From Measurements of Instantaneous Surface Heat Flux". SAE Paper No. 2004-01-2996, 2004.

[135] J. Zheng, W. Yang, D.L. Miller, and N.P. Cernansky. "A Skeletal Chemical Kinetic Model for the HCCI Combustion Process". SAE Paper No. 2002-01-0423, 2002.

[136] H. Li, D.L. Miller, and N.P. Cernansky. "Development of a Reduced Chemical Kinetic Model for Prediction of Preignition Reactivity and Autoignition of Primary Reference Fuels". SAE Paper No. 960498, 1996.

[137] S. Tanaka, F. Ayala, and J. C. Keck. "A Reduced Chemical Kinetic Model for HCCI Combustion of Primary Reference Fuels in a Rapid Compression Machine". *Combustion and Flame*, 133(4):467–481, 2003.

[138] M. Shahbakhti and C.R. Koch. "Physics Based Control Oriented Model for HCCI Combustion Timing". *Journal of Dynamic Systems, Measurement and Control*, pages 1-58, to appear, accepted in May, 22, 2009.

[139] K. Swan, M. Shahbakhti, and C. R. Koch. "Predicting Start of Combustion Using a Modified Knock Integral Method for an HCCI Engine". *SAE 2006 Transactions Journal of Engines*, pages 611–620, 2007.

[140] M. Embouazza, D. C. Haworth, and N. Darabiha. "Implementation of Detailed Chemical Mechanisms into Multidimensional CFD Using in situ Adaptive Tabulation: Application to HCCI Engines". SAE Paper No. 2002-01-2773, 2002.

[141] N. P. Komninos, D. T. Hountalas, and D. A. Kouremenos. "Description of in-Cylinder Combustion Processes in HCCI Engines Using a Multi-Zone Model". SAE Paper No. 2005-01-0171, 2005.

[142] D. L. Flowers, S. M. Aceves, J. Martinez-Frias, and R. W. Dibble. "Prediction of Carbon Monoxide and Hydrocarbon Emissions in Iso-Octane HCCI Engine Combustion Using Multizone Simulations". *Proceedings of the Combustion Institute*, 29:687–694, 2002.

[143] J. Bengtsson, M. Gafvert, and P. Strandh. "Modeling of HCCI Engine Combustion for Control Analysis". *IEEE conference on decision and control*, pages 1682–1687, 2004.

[144] M. Roelle, G. M. Shaver, and J. C. Gerdes. "Tackling the Transition: A Multi-Mode Combustion Model of SI and HCCI for Mode Transition Control". *Proceedings of IMechE2004*, pages 329–336, 2004.

[145] S. Karagiorgis, N. Collings, K. Glover, and T. Petridis. "Dynamic Modeling of Combustion and Gas Exchange Processes for Controlled Auto-Ignition Engines". *Proceeding of the 2006 American Control Conference*, 2006.

[146] M. Canova, L. Garzarella, M. Ghisolfi, Mohler S. M., Guezennec Y., and Rizzoni G. "A Control-Oriented Mean-Value Model for HCCI Diesel Engines with External Mixture Formation". *Proceedings of IMechE2005, ASME International Mechanical Engineering Congress*, 2005.

[147] G. M. Shaver, J. C. Gerdes, J. Parag, P. A. Caton, and C. F. Edwards. "Modeling for Control of HCCI Engines". *American Control Conference*, pages 749–754, 2003.

[148] M. Halstead, L. Kirsch, and J. Keck. "Autoignition of Hydrocarbon Fuels at High Temperatures and Pressures - Fitting of a Mathematical Model". *Combustion and Flame*, 30:45–60, 1977.

[149] G. M. Shaver, M. Roelle, and Gerdes J. C. "Tackling the Transition: Decoupled Control of Combustion Timing and Work Output in Residual-Affected HCCI Engines". *American Control Conference*, pages 3871–3876, 2005.

[150] Stephen R. Turns. *An Introduction to Combustion: Concepts and Applications*. McGraw-Hill series in mechanical engineering. McGraw-Hill, 2nd edition, 2000.

[151] D. J. Rausen, A. G. Stefanopoulou, J-M. Kang, J. A. Eng, and W. Kuo. "A Mean-Value Model for Control of Homogeneous Charge Compression Ignition (HCCI) Engines". *American Control Conference*, pages 125–131, 2004.

[152] C. J. Chiang and A. G. Stefanopoulou. "Dynamic Modeling of Combustion and Gas Exchange Processes for Controlled Auto-Ignition Engines". *Proceeding of the 2006 American Control Conference*, 2006.

[153] J. C. Livengood and P. C. Wu. "Correlation of Autoignition Phenomena in Internal Combustion Engines and Rapid Compression Machines". *Fifth Symposium (International) on Combustion*, pages 347–356, 1955.

[154] Y. Ohyama. "Engine Control Using a Real-Time Combustion Model". SAE paper No. 2001-01-0256, 2001.

[155] J. S. Souder, P. Mehresh, J. K. Hedrick, and R. W. Dibble. "A Multi-Cylinder HCCI Engine Model for Control". *Proceedings of IMechE2004*, pages 307–316, 2004.

[156] M. Iida, T. Aroonsrisopon, M. Hayashi, D. Foster, and J. Martin. "The Effect of Intake Air Temperature, Compression Ratio and Coolant Temperature on the Start of Heat Release in an HCCI Engine". SAE Paper No. 2001-01-1880, 2001.

[157] K. Swan, M. Shahbakhti, and C. R. Koch. "Predicting Start of Combustion Using a Modified Knock Integral Method for an HCCI Engine". SAE Paper No. 2006-01-1086, 2006.

[158] Y. Ohyama. "Engine Control Using Combustion Model". SAE paper No. 2000-01-0198, 2000.

[159] J. Bengtsson, P. Strandh, R. Johansson, P. Tunesta, and B. Johansson. "Closed-Loop Combustion Control Of Homogeneous Charge Compression Ignition (HCCI) Engine Dynamics". *International Journal of Adaptive Control and Signal Processing*, 18:167–179, 2004.

[160] J. Bengtsson, P. Strandh, R. Johansson, P. Tunesta, and B. Johansson. "Hybrid Control Of Homogeneous Charge Compression Ignition (HCCI) Engine Dynamics". *International Journal of Control*, 79:422–448, 2006.

[161] M. Shahbakhti, R. Lupul, and C. R. Koch. "Predicting HCCI Auto-Ignition Timing by Extending a Modified Knock-Integral Method". *SAE Paper No. 2007-01-0222*, 2007.

[162] M. Shahbakhti, R. Lupul, and C. R. Koch. "Sensitivity Analysis and Modeling of HCCI Auto-Ignition Timing". *Proceeding of the Fifth IFAC Symposium on Advances in Automotive Control*, pages 303 – 310, 2007.

[163] H. Zhao, Z. Peng, J. Williams, and N. Ladommatos. "Understanding the Effects of Recycled Burnt Gases on the Controlled Autoignition (CAI) Combustion in Four-Stroke Gasoline Engines". SAE Paper No. 2001-01-3607, 2001.

[164] T. Noda, K. Hasegawa, M. Kubo, and T. Itoh. "Development of Transient Knock Prediction Technique by Using a Zero-Dimensional Knocking Simulation with Chemical Kinetics". SAE Paper No. 2004-01-0618, 2004.

[165] J. A. Nelder and R. Mead. "A Simplex Method for Function Minimization". *Computer Journal*, pages 308–313, 1965.

[166] M. Shahbakhti and C. R. Koch. "Control Oriented Modeling of Combustion Phasing for an HCCI Engine". *Proceeding of American Control Conference*, 2007.

[167] J. Bengtsson, P. Strandh, R. Johansson, P. Tunesta, and B. Johansson. "Hybrid Modelling Of Homogeneous Charge Compression Ignition (HCCI) Engine Dynamics - A Survey". *International Journal of Control*, 80:1814–1847, 2007.

[168] D. Gérard, M. Besson, J. P. Hardy, S. Croguennec, M. Thomine, S. Aoyama, and M. Tomita. "HCCI Combustion on a Diesel VCR Engine". *SAE Paper No. 2008-01-1187*, 2008.

[169] J. Kamio, T. Kurotani, T. Sato, Y. Kiyohiro, K. Hashimoto, and T. Gunji. "A Study on Combustion Control by Dual-Fuel Strategies". *SAE Paper No. 2007-08-0242*, 2007.

[170] N. J. Killingsworthy, S. M. Acevesz, D. L. Flowersz, and M. Krsti. "A Simple HCCI Engine Model for Control". *IEEE International Conference on Control Applications*, 2006.

[171] N. Jia, J. Wang, K. Nuttall, J. Wei, H. Xu, M. L. Wyszynski, J. Qiao, and M. J. Richardson. "HCCI Engine Modeling for Real-Time Implementation and Control Development". *IEEE/ASME Transactions on Mechatronics*, 12(6):581 – 9, 2007.

[172] R. Pfeiffer, G. Haraldsson, J. O. Olsson, P. Tunestal, R. Johansson, and B. Johansson. "System Identification and LQG Control of Variable-Compression HCCI Engine Dynamics". *Proceeding of IEEE International Conference on Control Applications*, pages 1442–1447, 2004.

[173] A. Audet. "Closed Loop Control of HCCI Using Camshaft Phasing and Dual Fuels". M.Sc. Thesis, University of Alberta, 2008.

[174] C. S. Daw, R. M. Wagner, K. D. Edwards, and J. B. Green Jr. "Understanding the Transition Between Conventional Spark-Ignited Combustion and HCCI in a Gasoline Engine". *Proceedings of the Combustion Institute*, 31:2887–2894, 2007.

[175] A. Ghazimirsaied, M. Shahbakhti, and C. R. Koch. "HCCI Combustion Phasing Prediction Using a Symbol-Statistic Approach". *Journal of Engineering for Gas Turbines and Power*, 2009. to appear.

[176] S. Karagiorgis, N. Collings, K. Glover, N. Coghlan, and A. Petridis. "Residual Gas Fraction Measurement and Estimation on a Homogeneous Charge Compression Ignition Engine Utilizing the Negative Valve Overlap Strategy". SAE Paper No. 2006-01-3276, 2006.

[177] N. Cavina, C. Siviero, and C. Suglia. "Residual Gas Fraction Estimation: Application to a GDI Engine With Variable Valve Timing and EGR". SAE Paper No. 2004-01-2943, 2004.

[178] Alexander Burcat. "Third Millenium Ideal Gas and Condensed Phase Thermochemical Database for Combustion". Technical Report TAE 867, Faculty of Aerospace Engineering, Israel Institute of Technology, January 2001. ftp.technion.ac.il/pub/supported/aetdd/thermodynamics.

[179] C. F. Aquino. "Transient A/F Control Characteristics of the 5 Liter Central Fuel Injection Engine". SAE Paper No. 810494, 1981.

[180] P. Berggren and A. Perkovic. *"Cylinder Individual Lambda Feedback Control in an SI Engine"*. M.Sc. Thesis, Linkoping University, 1996.

[181] H. Melgaard and E. Hendricks. "Continuous Identification of a Four-Stroke SI Engine". *Proceeding of American Control Conference*, pages 1876–1881, 1990.

[182] C. Chang, N. P. Fekete, and J. D. Powell. "Engine Air-Fuel Ratio Control Using an Event-Based Observer". SAE Paper No. 930766, 1993.

[183] A. G. Stefanopoulou and J. A. Cook. "Joint Air-Fuel Ratio and Torque Regulation Using Secondary Cylinder Air Flow Actuators". *ASME Journal of Dynamic Systems, Measurement and Control*, 121:638–647, 1999.

[184] G. Almkvist and S. Eriksson. "An Analysis of Air to Fuel Ratio Response in a MPFI Engine Under Transient Conditions". SAE Paper No. 932753, 1993.

[185] J.J. Moskwa. *"Automotive Engine Modeling for Real- Time Control"*. P.hD. Thesis, Massachusetts Institute of Technology, 1988.

[186] M. Shahbakhti, M. Ghafuri, A. R. Aslani, A. Sahraeian, S. A. Jazayeri, and S. Azadi. "A Novel Method to Estimate Parameters of the Wall-Wetting Fuel Model in MPFI Engines for Cold Start and Warm Up Conditions".

Proceeding of ASME Internal Combustion Engine Fall Technical Conference, 2004.

[187] L. Ljung. *System Identification: Theory for the User*. Prentice Hall PTR, Second Edition, 1999.

[188] X. Tang and J. R. Asik. "Optimal A/F Ratio Estimation Model (Synthetic UEGO) for SI Engine Cold Transient AFR Feedback Control". SAE Paper No. 980798, 1998.

[189] E. Hendricks and S. C. Sorenson. "Mean Value Modelling of Spark Ignition Engines". SAE Paper No. 900616, 1990.

[190] M. Shahbakhti, A. Ghazimirsaied, and C. R. Koch. "Predicting the Distribution of Combustion Timing Ensemble in an HCCI Engine". *ASME Internal Combustion Engine Division Spring Technical Conference*, Paper No. ICES2009-76007, 2009.

[191] J. Chang, Z. Filipi, D. Assanis, T. Kuo, P. Najt, and R. Rask. "NIST/SEMATECH e-Handbook of Statistical Methods". *http://www.itl.nist.gov/div898/handbook/*, 2008.

[192] A. Ghazimirsaied, M. Shahbakhti, A. Audet, and C. R. Koch. "Chaotic and Statistical Methods Approach to Characterize Cyclic Variation in an HCCI Engine". *Proceeding of Combustion Institute/Canadian Section (CI/CS) Spring Technical Conference*, 2008.

[193] MathWorks. *Statistics Toolbox in Matlab®*. R2006a, Version 7.2.

[194] E. Castillo, A. S. Hadi, N. Balakrishnan, and J. M. Sarabia. *Extreme Value and Related Models with Applications in Engineering and Science*. John Wiley & Sons Publication, 2005.

[195] S. Kotz and S. Nadarajah. *Extreme Value Distributions: Theory and Applications*. Imperial College Press, 2000.

[196] S. Coles. *An Introduction to Statistical Modeling of Extreme Values*. Springer Series in Statistics, 2001.

[197] R.R. Chladny and C.R. Koch. "Flatness-Based Tracking of an Electromechanical VVT Actuator with Disturbance Observer Feed-Forward Compensation", journal = IEEE Transactions on Control Systems Technology, year = 2008, volume = 16, pages = 652-663.

[198] A. Ghazimirsaied, M. Shahbakhti, and C. R. Koch. "Partial-Burn Crank Angle Limit Criteria Comparison on an Experimental HCCI Engine". *Proceeding of Combustion Institute/Canadian Section (CI/CS) Spring Technical Conference*, 2009.

[199] E. Korin, R. Reshef, D. Tshernichovesky, and E. Sher. "Reducing Cold-Start Emission from Internal Combustion Engines by Means of a Catalytic Converter Embedded in a Phase-Change Material". *Proceeding of IMechE - Part D*, 213:575 – 583, 1999.

[200] M. D. Checkel and J. D. Dale. "Computerized Knock Detection from Engine Pressure Records". SAE Paper No. 860028, 1986.

[201] Y. A. Cengel and M. A. Boles. *Thermodynamics: An Engineering Approach*. McGraw Hill, 3rd edition, 1998.

[202] N. M. Marinov, C. K. Westbrook, and W. J. Pitz. "Detailed and Global Chemical Kinetics Model for Hydrogen". *Lawrence Livermore National Laboratory*.

[203] S. Soylu. "Examination of Combustion Characteristics of an HCCI Engine". *ASME Internal Combustion Engine Fall Technical Conference*, ICEF2004-840, 2004.

Appendix A

HCCI Cyclic Variation Experimental Data Summary

Summary of HCCI cyclic variation experiments from Ricardo engine

#	Fuel	Engine operating conditions						Combustion timing Mean of 200 individual cycles (CAD aTDC)				Cyclic variation of combustion timing STD (CAD)				IMEP		P_{max}		BD	
		Speed	EGR	Φ	T_m	P_m	T_c	SOC_{CF}	SOC	CA_{50}	$\theta_{P_{max}}$	SOC_{CF}	SOC	CA_{50}	$\theta_{P_{max}}$	Mean	COV	Mean	COV	Mean	COV
	ON	(rpm)	(%)	(-)	(^{o}C)	(kPa)	(^{o}C)									(bar)	(%)	(bar)	(%)	(CAD)	(%)
1	0	800	0	0.49	140	93	75	-17.3	3.7	7.7	10.4	2.0	0.8	0.9	1.0	4.0	1.8	38.4	4.1	3.5	9.8
2	0	800	0	0.51	120	93	75	-14.6	5.2	9.3	12.1	0.8	0.9	1.1	1.2	4.3	1.9	38.1	4.8	3.7	10.8
3	0	800	19	0.68	100	93	75	-12.5	6.2	10.4	13.1	0.6	1.6	1.7	1.8	4.7	2.6	38.8	7.2	3.8	15.4
4	0	800	24	0.77	100	93	75	-13.7	2.6	6.2	8.6	0.6	0.5	0.6	0.6	4.8	1.6	44.9	2.4	2.8	4.5
5	0	800	28	0.85	100	93	75	-12.0	9.8	14.1	16.7	1.6	3.0	2.5	2.0	5.1	2.6	36.7	7.9	4.3	14.7
6	0	800	1	0.48	120	93	75	-15.8	1.3	4.9	7.5	0.8	0.3	0.4	0.4	4.1	1.3	41.0	1.5	3.0	3.6
7	0	800	2	0.51	120	93	75	-16.2	1.3	4.9	7.5	1.7	0.4	0.4	0.4	4.1	1.5	41.3	1.5	3.0	4.2
8	0	800	9	0.53	120	93	75	-15.6	4.1	8.1	11.1	2.4	0.6	0.6	0.7	3.9	1.6	36.5	2.7	4.0	6.4
9	0	800	5	0.60	80	93	75	-10.4	6.8	11.0	13.7	0.4	1.0	1.1	1.2	4.9	2.0	40.0	4.8	3.6	12.0
10	0	800	9	0.65	80	93	75	-10.7	5.7	9.7	12.2	0.4	0.8	1.0	1.1	5.0	1.8	42.3	4.1	3.2	9.6
11	0	800	12	0.68	80	93	75	-10.7	5.7	9.6	12.1	0.3	0.7	0.8	0.9	5.1	1.7	42.8	3.1	3.2	8.0
12	0	800	17	0.72	80	93	75	-11.5	3.9	7.6	10.0	0.5	0.6	0.7	0.8	5.1	1.8	45.8	3.0	2.8	5.7
13	0	800	21	0.79	80	92	75	-10.3	7.6	11.8	14.3	0.6	0.9	1.0	1.0	5.3	1.5	41.5	4.1	3.5	9.4
14	0	800	25	0.87	80	93	75	-11.3	3.9	7.5	9.8	0.6	0.6	0.6	0.7	5.2	1.9	46.6	2.6	2.8	4.5
15	0	800	28	0.94	80	93	75	-10.5	7.4	11.5	14.0	0.8	0.6	0.7	0.8	5.6	1.4	43.0	3.2	3.3	6.8
16	0	800	14	0.62	100	93	75	-13.1	5.7	9.9	12.7	1.1	1.2	1.3	1.5	4.4	2.9	37.9	6.2	3.9	14.4
17	0	800	24	0.87	118	93	75	-15.4	4.3	8.1	10.4	1.4	1.0	1.2	1.3	5.0	2.6	44.3	5.6	2.9	10.2
18	0	800	27	0.93	125	91	75	-14.2	12.2	16.4	19.1	1.4	3.7	2.9	2.5	5.1	4.6	34.7	10.8	4.6	20.2
19	0	800	0	0.56	121	94	75	-15.3	2.7	6.4	8.8	0.7	0.9	1.0	1.1	4.4	2.1	42.3	3.4	2.9	6.7
20	0	800	8	0.63	106	95	75	-15.0	2.4	6.0	8.5	0.8	0.8	0.9	0.9	4.5	2.6	43.5	3.8	2.9	7.9
21	0	800	16	0.69	109	96	75	-14.9	2.9	6.7	9.1	0.7	0.9	1.0	1.1	4.6	2.1	43.3	4.4	2.9	8.3
22	0	800	22	0.79	114	96	75	-14.5	5.8	10.0	12.6	1.3	0.9	1.1	1.3	4.9	2.4	40.7	5.1	3.5	11.9
23	0	1000	0	0.56	120	93	75	-14.6	7.9	12.0	14.7	0.5	2.2	2.1	2.0	4.7	2.8	37.9	7.7	3.8	17.3
24	0	1000	0	0.57	100	93	75	-12.8	10.2	14.2	16.6	2.5	4.0	3.3	2.6	4.8	4.6	36.5	10.3	4.1	16.9
25	0	1000	12	0.63	100	94	75	-13.0	7.3	11.5	14.3	0.4	1.9	1.9	2.0	4.7	3.3	38.2	8.2	4.1	17.7
26	0	1000	18	0.67	100	94	75	-13.3	6.8	11.0	13.7	0.5	2.1	2.1	2.3	4.7	3.8	39.0	9.4	4.0	21.4
27	0	1000	23	0.72	100	94	75	-13.7	5.4	9.5	12.1	0.6	1.4	1.6	1.7	4.9	3.1	41.5	6.8	3.5	16.1
28	0	1000	27	0.80	100	94	75	-14.0	5.5	9.5	12.1	0.6	1.6	1.8	2.0	5.0	3.2	42.5	7.5	3.4	16.3
29	0	1000	1	0.49	100	94	75	-13.7	6.2	10.3	13.0	0.3	2.1	1.9	1.7	4.4	3.2	38.2	6.9	3.9	15.0
30	0	1000	9	0.58	100	94	75	-13.1	8.6	12.6	15.2	0.4	3.5	2.8	2.2	4.6	3.7	36.3	9.0	4.3	18.3
31	0	900	0	0.56	100	93	75	-12.7	7.3	11.6	14.3	0.9	1.2	1.3	1.4	4.8	2.2	38.5	5.7	3.8	12.9
32	0	900	0	0.56	120	93	75	-14.5	5.6	9.7	12.3	0.8	1.2	1.4	1.5	4.5	2.2	39.5	5.6	3.5	11.8
33	0	900	0	0.51	140	93	75	-16.8	6.7	10.9	13.7	1.5	1.9	1.7	1.5	4.2	2.3	35.7	6.2	4.1	13.5
34	0	900	2	0.49	100	94	75	-14.0	3.5	7.4	10.1	0.4	1.0	1.2	1.3	4.4	2.6	41.0	5.0	3.4	12.2
35	0	900	7	0.54	100	94	75	-13.6	5.3	9.4	12.2	0.4	1.9	1.8	1.8	4.4	3.3	38.5	7.0	3.9	15.6

continued on next page...

#	Fuel	Engine operating conditions						Combustion timing Mean of 200 individual cycles (CAD aTDC)				Cyclic variation of combustion timing STD (CAD)				IMEP		P_{max}		BD	
	ON	Speed (rpm)	EGR (%)	Φ (-)	T_m (^{o}C)	P_m (kPa)	T_c (^{o}C)	SOC_{CF}	SOC	CA_{50}	$\theta_{P_{max}}$	SOC_{CF}	SOC	CA_{50}	$\theta_{P_{max}}$	Mean (bar)	COV (%)	Mean (bar)	COV (%)	Mean (CAD)	COV (%)
36	0	900	10	0.58	100	94	75	-13.5	4.4	8.4	11.1	0.5	1.3	1.5	1.6	4.5	2.8	40.6	6.4	3.5	14.8
37	0	900	15	0.63	100	94	75	-13.2	5.6	9.7	12.4	0.7	1.7	1.9	2.1	4.6	3.4	39.7	8.2	3.8	19.3
38	0	900	19	0.67	100	94	75	-13.2	5.7	9.8	12.5	1.0	1.5	1.8	2.0	4.7	3.1	39.9	7.9	3.7	17.2
39	0	900	22	0.71	100	94	75	-13.7	4.0	7.9	10.4	0.6	1.2	1.3	1.5	4.8	2.6	43.1	5.6	3.2	11.9
40	0	1100	0	0.57	140	93	75	-17.3	8.0	12.1	14.7	0.9	2.8	2.8	2.7	4.6	2.8	37.7	9.6	3.8	18.9
41	0	1100	6	0.58	100	94	75	-13.3	7.8	12.1	14.9	0.5	2.2	2.0	1.9	4.7	3.8	37.5	8.1	4.2	17.3
42	0	1100	12	0.64	100	94	75	-12.6	10.1	14.3	16.9	2.3	3.5	2.8	2.2	4.7	6.6	35.7	9.4	4.5	18.6
43	0	1100	15	0.68	100	94	75	-12.0	9.7	13.9	16.5	4.3	3.5	2.9	2.4	4.8	6.0	36.8	9.5	4.3	18.7
44	0	1100	20	0.75	100	94	75	-14.1	5.1	9.0	11.5	0.4	1.3	1.5	1.7	5.0	2.7	43.6	6.5	3.2	13.0
45	0	1100	4	0.54	120	94	75	-15.6	5.8	9.9	12.7	0.4	1.8	1.8	1.8	4.4	2.9	38.1	7.2	3.9	17.1
46	0	1100	14	0.63	120	94	75	-15.2	8.2	12.3	15.0	0.5	3.5	3.0	2.5	4.5	3.6	36.4	10.4	4.4	20.0
47	0	1100	17	0.68	120	94	75	-15.0	8.8	13.1	16.0	0.5	2.5	2.2	2.1	4.6	4.2	36.1	8.9	4.4	18.6
48	0	1100	2	0.48	140	94	75	-18.1	5.2	9.3	12.3	0.7	1.0	1.1	1.3	4.0	2.5	36.3	5.2	4.1	12.6
49	0	1100	8	0.54	140	93	75	-17.7	7.6	11.8	14.6	0.9	2.3	2.0	1.7	4.0	3.5	34.1	7.4	4.6	17.7
50	0	1100	14	0.61	140	93	75	-17.2	7.9	12.1	14.9	0.7	2.8	2.5	2.0	4.2	3.4	34.8	8.1	4.5	16.7
51	0	1100	23	0.71	140	93	75	-16.5	9.4	13.6	16.4	0.6	2.7	2.2	1.9	4.5	3.8	35.0	7.9	4.5	15.7
52	0	1193	0	0.56	100	102	68	-12.0	12.6	16.5	19.1	0.5	3.5	2.5	1.6	5.2	2.1	34.7	6.6	4.9	16.2
53	0	1193	0	0.57	101	99	71	-12.6	8.8	13.1	15.9	0.5	1.1	1.1	1.2	5.2	1.9	39.0	4.5	4.2	10.0
54	0	1193	0	0.58	100	100	54	-10.8	12.5	16.6	19.2	0.3	3.3	2.3	1.6	5.4	2.1	35.8	6.4	4.9	16.1
55	0	1193	0	0.60	99	102	52	-10.6	8.9	13.3	16.1	0.4	2.0	1.4	1.5	5.6	1.9	40.7	5.2	4.0	10.7
56	0	908	0	0.42	102	110	74	-14.8	0.9	4.8	7.6	1.3	1.3	0.7	0.8	4.7	1.8	45.9	2.6	3.4	21.8
57	0	1038	0	0.42	100	110	77	-14.5	4.6	8.8	11.8	0.7	1.1	1.1	1.1	4.7	1.8	41.0	4.1	4.4	10.1
58	0	907	0	0.49	100	90	78	-13.6	11.6	15.0	17.2	0.5	3.7	2.3	1.2	4.0	1.9	30.5	4.8	4.7	21.1
59	0	907	0	0.49	100	94	78	-14.3	3.6	7.5	10.1	0.8	0.6	0.5	0.6	4.4	1.7	40.4	1.9	3.3	5.4
60	0	907	0	0.49	101	98	79	-14.6	2.0	5.7	8.2	1.0	0.5	0.5	0.5	4.5	2.2	43.6	1.5	3.0	4.7
61	0	908	0	0.49	99	99	80	-14.5	1.7	5.3	7.7	0.5	0.5	0.5	0.5	4.5	2.6	44.5	1.6	2.9	4.0
62	0	908	0	0.49	100	101	80	-14.9	0.3	4.0	6.4	0.8	1.5	0.4	0.4	4.6	2.9	46.5	1.4	2.8	22.9
63	0	901	0	0.51	80	91	71	-9.8	9.0	13.5	16.4	0.3	3.3	1.6	1.1	4.3	1.9	33.2	4.7	4.9	38.0
64	0	900	0	0.47	88	91	74	-11.1	14.0	16.7	17.7	2.7	4.4	2.9	1.1	3.8	3.9	27.7	9.6	4.6	29.6
65	0	899	0	0.48	88	91	75	-11.6	9.3	13.3	16.1	0.7	3.0	2.1	1.2	4.0	1.8	31.8	5.4	4.8	16.7
66	0	899	0	0.50	87	90	75	-11.5	5.9	10.0	12.8	0.5	0.7	0.8	0.9	4.2	1.5	36.7	3.4	3.8	8.1
67	0	901	0	0.43	90	100	71	-11.6	8.2	12.3	14.7	0.5	4.5	2.4	1.1	4.1	2.1	34.3	5.5	5.1	50.2
68	0	900	0	0.36	91	110	71	-12.6	8.9	12.4	13.4	2.6	5.8	2.6	1.0	3.8	7.0	32.3	10.5	5.5	77.9
69	0	900	0	0.37	92	111	68	-12.8	6.4	10.6	12.7	0.5	5.8	2.6	1.1	4.0	3.0	36.4	6.8	5.4	66.8
70	0	968	0	0.55	91	89	76	-11.3	6.2	10.2	12.8	0.6	0.9	1.0	1.1	4.4	1.8	38.1	3.6	3.4	8.0
71	0	1065	0	0.56	92	89	76	-11.3	9.3	13.8	16.5	0.4	2.8	1.7	1.5	4.6	2.2	34.5	6.2	4.3	20.1
72	0	1113	0	0.56	91	89	76	-7.7	16.5	20.5	21.9	8.5	7.1	3.3	1.9	4.2	12.6	24.2	15.4	4.9	45.3
73	0	873	0	0.48	60	113	77	-10.5	-1.2	1.8	4.3	0.4	1.1	0.6	0.6	5.3	3.1	56.2	2.0	9.3	5.4

continued on next page...

#	Fuel	Engine operating conditions						Combustion timing Mean of 200 individual cycles (CAD aTDC)				Cyclic variation of combustion timing STD (CAD)				IMEP		P_{max}		BD	
	ON	Speed (rpm)	EGR (%)	Φ (-)	T_m (^{o}C)	P_m (kPa)	T_c (^{o}C)	SOC_{CF}	SOC	CA_{50}	$\theta_{P_{max}}$	SOC_{CF}	SOC	CA_{50}	$\theta_{P_{max}}$	Mean (bar)	COV (%)	Mean (bar)	COV (%)	Mean (CAD)	COV (%)
74	0	919	0	0.48	60	113	75	-9.7	0.2	3.7	6.2	0.3	2.1	0.9	1.0	5.4	2.7	54.1	3.7	10.1	11.9
75	0	1064	0	0.49	61	113	77	-9.3	3.1	6.7	9.4	0.5	2.5	2.0	2.1	5.7	2.6	51.5	7.2	11.3	27.4
76	0	1112	0	0.48	63	113	78	-9.2	5.2	8.9	11.7	0.6	2.8	2.3	2.3	5.6	2.2	47.7	8.0	12.0	37.0
77	0	1160	0	0.48	65	113	79	-9.6	4.7	9.1	11.9	0.5	4.3	2.9	3.1	5.6	2.8	48.0	11.2	11.6	41.9
78	0	1016	0	0.45	88	99	80	-12.2	7.6	12.6	15.2	2.2	5.6	2.9	1.1	4.1	3.9	29.3	10.2	5.4	42.9
79	0	1016	0	0.44	88	103	79	-11.9	12.3	15.9	17.4	0.3	5.7	2.2	1.3	4.4	2.8	35.0	6.1	5.7	65.1
80	10	800	1	0.54	116	94	75	-13.6	10.4	14.6	17.3	0.3	3.5	2.3	1.4	4.6	2.7	33.9	5.6	4.6	16.4
81	10	800	4	0.61	128	94	75	-15.9	4.0	7.8	10.3	0.5	1.0	1.1	1.1	4.6	2.2	41.9	3.2	3.1	5.8
82	10	800	6	0.67	79	94	75	-10.8	5.5	9.3	11.7	0.4	0.5	0.6	0.6	5.3	1.7	44.6	1.9	3.0	4.3
83	10	800	1	0.48	120	93	75	-13.7	5.3	9.4	11.9	0.6	1.1	1.2	1.2	4.7	1.8	40.6	3.4	3.3	6.9
84	10	800	0	0.49	130	94	75	-15.2	5.5	9.5	12.2	0.6	1.3	1.5	1.6	4.4	2.6	38.8	5.8	3.5	13.1
85	10	800	1	0.43	133	93	75	-14.6	5.9	10.0	12.6	0.5	1.2	1.3	1.4	4.5	2.7	38.8	4.8	3.5	9.7
86	10	800	1	0.47	127	94	75	-14.5	6.3	10.5	13.1	0.4	1.2	1.3	1.5	4.5	2.9	38.1	5.4	3.6	12.7
87	10	800	7	0.65	105	94	75	-14.8	2.6	6.1	8.5	0.9	0.4	0.5	0.5	4.7	1.7	44.9	1.8	2.7	3.2
88	10	800	19	0.80	82	94	75	-11.7	6.7	10.6	13.0	0.9	0.7	0.7	0.8	5.3	1.3	43.4	2.8	3.0	5.7
89	10	800	0	0.53	70	94	75	-10.4	6.4	11.3	14.1	0.8	4.4	2.3	2.1	4.6	4.3	37.8	9.0	4.5	54.0
90	10	800	0	0.53	80	94	75	-11.2	4.7	9.6	12.3	1.7	3.7	1.5	1.6	4.7	3.1	39.7	7.0	4.1	41.2
91	10	800	0	0.52	90	94	75	-12.1	4.6	9.4	12.2	0.5	3.3	1.4	1.6	4.5	3.0	38.7	6.7	4.1	39.4
92	10	800	5	0.55	90	93	75	-12.4	5.1	9.7	12.5	0.5	2.6	1.3	1.4	4.5	2.9	38.2	6.0	4.1	23.1
93	10	800	10	0.59	90	93	75	-12.0	8.2	12.5	15.2	0.5	3.0	2.4	1.9	4.5	3.6	35.4	8.1	4.6	18.0
94	10	800	15	0.66	90	93	75	-10.9	8.5	12.9	15.7	0.4	3.5	2.4	2.0	4.7	3.7	36.4	8.4	4.4	19.2
95	10	800	20	0.72	90	93	75	-12.3	4.3	8.4	11.0	0.8	2.6	0.9	1.0	5.0	2.3	42.9	4.3	3.4	48.6
96	10	800	24	0.79	90	93	75	-11.7	6.4	10.5	13.1	0.7	1.3	1.5	1.7	5.1	3.0	41.1	7.0	3.5	14.8
97	10	1000	0	0.55	80	94	75	-11.9	9.0	13.1	15.6	0.3	3.4	2.8	2.2	4.7	3.6	36.8	9.2	4.2	19.3
98	10	1000	7	0.59	80	94	75	-9.7	10.7	14.8	17.6	5.1	2.9	2.2	1.9	4.8	8.7	35.9	8.1	4.6	17.6
99	10	1000	10	0.63	80	94	75	-11.2	7.6	11.8	14.5	0.5	2.7	2.6	2.6	5.1	3.8	40.1	9.8	3.9	21.5
100	10	1000	6	0.59	90	94	75	-12.4	9.6	14.9	17.5	2.4	6.6	3.0	2.4	4.7	4.9	34.7	10.2	5.3	60.4
101	10	1000	9	0.63	90	94	75	-11.9	10.3	14.3	16.8	1.7	3.9	3.0	2.3	4.8	5.9	36.2	9.3	4.3	19.8
102	10	1000	13	0.68	90	94	75	-12.3	7.8	12.3	15.0	2.9	3.7	2.5	2.4	5.0	3.7	38.9	9.2	4.3	56.4
103	10	1000	9	0.60	100	94	75	-12.6	10.0	14.3	16.4	3.5	5.9	4.4	2.3	4.6	5.2	35.4	9.4	4.6	49.9
104	10	1000	12	0.63	100	94	75	-11.8	10.7	15.1	17.6	4.3	4.7	3.1	2.2	4.7	5.3	34.6	9.3	4.9	35.1
105	10	1000	16	0.68	100	94	75	-12.0	10.8	15.4	17.8	4.6	6.4	3.6	2.6	4.8	4.9	35.0	10.7	5.0	71.5
106	10	1000	0	0.51	100	94	75	-13.9	8.9	12.9	15.6	0.4	3.2	2.5	2.0	4.3	4.8	34.8	8.5	4.6	20.0
107	10	1000	0	0.52	110	94	75	-15.2	6.4	11.0	13.8	0.5	3.3	1.8	1.6	4.3	2.6	36.1	6.5	4.4	53.9
108	10	1000	0	0.53	90	94	75	-12.8	7.5	12.1	14.8	0.6	4.4	2.2	1.9	4.6	3.6	37.2	8.0	4.5	54.6
109	10	1000	0	0.50	120	94	75	-15.1	7.2	11.4	14.3	0.5	2.2	1.8	1.6	4.3	3.4	35.4	6.8	4.4	15.0
110	10	1000	7	0.56	120	94	75	-15.2	8.3	12.5	15.3	0.4	2.9	2.2	1.7	4.3	3.4	34.5	7.3	4.7	17.6
111	10	1000	7	0.56	110	94	75	-14.0	9.5	13.7	16.2	2.4	4.3	2.8	1.9	4.3	4.9	34.1	8.4	4.7	21.2

continued on next page...

#	Fuel	Engine operating conditions						Combustion timing Mean of 200 individual cycles (CAD aTDC)				Cyclic variation of combustion timing STD (CAD)				IMEP		P_{max}		BD	
	ON	Speed (rpm)	EGR (%)	Φ (-)	T_m (^{o}C)	P_m (kPa)	T_c (^{o}C)	SOC_{CF}	SOC	CA_{50}	$\theta_{P_{max}}$	SOC_{CF}	SOC	CA_{50}	$\theta_{P_{max}}$	Mean (bar)	COV (%)	Mean (bar)	COV (%)	Mean (CAD)	COV (%)
112	10	1000	7	0.59	100	94	75	-12.5	10.0	14.0	16.6	0.4	3.6	2.6	1.9	4.6	4.4	35.2	8.3	4.6	21.9
113	10	1000	2	0.56	80	94	75	-11.1	9.6	13.7	16.2	0.3	3.8	3.0	2.4	4.9	3.8	36.9	9.9	4.3	21.4
114	10	1000	1	0.50	90	94	75	-13.5	8.5	13.0	15.7	1.0	4.3	2.5	2.1	4.5	4.2	35.6	8.6	4.6	40.3
115	10	1000	0	0.54	90	94	75	-13.1	8.6	12.8	15.5	0.4	2.7	2.3	2.1	4.6	3.6	36.2	8.5	4.3	17.8
116	10	1100	0	0.57	90	93	75	-13.1	8.6	12.8	15.5	0.3	2.6	2.3	2.3	4.9	3.7	37.8	9.4	4.1	20.2
117	10	1100	0	0.55	100	93	75	-12.9	10.4	14.6	17.3	5.4	3.4	2.6	2.1	4.5	11.8	34.4	9.2	4.8	21.6
118	10	1100	0	0.55	110	93	75	-15.0	8.2	12.2	14.9	0.4	3.0	2.5	2.3	4.6	3.0	36.8	9.3	4.1	19.4
119	10	1100	0	0.56	110	93	75	-15.2	6.6	10.8	13.4	0.4	1.8	1.8	1.9	4.6	2.5	38.9	7.1	3.8	16.3
120	10	1100	0	0.53	120	93	75	-16.1	8.3	12.7	15.5	0.4	2.3	1.9	1.7	4.4	3.4	34.9	7.2	4.6	16.1
121	10	1100	0	0.52	130	93	75	-17.1	9.1	13.2	15.9	0.5	3.1	2.4	1.8	4.2	3.0	33.4	7.9	4.7	16.7
122	10	1100	0	0.50	130	93	75	-16.8	10.6	14.4	16.8	2.9	3.9	2.9	1.7	4.1	6.3	32.2	7.7	4.9	16.9
123	10	1100	3	0.55	130	93	75	-16.8	8.9	13.2	16.0	0.4	2.7	2.1	1.7	4.2	4.5	33.7	7.4	4.7	17.2
124	10	1100	9	0.63	130	93	75	-16.2	8.9	13.1	16.0	0.4	2.4	2.0	1.9	4.5	3.7	35.2	7.7	4.4	17.9
125	10	1100	14	0.67	130	93	75	-15.4	10.9	15.2	17.7	3.6	4.9	3.1	2.4	4.6	5.8	33.8	9.4	4.6	23.9
126	10	950	0	0.56	80	94	75	-10.8	7.1	11.9	14.6	1.2	4.0	1.9	2.1	5.0	2.8	39.0	8.2	4.2	46.8
127	10	950	0	0.57	80	94	75	-11.5	6.8	11.0	13.6	0.6	1.7	1.8	1.9	4.9	2.9	39.9	7.4	3.7	16.3
128	20	800	22	0.75	90	94	75	-14.2	4.1	7.9	10.4	0.5	0.8	1.0	1.1	4.9	2.0	43.0	4.4	3.1	8.9
129	20	800	25	0.83	90	94	75	-13.7	4.9	8.8	11.3	0.6	1.1	1.3	1.4	5.1	2.6	43.3	5.8	3.1	11.2
130	20	800	27	0.87	90	94	75	-12.7	8.2	12.8	15.4	0.5	3.2	1.7	1.5	5.2	2.0	39.0	5.9	4.0	49.0
131	20	800	28	0.95	90	94	75	-12.3	8.2	12.3	14.9	0.6	1.7	1.6	1.7	5.5	2.5	41.1	6.6	3.5	13.0
132	20	800	0	0.53	80	94	75	-12.8	7.2	11.6	14.4	0.4	2.8	1.4	1.6	4.6	2.9	39.8	6.6	3.8	33.8
133	20	800	0	0.53	90	94	75	-11.7	4.8	9.2	11.9	0.5	2.2	1.9	1.8	4.5	3.0	36.6	7.5	4.3	17.2
134	20	800	2	0.53	90	94	75	-13.4	5.4	9.5	12.2	0.4	1.1	1.3	1.5	4.6	2.5	39.5	5.9	3.6	14.3
135	20	800	10	0.63	90	94	75	-12.7	9.8	13.8	16.4	0.5	3.8	2.9	2.2	4.7	4.0	35.4	9.4	4.4	19.6
136	20	800	17	0.70	90	94	75	-14.4	3.1	6.7	9.2	0.5	0.7	0.8	0.9	4.8	2.1	44.5	3.7	2.9	7.5
137	20	1000	11	0.75	100	91	75	-14.2	6.8	10.6	13.0	0.4	0.6	0.6	0.6	5.5	1.8	45.5	2.0	2.9	3.2
138	20	1000	9	0.73	100	94	75	-14.8	6.4	10.2	12.5	0.4	0.5	0.5	0.5	5.4	2.1	45.2	1.8	3.0	3.6
139	20	1000	7	0.76	83	95	75	-12.7	10.0	14.1	16.5	0.4	0.7	0.8	0.9	5.9	1.8	42.9	2.9	3.3	7.0
140	20	1000	0	0.66	113	93	75	-16.6	3.5	7.0	9.2	0.8	0.7	0.7	0.7	5.0	2.9	47.6	1.8	2.5	4.3
141	20	1000	2	0.65	110	92	75	-16.0	5.5	9.2	11.5	1.2	0.5	0.5	0.6	5.1	2.5	44.8	1.6	2.8	3.6
142	20	1053	0	0.49	105	111	79	-13.6	9.1	12.9	15.2	1.7	1.1	1.2	1.2	7.4	2.1	49.9	4.1	3.3	8.3
143	20	801	0	0.51	100	91	77	-12.0	21.9	24.9	26.4	2.5	4.1	2.7	1.1	5.7	3.1	29.1	4.8	5.2	25.1
144	20	801	0	0.51	100	95	77	-12.2	11.9	16.0	18.6	2.5	0.6	0.6	0.7	6.4	1.3	39.9	2.4	3.9	5.8
145	20	801	0	0.51	100	100	77	-12.3	7.3	10.8	13.1	2.2	0.6	0.7	0.7	6.7	2.3	47.6	1.6	3.0	4.9
146	20	801	0	0.44	100	101	77	-12.6	18.1	21.7	23.5	2.5	4.0	2.6	1.0	5.9	2.8	32.2	4.1	5.8	19.2
147	20	801	0	0.44	100	104	76	-12.3	12.6	17.1	20.0	2.1	1.0	1.0	1.1	6.3	1.6	37.6	4.4	5.4	9.8
148	20	801	0	0.44	101	111	76	-12.9	8.7	12.7	15.3	2.4	0.8	0.9	0.9	6.9	1.6	45.6	3.1	4.2	6.8
149	20	801	0	0.43	101	116	76	-13.1	5.5	9.5	11.9	2.2	2.1	0.9	0.9	7.3	2.0	51.0	2.7	4.0	31.7

continued on next page...

#	Fuel	Engine operating conditions						Combustion timing Mean of 200 individual cycles (CAD aTDC)				Cyclic variation of combustion timing STD (CAD)				IMEP		P_{max}		BD	
	ON	Speed (rpm)	EGR (%)	Φ (-)	T_m (^{o}C)	P_m (kPa)	T_c (^{o}C)	SOC_{CF}	SOC	CA_{50}	$\theta_{P_{max}}$	SOC_{CF}	SOC	CA_{50}	$\theta_{P_{max}}$	Mean (bar)	COV (%)	Mean (bar)	COV (%)	Mean (CAD)	COV (%)
150	20	801	0	0.47	120	92	75	-13.3	21.2	24.1	25.1	3.5	4.1	2.7	1.2	5.1	5.8	28.3	5.2	5.6	35.1
151	20	801	0	0.46	119	95	75	-13.4	13.2	17.7	20.6	2.8	1.1	0.9	0.9	5.8	1.2	34.6	3.5	5.3	7.8
152	20	801	0	0.46	120	101	75	-13.2	10.1	14.2	16.8	2.5	0.6	0.6	0.7	6.2	1.2	40.3	2.4	4.3	6.7
153	20	801	0	0.47	119	105	75	-13.5	6.2	9.7	12.1	2.4	0.4	0.5	0.5	6.6	2.1	47.5	1.6	3.4	5.2
154	20	801	0	0.34	120	114	75	-14.8	13.4	17.1	18.5	2.6	3.9	2.5	0.7	5.7	2.5	36.6	2.8	6.7	16.8
155	20	801	0	0.38	120	115	74	-14.4	6.8	11.0	13.8	2.3	0.6	0.7	0.7	6.5	1.1	44.6	2.3	5.3	6.5
156	20	800	0	0.39	120	114	74	-14.5	6.5	10.6	13.3	2.7	0.6	0.7	0.7	6.5	1.3	45.4	2.1	5.1	7.2
157	20	800	0	0.41	121	116	74	-14.2	4.8	8.5	11.1	2.4	0.5	0.6	0.6	6.8	1.6	48.9	1.6	4.3	8.9
158	20	801	0	0.43	120	115	75	-14.3	3.9	7.6	10.1	2.4	1.1	0.5	0.5	6.9	2.1	50.4	1.4	4.1	18.5
159	20	800	0	0.43	100	100	74	-12.8	18.0	21.6	23.4	2.8	3.8	2.4	0.7	5.7	2.7	31.7	3.2	6.1	18.3
160	20	800	0	0.46	100	100	74	-12.4	11.3	15.6	18.3	2.8	0.7	0.7	0.7	6.4	1.2	39.7	2.7	4.5	7.0
161	20	800	0	0.49	100	100	74	-12.2	9.6	13.5	16.0	2.6	0.5	0.5	0.6	6.6	1.3	43.3	2.0	3.7	5.3
162	20	800	0	0.52	100	99	75	-12.4	5.9	9.3	11.6	2.6	0.6	0.6	0.6	6.6	2.4	48.8	1.4	2.8	5.6
163	20	1003	0	0.29	123	145	77	-16.2	7.2	12.7	16.7	2.3	0.7	0.7	0.7	7.0	1.9	45.5	3.4	9.5	5.6
164	20	1004	0	0.37	119	134	78	-15.2	4.8	9.0	11.8	2.0	0.5	0.5	0.6	7.7	1.4	53.9	1.8	5.6	7.6
165	20	1003	0	0.34	117	133	78	-15.0	7.7	12.6	15.8	2.3	0.7	0.8	0.8	7.1	1.7	46.8	3.2	6.9	7.3
166	20	1003	0	0.37	128	126	78	-15.6	6.4	10.5	13.3	2.5	0.9	0.9	0.9	7.1	1.3	49.1	2.9	5.4	7.5
167	20	1003	0	0.36	133	125	78	-16.1	6.6	11.0	13.9	2.2	0.9	1.0	1.0	6.9	1.4	47.5	3.2	5.8	6.9
168	20	1003	0	0.39	132	118	78	-16.1	7.8	11.9	14.7	2.6	1.0	1.0	1.1	6.7	1.6	45.3	3.5	5.0	7.4
169	20	1003	0	0.42	129	117	79	-15.7	6.2	9.9	12.5	2.4	0.8	0.9	0.9	7.0	1.9	49.4	2.7	4.0	8.7
170	20	1003	0	0.43	124	109	79	-15.1	10.6	14.8	17.5	2.7	0.8	0.9	0.9	6.5	1.3	41.5	3.2	4.7	7.6
171	20	1003	0	0.46	120	108	80	-14.5	9.4	13.4	15.9	2.7	0.8	0.7	0.8	6.8	1.4	44.6	2.6	4.0	6.2
172	20	1003	0	0.48	116	104	80	-14.4	11.8	16.0	18.6	2.6	0.7	0.7	0.7	6.6	1.1	40.8	2.5	4.3	6.6
173	20	1003	0	0.44	116	104	80	-14.5	20.5	23.4	24.3	2.9	4.0	2.7	1.0	6.0	2.6	32.1	4.0	5.5	23.2
174	20	1004	0	0.48	65	123	74	-10.1	-1.2	14.7	17.5	2.6	4.0	1.7	1.8	8.9	2.2	54.4	6.4	13.1	25.8
175	20	1003	0	0.54	77	100	76	-11.9	19.0	23.0	25.6	3.2	3.6	2.5	1.7	7.0	2.2	35.6	6.8	5.0	15.2
176	20	1003	0	0.53	72	106	78	-11.6	12.4	17.0	19.5	3.1	2.9	1.0	1.0	7.6	1.3	45.8	3.6	4.0	46.7
177	20	1003	0	0.52	70	108	79	-11.3	12.1	16.5	19.0	2.8	2.3	1.2	1.3	7.8	1.6	47.0	4.5	3.9	35.1
178	20	1003	0	0.54	65	102	80	-10.6	19.8	24.1	26.5	3.2	5.5	2.7	1.8	7.2	2.5	35.7	7.1	5.3	46.2
179	20	1003	0	0.46	64	130	83	-10.9	-4.6	10.7	13.3	2.4	0.4	0.6	0.6	9.1	1.4	61.1	1.9	12.4	5.5
180	20	800	0	0.40	120	118	84	-15.0	4.7	8.4	11.0	2.9	0.6	0.7	0.7	6.9	1.9	49.8	2.3	4.4	10.3
181	20	800	0	0.40	121	119	80	-14.7	4.3	8.0	10.5	2.6	0.6	0.6	0.6	6.9	2.0	50.2	2.1	4.4	10.2
182	20	800	0	0.40	120	119	75	-14.5	4.4	8.2	10.8	2.7	0.6	0.6	0.6	6.9	1.8	50.0	2.2	4.5	10.2
183	20	800	0	0.40	121	120	70	-14.2	4.7	8.4	11.1	2.3	0.6	0.6	0.6	6.9	1.8	49.9	2.1	4.6	9.6
184	20	800	0	0.40	121	119	55	-13.6	6.5	10.6	13.3	2.6	0.7	0.8	0.8	7.0	1.3	47.9	2.6	5.1	7.1
185	20	800	0	0.40	121	117	50	-13.3	7.6	11.9	14.7	3.0	0.8	0.9	1.0	6.9	1.6	45.9	3.4	5.4	7.1
186	20	800	0	0.38	120	119	31	-12.4	12.5	17.2	19.4	2.7	5.7	2.8	1.3	6.7	2.9	40.4	5.6	6.8	42.0
187	20	800	0	0.38	119	119	25	-12.7	16.0	20.1	20.8	2.8	6.9	2.7	0.9	6.5	4.9	38.7	4.4	6.9	60.8

continued on next page...

#	Fuel	Engine operating conditions						Combustion timing Mean of 200 individual cycles (CAD aTDC)				Cyclic variation of combustion timing STD (CAD)				IMEP		P_{max}		BD	
	ON	Speed (rpm)	EGR (%)	Φ (-)	T_m (^{o}C)	P_m (kPa)	T_c (^{o}C)	SOC_{CF}	SOC	CA_{50}	$\theta_{P_{max}}$	SOC_{CF}	SOC	CA_{50}	$\theta_{P_{max}}$	Mean (bar)	COV (%)	Mean (bar)	COV (%)	Mean (CAD)	COV (%)
188	20	907	0	0.59	98	91	74	-14.9	2.3	5.8	8.0	1.4	0.9	0.9	1.0	4.5	3.3	45.4	2.3	2.6	5.1
189	20	907	0	0.59	99	91	75	-15.7	1.4	4.9	7.1	1.5	1.6	0.7	0.8	4.4	3.8	45.9	1.9	2.5	39.6
190	20	810	0	0.56	103	91	78	-16.2	0.1	3.5	5.8	1.1	0.6	0.7	0.7	4.2	3.8	45.3	1.7	2.5	4.1
191	20	907	0	0.56	102	91	79	-13.5	12.4	16.0	18.4	1.0	4.1	2.9	2.0	4.5	1.8	32.2	7.6	4.4	20.0
192	20	810	0	0.46	103	112	78	-15.6	-1.2	2.7	5.2	0.6	2.3	0.7	0.8	4.7	2.8	50.3	2.5	2.8	25.9
193	20	907	0	0.46	104	111	79	-15.7	0.8	4.4	7.0	0.8	0.9	0.8	0.8	4.8	2.0	49.0	2.7	2.9	5.3
194	20	955	0	0.46	103	112	80	-15.3	2.9	6.8	9.5	0.6	1.2	1.4	1.5	4.9	2.0	46.0	5.3	3.3	12.7
195	20	1003	0	0.46	103	111	80	-15.2	4.3	8.5	11.2	0.4	1.6	1.8	1.9	4.9	2.1	44.1	6.8	3.7	14.8
196	20	1052	0	0.46	104	112	80	-15.2	6.8	10.7	13.3	0.4	4.0	3.4	2.8	4.9	3.0	41.7	10.7	4.1	19.1
197	20	1052	0	0.49	104	112	81	-16.1	1.5	5.2	7.6	0.4	1.1	1.2	1.2	5.0	2.7	50.5	4.2	2.8	6.6
198	20	1099	0	0.49	103	111	77	-15.0	5.4	9.6	12.3	0.5	2.1	1.9	2.1	5.2	2.1	44.4	7.4	3.8	15.3
199	40	811	0	0.71	80	89	71	-10.9	9.4	13.4	15.8	1.0	0.9	0.9	0.9	5.6	1.3	41.2	3.1	3.2	6.7
200	40	811	0	0.71	83	89	72	-11.6	7.7	11.5	13.7	1.3	0.7	0.8	0.8	5.5	1.7	43.6	2.6	2.8	4.8
201	40	811	0	0.71	86	89	72	-12.0	7.2	11.0	13.2	1.4	0.8	0.8	0.9	5.4	2.0	44.0	2.8	2.8	5.1
202	40	811	0	0.71	88	89	73	-12.2	6.5	10.2	12.3	1.2	0.6	0.7	0.7	5.4	2.2	45.1	2.1	2.6	4.0
203	40	811	0	0.72	90	89	73	-12.8	6.0	9.5	11.7	1.6	0.6	0.7	0.7	5.3	2.4	45.7	2.0	2.6	4.1
204	40	811	0	0.69	91	89	75	-13.2	7.0	10.8	13.0	1.3	0.7	0.7	0.7	5.3	1.9	42.8	2.5	2.9	5.0
205	40	810	0	0.69	94	89	74	-13.7	6.3	10.0	12.2	1.5	0.6	0.7	0.7	5.2	2.1	43.7	2.2	2.8	4.3
206	40	811	0	0.69	97	89	74	-14.2	5.7	9.3	11.5	1.7	0.6	0.6	0.7	5.2	2.2	44.4	2.2	2.7	4.5
207	40	810	0	0.70	99	89	75	-14.5	4.7	8.2	10.3	1.7	0.5	0.5	0.5	5.1	2.8	45.9	1.8	2.5	3.5
208	40	810	0	0.69	99	89	75	-14.5	5.2	8.8	11.0	1.5	0.5	0.5	0.6	5.1	2.5	44.7	1.9	2.6	3.6
209	40	810	0	0.67	109	89	74	-15.0	6.0	9.8	12.1	1.5	0.7	0.7	0.8	5.0	2.0	42.5	2.5	2.9	5.3
210	40	810	0	0.67	112	89	75	-15.4	5.3	9.0	11.3	1.4	0.6	0.6	0.7	4.9	2.2	43.0	2.2	2.8	4.6
211	40	810	0	0.67	115	89	75	-15.5	5.9	9.7	12.0	1.4	0.7	0.7	0.8	4.9	1.9	41.9	2.4	2.9	5.0
212	40	810	0	0.67	118	89	75	-16.0	5.0	8.6	10.9	1.5	0.6	0.6	0.7	4.9	2.5	43.1	2.2	2.7	4.4
213	40	810	0	0.67	120	89	75	-16.3	4.5	8.2	10.5	1.6	1.7	0.7	0.7	4.8	2.5	43.3	2.1	2.8	38.9
214	40	810	0	0.67	122	89	75	-16.3	4.6	8.2	10.5	1.2	0.6	0.6	0.7	4.8	2.4	43.1	2.2	2.7	4.2
215	40	810	0	0.67	122	89	75	-16.5	4.5	8.1	10.4	1.3	0.6	0.6	0.6	4.8	2.5	43.1	2.0	2.7	4.3
216	40	810	0	0.66	123	90	75	-16.5	4.7	8.4	10.6	1.4	0.6	0.6	0.7	4.8	2.5	42.8	2.1	2.7	4.6
217	40	810	0	0.61	115	96	73	-13.9	13.6	17.2	19.6	1.3	4.6	3.4	2.5	5.0	2.1	33.6	9.3	4.8	26.9
218	40	810	0	0.59	115	99	72	-14.2	11.1	15.5	18.3	1.6	3.0	2.3	1.8	5.1	1.8	35.3	6.9	4.8	18.0
219	40	810	0	0.58	115	101	72	-14.0	10.2	14.6	17.4	1.7	2.3	1.7	1.5	5.2	1.5	36.7	5.7	4.6	14.4
220	40	810	0	0.56	115	104	72	-14.4	7.4	11.8	14.5	1.3	0.9	1.0	1.1	5.2	1.4	40.7	4.1	3.9	10.3
221	40	810	0	0.52	116	111	71	-14.9	5.3	9.4	12.2	1.1	1.1	1.2	1.3	5.3	1.5	44.2	4.7	3.7	10.8
222	40	810	0	0.51	115	114	71	-15.5	4.2	8.1	10.8	1.3	1.1	1.3	1.4	5.3	1.8	46.3	4.9	3.4	10.3
223	40	810	0	0.49	115	116	71	-15.8	3.6	7.5	10.2	1.2	1.0	1.1	1.2	5.3	1.4	47.4	4.0	3.4	8.3
224	40	810	0	0.46	115	120	71	-15.6	3.8	7.8	10.5	1.0	0.7	0.8	0.9	5.3	1.3	47.0	2.9	3.6	7.4
225	40	809	0	0.44	115	123	70	-15.5	4.6	8.8	11.7	1.3	1.2	1.4	1.5	5.3	1.6	45.5	5.2	4.1	11.6

continued on next page...

#	Fuel	Engine operating conditions						Combustion timing Mean of 200 individual cycles (CAD aTDC)				Cyclic variation of combustion timing STD (CAD)				IMEP		P_{max}		BD	
	ON	Speed (rpm)	EGR (%)	Φ (-)	T_m (^{o}C)	P_m (kPa)	T_c (^{o}C)	SOC_{CF}	SOC	CA_{50}	$\theta_{P_{max}}$	SOC_{CF}	SOC	CA_{50}	$\theta_{P_{max}}$	Mean (bar)	COV (%)	Mean (bar)	COV (%)	Mean (CAD)	COV (%)
226	40	809	0	0.42	115	127	70	-16.2	2.7	6.8	9.6	1.2	1.0	1.1	1.2	5.4	1.4	49.2	3.8	3.7	8.9
227	40	809	0	0.41	115	130	70	-16.1	2.1	6.2	9.1	0.7	0.5	0.5	0.6	5.4	1.2	50.1	2.1	3.8	5.9
228	40	810	0	0.39	115	135	69	-16.2	2.2	6.5	9.6	0.9	0.8	1.0	1.0	5.4	1.8	49.7	3.8	4.3	9.5
229	40	810	0	0.38	115	138	69	-16.5	1.5	6.0	9.1	0.7	0.8	1.0	1.0	5.4	1.7	50.9	3.7	4.5	8.6
230	40	810	0	0.39	103	131	67	-13.3	13.9	16.0	16.1	3.9	3.7	2.4	0.7	4.8	9.8	40.1	3.2	4.4	24.9
231	40	810	0	0.39	105	132	67	-14.4	8.4	12.3	14.4	0.9	4.2	2.8	1.2	5.3	3.5	42.8	5.5	5.3	17.4
232	40	810	0	0.40	106	132	67	-14.4	4.2	8.8	11.8	1.0	0.9	1.0	1.0	5.6	2.0	47.7	4.4	4.7	10.3
233	40	810	0	0.43	108	132	68	-14.5	2.3	6.3	9.1	0.7	0.5	0.6	0.7	5.8	1.3	52.6	2.6	3.6	6.9
234	40	810	0	0.43	109	132	68	-14.7	1.5	5.5	8.2	0.7	1.2	0.6	0.7	5.9	1.5	54.2	2.4	3.4	27.9
235	40	810	0	0.45	110	132	68	-14.8	0.8	4.5	7.1	0.7	0.5	0.5	0.6	5.9	1.8	56.1	2.0	3.0	5.1
236	40	810	0	0.45	110	132	60	-14.0	1.5	5.3	8.0	0.3	0.5	0.6	0.6	6.0	1.8	55.3	2.3	3.2	5.9
237	40	810	0	0.43	116	124	66	-15.0	5.9	9.9	12.5	0.5	3.8	3.2	2.6	5.2	4.0	44.3	10.2	4.4	19.2
238	40	860	0	0.43	115	125	67	-15.0	6.4	10.5	13.1	0.5	3.6	3.0	2.5	5.3	3.7	44.3	9.6	4.6	17.7
239	40	907	0	0.42	116	124	68	-14.0	7.5	11.6	14.3	7.3	3.5	2.9	2.3	4.7	26.6	36.9	22.3	4.7	15.9
240	40	907	0	0.49	114	126	68	-15.0	2.3	6.0	8.6	0.6	1.4	1.0	1.0	6.0	1.5	54.4	2.8	3.0	22.8
241	40	955	0	0.49	114	125	70	-15.5	2.6	6.7	9.3	0.6	2.7	0.9	0.9	6.0	1.8	53.6	2.7	3.2	42.1
242	40	1003	0	0.50	115	125	70	-15.1	5.6	9.7	12.4	0.5	1.4	1.5	1.6	6.0	1.8	49.0	5.4	3.7	11.3
243	40	1052	0	0.50	116	125	72	-15.2	6.3	10.3	13.0	0.4	3.4	3.3	3.3	6.1	3.4	49.1	12.1	3.9	23.6
244	40	1099	0	0.50	115	126	72	-15.1	7.2	11.5	14.2	0.5	2.6	2.6	2.7	6.2	2.6	47.9	9.9	4.2	20.3
245	40	1147	0	0.42	126	140	74	-17.3	4.4	8.6	11.5	0.4	1.0	1.1	1.2	6.1	1.7	51.9	4.2	4.1	9.4
246	40	1194	0	0.42	127	141	74	-17.4	5.4	9.8	12.7	0.4	1.5	1.6	1.7	6.1	1.9	50.5	6.6	4.5	13.7
247	40	1243	0	0.42	131	140	75	-17.7	6.9	11.2	14.0	0.7	3.2	2.5	2.0	6.1	2.5	48.4	8.0	4.8	14.3
248	40	1291	0	0.42	133	140	75	-17.7	9.2	13.1	15.2	1.9	4.9	3.8	2.5	6.0	4.9	46.5	10.3	4.8	16.2
249	40	1340	0	0.42	136	140	76	-18.2	9.3	13.3	15.6	0.5	4.7	3.7	2.3	6.1	3.9	46.3	9.6	4.9	17.5
250	40	1196	0	0.43	114	145	75	-15.8	5.5	9.9	12.7	0.4	1.0	1.2	1.3	6.5	1.6	53.1	4.9	4.2	12.1
251	40	1196	0	0.42	118	145	75	-16.3	5.0	9.3	12.1	0.4	1.1	1.3	1.4	6.5	2.0	53.8	5.0	4.0	11.4
252	40	1196	0	0.42	121	143	75	-16.7	4.8	9.1	11.9	0.4	1.1	1.3	1.3	6.4	2.0	53.7	4.9	4.0	11.7
253	40	1196	0	0.40	124	136	75	-17.0	7.2	11.4	14.1	0.4	3.3	2.6	1.9	6.1	2.2	48.4	7.6	4.8	14.3
254	40	1196	0	0.40	127	137	75	-17.5	6.0	10.4	13.3	0.4	2.3	2.0	1.8	6.0	2.3	49.3	7.1	4.7	13.3
255	40	1196	0	0.40	129	142	75	-17.7	5.9	10.2	13.1	0.4	2.6	2.1	1.8	6.0	2.0	49.4	6.9	4.7	13.5
256	40	1196	0	0.40	132	141	75	-18.2	4.4	8.7	11.7	0.5	1.2	1.4	1.5	6.0	1.9	51.7	5.4	4.3	11.2
257	40	1196	0	0.40	135	144	75	-18.6	3.7	7.9	10.8	0.5	1.2	1.3	1.4	6.0	1.8	52.8	5.0	4.0	11.0
258	40	1196	0	0.38	132	141	75	-18.3	8.4	12.2	14.4	0.5	4.7	3.4	1.9	5.6	3.5	45.9	8.0	5.0	14.2
259	40	1196	0	0.39	132	142	75	-18.2	7.0	11.2	13.8	0.5	3.7	2.9	1.9	5.8	2.7	47.1	7.6	5.0	12.9
260	40	1196	0	0.39	132	140	75	-18.3	7.9	11.9	14.1	0.8	4.5	3.4	2.0	5.7	2.7	46.3	8.4	4.9	14.3
261	40	1196	0	0.40	131	135	75	-17.9	5.9	10.3	13.2	0.5	2.2	2.0	1.8	5.9	2.1	48.9	7.1	4.8	13.6
262	40	909	0	0.60	101	90	77	-15.7	3.9	7.5	9.7	1.0	0.8	0.9	0.9	4.7	3.0	44.3	2.4	2.7	5.1
263	40	909	0	0.44	105	113	78	-14.5	7.2	11.4	14.2	0.5	2.6	2.1	1.9	5.0	2.2	40.7	7.4	4.5	17.3

continued on next page...

#	Fuel	Engine operating conditions						Combustion timing Mean of 200 individual cycles (CAD aTDC)				Cyclic variation of combustion timing STD (CAD)				IMEP		P_{max}		BD	
	ON	Speed (rpm)	EGR (%)	Φ (-)	T_m (^{o}C)	P_m (kPa)	T_c (^{o}C)	SOC_{CF}	SOC	CA_{50}	$\theta_{P_{max}}$	SOC_{CF}	SOC	CA_{50}	$\theta_{P_{max}}$	Mean (bar)	COV (%)	Mean (bar)	COV (%)	Mean (CAD)	COV (%)
264	40	909	0	0.46	110	114	77	-15.2	3.2	7.1	9.7	0.4	1.0	1.1	1.1	5.2	1.7	47.8	3.9	3.2	8.4
265	40	909	0	0.47	109	114	78	-15.3	2.8	6.5	9.0	0.5	0.8	1.0	1.0	5.2	1.8	48.8	3.4	3.0	7.8
266	40	909	0	0.48	108	114	79	-16.0	0.5	3.9	6.3	0.7	0.7	0.8	0.8	5.2	2.9	53.0	2.3	2.6	4.3
267	40	909	0	0.38	121	123	78	-17.3	3.1	7.2	10.1	1.0	1.9	2.0	2.1	4.8	2.8	45.4	7.8	4.1	17.1
268	40	909	0	0.40	124	123	78	-17.6	1.4	5.3	8.1	0.7	1.2	1.4	1.4	4.9	2.2	48.5	5.0	3.4	11.0
269	40	909	0	0.41	124	123	78	-17.6	-0.0	3.6	6.2	0.5	1.0	1.1	1.1	5.1	2.4	51.9	3.8	2.9	7.6
270	40	909	0	0.43	125	123	79	-18.1	-1.1	2.4	4.9	1.2	0.8	0.9	0.9	5.1	2.6	53.8	3.0	2.7	5.1
271	40	909	0	0.43	125	123	79	-18.2	-1.6	1.9	4.4	1.0	0.8	0.8	0.9	5.1	2.8	54.6	2.8	2.6	4.7
272	40	1015	0	0.53	106	124	79	-13.5	9.0	13.2	15.8	1.0	2.8	3.0	3.1	6.9	2.2	49.5	10.2	3.7	20.5
273	40	1014	0	0.51	115	124	81	-16.6	4.6	8.5	10.9	0.7	1.9	2.1	2.3	5.9	2.8	52.9	6.8	3.0	13.0
274	40	1014	0	0.50	117	124	82	-16.4	6.3	10.4	13.0	0.5	2.1	2.3	2.4	5.9	2.1	49.0	8.0	3.5	16.3
275	40	1014	0	0.51	125	124	76	-17.5	3.5	7.1	9.5	0.9	1.8	2.0	2.1	5.8	3.2	54.1	6.1	2.8	10.9
276	40	1014	0	0.50	127	124	77	-17.7	3.8	7.5	10.0	1.1	1.8	2.0	2.1	5.7	3.2	53.1	6.4	3.0	11.7
277	40	1014	0	0.49	130	124	78	-17.4	5.8	9.9	12.6	0.7	1.7	2.0	2.1	5.7	1.9	48.3	7.4	3.6	15.0
278	40	1014	0	0.48	133	124	79	-18.1	6.2	10.5	13.3	1.3	1.8	2.1	2.2	5.6	2.1	46.5	8.1	3.9	16.9
279	40	1014	0	0.45	140	124	80	-19.1	7.7	11.9	14.7	1.6	3.4	3.0	2.6	5.3	3.2	42.1	11.2	4.5	20.5
280	40	1014	0	0.46	144	125	81	-19.7	5.5	9.7	12.5	1.9	2.0	2.1	2.2	5.3	2.6	46.0	7.9	3.9	15.9
281	40	1014	0	0.42	148	133	81	-20.7	3.1	7.1	9.9	1.5	0.9	1.0	1.0	5.2	1.9	49.6	3.6	3.6	8.1
282	40	1014	0	0.39	152	135	81	-21.1	3.3	7.4	10.3	1.2	1.0	1.1	1.1	5.1	1.9	48.1	3.8	4.0	8.6
283	40	1014	0	0.41	144	135	81	-20.3	2.7	6.7	9.5	0.7	0.8	0.8	0.8	5.3	1.9	50.7	3.0	3.6	6.3
284	40	1014	0	0.41	140	135	82	-20.1	2.6	6.5	9.2	1.5	0.8	0.8	0.9	5.4	2.5	52.0	2.9	3.4	6.4
285	40	1014	0	0.42	135	135	82	-19.5	2.7	6.6	9.3	1.4	0.7	0.8	0.9	5.5	1.9	52.5	3.1	3.3	7.1
286	40	1014	0	0.44	129	135	83	-18.6	2.4	6.1	8.7	0.8	0.7	0.8	0.8	5.7	2.0	54.8	2.7	3.1	5.8
287	40	1014	0	0.46	126	135	83	-18.5	1.4	5.0	7.4	0.7	0.7	0.7	0.8	5.8	3.1	57.6	2.4	2.8	4.5
288	40	1014	0	0.42	122	134	84	-17.9	5.0	9.3	12.1	0.5	1.0	1.2	1.3	5.6	1.8	48.9	4.7	4.0	11.2
289	40	1014	0	0.46	120	135	84	-18.0	1.3	4.9	7.3	0.6	0.7	0.7	0.7	5.9	2.9	58.6	2.3	2.7	4.7
290	40	1014	0	0.44	119	135	84	-17.6	1.5	5.2	7.7	0.7	0.7	0.8	0.8	5.8	2.2	56.5	2.6	2.9	5.2
291	40	1014	23	0.66	119	132	75	-15.1	6.0	10.1	12.7	0.6	1.1	1.2	1.3	6.5	2.0	52.6	4.8	3.5	11.1
292	40	1014	23	0.61	123	142	77	-16.5	2.9	6.6	9.1	0.6	0.9	1.0	1.1	6.4	2.3	59.0	3.5	3.0	6.8
293	40	1014	24	0.59	133	149	79	-18.2	-0.5	3.0	5.4	0.4	0.4	0.4	0.4	6.4	2.4	65.4	1.3	2.6	2.7
294	40	1014	21	0.57	129	140	79	-17.4	2.4	6.2	8.7	0.5	0.9	0.9	1.0	6.1	2.2	57.4	3.3	3.1	6.0
295	40	1014	23	0.44	155	161	80	-21.3	-1.2	3.1	6.4	1.0	0.4	0.4	0.5	5.5	2.3	58.6	1.6	4.1	4.7
296	40	1014	22	0.60	117	142	75	-16.0	2.6	6.3	8.8	0.6	0.7	0.8	0.8	6.5	2.3	60.4	2.6	2.9	4.5
297	40	1017	8	0.52	118	128	79	-16.4	4.0	7.9	10.5	0.4	1.0	1.1	1.1	5.9	1.8	52.6	3.8	3.2	7.5
298	40	1016	9	0.50	123	130	79	-16.8	4.4	8.5	11.2	0.5	0.7	0.8	0.8	5.8	1.7	50.7	2.9	3.5	7.2
299	40	1016	9	0.51	128	130	80	-17.9	1.8	5.5	8.0	0.4	0.6	0.7	0.7	5.7	2.7	55.7	2.1	2.9	4.2
300	40	1016	9	0.49	130	129	80	-18.0	3.4	7.3	10.0	0.7	1.0	1.1	1.1	5.6	1.7	51.4	3.9	3.4	8.4
301	40	1016	9	0.48	132	129	79	-18.4	2.6	6.5	9.2	0.5	0.8	0.9	0.9	5.5	1.8	52.0	3.1	3.3	7.5

continued on next page...

#	Fuel	Engine operating conditions						Combustion timing Mean of 200 individual cycles (CAD aTDC)				Cyclic variation of combustion timing STD (CAD)				IMEP		P_{max}		BD	
	ON	Speed (rpm)	EGR (%)	Φ (-)	T_m (^{o}C)	P_m (kPa)	T_c (^{o}C)	SOC_{CF}	SOC	CA_{50}	$\theta_{P_{max}}$	SOC_{CF}	SOC	CA_{50}	$\theta_{P_{max}}$	Mean (bar)	COV (%)	Mean (bar)	COV (%)	Mean (CAD)	COV (%)
302	40	1016	9	0.46	136	136	80	-19.0	1.3	5.1	7.7	0.6	0.7	0.8	0.8	5.4	2.1	54.4	2.8	3.2	5.4
303	40	1016	9	0.44	142	137	80	-19.7	1.1	5.0	7.8	0.9	0.7	0.8	0.8	5.3	2.0	53.5	2.7	3.3	6.3
304	40	1016	10	0.43	144	137	79	-19.8	2.0	6.1	9.0	0.6	0.9	1.0	1.1	5.1	1.9	50.6	3.8	3.8	8.3
305	40	1016	10	0.41	147	137	79	-20.6	2.4	6.7	9.7	1.5	1.0	1.2	1.2	5.0	2.4	48.5	4.6	4.3	10.0
306	40	1016	9	0.39	148	137	79	-20.5	4.5	8.8	11.7	1.0	2.7	2.0	1.4	4.7	2.5	44.3	5.8	5.1	13.9
307	40	1016	10	0.38	149	137	78	-20.7	7.0	10.7	12.7	1.5	4.4	2.9	1.2	4.5	4.0	40.3	8.9	5.0	22.6
308	40	1015	11	0.33	162	157	77	-22.8	0.1	5.2	9.6	1.1	0.5	0.5	0.6	4.5	2.1	47.8	2.8	7.1	6.8
309	40	804	9	0.47	118	132	80	-16.6	0.0	3.8	6.5	0.8	1.2	0.5	0.5	5.4	1.8	54.7	1.8	3.0	21.6
310	40	804	9	0.42	128	133	80	-18.3	1.1	5.3	8.3	0.8	0.4	0.5	0.5	4.9	1.4	48.9	2.0	3.8	5.5
311	40	804	21	0.50	130	133	81	-17.9	1.9	6.0	9.0	1.3	0.5	0.5	0.5	5.1	1.1	49.4	2.0	3.8	5.4
312	40	803	21	0.52	132	133	79	-17.8	1.3	5.2	8.0	1.3	0.4	0.5	0.5	5.2	1.3	51.1	1.8	3.4	4.6
313	40	803	21	0.54	133	133	79	-18.2	-0.2	3.4	6.1	1.2	0.4	0.4	0.4	5.3	1.7	54.8	1.5	2.9	3.8
314	40	803	22	0.45	138	139	75	-19.1	1.9	6.6	9.9	1.2	1.2	1.1	1.1	4.7	1.9	46.6	4.2	5.0	10.0
315	40	803	22	0.46	144	140	75	-19.5	0.2	4.6	7.7	1.0	0.7	0.8	0.8	4.9	1.5	50.2	3.0	4.2	7.3
316	40	803	21	0.44	145	140	74	-19.9	1.5	6.2	9.6	1.3	0.9	1.0	1.0	4.6	1.9	46.3	3.9	5.3	8.7
317	40	822	0	0.38	98	136	74	-14.7	3.6	8.9	11.8	0.4	4.7	2.2	1.7	5.3	2.4	47.3	6.9	5.4	55.4
318	40	803	0	0.57	80	104	75	-10.7	10.1	14.6	17.3	1.9	3.2	2.5	2.3	5.5	2.3	39.1	9.2	4.5	27.6
319	40	803	0	0.36	130	135	75	-18.6	0.7	5.1	8.2	1.2	0.7	0.8	0.9	4.7	1.9	48.3	3.3	4.3	8.4
320	40	803	0	0.39	132	129	74	-18.4	1.0	5.1	8.0	1.3	1.2	1.4	1.5	4.7	2.2	48.3	5.3	3.8	11.3
321	40	803	0	0.41	134	123	74	-18.5	1.3	5.2	8.0	1.4	0.7	0.8	0.8	4.7	1.5	47.5	3.1	3.4	6.8
322	40	803	0	0.43	129	115	74	-17.9	3.3	7.5	10.4	1.1	0.9	1.0	1.1	4.6	1.5	43.1	3.9	3.9	9.3
323	40	803	30	0.82	121	115	77	-17.5	2.6	6.2	8.5	1.7	0.8	0.9	0.9	5.6	2.7	53.1	2.8	2.7	4.5
324	40	802	26	0.73	121	118	80	-19.1	-0.6	2.8	5.0	1.9	0.6	0.6	0.7	5.2	3.8	55.9	2.0	2.4	3.5
325	40	802	24	0.65	130	123	79	-17.2	1.5	5.1	7.5	1.2	1.0	1.0	1.1	5.5	2.1	53.1	3.2	2.8	5.6
326	40	803	25	0.61	133	129	79	-17.4	1.6	5.4	8.0	1.2	1.1	1.2	1.3	5.5	1.8	52.6	4.2	3.0	7.2
327	40	802	27	0.61	137	130	79	-17.8	2.3	6.2	8.9	1.6	1.4	1.5	1.6	5.4	1.9	50.7	5.6	3.3	11.2
328	40	802	27	0.59	142	133	79	-18.7	0.8	4.6	7.3	1.4	0.5	0.5	0.5	5.3	1.6	53.0	1.8	3.1	4.2
329	40	802	29	0.58	147	137	79	-19.3	0.3	4.1	6.9	1.5	0.6	0.6	0.7	5.3	1.8	53.0	2.5	3.2	5.7

Appendix B

HCCI Exhaust Temperature Experimental Data Summary

Summary of steady-state HCCI exhaust temperature experiments[1]

	Engine operating conditions								Engine emissions		
#	N (rpm)	Φ	P_m (kPa)	T_m (°C)	EGR (%)	T_{exh} (°C)	CA50 (CAD)	IMEP (bar)	CO (%)	HC (ppm)	NOx (ppm)
1	810	0.50	101	82	0	321	7.7	4.9	0.09	2839	1
2	810	0.52	101	82	0	315	5.7	4.9	0.07	2441	2
3	810	0.53	101	82	0	313	4.7	4.9	0.07	2414	2
4	810	0.53	101	82	0	309	4.6	4.9	0.06	2170	16
5	810	0.54	101	82	0	306	2.8	4.8	0.06	2221	19
6	810	0.45	101	92	0	303	7.5	4.5	0.12	2905	1
7	810	0.46	101	91	0	304	8.5	4.5	0.11	2789	1
8	810	0.47	101	91	0	305	7.9	4.6	0.11	2810	1
9	810	0.48	101	92	0	306	6.3	4.7	0.10	2789	1
10	810	0.49	101	93	0	308	6.1	4.7	0.09	2653	1
11	810	0.44	101	102	0	298	7.6	4.3	0.13	2967	1
12	810	0.45	101	103	0	299	6.0	4.4	0.12	2861	1
13	809	0.47	101	102	0	301	5.5	4.5	0.10	2612	1
14	810	0.49	101	102	0	302	4.2	4.6	0.09	2606	1
15	810	0.51	101	102	0	303	2.9	4.6	0.07	2344	4
16	1193	0.56	102	100	0	397	16.0	5.2	0.12	3341	2
17	1193	0.57	99	101	0	389	13.0	5.2	0.09	2586	4
18	1193	0.58	101	100	0	387	11.4	5.3	0.08	2411	5
19	1193	0.58	100	100	0	398	16.1	5.4	0.11	3070	2
20	1193	0.60	102	99	0	400	13.4	5.6	0.09	2812	5
21	810	0.42	110	100	0	287	3.6	4.6	0.11	2902	0
22	860	0.42	111	100	0	291	4.2	4.7	0.10	2760	0

continued on next page...

[1]Data points 1-95 run with PRF0 fuel, points 96-100 use PRF10 fuel, points 101-163 use PRF20 fuel and points use 164-304 PRF40 fuel.

	Engine operating conditions								Engine emissions		
#	N (rpm)	Φ	P_m (kPa)	T_m (°C)	EGR (%)	T_{exh} (°C)	CA50 (CAD)	IMEP (bar)	CO (%)	HC (ppm)	NOx (ppm)
23	908	0.42	110	102	0	299	4.8	4.7	0.11	2599	0
24	956	0.42	110	101	0	305	6.6	4.7	0.12	2677	0
25	1004	0.42	110	100	0	313	8.8	4.7	0.13	2776	0
26	908	0.49	90	100	0	348	14.7	4.0	0.12	2872	0
27	907	0.49	94	100	0	331	7.5	4.4	0.08	2029	1
28	908	0.49	98	101	0	325	5.7	4.5	0.07	1991	2
29	908	0.49	99	99	0	321	5.2	4.5	0.07	1988	3
30	908	0.49	101	100	0	315	4.0	4.6	0.06	1956	8
31	901	0.51	91	81	0	350	13.4	4.3	0.12	3035	0
32	901	0.52	90	81	0	349	10.4	4.4	0.10	2670	0
33	902	0.54	90	81	0	346	8.1	4.4	0.09	2237	4
34	901	0.54	91	81	0	343	7.9	4.4	0.08	1920	28
35	900	0.55	91	81	0	345	7.3	4.5	0.09	2104	19
36	900	0.57	91	82	0	321	1.8	4.1	0.07	1648	127
37	900	0.47	91	88	0	341	16.2	3.8	0.17	3510	0
38	899	0.48	91	88	0	341	13.4	4.0	0.13	3161	0
39	899	0.49	91	88	0	343	11.3	4.1	0.12	2953	0
40	899	0.50	90	87	0	343	10.0	4.2	0.11	2720	0
41	899	0.52	91	88	0	341	7.3	4.3	0.09	2285	0
42	899	0.55	91	88	0	331	4.1	4.2	0.08	1884	44
43	899	0.56	91	88	0	315	2.1	4.0	0.07	1541	144
44	901	0.43	100	90	0	314	12.0	4.1	0.17	3033	0
45	901	0.44	100	89	0	316	9.3	4.2	0.14	2702	0
46	901	0.46	101	87	0	318	6.9	4.4	0.12	2572	0
47	901	0.47	100	88	0	319	5.8	4.5	0.11	2346	0
48	901	0.48	100	89	0	319	5.2	4.5	0.10	2096	0

continued on next page...

	Engine operating conditions								Engine emissions		
#	N (rpm)	Φ	P_m (kPa)	T_m (°C)	EGR (%)	T_{exh} (°C)	CA50 (CAD)	IMEP (bar)	CO (%)	HC (ppm)	NOx (ppm)
49	900	0.49	101	89	0	316	3.6	4.5	0.09	1832	1
50	900	0.50	101	89	0	312	2.9	4.4	0.08	1642	11
51	900	0.36	110	91	0	278	13.0	3.8	0.34	3108	0
52	900	0.37	111	92	0	282	11.0	4.0	0.32	3142	0
53	900	0.38	111	92	0	284	7.2	4.3	0.25	2939	0
54	900	0.40	110	92	0	289	5.4	4.4	0.15	2429	1
55	900	0.41	110	93	0	291	3.6	4.4	0.13	2175	3
56	900	0.43	110	92	0	295	2.5	4.6	0.12	2122	5
57	812	0.43	105	102	0	291	2.2	4.2	0.14	2288	8
58	872	0.43	105	102	0	298	2.7	4.2	0.11	2055	10
59	919	0.44	105	103	0	304	3.3	4.3	0.11	2040	7
60	967	0.43	105	103	0	311	5.6	4.3	0.11	2034	7
61	813	0.55	90	91	0	312	2.0	4.0	0.06	1521	129
62	873	0.55	89	92	0	315	1.9	4.0	0.06	1420	144
63	920	0.55	89	91	0	335	6.1	4.2	0.07	1551	81
64	968	0.56	89	91	0	364	10.3	4.4	0.08	1897	18
65	1016	0.56	89	91	0	379	12.0	4.5	0.09	2207	3
66	1065	0.56	89	92	0	393	13.6	4.6	0.09	2374	1
67	1113	0.56	89	91	0	418	20.2	4.2	0.14	3576	0
68	812	0.49	113	60	0	292	0.9	5.2	0.07	1517	14
69	873	0.48	113	60	0	300	1.8	5.3	0.07	1567	5
70	919	0.48	113	60	0	307	3.7	5.4	0.07	1452	7
71	968	0.48	114	62	0	325	6.4	5.6	0.09	1795	0
72	1016	0.48	113	60	0	330	6.7	5.6	0.10	1840	0
73	1064	0.49	113	61	0	332	6.7	5.7	0.09	1744	0
74	1112	0.48	113	63	0	341	8.9	5.6	0.10	1811	0

continued on next page...

	Engine operating conditions								Engine emissions		
#	N (rpm)	Φ	P_m (kPa)	T_m (°C)	EGR (%)	T_{exh} (°C)	CA50 (CAD)	IMEP (bar)	CO (%)	HC (ppm)	NOx (ppm)
75	1161	0.48	114	64	0	350	9.6	5.6	0.12	2068	0
76	1160	0.48	113	65	0	348	9.0	5.6	0.11	1893	0
77	1017	0.54	88	93	0	386	16.1	4.2	0.11	2816	0
78	1016	0.54	93	91	0	356	8.3	4.5	0.08	1819	8
79	1017	0.54	95	93	0	333	4.6	4.4	0.07	1499	50
80	1016	0.54	98	93	0	311	1.6	4.2	0.06	1296	76
81	1016	0.45	99	88	0	341	15.7	4.1	0.17	2787	0
82	1016	0.44	103	88	0	332	12.3	4.4	0.15	2531	0
83	1016	0.44	105	87	0	325	8.9	4.6	0.13	2294	0
84	1016	0.44	109	88	0	317	6.2	4.7	0.11	1971	0
85	1016	0.44	113	86	0	310	4.3	4.9	0.10	1673	0
86	1016	0.45	117	87	0	303	1.7	5.1	0.08	1565	1
87	1016	0.38	119	89	0	287	8.6	4.6	0.25	2358	0
88	1016	0.37	124	90	0	279	5.8	4.7	0.20	2049	1
89	1016	0.37	127	89	0	277	4.1	4.9	0.17	1899	1
90	1016	0.37	128	92	0	276	2.4	4.9	0.15	1798	2
91	1016	0.37	131	94	0	273	1.6	5.0	0.15	1754	3
92	1016	0.51	99	95	0	324	4.7	4.4	0.07	1550	3
93	1016	0.51	99	95	0	339	6.6	4.6	0.09	1816	2
94	1015	0.51	99	94	0	350	10.7	4.7	0.10	2338	1
95	1015	0.51	99	96	0	360	13.0	4.8	0.14	3342	2
96	997	0.42	120	73	0	339	14.9	6.5	0.16	2613	0
97	997	0.41	120	81	0	336	12.7	6.5	0.14	2267	0
98	997	0.41	120	91	0	333	10.8	6.4	0.13	2062	0
99	997	0.42	120	102	0	331	8.0	6.4	0.10	1827	0
100	997	0.42	120	112	0	329	6.0	6.3	0.09	1719	0

continued on next page...

	Engine operating conditions								Engine emissions		
#	N (rpm)	Φ	P_m (kPa)	T_m (°C)	EGR (%)	T_{exh} (°C)	CA50 (CAD)	IMEP (bar)	CO (%)	HC (ppm)	NOx (ppm)
101	1053	0.49	111	105	0	333	12.8	7.4	0.06	2376	10
102	1101	0.49	112	105	0	347	15.3	7.6	-0.00	502	6
103	1100	0.49	111	105	0	348	14.5	7.6	0.08	2498	2
104	1149	0.49	112	106	0	360	17.0	7.6	0.09	2689	2
105	801	0.51	91	100	0	357	24.8	5.7	0.13	3054	1
106	801	0.51	95	100	0	339	16.0	6.4	0.09	2568	5
107	801	0.51	100	100	0	316	10.9	6.7	0.07	2243	36
108	801	0.44	101	100	0	321	21.7	5.9	0.22	3728	1
109	801	0.44	104	100	0	311	17.1	6.3	0.14	3449	1
110	801	0.44	111	101	0	302	12.6	6.9	0.11	3195	1
111	801	0.43	116	101	0	290	9.4	7.3	0.08	3214	1
112	801	0.43	120	100	0	287	8.1	7.6	0.08	3294	1
113	801	0.47	92	120	0	338	24.1	5.1	0.17	3475	1
114	801	0.46	95	119	0	324	17.6	5.8	0.12	3142	1
115	801	0.46	101	120	0	315	14.1	6.2	0.10	2714	1
116	801	0.47	105	119	0	305	9.8	6.6	0.08	2483	2
117	801	0.46	110	121	0	292	7.5	6.9	0.07	2593	5
118	801	0.34	114	120	0	258	17.1	5.7	0.50	5019	1
119	801	0.35	114	121	0	265	13.8	6.1	0.24	3847	1
120	800	0.36	115	121	0	269	13.5	6.1	0.18	3644	1
121	801	0.38	115	120	0	274	10.9	6.5	0.16	3387	1
122	800	0.39	114	120	0	276	10.5	6.5	0.12	3361	1
123	800	0.41	116	121	0	280	8.5	6.8	0.10	3004	0
124	801	0.43	115	120	0	283	7.6	6.9	0.07	2902	1
125	800	0.43	100	100	0	312	21.6	5.7	0.20	3806	1
126	800	0.44	100	101	0	314	18.1	6.1	0.17	3821	1

continued on next page...

	Engine operating conditions								Engine emissions		
#	N (rpm)	Φ	P_m (kPa)	T_m (°C)	EGR (%)	T_{exh} (°C)	CA50 (CAD)	IMEP (bar)	CO (%)	HC (ppm)	NOx (ppm)
127	800	0.46	100	100	0	317	15.5	6.4	0.12	3317	1
128	800	0.49	100	100	0	319	13.5	6.6	0.09	2955	1
129	800	0.52	99	100	0	311	9.3	6.6	0.06	2213	45
130	1004	0.34	153	115	0	264	7.0	8.7	0.14	3266	1
131	1004	0.34	157	127	0	264	5.4	8.9	0.12	3117	1
132	1003	0.29	145	123	0	242	12.7	7.0	0.36	3024	1
133	1004	0.37	134	119	0	275	9.0	7.7	0.12	3022	1
134	1003	0.34	133	117	0	270	12.6	7.1	0.19	2992	1
135	1003	0.37	126	128	0	287	10.5	7.1	0.14	2945	1
136	1003	0.36	125	133	0	284	11.0	6.9	0.15	2932	1
137	1003	0.39	118	132	0	297	11.9	6.7	0.13	2602	1
138	1003	0.42	117	129	0	303	9.9	7.0	0.09	2512	1
139	1003	0.43	109	124	0	323	14.7	6.5	0.11	2389	1
140	1003	0.46	108	120	0	329	13.4	6.8	0.09	2329	1
141	1003	0.48	104	116	0	341	15.9	6.6	0.09	2164	3
142	1003	0.44	104	116	0	340	23.4	6.0	0.14	2628	1
143	1003	0.52	97	115	0	371	19.6	6.3	0.10	3259	2
144	1003	0.54	97	117	0	359	14.1	6.5	0.07	2071	28
145	1004	0.48	123	65	0	333	14.6	8.9	0.08	3246	3
146	1004	0.45	133	72	0	310	11.2	9.2	0.08	3262	2
147	1004	0.41	133	79	0	296	12.8	8.6	0.12	3297	2
148	1004	0.38	144	94	0	277	9.5	8.9	0.12	3240	1
149	1004	0.31	145	104	0	246	15.8	7.3	0.61	3263	1
150	1003	0.54	100	77	0	381	22.5	7.0	0.09	2770	2
151	1003	0.53	106	72	0	362	17.0	7.6	0.08	2457	9
152	1003	0.52	108	70	0	353	16.5	7.8	0.07	2561	11

continued on next page...

	Engine operating conditions								Engine emissions		
#	N (rpm)	Φ	P_m (kPa)	T_m (°C)	EGR (%)	T_{exh} (°C)	CA50 (CAD)	IMEP (bar)	CO (%)	HC (ppm)	NOx (ppm)
153	1003	0.54	102	65	0	384	23.6	7.2	0.08	2454	5
154	1003	0.46	130	64	0	319	10.7	9.1	0.07	3393	4
155	1003	0.52	107	64	0	364	18.9	7.7	0.08	2797	4
156	800	0.40	118	120	0	285	8.4	6.9	0.10	2948	2
157	800	0.40	119	121	0	281	7.9	6.9	0.09	3038	1
158	800	0.40	119	120	0	278	8.2	6.9	0.09	3002	1
159	800	0.40	120	121	0	277	8.4	6.9	0.10	3005	1
160	800	0.40	118	121	0	275	9.1	7.0	0.11	3151	1
161	800	0.40	119	121	0	274	9.7	7.0	0.12	3237	1
162	800	0.40	119	121	0	273	10.5	7.0	0.13	3399	1
163	800	0.40	117	121	0	271	11.8	6.9	0.13	3552	1
164	811	0.71	89	80	0	400	13.4	5.6	0.05	1808	1301
165	811	0.72	89	83	0	393	11.5	5.5	0.05	1762	1320
166	811	0.71	89	86	0	387	10.9	5.4	0.04	1676	1505
167	811	0.72	89	88	0	384	10.1	5.4	0.04	1680	1523
168	811	0.72	89	90	0	382	9.5	5.3	0.04	1618	1654
169	811	0.69	89	91	0	382	10.7	5.3	0.05	1894	1064
170	810	0.69	89	94	0	380	9.9	5.2	0.05	1708	1063
171	810	0.69	89	97	0	377	9.3	5.2	0.05	1664	1099
172	810	0.70	89	99	0	370	8.2	5.1	0.04	1613	1345
173	810	0.69	89	99	0	372	8.8	5.1	0.04	1549	1255
174	810	0.67	89	109	0	378	9.7	5.0	0.07	2309	679
175	810	0.67	89	112	0	369	9.0	4.9	0.05	1716	869
176	810	0.67	89	115	0	371	9.6	4.9	0.05	1710	789
177	810	0.67	89	118	0	367	8.6	4.9	0.05	1735	766
178	810	0.67	89	120	0	365	8.2	4.8	0.05	1678	804

continued on next page...

	Engine operating conditions								Engine emissions		
#	N (rpm)	Φ	P_m (kPa)	T_m (°C)	EGR (%)	T_{exh} (°C)	CA50 (CAD)	IMEP (bar)	CO (%)	HC (ppm)	NOx (ppm)
179	810	0.67	89	122	0	362	8.2	4.8	0.05	1649	885
180	810	0.66	89	122	0	359	8.1	4.8	0.05	1606	900
181	810	0.66	90	123	0	365	8.4	4.8	0.05	1706	699
182	910	0.60	90	101	0	361	7.5	4.7	0.04	1634	473
183	810	0.59	99	115	0	368	15.1	5.1	0.09	3213	5
184	810	0.58	101	115	0	359	14.4	5.2	0.09	3090	7
185	810	0.57	104	115	0	349	11.7	5.2	0.09	3477	3
186	810	0.52	111	116	0	326	9.3	5.3	0.09	3740	2
187	810	0.51	114	115	0	318	8.1	5.3	0.10	3874	2
188	810	0.49	116	115	0	311	7.5	5.3	0.10	3920	2
189	810	0.46	120	115	0	305	7.7	5.3	0.11	4048	1
190	809	0.44	123	115	0	298	8.7	5.3	0.13	4255	2
191	809	0.42	127	115	0	286	6.7	5.4	0.13	4100	1
192	809	0.41	130	115	0	282	6.2	5.4	0.14	4139	1
193	810	0.39	135	115	0	271	6.5	5.4	0.14	3950	2
194	810	0.38	138	115	0	264	5.9	5.4	0.15	3941	2
195	811	0.39	131	103	0	264	16.0	4.8	0.35	5127	1
196	810	0.39	132	105	0	275	12.1	5.3	0.28	4950	1
197	810	0.41	132	106	0	278	8.7	5.6	0.17	4400	1
198	810	0.43	132	108	0	283	6.3	5.8	0.11	4063	1
199	810	0.43	132	109	0	285	5.5	5.9	0.10	3925	1
200	810	0.45	132	110	0	286	4.5	5.9	0.07	3083	1
201	810	0.45	132	110	0	287	5.3	6.0	0.08	3752	1
202	810	0.43	124	116	0	291	9.1	5.2	0.16	4279	1
203	860	0.43	125	115	0	296	9.9	5.3	0.15	4122	1
204	907	0.42	124	116	0	295	11.0	4.7	0.23	4739	1

continued on next page...

	Engine operating conditions								Engine emissions		
#	N (rpm)	Φ	P_m (kPa)	T_m (°C)	EGR (%)	T_{exh} (°C)	CA50 (CAD)	IMEP (bar)	CO (%)	HC (ppm)	NOx (ppm)
205	907	0.49	126	114	0	314	6.0	6.0	0.08	3688	1
206	955	0.49	125	114	0	318	6.6	6.0	0.07	3349	1
207	1003	0.50	125	115	0	333	9.6	6.0	0.08	3466	1
208	1052	0.50	125	116	0	339	10.0	6.1	0.09	3433	2
209	1099	0.50	126	115	0	350	11.3	6.2	0.10	3674	1
210	1147	0.42	140	126	0	315	8.5	6.1	0.12	3250	1
211	1194	0.42	141	127	0	320	9.7	6.1	0.13	3220	1
212	1243	0.42	140	131	0	327	10.8	6.1	0.15	3378	1
213	1291	0.42	140	133	0	333	12.5	6.0	0.15	3328	1
214	1339	0.42	140	136	0	340	12.7	6.1	0.15	3290	1
215	810	0.61	96	115	0	375	17.1	5.0	0.09	2995	27
216	909	0.44	113	105	0	327	11.1	5.0	0.11	3415	2
217	909	0.46	114	110	0	326	7.0	5.2	0.09	3272	1
218	909	0.47	114	109	0	323	6.4	5.2	0.06	2704	3
219	909	0.48	114	108	0	320	3.9	5.2	0.06	2787	4
220	909	0.38	123	121	0	295	7.1	4.8	0.13	3497	1
221	909	0.40	123	124	0	296	5.3	4.9	0.10	3267	1
222	909	0.42	123	124	0	301	3.5	5.1	0.08	3120	1
223	909	0.43	123	125	0	301	2.4	5.1	0.06	3091	1
224	909	0.43	123	125	0	300	1.9	5.1	0.06	3005	1
225	1015	0.53	124	106	0	359	13.2	6.9	0.07	2908	40
226	1014	0.51	124	115	0	348	8.4	6.0	0.07	2795	31
227	1014	0.50	124	117	0	357	10.4	5.9	0.08	3089	2
228	1014	0.51	124	125	0	338	7.1	5.8	0.07	2721	37
229	1014	0.50	124	127	0	346	7.5	5.7	0.08	2976	8
230	1014	0.49	124	130	0	353	9.8	5.7	0.09	3355	0

continued on next page...

	Engine operating conditions								Engine emissions		
#	N (rpm)	Φ	P_m (kPa)	T_m (°C)	EGR (%)	T_{exh} (°C)	CA50 (CAD)	IMEP (bar)	CO (%)	HC (ppm)	NOx (ppm)
231	1014	0.48	124	133	0	350	10.4	5.6	0.09	3323	0
232	1014	0.46	124	136	0	348	12.1	5.3	0.10	3401	0
233	1014	0.45	124	140	0	343	11.4	5.3	0.13	3888	0
234	1014	0.46	124	144	0	338	9.6	5.3	0.10	3325	0
235	1014	0.42	133	148	0	317	7.0	5.2	0.11	3345	0
236	1014	0.39	135	152	0	305	7.4	5.1	0.12	3221	0
237	1014	0.41	135	144	0	310	6.7	5.3	0.11	3211	0
238	1014	0.42	135	140	0	312	6.4	5.4	0.11	3157	0
239	1014	0.42	135	135	0	316	6.5	5.5	0.10	3067	0
240	1014	0.44	135	129	0	319	6.1	5.7	0.08	2884	0
241	1014	0.46	135	126	0	315	5.0	5.8	0.07	2822	0
242	1014	0.42	134	122	0	320	9.2	5.6	0.12	3276	0
243	1014	0.46	135	120	0	315	4.8	5.9	0.07	2826	0
244	1014	0.44	135	119	0	316	5.2	5.8	0.09	2970	0
245	1014	0.63	134	120	23	358	11.6	6.3	0.10	3387	0
246	1014	0.66	132	119	23	367	10.0	6.5	0.12	4046	0
247	1014	0.61	142	123	23	335	6.5	6.4	0.10	3182	0
248	1014	0.59	149	133	24	317	3.0	6.4	0.08	2783	0
249	1014	0.62	128	124	19	363	11.1	6.1	0.11	3457	0
250	1014	0.60	135	126	20	344	7.6	6.1	0.10	3278	0
251	1014	0.57	140	129	21	327	6.1	6.1	0.09	2946	0
252	1014	0.63	129	116	20	370	12.6	6.2	0.12	3704	0
253	1014	0.44	161	155	23	277	3.0	5.5	0.16	2961	0
254	1014	0.60	142	117	22	325	6.3	6.5	0.07	2754	2
255	1017	0.54	124	112	8	354	11.0	5.9	0.10	3394	0
256	1017	0.54	124	115	8	352	10.7	5.8	0.08	3059	1

continued on next page...

	Engine operating conditions								Engine emissions		
#	N (rpm)	Φ	P_m (kPa)	T_m (°C)	EGR (%)	T_{exh} (°C)	CA50 (CAD)	IMEP (bar)	CO (%)	HC (ppm)	NOx (ppm)
257	1017	0.52	128	118	8	333	7.9	5.9	0.08	2884	0
258	1016	0.50	130	123	9	335	8.5	5.8	0.09	3261	0
259	1017	0.51	130	128	9	328	5.5	5.7	0.08	2933	0
260	1016	0.49	129	130	9	330	7.3	5.6	0.10	3157	0
261	1016	0.49	129	132	9	323	6.4	5.5	0.11	3237	0
262	1016	0.46	136	136	9	309	5.1	5.4	0.10	3284	0
263	1016	0.44	137	142	9	302	5.0	5.3	0.11	3139	0
264	1016	0.43	137	144	10	300	6.1	5.1	0.13	3341	0
265	1016	0.41	137	147	10	294	6.7	5.0	0.16	3537	0
266	1016	0.39	137	148	9	290	8.4	4.7	0.20	3764	0
267	1016	0.39	137	149	10	286	10.5	4.5	0.26	4045	0
268	1016	0.38	141	152	10	279	7.5	4.7	0.27	3991	0
269	1015	0.33	157	162	11	247	5.2	4.5	0.42	3680	0
270	804	0.49	132	112	9	294	3.1	5.6	0.11	3829	0
271	804	0.47	132	118	9	290	3.8	5.4	0.09	3538	0
272	804	0.46	132	123	10	287	2.8	5.2	0.12	3875	0
273	804	0.45	133	126	9	284	3.4	5.2	0.11	3678	0
274	803	0.42	133	128	9	280	5.3	4.9	0.13	3668	0
275	804	0.51	133	130	21	291	6.0	5.1	0.16	4034	0
276	803	0.52	133	132	21	294	5.2	5.2	0.12	3624	0
277	803	0.54	133	133	21	297	3.4	5.3	0.11	3674	0
278	803	0.45	139	138	22	269	6.5	4.7	0.20	3962	0
279	803	0.46	140	144	22	270	4.5	4.9	0.17	3759	0
280	803	0.44	140	145	21	260	6.2	4.6	0.21	4038	0
281	823	0.51	118	75	0	328	9.1	5.9	0.08	3591	6
282	823	0.44	126	83	0	307	9.7	5.7	0.15	4572	0

continued on next page...

	Engine operating conditions								Engine emissions		
#	N (rpm)	Φ	P_m (kPa)	T_m (°C)	EGR (%)	T_{exh} (°C)	CA50 (CAD)	IMEP (bar)	CO (%)	HC (ppm)	NOx (ppm)
283	823	0.47	127	87	0	308	6.0	6.0	0.08	3674	0
284	822	0.38	136	98	0	274	8.5	5.3	0.27	4744	0
285	823	0.53	109	96	0	336	9.3	5.4	0.09	3329	13
286	803	0.57	104	80	0	366	14.4	5.5	0.10	3666	11
287	803	0.54	104	92	0	357	15.2	5.2	0.09	3262	13
288	803	0.52	112	92	0	333	9.8	5.4	0.09	3397	11
289	803	0.50	118	94	0	319	5.8	5.6	0.09	3886	0
290	803	0.47	127	99	0	302	3.8	5.7	0.09	3698	0
291	803	0.41	133	108	0	279	3.9	5.3	0.13	3982	0
292	803	0.39	134	113	0	273	4.2	5.2	0.15	4068	0
293	803	0.36	135	130	0	262	5.0	4.7	0.18	3945	0
294	803	0.39	129	132	0	272	5.0	4.7	0.14	3749	0
295	803	0.41	123	134	0	287	5.1	4.7	0.12	3739	0
296	803	0.43	115	129	0	301	7.5	4.6	0.12	3720	0
297	803	0.71	115	124	23	330	9.6	5.3	0.07	3087	84
298	803	0.83	115	121	30	353	6.1	5.6	0.08	3495	160
299	802	0.73	118	121	26	322	2.8	5.2	0.07	3125	112
300	802	0.65	123	130	24	329	5.0	5.5	0.09	3676	1
301	803	0.61	129	133	25	314	5.3	5.5	0.11	3686	0
302	802	0.61	130	137	27	311	6.2	5.4	0.11	3653	0
303	802	0.60	133	142	27	304	4.6	5.3	0.12	3808	0
304	802	0.58	137	147	29	294	4.1	5.3	0.12	3524	0

Appendix C

SOC Calculation Method

HCCI combustion of PRF fuels in this study exhibit two stages of heat release as shown in Figure C.1. SOC for the second stage of HCCI combustion is detected by adapting a method designed to detect engine knock from an SI engine pressure trace. Checkel and Dale [200] presented a robust method in which the onset of knock is characterized by a change in the third derivative of the pressure trace. This corresponds to a rapid change of concavity of the pressure history from positive to negative during knocking. In HCCI engines it is at the point where the reaction exothermicity becomes substantial and begins to increase the cylinder pressure which must be detected. In the crank angle region near TDC during compression, the pressure history has a negative concavity, which becomes positive during ignition (i.e. a positive third derivative) as indicated in Figure C.1-a. By detecting this transition from negative to positive concavity, the point of ignition can be determined. In this thesis, ignition is defined as being the point at which the third derivative of the pressure trace with respect to the crank angle, θ, exceeds a heuristically determined limit:

$$\frac{d^3P}{d\theta^3} > \left.\frac{d^3P}{d\theta^3}\right|_{lim} \tag{C.1}$$

where, $\left.\frac{d^3P}{d\theta^3}\right|_{lim} = 25\left[\frac{\text{kPa}}{\text{CAD}^3}\right]$ is chosen for the Ricardo engine.

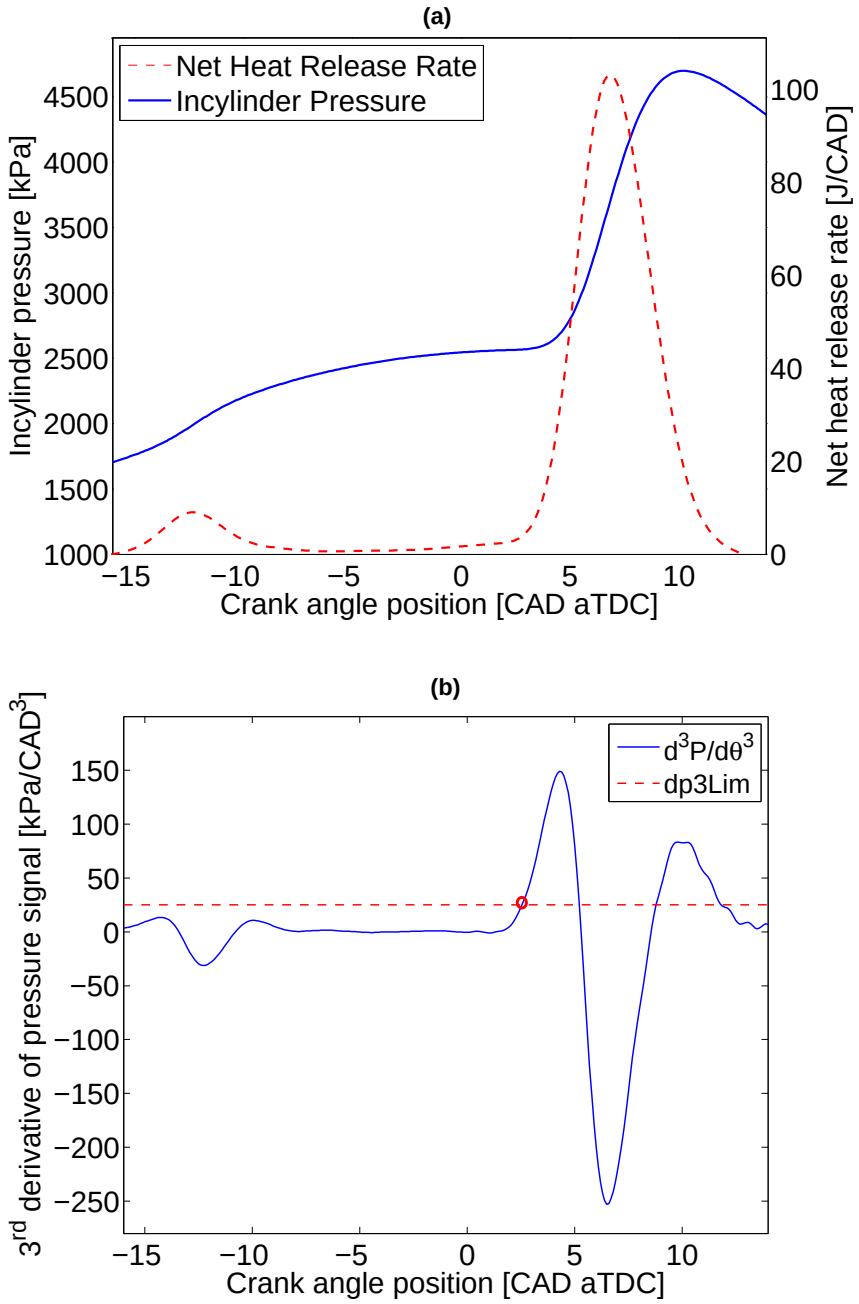

Figure C.1: Using dp3Lim criteria (Eq. C.1) to find SOC of the main stage of HCCI combustion. SOC of 2.6 CAD aTDC is calculated for this sample operating point. (PRF40, N= 909 rpm, Φ= 0.46, EGR= 0%, T_m= 110 ^oC, P_m= 114 kPa)

The performance of dp3Lim criteria is indicated for a sample operating point in Figure C.1. This method works well on normal HCCI operating points. However, if the ignition process is too slow that this algorithm does not detect it, the mixture does not go through the second ignition stage and is therefore not of interest. The limit is selected such that the point of ignition represented the change in concavity and is not effected by noise in the differentiated signal.

Appendix D

KIM Development towards MKIM

D.1 KIM APPLICATION IN HCCI

As explained in Section 4.2.2.1, the Knock Integral Model in the crank angle domain yields:

$$\frac{(x)}{(x)_c} = \int_{\theta_o=0}^{\theta=\theta_e} \frac{1}{\omega\tau}\, d\theta = \int_{\theta_o=0}^{\theta=\theta_e} \frac{1}{\mathrm{A}\omega e^{(\mathrm{b}/T)p^{\mathrm{n}}}}\, d\theta = 1.0 \tag{D.1}$$

To test the performance of the KIM, the engine simulations are used to determine the model parameters. Then the SOC is predicted for these same simulations to show if the correlation can capture the relationship between the changing engine operating conditions and the start of combustion.

D.1.1 Thermokinetic Model Simulations

The TKM from Chapter 3 is used as a virtual engine and each engine parameter is varied independently and simulated to determine the effects of engine parameters on the ignition timing. In particular, the engine speed, initial mixture temperature and pressure, EGR percentage, and equivalence ratio are varied over the ranges outlined in Table D.1. The parameter ranges given in Table D.1 are chosen to represent typical HCCI operation.

TKM simulations for the complete parameter variation of Table D.1 for two primary reference fuels n-Heptane ($ON = 0$) and iso-Octane ($ON = 100$) are

Table D.1: Parameter variations carried out using the TKM.

Engine Speed	1000, 2000, 3000 rpm
Initial Temperature	300, 310,..., 440, 450 ^oK
EGR(%)	0%, 0.25%, 0.5%
Equivalence Ratio	0.5, 0.7, 0.9
Initial Pressure	50, 100 kPa
Fuel	n-Heptane, iso-Octane
Compression Ratio	12:1
Cylinder Bore	8.3 cm
Piston Stroke	11.4 cm
Intake Valve Closing	-146 CAD aTDC
Exhaust Valve Opening	130 CAD aTDC
Wall temperature	390 K

performed. From the resulting 1621 simulations, complete combustion occurred in 176 simulations including 92 simulations with n-Heptane and 84 simulations with iso-Octane. Both the KIM and the MKIM are only valid for a complete combustion thus only these 176 simulations are used for both parametrization, and validation of the KIM and the MKIM ignition correlations.

D.1.2 KIM Evaluation

Two different SOCs are defined. In the first approach, SOC is defined as the crank angle as 1% of the mass fraction fuel burns, while in the second approach SOC is defined as a threshold of the third derivative of pressure with respect to CAD (see Section 2.2.2.1). Figures D.1 and D.2 are two samples of simulation results showing the ability of the KIM to predict the SOC for the two fuels. The resulting parameters are also shown. The KIM predicts the SOC for both definitions well. For both 1% mass burned and the pressure derivative limit definitions of SOC

and for both n-Heptane and iso-Octane fuels, the average error of the ignition prediction is less than 1.0 CAD.

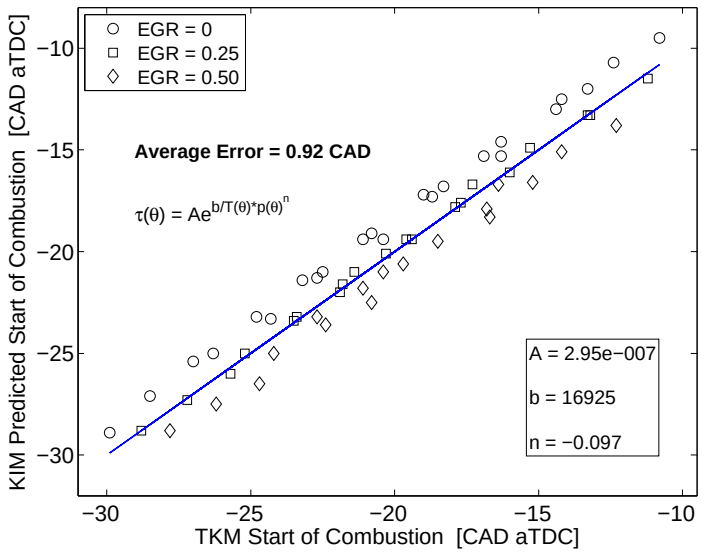

Figure D.1: Predicted SOC based on 1% mass burned, using the KIM with iso-Octane as fuel. The line represents where the prediction is the same as the SOC from the TKM.

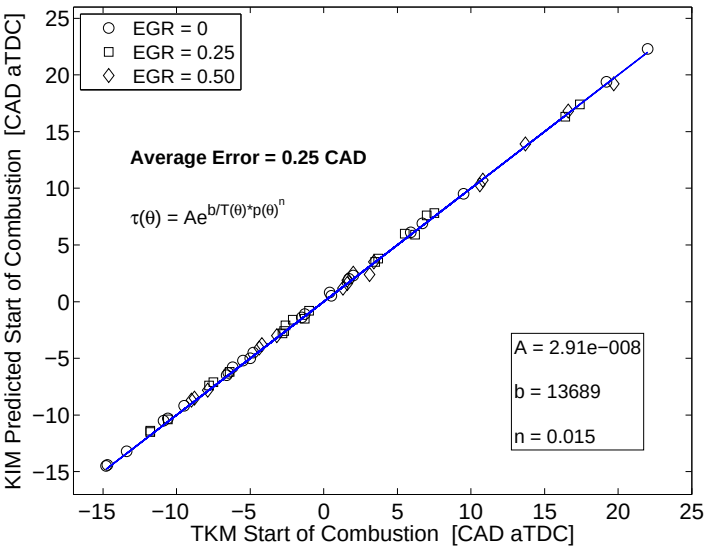

Figure D.2: Predicted SOC based on the pressure derivative limit, using the KIM with iso-Octane as fuel. The line represents where the prediction is the same as the SOC from the TKM.

D.2 MKIM DEVELOPMENT

Although the KIM predicts HCCI ignition accurately, it is impractical for a real engine operation. Engine conditions, such as temperature, pressure must be available during compression (here every 0.1 CAD). In the TKM simulations this is possible, but on a real engine, it is not. In addition th equation (D.1) is for an engine operating at a constant AFR with no EGR. To adapt this correlation to an HCCI engine with varying AFR rates and EGR typical of HCCI operation, these factors have to be accounted for.

D.2.1 Polytropic Compression

To avoid the requirement of crank angle measurements of temperature and pressure during the engine compression, the SOC can be predicted using the KIM if the temperature and pressure rise in the cylinder is assumed to occur as a polytropic process [151]. This assumption neglects any pre-ignition heating resulting from reactions that occur before the SOC. Thus, the start of combustion is defined as 1% of mass fraction burned since only a small amount of heat release has occurred.

The compression of the gases in an engine from IVC to SOC can be predicted by an isentropic / polytropic process [201]. To consider an isentropic process ($PV^{\gamma} = constant$), the ratio of specific heat capacity (γ) for the gases in the cylinder of an engine is needed. As the mixture and concentrations of species in the cylinder of the engine change, γ varies too. Two methods to obtain γ for the gases in the cylinder of an engine at θ_{IVC} are given. Knowing the initial pressure, temperature and species concentrations, the ratio of specific heat capacity can be found analytically using NASA polynomials [133]. This method requires significant computation and data for species concentrations and temperatures in the cylinder. The other method is to obtain the temperature or pressure at IVC

and SOC of multiple simulations and use a best fit method to find the ratio of specific heat capacity. The resulting equations to calculate the temperature and pressure at the SOC become:

$$T_{SOC} = T_{IVC}\ v_{SOC}^{\mathrm{k_c}-1} \tag{D.2}$$

$$P_{SOC} = P_{IVC}\ v_{SOC}^{\mathrm{k_c}} \tag{D.3}$$

$$where\ \ v_{SOC} = \frac{V_{IVC}}{V_{SOC}}$$

where the constant $\mathrm{k_c}$ does not represent the actual specific heat capacity, but rather the average of all the simulations are determined by a numeric best fit (i.e. assuming a polytropic process). The volume of the cylinder can be calculated at any crank angle from engine geometry.

To predict the SOC with only the initial temperature and pressure, equations (D.2) and (D.3) are substituted into the KIM (D.1). The resulting integral becomes:

$$\int_{\theta_{IVC}}^{\theta_{SOC}} \frac{1}{\tau}\ d\theta = \int_{\theta_{IVC}}^{\theta_{SOC}} \frac{1}{\mathrm{A}\omega\ exp\left(\frac{\mathrm{b}(P_{IVC}v_c^{\mathrm{k_c}})^{\mathrm{n}}}{T_{IVC}\ v_c^{\mathrm{k_c}-1}}\right)}\ d\theta = 1.0 \tag{D.4}$$

$$where\ \ v_c = v_c(\theta) = \frac{V(\theta_{IVC})}{V(\theta)}$$

Simulation results based on the Modified Knock Integral Model (MKIM) equation (D.4) show that the modified correlation does not predict the SOC as accurately as the original KIM. This is not surprising since in the MKIM only one value of each pressure and temperature (at IVC) is used, while the KIM uses the

whole time sequence of pressure and temperature from the IVC to SOC. However the equivalence ratio and EGR rate also affect the SOC [133]. These two parameters are incorporated into a further improved MKIM.

D.2.2 Fuel and Oxygen Concentrations

The concentrations of the fuel (C_iH_j) and oxygen (O_2) are indicative of the equivalence ratio and EGR rate [143, 147]. A crank angle measurement of these concentrations is required for the MKIM which is possible in the TKM simulations but not practical in the real engine. Thus an approach similar to that used to describe the polytropic process is developed to predict the concentrations during compression.

To predict the concentrations, it is assumed that the mass of the fuel and oxygen remains constant until the SOC. The change of concentration is proportionally related to the change in volume. The concentration, defined as mass divided by volume [kg/cm^3], of species N at any crank angle after the intake valve closes (θ_{IVC}) and before the SOC (θ_{SOC}) is:

$$[N](\theta) = [N](\theta_{IVC}) \left(\frac{V(\theta_{IVC})}{V(\theta)} \right) = [N]_{IVC} v_c \tag{D.5}$$

Using this relationship in MKIM equation (D.4), the new MKIM is:

$$\int_{\theta_{IVC}}^{\theta_{SOC}} \frac{1}{\mathrm{A}\omega \; exp\left(\frac{\mathrm{b}(P_{IVC} v_c^{\mathrm{kc}})^{\mathrm{n}}}{T_{IVC} v_c^{\mathrm{kc}-1}} \right)} ([C_iH_j]_{IVC} v_c)^{\mathrm{x}} \times \; ([O_2]_{IVC} v_c)^{\mathrm{y}} \; d\theta = 1.0 \tag{D.6}$$

where A, b, n, x and y are the constant parameters. These parameters are found using an optimization algorithm. The unknowns i and j are dependent on the chemical properties of the fuel. The increased complexity of MKIM in equation (D.6) increases the computational time to determine the parameters.

Once the parameters are determined, equation (D.6) can be simply integrated to predict the SOC for different initial conditions.

The TKM simulations for n-Heptane and iso-Octane are used to parameterize and evaluate equation (D.6). The results are not presented and showed a good ability to predict the SOC for both fuels with only the initial temperature, pressure, and concentrations of the fuel and oxygen as inputs.

D.2.3 Equivalence Ratio

In most engine applications, the initial concentrations of the fuel and oxygen are not available. Although it is possible to determine these parameters using an exhaust gas analyzer and oxygen sensors, an exhaust analyzer is not present on production engines. Representing the initial concentrations of fuel and oxygen as the parameters that are easy to measure, but still describe the amount of fuel and air in the engine is more practical.

The equivalence ratio (ϕ) is a good indication of both the amount of fuel and air available in the engine charge and it can also be measured on an operating engine without difficulty using a broadband oxygen sensor. Therefore, an equivalence ratio term replaces the species concentrations in the MKIM. The equivalence ratio is represented in the MKIM equation (D.6) as follows:

$$\int_{\theta_{IVC}}^{\theta_{SOC}} \frac{1}{\mathrm{A}\omega \; exp\left(\frac{\mathrm{b}(P_{IVC}v_c^{\mathrm{kc}})^{\mathrm{n}}}{T_{IVC}v_c^{\mathrm{kc}-1}}\right)} \; \phi^{\mathrm{x}} \; d\theta = 1.0 \tag{D.7}$$

where, A, b, n, x are the model parameters.

D.2.4 Model Setup

To parameterize the MKIM, two steps are required here. First, the polytropic parameter ($\mathrm{k_c}$) is determined using a best-fit methodology over compression part

of simulation data. Second, an optimization is used to find the best values for the parameters of the MKIM. These two steps are detailed below.

D.2.4.1 Finding the Polytropic Parameter

Using the engine parameter variations for n-Heptane and iso-Octane, the values of k_c can be determined by fitting a best polytropic relation between the temperature or pressure at IVC and SOC of the simulations. Figure D.3 show the resulting constant k_c and the predicted temperature at the SOC as a function of the actual temperature at the SOC. From Figure D.3, it can be concluded that the equivalence ratio (ϕ) has an effect on the temperature required for the SOC with both fuels and since the MKIM is using a constant k_c for each of these two fuels, it overpredicts T_{SOC} for high equivalence ratios and underpredicts T_{SOC} for low equivalence ratios.

An additional analysis was done using NASA polynomials [133] to determine the magnitude of the effect of the equivalence ratio on the calculated constant k_c. It was found that in the simulations using equivalence ratios of 0.5, 0.7 and 0.9 and EGR rates of 0%, 0.25% and 0.50%, the value of k_c only differed by 0.021. The values of k_c found for the simulations involving n-Heptane and iso-Octane also agree with the calculated specific heat capacity ratios using analytical techniques. The simulation results for n-Heptane in Figure D.3-a show more scatter of the data compared to the iso-Octane simulation results in Figure D.3-b. Furthermore, the temperatures at the SOC are higher for iso-Octane compared to n-Heptane. This result agrees with other investigations of the pre-ignition chemistry leading up to combustion in HCCI engines [202, 203].

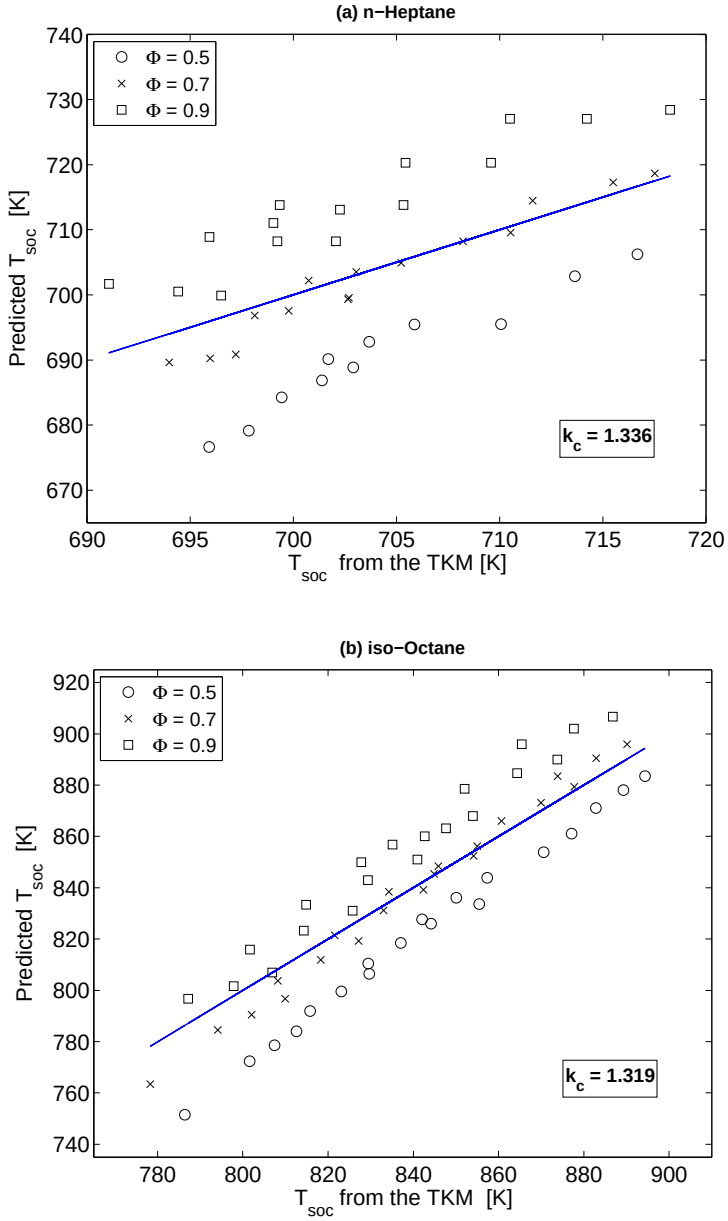

Figure D.3: Optimum value of k_c, defined in (D.2), for simulations at three equivalence ratios. The line represents where the prediction is the same as the T_{SOC} from the TKM.

D.2.4.2 Optimizing the MKIM Parameters

In order to fit the parameters of the MKIM equation (D.7) the error of the integration should be minimized, where the target value is 1.0. The numerical minimization is performed using the built-in Matlab function $fminsearch$, which

uses the Nelder-Mead simplex minimization method [165]. The integration is carried out numerically with the rectangular method with a step size of 0.1 CAD. The program then uses the pre-determined optimized parameters and computes the predicted ignition point by integrating (D.7) until it equals 1.0. The resulting crank angle is taken as the predicted angle of ignition.

D.2.5 Results

Using 176 TKM simulations from Section D.1.1, the parameters of the MKIM are determined. Figure D.4 shows the ability of equation (D.7) in predicting the SOC for both n-Heptane and iso-Octane fuels. In this case of n-Heptane (Figure D.4-a) the SOC is not affected substantially by EGR, but for the iso-Octane case the amount of EGR changes the ability of the correlation to accurately predict the SOC as shown in Figure D.4-b.

To determine the relationship that EGR has on the SOC, the parameter A was determined for different rates of EGR while keeping the other parameters (b, n, and x) constant. It is found that the parameter A is linearly dependent on the rate of EGR for iso-Octane. This is generalized for all fuels resulting in a further improved MKIM:

$$\int_{\theta_{IVC}}^{\theta_{SOC}} \frac{\phi^{\mathrm{x}}}{A\omega \; exp\left(\frac{\mathrm{b}(P_{IVC}v_c^{\mathrm{k_c}})^{\mathrm{n}}}{T_{IVC}v_c^{\mathrm{k_c}-1}}\right)} \, d\theta = 1.0 \tag{D.8}$$

$$where \quad A = \mathrm{E}_1 \, EGR + \mathrm{E}_2$$

Here, E_1 and E_2 are constant parameters.

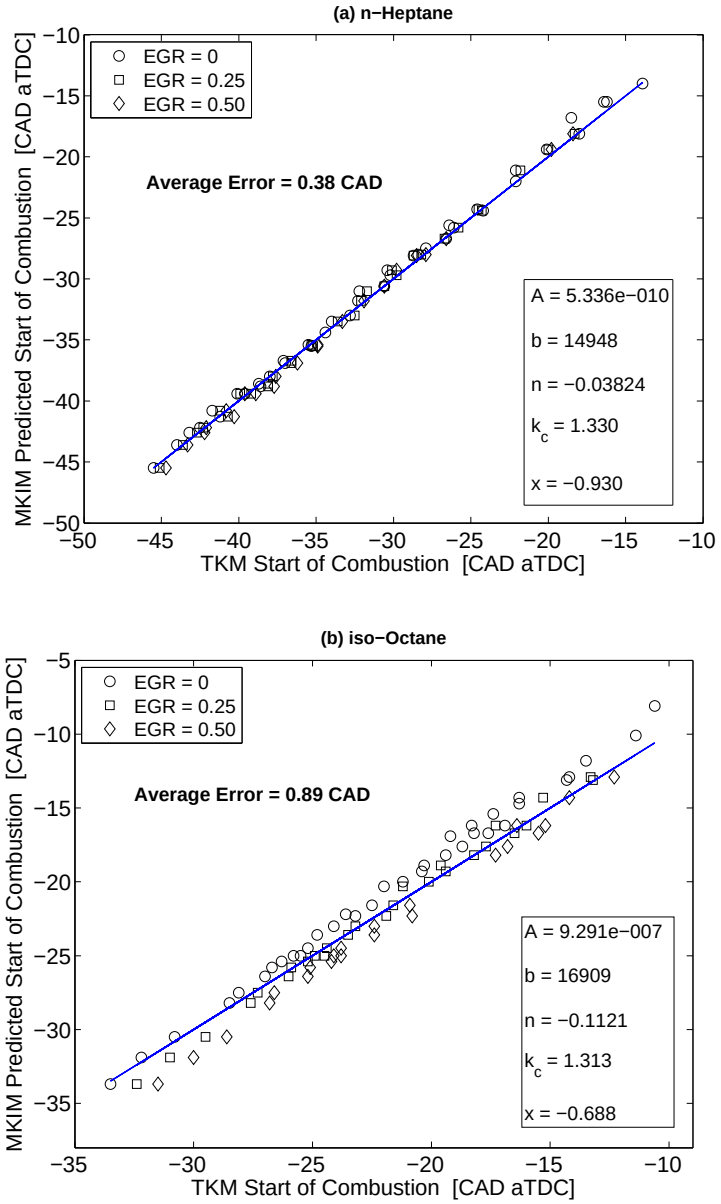

Figure D.4: Predicted SOC simulations at various engine conditions using the MKIM (D.7). The line represents where the prediction is the same as the SOC from the TKM.

The performance of equation (D.8) is shown in Figures D.5. The new correlation does an excellent job predicting the SOC in the presence of EGR. Comparing Figure D.5 with Figure D.4, it can be seen that the average error in predicting the SOC for iso-Octane was substantially reduced from 0.89 CAD to 0.44 CAD, while for n-Heptane it was reduced slightly from 0.38 CAD to 0.35 CAD. Clearly

n-Heptane improved less because it did not have a strong dependence on EGR. This is also evident by comparing parameter A in Figures D.5 where the slope of A (parameter E_1) for n-Heptane is smaller than that of iso-Octane.

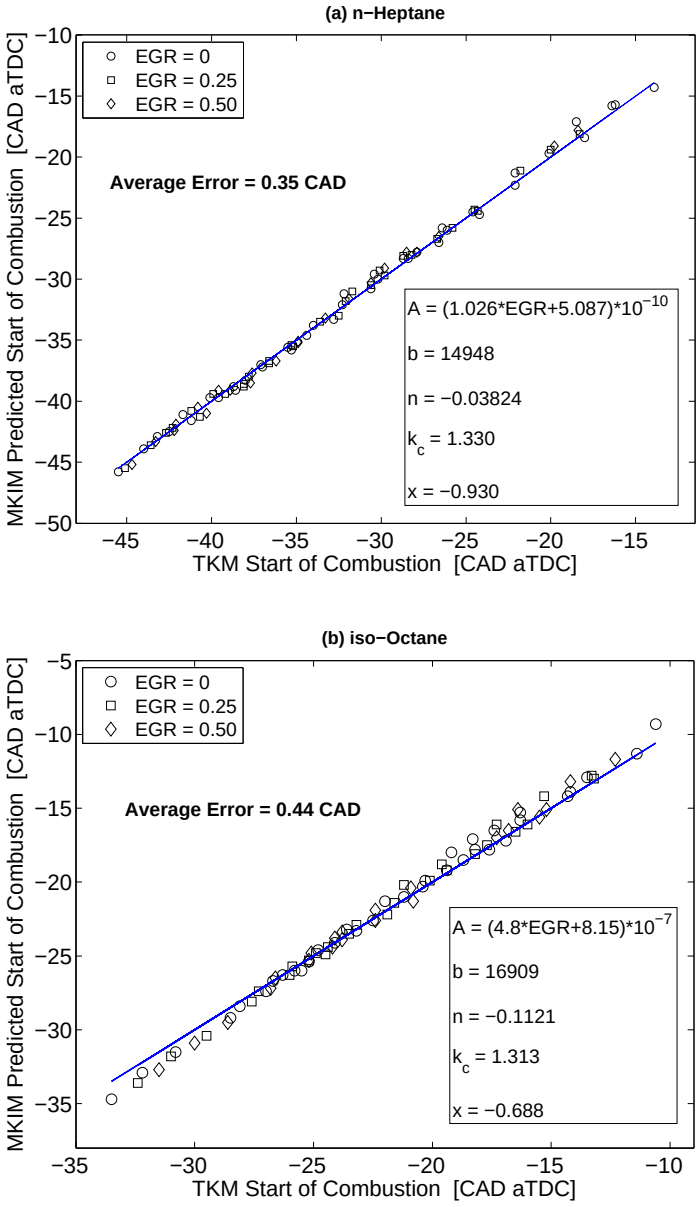

Figure D.5: Predicted SOC at various engine conditions using MKIM (D.8). The line represents where the prediction is the same as the SOC from the TKM.

The values of parameter x from equation (D.8) in Figures D.5 indicate that equivalence ratio is more effective on the SOC of n-Heptane than that of iso-

Octane. Therefore, with the same amount of change in ϕ, the SOC of n-Heptane changes more. The 176 points in Figure D.5 cover a diverse range of engine speed, initial temperature, initial pressure, EGR rate and equivalence ratio. The results presented in Figure D.5 indicate SOC can be accurately predicted by the MKIM over a range of HCCI operating conditions.

Appendix E

Injector Calibration and C_D Calculation for Exhaust Valve Flow

E.1 INJECTOR CALIBRATION

Dynamic fuel flow rate of injectors can be determined from injector's pulse width in terms of time or crank angle interval when the fuel injector is on. Injected fuel mass per cycle ($m_{f,i}$) for both injectors is estimated from the PW of the injectors [185]:

$$m_{f,inj}\left[\frac{\text{g}}{\text{cycle}}\right] = \text{C}_\text{f} \ . \ PW_{inj}\,[\text{ms}] + \text{C}_\text{offset} \tag{E.1}$$

where, C_f and C_offset are constant parameters that are determined by injector calibration from steady state fuel flow measurements. A series of steady-state tests are carried out in the Ricardo engine test cell using Pierburg fuel flow measuring system to measure the mass amount of the fuel delivered by injectors. Tests are done for both n-Heptane injector and iso-Octane injector separately at different conditions. The mass of the fuel injected per cycle is calculated from Pierburg measurements and engine speed. A linear correlation is fit between fuel injection pulse width and fuel mass per cycle. Figure E.1 shows the results of injectors' calibration. The resulting C_f and C_offset are 2.95 $\left[\frac{\text{g}}{\text{ms.cycle}}\right]$ and -2.74 $\left[\frac{\text{g}}{\text{cycle}}\right]$ for the n-Heptane injector and 3.30 $\left[\frac{\text{g}}{\text{ms.cycle}}\right]$ and -2.90 $\left[\frac{\text{g}}{\text{cycle}}\right]$ for the iso-Octane injector.

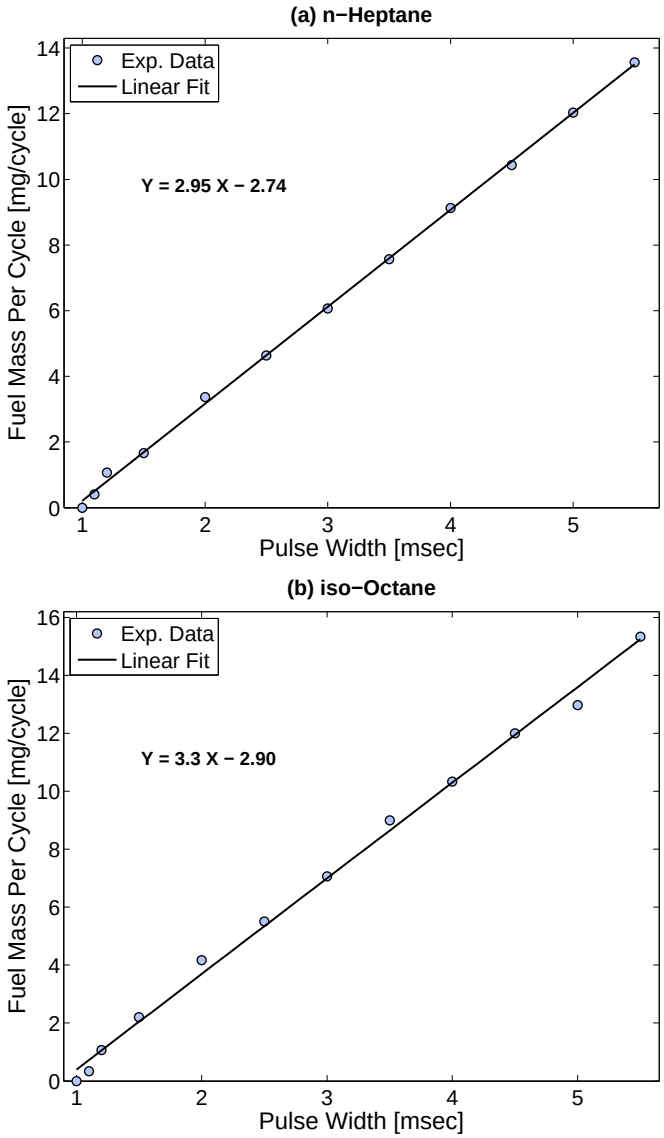

Figure E.1: Calibration plot of injectors for the operating battery voltage.

The average error of the correlation is 0.08 mg/cycle for n-Heptane injector and 0.22 mg/cycle for iso-Octane injector. These two linear fits are used to calculate the octane number and mass of the injected fuel per cycle. These correlations are essential particularly for transient tests where on-line measurement of the fuel flow rate is difficult and expensive.

E.2 C_D FOR EXHAUST VALVE FLOW

Coefficient of discharge (C_D) for the flow across the exhaust valves is determined using the flow measurements from [173] for a Mercedes E550 cylinder head. Flow measurements at 45 different valve lifts and pressure ratios are shown in Figure E.2:

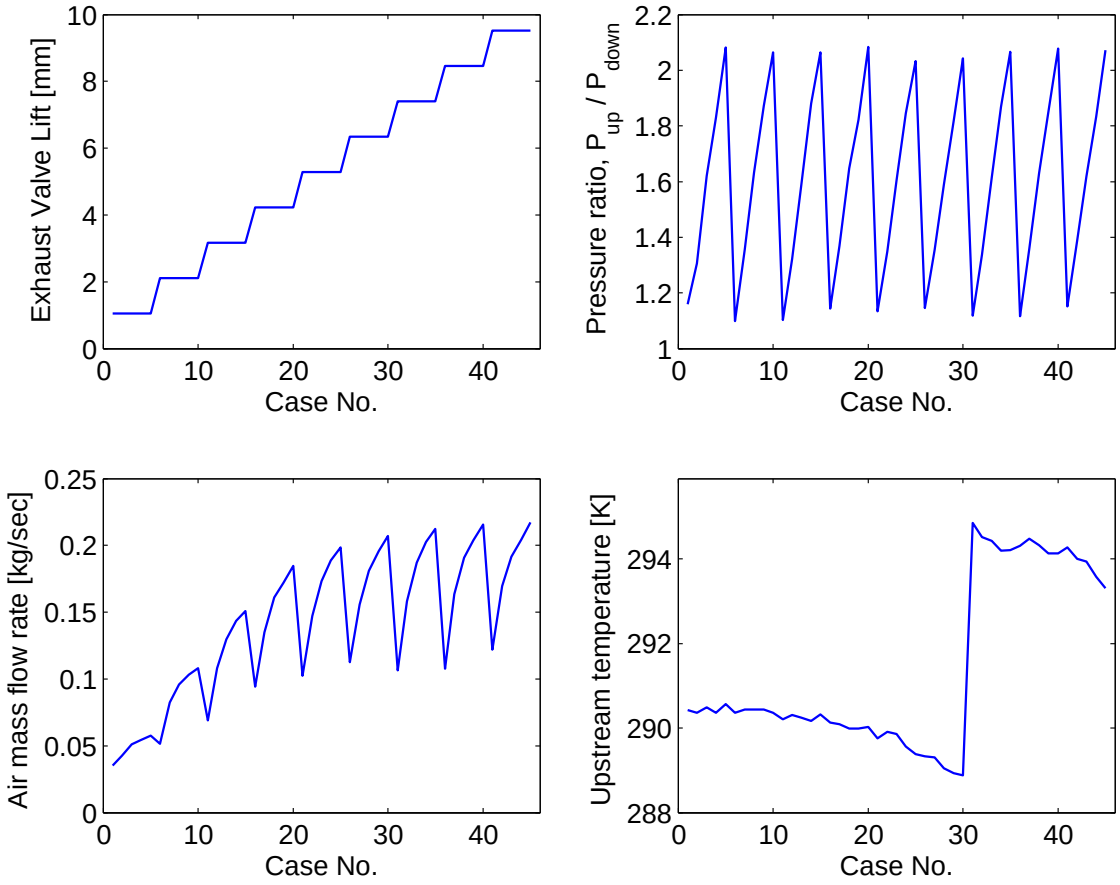

Figure E.2: Air mass flow measurements across the exhaust valves of the engine [173].

Steady-state, compressible, isentropic flow equations [101] are used to calculate C_D for each of the 45 data points in Figure E.2. Results are shown in Figure E.3 and Figure E.4.

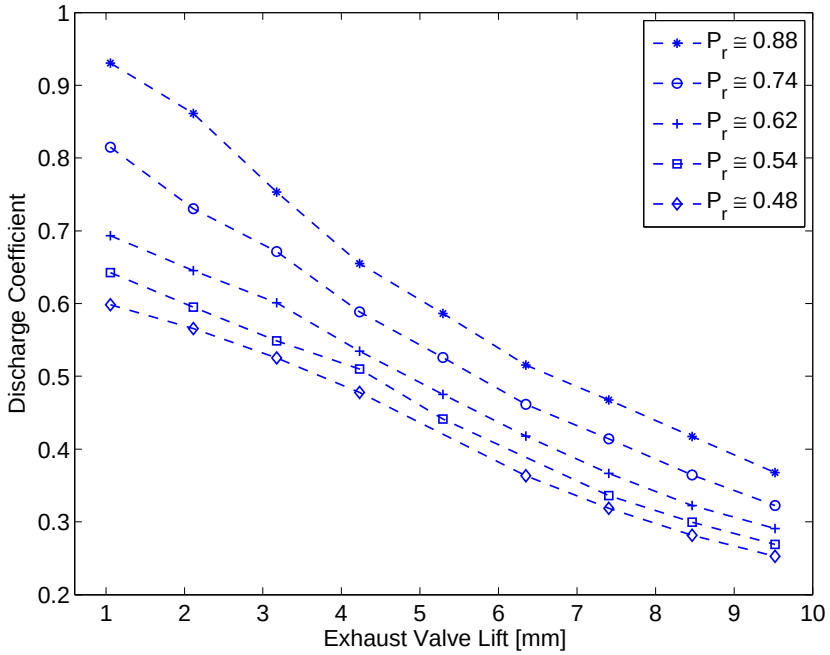

Figure E.3: Calculated C_D values versus exhaust valve lifts at different pressure ratios.

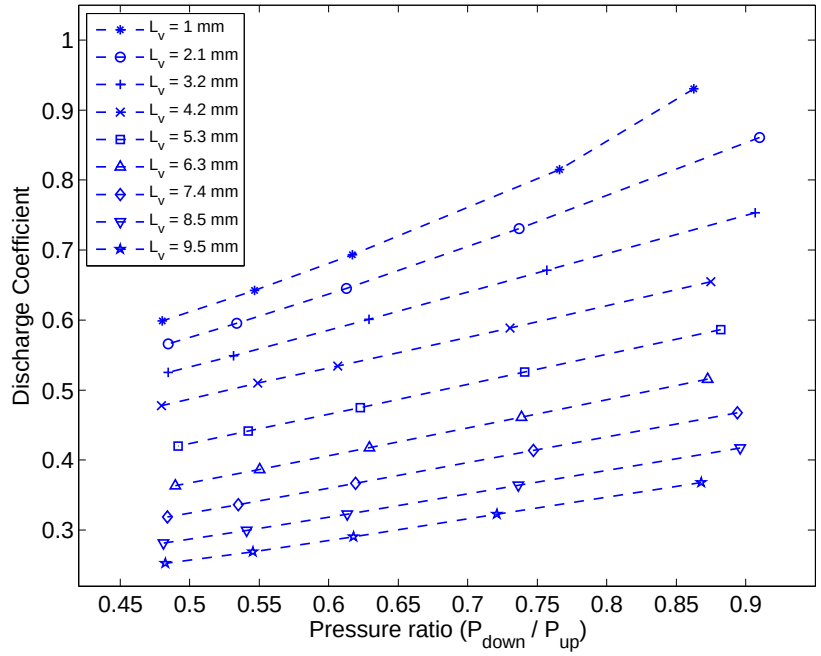

Figure E.4: Calculated C_D values versus pressure ratios at different valve lifts (L_v).

Calculated values for C_D at different conditions are studied to find a correlation to fit the measurements. The following correlation is found to work well on the available data:

$$C_{_D} = \mathrm{A} + \mathrm{B}\ \ln\left(\frac{L_v}{d_v}\right) + \mathrm{C}\ \left(\ln\left(\frac{L_v}{d_v}\right)\right)^2 + \mathrm{D}\ \ln\left(\frac{P_o}{P_T}\right) \tag{E.2}$$

where, P_o and P_T refer to the gas pressure at the upstream and the downstream of the exhaust valves. d_v and L_v are the diameter of the exhaust valves and the axial valve lift. A, B, C, and D are the constants that need to be determined. For the 45 flow measurements, predicted values of C_D from the correlation (E.2) are compared with those from experiments in Figure E.5. The uncertainty analysis results indicate an uncertainty of ± 0.06 in predicted $C_{_D}$.

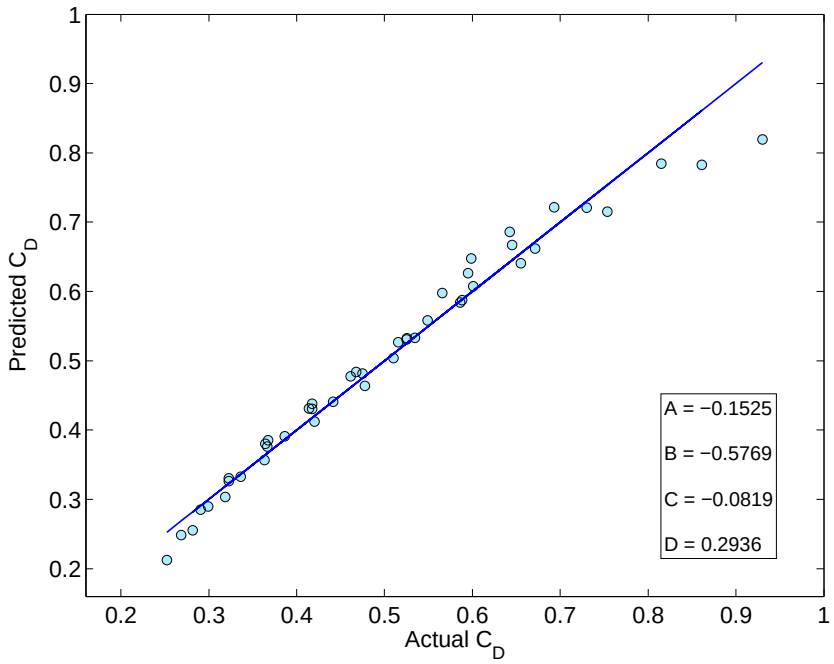

Figure E.5: Comparing measured C_D values with those predicted from the correlation (E.2). The line represents where predicted and measured C_D are the same.

Appendix F

Ph.D. Publications

F.1 Peer Reviewed Journal Papers

1. M. Shahbakhti, C. R. Koch, " Physics Based Control Oriented Model for HCCI Combustion Timing ", to appear in Journal of Dynamic Systems, Measurement and Control, 58 pages, accepted in May, 22, 2009.

2. A. Ghazimirsaied, M. Shahbakhti, C. R. Koch, " HCCI Combustion Phasing Prediction Using a Symbol-Statistic Approach ", to appear in Journal of Engineering for Gas Turbines and Power, 21 pages, accepted in May, 18, 2009.

3. M. Shahbakhti, C. R. Koch, " Dynamic Modeling of HCCI Combustion Timing in Transient Fueling Operation ", to appear in SAE 2009 Transactions Journal of Engines, 16 pages, accepted in Apr., 27, 2009.

4. M. Shahbakhti, C. R. Koch, " Characterizing the Cyclic Variability of Ignition Timing in an HCCI Engine Fueled with n-Heptane/iso-Octane Blend Fuels ", International Journal of Engine Research, Volume 9, Issue 5, pages 361-397, October 2008.

5. P. Kirchen, M. Shahbakhti, C. R. Koch, " A Skeletal Kinetic Mechanism for PRF Combustion in HCCI Engines ", Journal of Combustion Science and Technology, Volume 179, Issue 6, pages 1059 - 1083, June 2007.

6. K. Swan, M. Shahbakhti, C. R. Koch, " Predicting Start of Combustion Using a Modified Knock-Integral Method for an HCCI Engine ", SAE 2006 Transactions Journal of Engines, pages 611-620, March, 2007.

F.2 Refereed Conference Papers

1. M. Shahbakhti, A. Ghazimirsaied, C. R. Koch, " Predicting the Distribution of Combustion Timing Ensemble in an HCCI Engine ", ASME Internal Combustion Engine Division Spring Technical Conference, Paper No. ICES2009-76007, 12 pages, May 3-6, 2009, Milwaukee, Wisconsin, USA.

2. A. Ghazimirsaied, M. Shahbakhti, C. R. Koch, " Nonlinear Dynamics in Cyclic Variations of Combustion Phasing in an HCCI Engine ", ASME Internal Combustion Engine Division Spring Technical Conference, Paper No. ICES2009-76157, 7 pages, May 3-6, 2009, Milwaukee, Wisconsin, USA.

3. M. Shahbakhti, A. Ghazimirsaied, C. R. Koch, " The Effect of Operating Conditions on HCCI Exhaust Gas Temperature ", Proceeding of Combustion Institute-Canadian Section (CICS) Spring Technical Conference, Paper No. CICS-A02, 6 pages, May 10-13, 2009, Montreal, Canada.

4. A. Ghazimirsaied, M. Shahbakhti, C. R. Koch, " Partial-Burn Crank Angle Limit Criteria Comparison on an Experimental HCCI Engine ", Proceeding of Combustion Institute-Canadian Section (CICS) Spring Technical Conference, Paper No. CICS-A52, 6 pages, May 10-13, 2009, Montreal, Canada.

5. M. Shahbakhti, C. R. Koch, " Dynamic Modeling of HCCI Combustion Timing in Transient Fueling Operation ", Proceeding of SAE World Congress, SAE Paper No. 2009-01-1136, 16 pages, April 20-23, 2009, Detroit, USA.

6. A. Ghazimirsaied, M. Shahbakhti, A. Audet, C. R. Koch, " HCCI En-

gine Cyclic Variation Characterization Using Both Chaotic and Statistical Approach ", Proceeding of Combustion Institute-Canadian Section (CICS) Spring Technical Conference, 6 pages, May 12-14, 2008, Toronto, Canada.

7. M. Shahbakhti, R. Lupul, C. R. Koch, " Sensitivity Analysis and Modeling of HCCI Auto-Ignition Timing ", Proceeding of Fifth IFAC Symposium on Advances in Automotive Control, pages 303 - 310, August 20-22, 2007, Monterey Coast, California, USA.

8. M. Shahbakhti, R. Lupul, A. Audet, C. R. Koch, " Experimental Study of HCCI Cyclic Variations for Low-Octane PRF Fuel Blends ", Proceeding of Combustion Institute-Canadian Section (CICS) Spring Technical Conference, 6 pages, May 13-16, 2007, Banff, Canada.

9. M. Shahbakhti, C. R. Koch, " Thermo-kinetic Combustion Modeling of an HCCI Engine to Analyze Ignition Timing for Control Applications ", Proceeding of Combustion Institute-Canadian Section (CICS) Spring Technical Conference, 6 pages, May 13-16, 2007, Banff, Canada.

10. M. Shahbakhti, C. R. Koch, " Control Oriented Modeling of Combustion Phasing for an HCCI Engine ", Proceeding of 2007 American Control Conference, pages 3694-3699, July 11-13, 2007, New York, USA.

11. M. Shahbakhti, R. Lupul, C. R. Koch, " Cyclic Variations of Ignition Timing in an HCCI Engine ", Proceeding of Annual ASME/IEEE Joint Rail Conference (JRC) and the ASME Internal Combustion Engine Division (ICED) Conference, Paper No. JRCICE2007/40032, 11 pages, March 13-16, 2007, Pueblo, Colorado, USA.

12. M. Shahbakhti, R. Lupul, C. R. Koch, " Predicting HCCI Ignition Timing by Extending a Modified Knock-Integral Method ", Proceeding of SAE

World Congress Conference, SAE Paper No. 2007-01-0222, 13 pages, April 16-19, 2007, Detroit, USA.

13. K. Swan, M. Shahbakhti, C. R. Koch, " Predicting Start of Combustion Using a Modified Knock-Integral Method for an HCCI Engine ", Proceeding of SAE World Congress Conference, SAE Paper No. 2006-01-1086, 10 pages, April 3-7, 2006, Detroit, USA.

Appendix G

Program and Data File Summary

G.1 EXPERIMENTAL DATA AND POSTPROCESSING FILES

The following lists the experimental data and script files used to study HCCI cyclic variation and exhaust temperature variations in Ricardo and CFR engines.

Table G.1: Experimental data files

File Name	**File Description**
Ricardo_ExpData_CyclicVariationStudy.mat	329 data points used to study cyclic variation in Ricardo engine
CFR_ExpData_CyclicVariationStudy.mat	105 data points used to study cyclic variation in CFR engine
Ricardo_ExpData_HCCI_Texh.mat	304 data points used to study HCCI T_{exh} variations in Ricardo engine
Ricardo_ExpData_SI_Texh.xls	36 data points used to study SI T_{exh} variations in Ricardo engine

Table G.2: Postprocessing script files

File Name	**File Description**
CombAnalyzerForHCCI.m	Calculates HCCI combustion metrics
GetHeatRelease.m	Determines net and gross heat release using filtered pressure traces
GetTcyl.m	Estimates in-cylinder gas temperature by applying the ideal gas law on recorded in-cylinder pressure data
KnockDetectionPars.m	Calculates three main parameters to characterize the knocking intensity
Predict_Texh3D.m	Parameterized the correlation for predicting the HCCI exhaust temperature
PlottingCyclicVariations.m	Postprocess the cyclic variation experimental data to create desirable figures
Plotting4SI.m	Generates the plots indicating the impact from changing engine speed and intake pressure on the SI exhaust temperature
MakeTableOfConditions.m	Creates a text file called "TestConditions.txt" which can be used in LaTex to report operating conditions of the experimental data set

G.2 TKM AND SENSITIVITY ANALYSIS FILES

The following lists the simulation data and script files used to evaluate the developed TKM for predicting HCCI ignition timing as well as performing ignition timing sensitivity analysis for different engine variables.

Table G.3: Experimental data files

File Name	**File Description**
TKM Simulation - Validation	Original TKM simulations to validate/ parameterize the TKM
TKM Simulations - Sensitivity	Original TKM simulations to carry out sensitivity analysis
SensitivityWithTKM.xls	Processed TKM simulations used for sensitivity analysis

Table G.4: MATLAB script files

File Name	**File Description**
start_exothermic_v1.m	Initiates running the TKM. The main body of the TKM is formed by kinetics_fun_v1.m
MotoringSimulator.m	Simulates in-cylinder pressure at motoring conditions
postprocessHCCI.m	Postprocess TKM simulations to calculate SOC
Comp_Exp_CICS.m	Calculates SOC from the experimental pressure data and compares SOC from the experiment with SOC from the TKM

G.3 IGNITION TIMING MEAN-VALUE MODEL FILES

The following lists the experimental and simulation data files required to parameterize and validate the CA_{50} mean-value model developed in Chapter 4. In addition, the script file of the final model as well as the required script files to determine model parameters are listed.

Table G.5: Experimental data files

File Name	**File Description**
MKIM_TKM_Simulations.mat	Processed TKM simulations used to parameterize the MKIM
MeanCA50_ExpData.mat	Experimental data to parameterize and to validate the final model which predicts CA_{50}

Table G.6: MATLAB script files

File Name	**File Description**
CA50Modeling_Static.m	Initiates running the mean-value CA_{50} model. The main body of the model is formed by CA50Modeling_MeanValue.m which predicts CA_{50}.
Postprocess_MKIM.m	Postprocess TKM simulations to parameterize the MKIM
get_ModelPar.m	Determines MKIM parameters A, B, C, and D using TKM simulations at a fixed EGR rate
get_parA_egr.m	Calculates the MKIM parameter A as a function of EGR using TKM simulations at four EGR rates
get_Pivc_correlation.m	Optimization code to parameterize the correlation used to predict Pivc
get_Tivc_correlation.m	Optimization code to parameterize the correlation used to predict Tivc

G.4 DYNAMIC HCCI MODEL FILES

The following lists the MATLAB model and script files used to develop a dynamic model which predicts cycle-to-cycle HCCI combustion timing. To run the model, experimental data file from Table G.8 is loaded. Then, the following command is run: CA50DynamicModeling_Cyclic(*ExpData*, sp_DynamicModeling, Exhaust-Valve)

where, *ExpData* is a structure data file (e.g. ExpData_Oct26_Test3) and includes the experimental conditions for an array of consecutive cycles.

Table G.7: MATLAB script files

File Name	**File Description**
CA50DynamicModeling_Cyclic.m	Initiates running the dynamic HCCI model. The main body of the model is formed by CA50DynamicModeling_VO.m which predicts cycle-to-cycle CA_{50}.
Postprocess_MKIM.m	Postprocess TKM simulations to parameterize the MKIM
Get_ON.m	Determines the fuel octane number using injectors' pulse widths
Get_CD.m	Calculates the discharge coefficient for the flow across the exhaust valves
LHV_Finder.m	Calculates lower heating value of PRF blends
GetFuelDynPars.m	Determines fuel dynamic parameters
GetCOC.m	Calculates Completeness of Combustion using the experimental data
ExertUegoLag.m	Prepares the experimental data for use in system identification toolbox in MATLAB
FuelDyn_Simulator.mdl	Simulates fuel transport dynamics in the intake ports

Table G.8: Experimental data file

File Name	File Description
ExpData_DynamicModeling.mat	Transient experimental data used to validate the dynamic HCCI model

G.5 FILES OF IGNITION TIMING ENSEMBLE STUDY

The following lists the script files used to analyze the distribution shapes of the experimental ignition timings. In addition, the experimental data file and the model script file to predict ranges of CA_{50} cyclic variations are listed.

Table G.9: Experimental data file

File Name	File Description
ExpData_ProbabilityStudy.mat	Experimental data used for modeling the distribution of HCCI combustion timing ensemble

Table G.10: MATLAB script files

File Name	File Description
Predict_HighVariationLimit.m	Predicts ranges of HCCI ignition timing cyclic variations
DistTest.m	Evaluates whether the experimental ignition timing distribution is normal and generates the desirable probability plots
CompareSimExpDistributions.m	Simulates CDF of ignition timing ensemble and compares with the empirical CDF